WIRELESS COMMUNICATION IMPACT OF HIGH-VOLTAGE CORONA FORMATION ON AN ANTENNA

A Dissertation
Presented to
The Academic Faculty

by

Marcin M. Morys

In Partial Fulfillment
of the Requirements for the Degree
Doctor of Philosophy in the
School of Electrical and Computer Engineering

Georgia Institute of Technology
August 2015

WIRELESS COMMUNICATION IMPACT OF HIGH-VOLTAGE CORONA FORMATION ON AN ANTENNA

Approved by:

Professor Gregory D. Durgin, Advisor
School of Electrical and Computer Engineering
Georgia Institute of Technology

Professor Santiago C. Grijalva
School of Electrical and Computer Engineering
Georgia Institute of Technology

Professor Morris B. Cohen
School of Electrical and Computer Engineering
Georgia Institute of Technology

Professor Christopher R. Anderson
Electrical and Computer Engineering Department
United States Naval Academy

Professor Andrew F. Peterson
School of Electrical and Computer Engineering
Georgia Institute of Technology

Date Approved: 20 July 2015

DEDICATION

To my family and friends,

who supported me throughout this work.

ACKNOWLEDGEMENTS

I would like to thank Southern States, LLC, for their support and allowing me to utilize their high-voltage test set in my experimentation. A special thank you to Joe Rostron, Tan Tran, and Ryan Gerhart for their help in facilitating my experimental work.

I would also like to thank the SMART Scholarship Program for the financial support during my graduate career. Thank you to the Air Force Research Lab RYWD branch for sponsoring me, and the exciting work opportunities they have afforded me.

Thank you also to the Van Leer 5th floor group for working by my side all these years, my advisor Gregory Durgin for always being a source of good advice and encouragement, and my friends and family.

TABLE OF CONTENTS

LIST OF TABLES

LIST OF FIGURES

SUMMARY

Owing to their inherent isolation and ability for remote interrogation, wireless sensors are an effective way to monitor the operation of high-voltage power transmission lines. A wireless sensor on a high-voltage line has the potential to form corona discharges, particularly on an exposed antenna. The effects of corona formation on the antenna of a wireless radio frequency (RF) communication system were studied. The physics of corona plasma formation and charge composition was analyzed, leading to a theoretical understanding of corona interaction with the antenna. Through a series of high-voltage experiments, the effects of corona on the impedance and gain of an antenna, as well as the RF interference generated by corona current pulses, were identified. RF interference and low-frequency corona current were observed to have the largest impact on a wireless RF system. Corona was found to have no significant impact on the impedance or gain of an antenna. Based on the results, design guidelines were proposed for an antenna and RF front end to be used in wireless high-voltage sensing applications.

CHAPTER I

INTRODUCTION

1.1 Problem Statement

The objective of this research is to examine the effects of antenna corona formation on a wireless link through physical models and high-voltage experiments, and propose design guidelines to assist future high-voltage wireless system design. Owing to their inherent isolation and ability for remote interrogation, wireless sensors are an effective way to monitor the operation of high-voltage power lines and equipment, placing the sensor and radio transceiver at the high-voltage line potential. Strong electric fields around the sensor can lead to the ionization of air creating corona discharges, a form of non-thermal plasma composed of free electrons and ions. Corona on or in the vicinity of the transceiver antenna has the potential to impact communication performance by adding loss to the propagation medium, generating interference, or by causing eletromagnetic compatibility issues for the communication electronics themselves. A degradation in high-voltage sensor communication links has been observed [95], but a detailed characterization of the sources of degradation has not been performed. This research provides a comprehensive look at the the characteristics of a wireless RF front end with corona formation on the antenna.

The contributions of this work include:

- The first synthesis of work in the fields of RF communications, high-voltage engineering, and plasma physics
- Detailed measurements of RF propagation in a high-voltage corona environment
- Proposal of design guidelines for an RF communication front end for use in high-voltage sensing applications

1.2 Background

1.2.1 Motivation

There are approximately 390,000 miles of power transmission lines in the United States supplying energy to households, businesses, farms, hospitals, and and a myriad of other facilities integral to the sustainability of a modern world [8]. The goal of the power transmission infrastructure is to deliver power to all these customers efficiently, reliably, and at a low cost, both financially and environmentally [5]. The process should be transparent to the user, allowing for automatic adaptation of the power grid to the load placed upon it.

Today we are at a turning point in the life of the energy industry. For decades, the state of energy production and delivery has been in a standstill, lacking in funding for research and development [5]. A majority of the power delivery infrastructure in the United States is over 40 years old, and in need of upgrades both to prevent failure due to deterioration as well as to implement more modern technologies and techniques [8],[5],[10]. Lines are susceptible to failures due to strong winds, snow and ice, falling or encroaching tree limbs, thermal stresses, and many other factors [23],[9]. The growing demand for power is also necessitating that the load capacity of these lines be pushed to operational limits, further increasing the rate of degradation through thermal stresses [18]. These factors have contributed to a push for a modern "smart grid" with improved qualities, among which is self healing from disturbances [7]. This requires improved sensing capabilities, necessitating massive distribution of low-cost and reliable power line sensors, which rely on wireless digital communication (Figure 1).

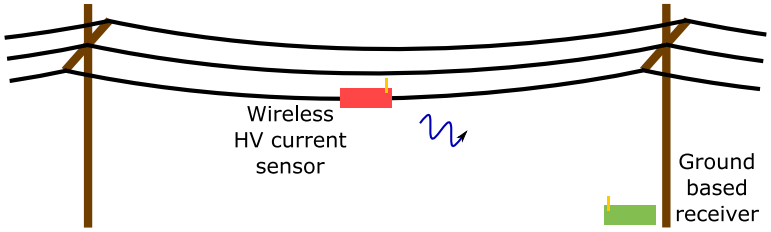

Figure 1: Diagram of wireless "smart grid" sensor implementation. Through the use of wireless communication, the need for expensive insulation measures is eliminated allowing for more widespread distribution on remote power lines as well as in centralized substations.

1.2.2 Power Grid Sensing

The "smart grid" is the vision for a next generation power grid. Through intelligent control of power distribution, great reductions in cost and environmental impact could be made [5],[9],[31],[60]. As discussed in Section 1.2, the future of the smart grid relies upon improvements in sensor technology. Specifically related to this work, much of effort is being put forth in developing a means for sensor communication.

Power distribution sensing is critical to a more efficient grid. A common problem in power distribution is a fault, or abnormal current draw, which might occur when a tree breaks a line and the line shorts to ground, for instance. In the modern power grid, various sensor-based fault location methodologies are employed to locate faults more accurately and quickly [49]. These methods include tracking the transient propagation generated by the fault, or using a transmission line circuit model to locate the fault through impedance measurements. Wider sensor deployment would allow for better fault localization. Sensing of line temperature, sag, and tension would increase the effectiveness and cost of preventative maintenance on lines. In addition, sensor deployment is necessary to handle the growing use of local renewable energy sources like home solar arrays [37]. The power grid must become more adaptive, where individual customers may act as loads or more complex sources on the grid.

There are two major categories into which power grid communication systems fall: wired and wireless. Among wired communications for the smart grid, power line communication (PLC) is a widely studied option, and one in use today. Essentially, the power transmission lines themselves are used as transmission lines for modulated information. Carrier frequencies for PLC range from kHz to tens of MHz. Implementations of PLC have been in existence for many years, allowing for both communication of power utility information, as well as third party applications such as telephone and internet. While wired technologies lie outside the scope of this work, they hold an important role in the smart grid, and a good overview can be found in [60],[34],[33],[32].

Wireless communication is a developing technology with respect to power grid sensing. It holds many advantages over a wired communication scheme. The deployment of wireless

infrastructure is less invasive, less expensive, and more flexible than a wired solution. As such, a lot of effort is being put forth to determine the best network and communication protocols for the future smart grid. In the 2012 smart grid technology survey [32], Fang et al. laid out the current state of wireless communications. They highlight the advantages of various existing protocols in different situations. IEEE 802.15.4 (ZigBee) is a good option for low power, short distance sensor deployment for smart metering. IEEE 802.11 and 802.15 are good candidates for wireless transmission of power usage on a local level, such as in a Home Area Network (HAN) and Neighborhood Area Network (NAN) [22]. Cellular technologies such as 3G/4G LTE are mature and widespread, and could be used for communication over longer distances using existing infrastructure. Microwave point-to-point communication provides a reliable way of communicating over longer distances with wide bandwidth. Satellite communication is also a feasible option for substation monitoring in remote locations. Lo and Ansari provide a similar overview of wireless technologies [60], as do Fan et al. in a more recent 2013 survey [31].

Recent surveys by Fang, Lo, and Fan show a lot of current research on the network layer and higher, as defined by the OSI model [102].Publications also show considerable effort being put into control [77] and grid management [72]. While many pressing issues still remain to be addressed in the higher layers, there are many questions to be addressed at the lower layers, where the proposed research focuses, to ensure proper system operation [37].

One promising technology currently being developed on the lower layers (physical and data link) is the IEEE 802.15.4g standard [31],[43]. This standard is being developed by the IEEE 802.15 Smart Utility Networks (SUN) Task Group 4g. It will provide a global standard for large scale networked sensor node deployment. 802.15.4g is defined in a number of frequency bands globally [91], with frequencies ranging from 450 MHz to 2483.5 MHz. In [91], Sum et al. provide a comprehensive analysis of interoperability challenges of this new standard with existing wireless protocols. Partly due to its global adaptation, the 2.45 GHz band is a common choice for new sensor network development.

Commercial developers have already emerged in the wireless sensing market. Sentient Energy, Inc. has developed a wireless power line sensor for fault detection. The Sentient

Figure 2: MM3 Line Monitor from Sentient Energy, Inc., rated up to 35 kV [90] for remote power line monitoring.

MM3 Line Monitor (Figure 2) can be mounted remotely on power lines up to 35 kV. It harvests its energy directly from the power line via magnetic induction and communicates via cellular data or an IEEE 802.15.4g mesh network [90]. Southern States, LLC has developed a wireless fault detection platform, the CMD II [1]. Intended for deployment on substation busbars, the CMD II (Figure 3) is rated for voltages up to 362 kV. The unit communicates with a ground based transceiver located directly below the busbar over a 2.45 or 5.8 GHz communication link. While development in the area of high-voltage sensing is growing, high-voltage systems as high as 1000 kV exist in North America and around the world. Wireless sensing applications are yet to be developed with compatibility up to these voltage levels.

1.2.3 Problem Overview

1.2.3.1 Wireless Digital Communication

The performance limitations of a wireless digital communication link can be simply described in two equations. The first equation is the free space link budget (1), a relationship between the transmitted and received power that conveniently bundles complex electromagnetic interactions into scalar constants allowing back-of-the-envelope calculations.

Figure 3: CMD II fault detection sensor from Southern States, LLC, rated up to 362 kV for substation monitoring [1].

$$P_R = \frac{P_T G_T G_R \lambda^2 (1 - |\Gamma_T|^2)(1 - |\Gamma_R|^2)}{(4\pi r)^2} \tag{1}$$

P_R is the received power, P_T is transmitted power, G_T is the gain of the transmit antenna, G_R is the gain of the receive antenna, λ is the RF carrier wavelength, Γ_T is the transmit antenna mismatch reflection, Γ_R is the receive antenna mismatch reflection, and r is the transmit-receive separation distance.

The second equation commonly used to asses a wireless link is the Shannon-Hartley theorem, which relates the maximum capacity of the channel to the bandwidth and signal to noise power ratio (SNR) of the system (2). Here C is the channel capacity, B is bandwidth, and noise is Additive White Gaussian Noise (AWGN).

$$C = B\log_2(1 + SNR) \tag{2}$$

Assuming the communication bandwidth is narrow enough that (1) evaluated at the carrier frequency adequately describes propagation across the band, the two equations can be combined into one (3). The received SNR is broken into its constitutive components, the received signal power P_R used in (1) divided by the noise power P_N. Equation (3)

provides a metric by which to understand the impact of changes in a communication link on the received bit rate. By individually measuring the system parameters in (3), such as the antenna gain G_R, the total impact on communication performance can be quantified. This study seeks to understand the impacts of antenna corona formation on communication performance.

$$C = B\log_2\left(1 + \frac{P_T G_T G_R \lambda^2 (1 - |\Gamma_T|^2)(1 - |\Gamma_R|^2)}{P_N (4\pi r)^2}\right) \tag{3}$$

1.2.3.2 Corona Effects on Communication

High-voltage power transmission lines can be described as long, relatively thin conductors at a high voltage above ground potential. The electric potential is used here interchangeably with voltage, referenced to earth ground potential of 0 V. Figure 4 illustrates a simple cross section of a line-to-ground geometry. Using Poisson's Equation for the electric potential around the line, it can be determined that the potential gradient, or electric field magnitude, decreases as $\sim 1/r$ in the vicinity of the line's surface, where r is the distance from the line center. In the immediate vicinity of a spherical point, the electric field magnitude decreases as $\sim 1/r^2$, where again r is the distance from the point center. Therefore, as the size of the high-voltage object decreases, the electric field magnitude at its surface increases significantly.

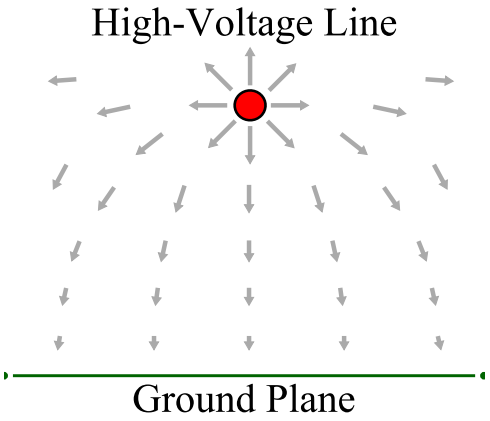

Figure 4: Cross section of basic power line geometry illustrating strong electric fields near line surface.

The strong electric field at the surface of power line, or other point-like geometry protruding from it, can induce corona discharge formation. Either positive or negative corona can form on an AC power line, depending on whether the line potential relative to ground is at the positive or negative phase. The spatial and transient characteristics of the corona are determined by the polarity, conductor geometry, and voltage.

Corona discharges are typically localized and impulsive, consisting of a nonthermal plasma of free electrons and ions [19]. In [75], the author used a dispersive Drude dielectric model for cold plasmas to simulate the effects of a plasma layer on a patch antenna, showing the relative impact on the antenna gain and impedance. Equation (3) is useful in quantifying the effects a corona discharge has on a high-voltage wireless sensor node antenna. The affected parameters could be G_R, Γ_R, and P_N when receiving, and G_T and Γ_T when transmitting. Figure 5 illustrates the problem.

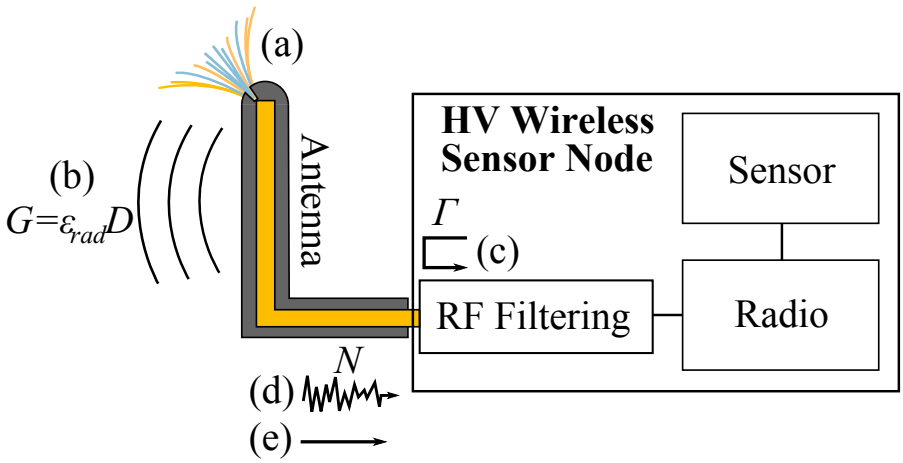

Figure 5: (a) Corona can form on a high-voltage wireless sensor node antenna through high electric field stresses. (b) It can affect the gain through power absorption, thereby decreasing ε_{rad}, or altering the directivity D. (c) Corona interaction with the antenna can alter the resonance and input reflection, Γ. (d) RF Noise generated in corona processes is coupled into the system increasing the noise power, P_N. (e) Electron flux in the corona induces a DC current on the antenna that could damage sensitive RF components in the radio front end.

The results in [75] show that the presence of the Drude conducting medium on the

antenna can affect both the gain (primarily through loss in efficiency) and impedance mismatch. The extent of these effects depends greatly on the plasma electron density, thickness, and antenna coverage. The study in [75] focuses on a generalized worst case scenario of complete antenna coverage, but the effects of point discharges on antenna gain and impedance remain largely unknown. These effects are depicted in Figure 5 (b) and (c), respectively. It is important to note here that the gain of the antenna is being defined as the net gain when including the corona in the physical system. Therefore, any wave attenuation in the plasma is accounted for as a decrease in radiation efficiency ε_{rad}.

Measurements show that the impulsive nature of atmospheric pressure discharges generates RF interference [46], [59], illustrated in Figure 5 (d). Interference that is flat over a narrow communication band constitutes an increase in the noise (P_N in (3)), which in turn corresponds to a loss in maximum bit rate. The net result of the corona impulses is to generate a DC current on the antenna, as in Figure 5 (e). The impact of a DC current on the system performance depends on the coupling of the antenna to the radio and the sensitivity of the RF front end electronics.

1.2.3.3 Research in Plasma Effects On Antennas

A study was performed in 1946 [51] related to corona effects on communication. The effect of precipitation-static corona on airplane antennas in flight was characterized, and methods for alleviating the issues were proposed. In this joint U.S. Army-Navy study, it was shown that high static charge can be built up on an airplane in flight, resulting in static discharges or corona at sharp points. A corona discharge on an antenna wire generates noise voltage levels orders of magnitude higher than in ambient conditions. Corona interference was the only metric considered.

This study proposed two methods for reduction of corona interference. The first, which was verified in non-flight conditions, acts by disrupting transient corona currents (which generate interference) by forcing the discharge to occur on a high-resistivity material. For instance, a sharp, high-resistivity wire near the antenna is able to charge up to the same potential as the aircraft. When corona forms on it, the high impedance conductor prevents

the corona from sustaining itself.

In the second method, a dielectric is used to coat and insulate the antenna wire. Dielectric breakdown occurs when the electric field strength surrounding a conductor, modified by the geometry as in Peek's law (22), exceeds the dielectric strength of a material. For air, the dielectric strength is on the order of 30 kV/cm. Surrounding the antenna with a material such as polyethylene with a dielectric strength of 100 kV/cm can prevent breakdown [51].

The limitations of the Army-Navy study, which will be addressed in the research, are as follows.

1. The study only characterized corona-antenna interactions at 300-900 kHz, while modern sensor RF communication operates at 700-5800 MHz.
   (a) The corona noise varies greatly with frequency [59],[83].
   (b) At UHF or microwave wavelengths, corona size would be on the order of the antenna, possibly impacting structural resonance.
2. The study only considers a DC static charge. There is no knowledge of behavior in an AC system with time varying fields and positive and negative corona.
3. The solution of fully relying on dielectric-coating for corona prevention is not ideal for high-voltage sensor applications.
   (a) Small dielectric imperfections can result in dielectric failure and corona, further damaging the insulation [81],[36].
   (b) Corona interference through compromised dielectric is comparable to the case of no dielectric at all [51].
   (c) Replacement of antennas on high-voltage lines is costly, so the system should be well characterized and functional even in the event of corona formation.

The current work expands the study of corona formation on an antenna to to higher frequencies and AC voltages.

There have been analytical calculations on how an antenna would perform if immersed in a uniform conducting medium like a plasma [29]. Early experiments utilized salt water to

emulate such behavior [44]. The results of these basic experiments show the reduction in the quality factor of the antenna resonance and a shifting up of the antenna resonant frequency due to the high dielectric constant of the water. A decrease in quality factor was observed in the author's previous simulations as well [75]. In terms of a simple antenna circuit model, the decrease in quality factor can be interpreted as the addition of a lossy plasma resistance, leading to reduced antenna radiation efficiency and increased input reflection.

Studies on antenna behavior in the presence of plasma have been focused on a few specific applications. Most notably, the performance of an antenna in plasma has been studied for space reentry vehicles [38]. Upon re-entring the atmosphere, a spacecraft experiences a tremendous amount of friction with the air molecules it moves through. The energy dissipated through this friction is high enough to generate a layer of plasma on the front surface of the spacecraft. The thickness of the plasma is on the order of 10s of cm [62],[53]. The plasma acts as a thick conductive layer, severely attenuating an electromagnetic wave passing through it, potentially causing a complete radio blackout. Similar plasma behavior is observed with supersonic aircraft and missiles [35]. Many studies were carried out in the early days of the space program to find solutions to this problem. In 2007, a study was performed for the U.S. Department of Transportation assessing the causes and methods of radio blackout mitigation [38]. A study in 2010 for NASA addresses methods for mitigating communication blackout [35].

One method of mitigating communication blackout for aircraft that could be translated to corona attenuation is the "magnetic window" [38],[52]. It has been shown that for space reentry plasma, propagation of circularly polarized modes through the plasma can be improved by applying a strong static magnetic field in the direction of propagation, creating a "magnetic window." This result follows directly from the Appleton-Hartree equation for cold plasma in a magnetic field. Unfortunately, application of this equation shows that gains in transmission through the plasma decrease with higher pressures (as in atmospheric pressure) [42]. If severe attenuation is an observed issue, a strong rare earth magnet could be used to to alleviate the plasma shielding effect.

The space reentry plasma problem differs from high-voltage corona on an antenna in

some fundamental aspects. The first difference is that the space reentry plasma is thick and typically assumed uniform across the antenna length. A corona discharge on the other hand occurs at points, such as a corner of the antenna. Secondly, the density of air is small at reentry altitudes, whereas high-voltage corona will occur at atmospheric pressure with much higher molecular density. Low density plasma exhibits a sharp frequency cutoff, where it appears opaque at low and transparent at high frequencies (transitioning at the plasma frequency), whereas high density plasma has a more gradual attenuation profile [20],[58]. Thirdly, a corona plasma is impulsive and driven by an electron current on the antenna, leading to different design considerations.

1.3 Problem Approach

The approach to understanding the effects of corona formation on wireless communications follows a comprehensive strategy involving theory, simulation, and experiment. This workflow is presented in Figure 6.

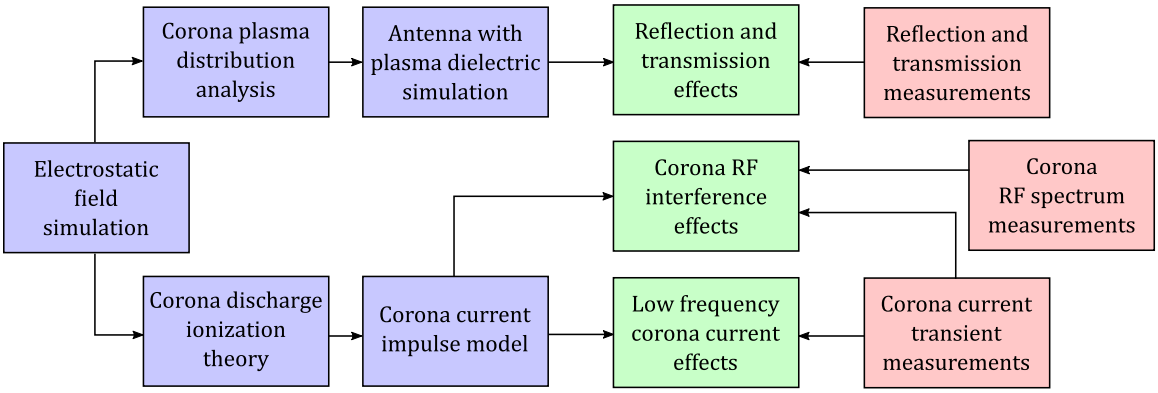

Figure 6: Approach to understanding corona effects on a wireless system. Blue sections represent analytical and simulation work, red sections represent experimental work, and green sections represent the results.

Electrostatic simulations are carried out for high-voltage geometries to gain knowledge of the electric fields surrounding the conductors. Knowing the electric fields, models for air ionization and attachment processes can be utilized to estimate the distribution and density of electrons in a corona formation. A complete air ionization study is beyond the scope of this work, but modeling methods and results outlined by other researchers are

utilized to create plasma distribution profile. From the electron density, an antenna can be simulated using an equivalent dielectric model. These results would highlight the expected impedance and transmission (related to antenna gain and loss) effects of corona on an antenna. Measurements using a vector network analyzer (VNA) are taken and compared with the simulation.

The radio frequency (RF) interference and low frequency (LF) corona current are both related to the transient profile of the corona current. With a knowledge of corona formation processes based on theory, the evolution of current at the corona electrode can be obtained. With a model for corona pulses, the RF and LF spectral content is derived. Measurements of the corona RF spectrum are taken using a spectrum analyzer. Corona current is also measured using an oscilloscope. The oscilloscope sampling rate is too low to obtain RF information. Nevertheless, these measurements provide information on the temporal distribution of corona current and the total average current in a pulse. This information is used in the corona impulse model to obtain the RF content.

CHAPTER II

HIGH-VOLTAGE SYSTEMS

The focus of this chapter is to provide the background for power transmission systems needed to support the research discussed in this dissertation, specifically the characteristics that determine electric field distribution and corona formation. High-voltage transmission systems exist in a variety of forms including underground and DC power systems, but due to their ubiquity, the primary focus here is on overhead AC line systems. This work is not intended as a comprehensive study of the transmission process, and will simply address high-voltage transmission as it relates to the potential for corona formation.

The information of interest includes:

- Voltage levels
- Conductor types and sizes
- Conductor configurations and spacing
- Clearance from earth
- Corona mitigation measures

2.1 High-Voltage Transmission Systems

The efficiencies of centralized power generation and the ability to balance the regional and temporal variations of power consumption were a strong force behind the creation of vast power distribution grids spanning most industrialized regions of the world. The North American grid (Figure 7) is particularly massive and complex, involving over 9,000 generation stations, over 200,000 miles of high voltage (HV) power lines rated at or above 230 kV, and thousands of substations providing power switching, transformation and monitoring capabilities [78].

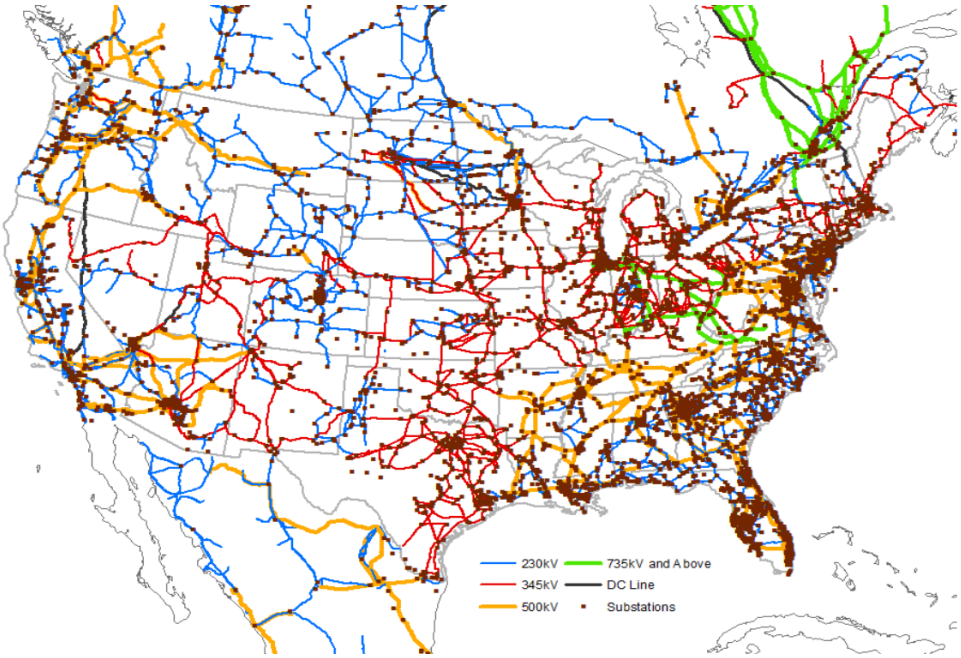

Figure 7: North American Electric Grid [78].

The basic structure of the power transmission system is shown in Figure 8 [4]. The voltage produced by power generators is transformed up to one of the standard values used for medium and long term power transmission. In North America the majority of power transmission lines are carrying AC at one of the standard voltages of 138kV, 230kV, 345kV, 500kV and 765kV. At a substation the voltage is transformed down into one of the Primary or Sub-transmission voltage levels between 4kV and 69kV. For secondary customers the voltage is transformed down again to a level of 120 or 240V.

This work will focus on the overhead AC transmission infrastructure operating above 100 kV that constitutes the majority of the North American power grid.

2.1.1 Transmission Lines

The conductors of high voltage transmission line are supported by towers. Their role is to maintain proper separation between conductors carrying three phases as well as the clearance from conductors to ground. Transmission lines commonly carry one or two separate 3-phase circuits (Figure 9). Construction of the towers as well as configuration of the wires vary greatly (Figure 10). In Figure 9 are three types of towers carrying 230 kV lines from

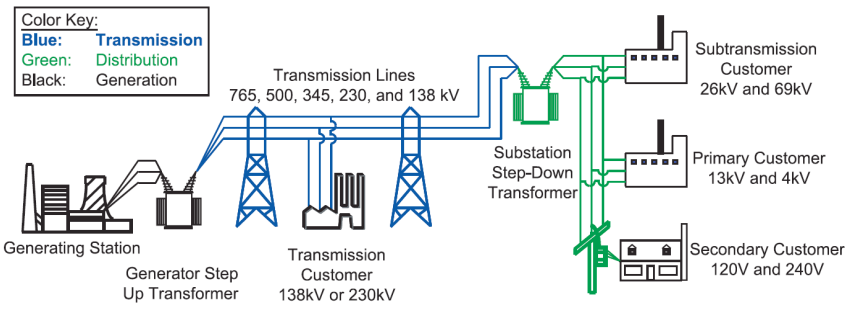

Figure 8: The structure of the power transmission grid [4].

Atlanta, Georgia's Plant McDonough-Atkinson. While design guidelines exist for certain safety related aspects of tower design, there are many different designs that can be implemented for any particular voltage. The choice of tower design may be influenced by the cost, materials, and regional terrain. The wires might be distributed horizontally, vertically or in an alternating pattern. Typically, one or more Earth Ground wires, called shield wires, are also carried on the top of the towers. These wires are electrically connected to the towers providing a direct path for lightning to ground through the tower structure and the ground straps at the base of each tower.

Figure 9: Example of 230 kV high-voltage transmission lines running from Atlanta's Plant McDonough-Atkinson. From left to right are a double circuit single pole davit arm, single circuit H-frame, and a different double circuit single pole davit arm.

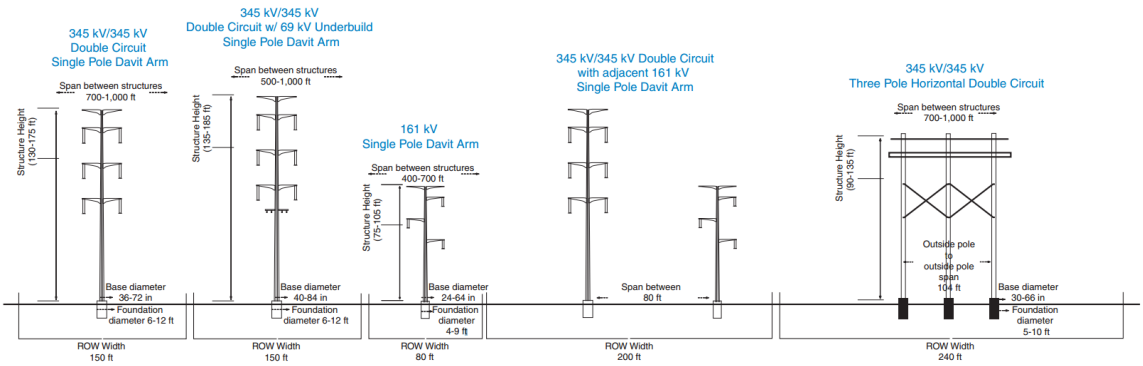

Figure 10: Examples of transmission line pole construction and conductor configurations [56].

High-voltage power lines are attached to the towers with insulating strands. Insulators for high-voltage power lines are typically built up from porcelain disks approximately 10 inches in diameter. Each insulator may consist of up to 30 disks. To minimize lateral motion of the wire two insulators might be used to support a wire in a V-shaped formation.

The conductors used in high power transmission lines are typically Aluminum Conductor Steel Reinforced (ACSR), All Aluminum Alloy Conductor (AAAC) or Aluminum Conductor Composite Core (ACCC) (Figure 11). Copper is rarely used due to its cost. In order to increase power transmission capacity and reduce the potential gradients near the wire, it is a common practice to use bundles of multiple parallel conductors (Figure 12). Subconductor spacings for bundled conductors range from $400mm$ to $600mm$ typically. In North America a common subconductor spacing is $18in$, or $457mm$ [50].

Figure 11: Examples of various conductors used in high-voltage power transmission.

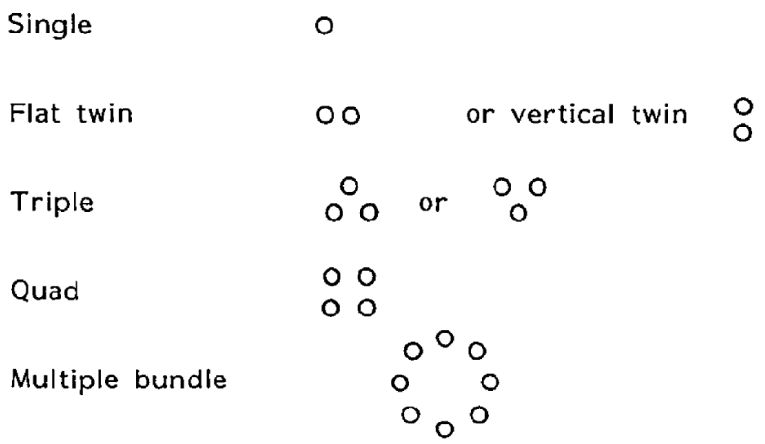

Figure 12: Common configurations of conductor bundles [18]. In the United States, the separation distance of subconductors in a bundle is commonly 18 inches.

Table 1: Basic electrical safety clearances for power substation high-voltage conductors based on the international standard IEC 60071 [18]

Nominal voltage (kV rms)	Phase-earth clearance (m)	Phase-phase clearance (m)
123	0.9	0.9
145	1.1	1.1
170	1.3	1.3
245	1.5	1.5
300	1.6	2.4
362	1.8	2.7
420	2.2	3.1
525	3.1	4.3
765	4.2	7.1

2.1.2 High-Voltage Transmission Line Clearances

The potential gradients around high-voltage power lines are dictated by the diameter of the conductor, the bundling if applicable, and the clearance of conductors from ground and each other. For the purposes of assessing the corona formation risks in high-voltage applications, recommended conductor and ground clearances have been found and are recorded in Tables 1-4.

2.1.2.1 Overhead Transmission Line Standards

Figures 14 and 13 show examples of power line configurations with dimensions for overhead AC transmission. The configurations are shown for 275 kV and 400 kV, respectively. The

Table 2: Recommended design vertical clearance of line to ground in open space, pedestrian access only (Table 4-1) [30]

Nominal line-line voltage (kV rms)	Line to open land clearance (ft)
46	17.2
69	17.7
115	18.6
138	19.1
161	19.5
230	20.9

Table 3: Recommended vertical separation between phases in span with horizontal separation $\geq$ 1.0 ft (Table 6-1) [30]

Nominal line-line voltage (kV rms)	Vertical separation (ft)
46	2.5
69	3.3
115	4.9
138	5.7
161	6.5
230	9.0

Table 4: Common wire configurations for a specified voltage and power handling capability. The multiplier indicates the number of wires in a bundle.

Line voltage	**Power capacity**	**Nominal Al area** [mm^2]	**Historical code**	**Single wire OD**
138 kV	100 MVA	200	1xPANTHER	21
230 kV	400 MVA	2x250	2xBEAR	23.5
345 kV	800 MVA	3x200	3xGOAT	26
500 kV	2 GVA	4x300	4xGOAT	26

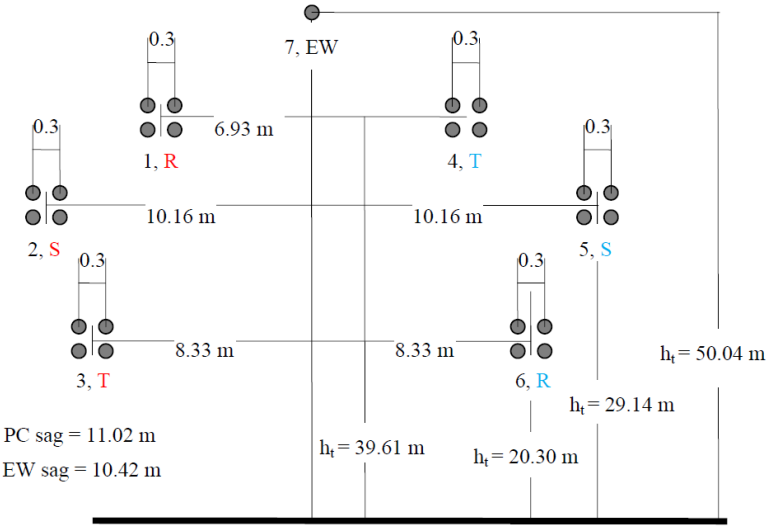

Figure 13: Sample cross section of the wire topology for a 500 kV overhead high-voltage transmission system. Two circuits with quad bundled conductors are used, with a single grounding wire above the lines.

power line cross sections illustrate the spacing between the three conductors of a circuit with the ground and ground wires. In the 500 kV topology, two circuits are run in parallel, with the three phases of each circuit running on either side. A single ground wire resides above the transmission lines for lightning protection. In the 345 kV topology (Figure 14), a single-circuit layout is used with the three phases spaced apart horizontally. Conductor bundles are used with two subconductors.

2.1.3 Electric Fields Around High-Voltage Lines

The design of high-voltage transmission lines takes into consideration the electric field magnitude around the lines. The diameter of the conductors and the separation distances between line conductors and ground must be sufficient to avoid the electrical breakdown of the surrounding air.

A model is created in COMSOL Multiphysics of the high-voltage setup in Figure 14. The geometry consists of a single-circuit of three phases with a line-to-line voltage of 345 kV. The line-to-line RMS voltage of 345 is related to the line-to-neutral voltage amplitude by (4).

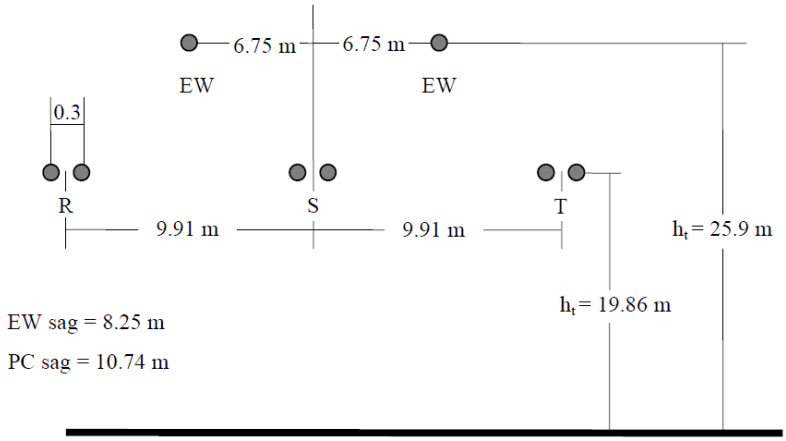

Figure 14: Sample cross section of the wire topology for a 345 kV overhead high-voltage transmission system. A single circuit with flat twin subconductor bundling is used are used, with two grounding wires above the lines.

$$V_{LN,amp} = V_{LL,RMS}\sqrt{2}/\sqrt{3} \tag{4}$$

A 2D simulation of the electric fields is performed over a single 60 Hz cycle. A cross section of the lines is used with translational symmetry, equivalent to assuming the measurement plane is far from the transmission towers or other nonuniformities.

The peak electric field over the course of a single cycle for this geometry occurs on the outer edges of the Phase 1 and 3 bundles when they are at their respective voltage peaks. Figure 15 shows the electric potential contour plot when Phase 3 is at its voltage peak. The equipotential lines show that even in a complex geometry, the potential near the conductor maintains a circular symmetry, seen in Figure 16, where the two subconductors of Phase 3 are shown. From the figure, an equipotential contour circle at 100 kV is seen to have a radius of 2.4 m around the conductor bundle, which has a peak voltage of 280 kV. The fields around these conductors could therefore be equivalently simulated with a circle at 0 V around the lines at $(280 - 100) = 180$ kV. This in turn equates to 130 kV RMS line-to-neutral. The conclusion here is that to experimentally measure peak corona formation for the 345 kV transmission topology in Figure 14, it is sufficient to use a setup of 130 kV over a distance of approximately 2.4 m.

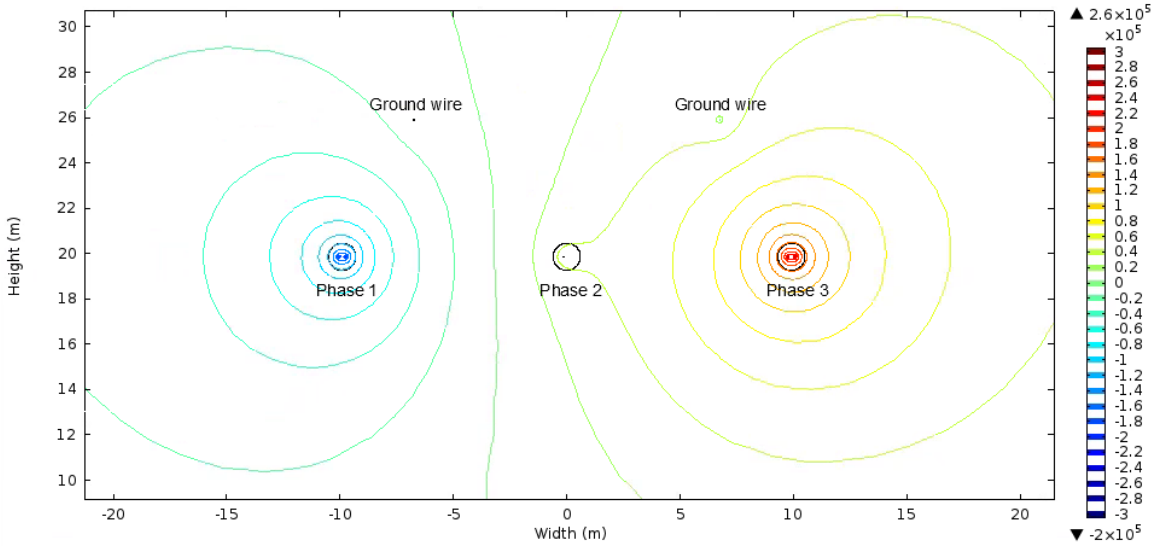

Figure 15: Electric potential contours for a 345 kV single-circuit H-frame transmission line topology with flat twin subconductor bundling. Phase 3 is at its peak amplitude at the time of this potential distribution.

The peak electric field at the conductor surface is 20 kV/cm, below the approximate 30 kV/cm threshold for electric breakdown in air. Simulations are then run in 3D to obtain the electric field magnitude that would develop around a wire antenna mounted with a sensor on the high-voltage transmission line. Figure 17 shows a COMSOL 3D meshed model of a sensor design that could be used in transmission line applications. The tubular sensor module shape is based on a prototype developed by Kreikeebaum et. al. [54]. The module is 30 cm in length with a 10 cm diameter and spherically tapered ends. In the model, a 5 cm wire monopole antenna is protruding from the sensor casing to simulate the electric fields experienced by the antenna.

An electric field heat map with equipotential contours is provided in Figure 18. The results show electric field magnitudes up to 400 kV/cm at the monopole corners, with fields above the 30 kV/cm air breakdown threshold extending 3 mm from the tip of the wire.These conditions are sufficient to induce corona formation on the wire antenna. Other antenna geometries, such as planar antennas flush with the module surface, could be used to reduce the potential gradient around the antenna. In designing high-voltage wireless sensors, potential gradients should be minimized around the unit to avoid corona formation.

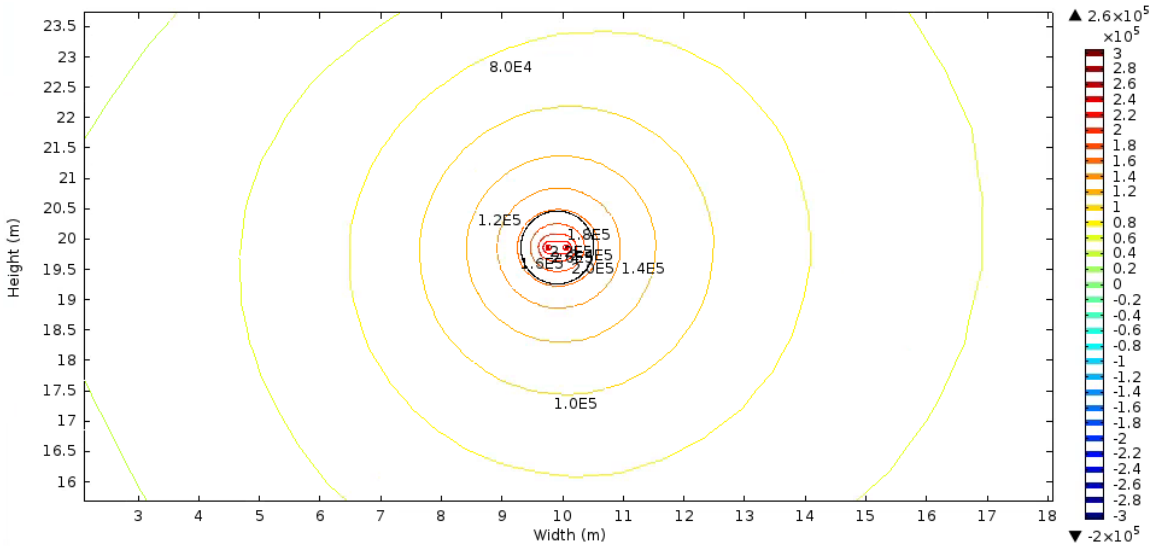

Figure 16: Electric potential contours for a 345 kV single-circuit H-frame transmission line topology with flat twin subconductor bundling. The figure is zoomed in on Phase 3 when it is at its peak amplitude.

Nevertheless, long-term environmental exposure may result in undesirable corona on or around the antenna and it is also important to understand the effects it may have on communication.

2.2 Corona Plasma

In high-voltage power transfer on overhead power lines, corona formation is an ever-present issue. If the electrical breakdown of air were not an issue, the power lines could be bundled much more closely together, saving cost and space in transmission tower construction. Unfortunately at the high voltages used in power transfer (>100 kV), the breakdown of air due to electric field stresses is a real issue [63]. Complete breakdown, the formation of an arc between two conductors, can be avoided by spacing the lines sufficiently far apart. However, even with a large spacing partial discharges in the air surrounding the line, called corona, can still form. The following discussion treats the physical nature of corona. With this knowledge, the impacts of corona on high-voltage wireless sensors can be analyzed.

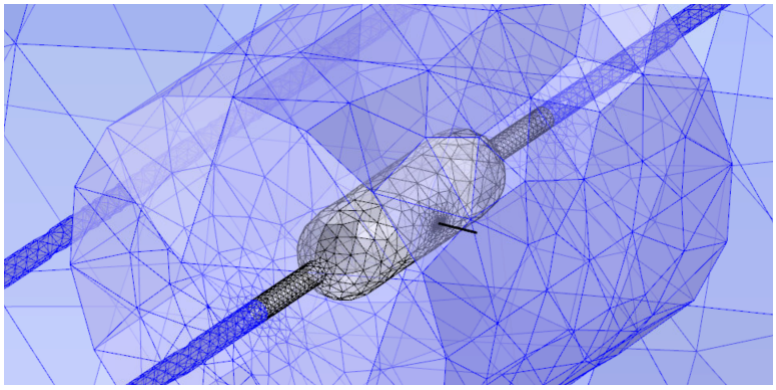

Figure 17: Meshed geometry in COMSOL of a generic sensor module mounted over a single subconductor of a flat twin 345 kV transmission line.

2.2.1 Corona Overview

Corona is a local non-thermal electrical discharge. It is a partial discharge, a type of plasma, that occurs in a gaseous medium whereby the discharge does not span the entire gap between two electrodes [14]. Corona forms in highly non-uniform electrode geometries, where large electric field gradients form around an electrode of small effective radius. A geometry commonly associated with the formation of corona is the point-to-plane, illustrated in Figure 19. A thin cylinder above and running parallel to a plane is related to the point-to-plane geometry with translational symmetry. In this geometry, most of the electric potential drop between the two conductors occurs in close proximity to the point. As a result, extremely high electric field magnitudes can be created near the surface of a small electrode much larger than would be created by two large parallel-plate electrodes. This is described mathematically in (5), where V is the potential difference between the the electrodes and d is the separation difference.

$$E_{point-to-plane} >> E_{plane-to-plane} = \frac{V}{d} \tag{5}$$

Corona formation occurs in the local region around the point-like electrode where the electric field magnitude is large enough to sustain ionization of the gaseous medium.

In addition to being local, corona formation is also non-thermal. In a non-thermal plasma, the constituent species are not in thermal equilibrium, meaning the exchange of

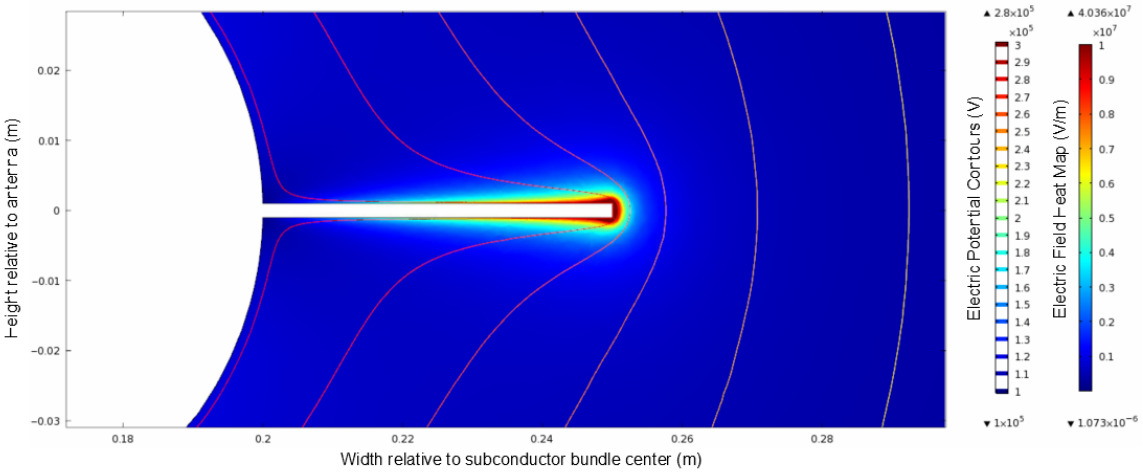

Figure 18: Electric field magnitude heat map and equipotential contours for cross section of the antenna and sensor geometry shown in Figure 17. The results show the peak electric field around the 2mm diameter wire monopole on the 345 kV transmission line.

energy through collisional interactions is insufficient to bring the different species of the gas to equilibrium. In the case of corona, the electron temperature is much larger than the average gas temperature, which remains close to the ambient temperature. This is largely due to the difference in mass between the electrons and molecules. Table 5 presents the weights of molecular nitrogen and oxygen, two abundant species in air largely involved in corona formation processes. While other species are involved in corona formation, it is sufficient to show that the mass of an electron is many orders of magnitude lower than that of the protons and neutrons that constitute molecules.

Equation (6) is the simple relation between the acceleration, a, of a particle of charge q and mass m in an electric field E.

$$a = \frac{qE}{m} \tag{6}$$

After a short time t (ignoring the effects of collisions) the particle will have accelerated to a velocity $v = at$. Equation (7) then relates the temperature of the particles T and the mass m, where k_B is the Boltzmann constant.

$$T = \frac{m\bar{v}^2}{3k_B} \Rightarrow \frac{q^2E^2t^2}{3mk_B} \propto \frac{q^2}{m} \tag{7}$$

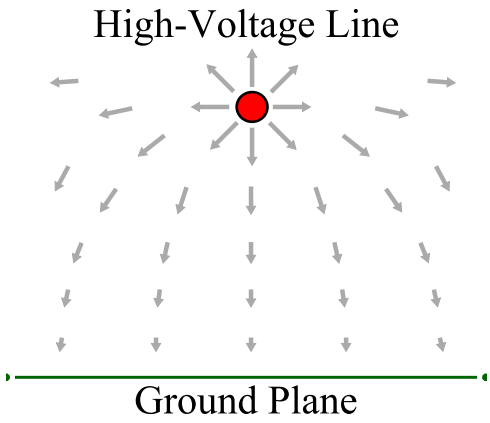

Figure 19: Cross section of basic power line geometry illustrating strong electric fields near line surface.

The average temperature of massive species such as oxygen and nitrogen ions in an electric field is inversely proportional to the mass, and hence many orders of magnitude lower than free electron temperature. Also, due to the small mass of electrons, energy exchange through collisions is inefficient. Assuming an elastic collision between an energetic electron and a stationary neutral molecule, the fraction of energy imparted to the molecule is approximately proportional to the ratio of the masses. Therefore, in an elastic collision between an energetic electron and air molecule in a corona, only 0.002% of the electron's energy is transferred to the molecule. The inefficient transfer of energy to relatively massive ions and molecules results in the non-thermal equilibrium observed in corona.

Table 5: Molecular weights of species largely active in dry air corona formation

Species	Mass (kg)	Ratio to electron mass
Electron	9.109×10^{-31}	1
Nitrogen (N_2)	3.986×10^{-26}	4.4×10^4
Oxygen (P_2)	5.315×10^{-26}	5.8×10^4

2.2.2 Non-uniform Electric Fields

High-voltage power transmission topologies are generally constructed of three parallel wires above ground with voltages that are 120^o out of phase with one another. At a 60 Hz frequency, the voltage wavelength traveling down the line is sufficiently long to treat the voltage at any point as constant, with translational symmetry. When computing the electric

fields near the power lines, one can assume translational symmetry to simplify the problem, utilizing a cross section of the power line topology. This also makes the assumption that the fields are being calculated sufficiently far from other translational asymmetries such as transmission towers.

The electrostatic fields surrounding a conductor in air can be computed using Poisson's equation (10), where V is the electric potential, ρ_f is the free charge volume density, and ε is the electric permittivity. In regular operating conditions in atmospheric air, the assumption can be made that the air is free of charge, and Poisson's equation can be further reduced to Laplace's equation, where $\rho_f = 0$. For complex geometries, Laplace's equation can be solved numerically, but great insights can be made into the nature of the electric fields surrounding a point or line through simplifying assumptions that allow for analytical solutions. The electric fields for coaxial cylinders and concentric spheres are presented in (8) and (9), respectively. R_0 is the radius of the outer shell, r_0 is the radius of the inner shell, and r is the distance where the field is sampled, all relative to the central axis or point. V is the potential difference between the inner and outer shell.

$$E_r\left(r\right) = \frac{V}{\ln\left(\frac{R_0}{r_0}\right)}\frac{1}{r} \tag{8}$$

$$E_r\left(r\right) = \frac{VR_0r_0}{R_0 - r_0}\frac{1}{r^2} \tag{9}$$

$$\nabla^2 V = -\frac{\rho_f}{\varepsilon} \tag{10}$$

For a small cylindrical or spherical electrode (inner shell) some distance away from an arbitrarily shaped ground (outer shell), if $R_0 \gg r_0$ then the electric field near the surface of the inner shell ($r \sim r_0$) will have a gradient similar to the concentric case. The electric field magnitude in close proximity to a high-voltage cylinder falls off as $1/r$, and in close proximity to a sphere falls off as $1/r^2$. This nonlinearity in the field magnitude allows for corona formation around high-voltage geometries of small effective radii. The large electric potential gradients in the local region provide the energy to accelerate electrons to

speeds capable of further ionizing molecules, leading to electron avalanches. The electric field induced electron avalanche is the starting mechanism for corona formation, which is further modified by the resulting distribution of positive and negative ions, and secondary ionization by photons.

Along with electric field magnitude, corona formation is affected by the polarity of the field. With the point electrode (electrode of small effective radius) at a higher voltage than ground, the point acts as the anode and the ground acts as the cathode. In this scenario, the electric field vectors point from the anode to the cathode, opposite the direction of electron acceleration. Positive corona formation occurs, where electrons accelerate toward the anode with increasing acceleration. When the point electrode is at a lower voltage than ground, the point is the cathode and the ground is the anode. In this scenario, negative corona formation occurs, where electrons accelerate away from the cathode with decreasing acceleration. The ions, being more massive than the electrons, slowly drift toward the electrode of opposite polarity.

Much of the high-voltage power transmission around the world is AC, either at 50 or 60 Hz. In an AC system, the voltage of the line alternates between being at higher and lower potential than ground. Corona formation on one of the high-voltage transmission lines will alternate polarity with the line voltage. Therefore, both positive and negative corona processes must be considered.

2.2.3 The Electron Avalanche

Corona is a partial electrical discharge that occurs when high voltage is applied to an electrode with a small effective radius in air. The process of corona formation is complex, involving the interactions of all the various species in the gas with a non-uniform spatial and electromagnetic field distribution. Electrical discharges have been studied experimentally and theoretically since the late 19th century. At the turn of the 20th century, Townsend's early contributions to the field paved the way for our current understanding of discharge formation by an avalanche of charged particles in a strong electric field [92]. The *first Townsend ionization coefficient*, α, relates the number of electrons formed per unit distance

through ionization by collision to the number of electrons present at a point in space. At lower electric field magnitudes, less energetic free electrons can also attach to an electronegative gas such as oxygen, resulting in an *attachment coefficient*, η. Empirically measured ionization and attachment coefficients for air are provided in Appendix A.

In a simplified scenario, α is the rate of electron (and positive ion) formation per unit distance while η is the rate of electron loss (and negative ion formation) per unit distance. The two can be combined into a net ionization coefficient, α', which is the net rate of electron formation per unit distance (11) [86].

$$\alpha' = \alpha - \eta \tag{11}$$

For every electron traversing one meter of distance, it generates α' new electrons along the way by means of collisions with neutral molecules (12).

$$dN_e(x) = N_e(x)\alpha'(x)dx \tag{12}$$

The ionization coefficient increases with electric field magnitude as the electrons gain sufficient kinetic energy to ionize a molecule in a shorter distance. In an electrode geometry where the field magnitude is not constant with distance (anything other than plane-to-plane), the net ionization coefficient will vary with position. In (12), N_e is the number of electrons at point x, and x is the distance from the origin of the avalanche, following along a path opposite that of the electric field vectors in space.

Integrating (12), the number of electrons at position x can be determined, assuming there are N_0 electrons at the beginning of the path (13). N_0 is commonly set to 1 because only one electron is needed to start an electron avalanche [86]. The exponential growth of the electrons with distance is characteristic of the electron avalanche. After an initial avalanche, the electric field and positive and negative ion distributions in space determine the type of electrical discharge that develops.

$$N_e(x) = N_0 e^{\int \alpha'(x)dx} \tag{13}$$

During a single electron avalanche, the ions that are formed can be assumed stationary because of their much lower mobility, resulting from their large mass. With that simplifying assumption, the number of positive ions at a point in space x can be determined from the number of new electrons formed at that point in the avalanche.

The net number of electrons formed per unit distance is simply the derivative of (13), given in (14). The rate of positive ion formation per unit distance is then proportional to the ionization coefficient (15), and the rate of negative ion formation per unit distance is proportional to the attachment coefficient (16). The number of positive ions formed in the avalanche in a region between x_1 and x_2 is given by (17), and similarly for negative ions (18). [86]

$$\frac{dN_e}{dx} = \alpha' N_0 e^{\int \alpha'(x)dx} = (\alpha - \eta) N_0 e^{\int \alpha'(x)dx} \tag{14}$$

$$\frac{dN_p}{dx} = \alpha N_0 e^{\int \alpha'(x)dx} \tag{15}$$

$$\frac{dN_n}{dx} = \eta N_0 e^{\int \alpha'(x)dx} \tag{16}$$

$$N_p(x) = \int_{x_1}^{x_2} \alpha N_0 e^{\int \alpha'(x)dx} dx \tag{17}$$

$$N_n(x) = \int_{x_1}^{x_2} \eta N_0 e^{\int \alpha'(x)dx} dx \tag{18}$$

2.2.4 Corona Polarity

Under an AC voltage, the polarity of the transmission line at any point in space with reference to its surroundings will vary from positive to negative at the voltage frequency, typically 50 or 60 Hz. As such, the direction of the electron avalanche will vary, propagating either toward or away from the point of corona formation. The direction of the electron avalanche affects the distribution of electrons and ions around the electrode, thereby affecting the spatial and temporal evolution of the ionization. The geometry of the electrodes

(size and separation distance) plays a role in the type of corona formations to occur around the point as well. In high-voltage transmission applications, specifically overhead transmission lines, there are four dominant observable modes of corona formation: negative Trichel pulses, negative glow, positive glow, and positive breakdown streamers [86]. In long gaps between a corona forming cathode and the anode, negative streamer formation is suppressed because the electron avalanches propagate away from the high field region into an area of weaker field, suppressing the transition from the negative glow to negative streamers [85].

2.2.4.1 Negative Corona

Negative corona forms around an electrode point at a lower electric potential than the surroundings, with electric field vectors pointing away from the electrode, known as the cathode. The corona formation process begins with at least one free electron near the cathode surface. Free electrons are constantly being produced in the atmosphere through ionization of molecules by energetic photons, such as cosmic rays. Near the cathode, at least one free electron is accelerated away at a sufficient rate to gain enough energy to ionize a molecule. Through successive ionizing collisions, the number of electrons increases with increasing distance from the cathode, as discussed in Section 2.2.3. As the distance from the cathode increases, the electric field magnitude decreases to the point where newly generated electrons do not gain sufficient energy to ionize molecules by collision. Ionization in this region primarily occurs by energetic photons generated closer to the cathode by photoionization. Electrons in the farther region are absorbed by oxygen molecules, which are electronegative, forming negative ions. The positive ions slowly drift toward the negative cathode, accumulating around it. The net electric field around the cathode decreases farther away due to the shielding by the positive ions, decreasing electron acceleration even further. With a decrease in electron production by ionization, free electrons and ions recombine to an initial equilibrium state. As the positive ions recombine with low energy electrons, the electric field magnitude around the cathode increases enough to re-initiate electron ionization. This cyclic process continues under a constant negative electric potential. These negative pulses are a form of corona called Trichel pulses, the primary form of negative

corona found in atmospheric pressure discharges. An illustration of the electron density buildup and charge flow is shown in Figure 20.

As the voltage of the negative cathode decreases (i.e. voltage magnitude increases), the frequency of the Trichel pulses increases. [86] Through measurements, an empirical formula relating the frequency of the Trichel pulses to the average current flow into the cathode has been formulated (19) [76].

$$h = \left(1.23 \times 10^5 \frac{I}{r}\right)^{1.21} \tag{19}$$

In this expression, I is the average current flow into the cathode in Amps and r is the radius of the cathode point (assuming a hemispherical point of a wire above a plane) in meters. The frequency of Trichel pulses ranges from a few kiloHertz to a few MegaHertz. The Trichel pulses have a rise time on the order of a nanosecond with a duration of tens of nanoseconds [89]. As their frequency approaches the MegaHertz regime (through an increase in the local field magnitude), the Trichel pulses transition into the negative glow corona. During negative glow formation, the processes of ionization and clearing of the residual positive space charge have reached temporal equilibrium. The form of the negative glow is similar to a Trichel pulse during ionization, except for its constant nature and an increased corona current. During Trichel pulse formation, the average surface current at the cathode surface is under 5 A/cm^2, while the negative glow can reach current densities of 10-30 A/cm^2 [76].

2.2.4.2 Positive Corona

Positive corona forms around an electrode at higher electric potential than the surroundings, with electric field vectors pointing toward the electrode, known as the anode. As in negative corona, the formation process begins with at least one free electron. Near the anode, the strong electric field accelerates the electron toward the anode. At a sufficiently close starting distance, the electron gains enough energy within a mean free path length to ionize a molecule upon collision, releasing another electron. These electrons continue to accelerate toward the anode, ionizing molecules further in an electron avalanche. Upon

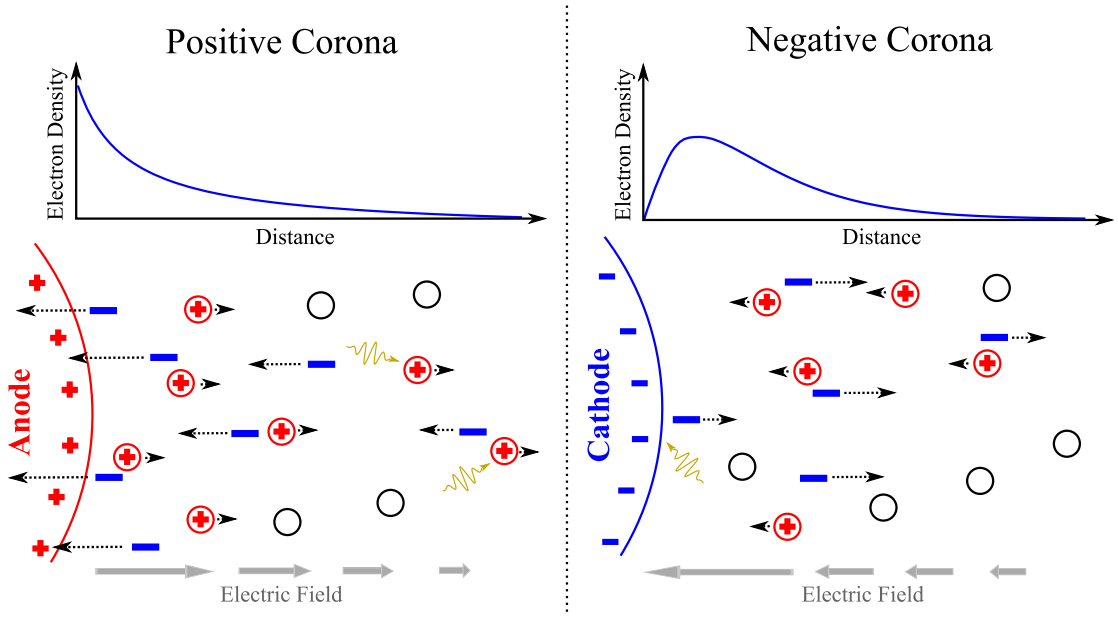

Figure 20: Qualitative illustration of positive and negative corona formation, and the resulting electron density profile. The strong fileds surrounding a positive anode accelerate negative electrons toward it, creating a sustained electron avalanche. The negative corona is not sustainable and pulsates because of slow positive ion accumulation around the cathode shielding the fields and preventing further ionization.

reaching the anode, the electrons spread over the surface ionizing molecules until they lose sufficient energy to be absorbed by the anode. Positive ions formed in the ionization process drift slowly away from the anode. The positive ion buildup at a distance from the anode suppresses the electric field near the anode, decreasing ionization. In the positive glow corona process, the corona formation process quickly migrates to adjacent areas of the anode when positive ion accumulation suppresses ionization. The net current of the positive glow corona appears as a steady direct current superimposed with small pulses in the hundreds of kiloHertz. An illustration of the electron density buildup and charge flow is shown in Figure 20.

Streamer formation is also a common corona mode on an anode point. With a greater voltage than that required for the positive glow, breakdown streamers may form. Under a higher electric field, positive ions are rapidly cleared from the anode region allowing the ionization process to continue farther from the anode surface. Streamer propagation occurs by

means of local field enhancement around corona globules. Large concentrations of positive ions can result from initial electron avalanches around the anode. The ions are accelerated away from the anode, but the local field surrounding the globule is sufficiently high to induce ionization by electron avalanches. While the positive ion globule is neutralized by the electron avalanche, the positive ions ahead of the original globule can now induce successive electron avalanches, resulting in a streamer capable of propagating beyond the high field region of the anode. It is shown in Dawson that a positive ion concentration of approximately 10^{15} positive ions per cubic centimeter in a 30 micrometer radius sphere is sufficient to continue streamer propagation in the absence of an external ionizing field source [86],[28].

2.2.4.3 AC Corona Formation

On AC power lines, corona formation is time varying with the voltage at the point of corona formation. The standard frequencies for AC power line transmission are 50 and 60 Hz. At these relatively low frequencies, the ionization process at any given time is approximated by the equivalent DC voltage process. However, due to the long gap between electrodes in a power line setup (on the order of meters), free ions at the end of a cycle do not all drift to the opposite electrode to be neutralized before the change in electrode polarity. The position of an ion can be computed as an integral of the ion velocity over time. The drift velocity is equal to the mobility times the electric field (20), and the electric field varies with time (voltage phase of the line) and position of the ion (decreasing field with increasing distance from the corona electrode).

$$\boldsymbol{r}(t) = \int_{t_1}^{t_2} \mu \boldsymbol{E}\left(t, \boldsymbol{r}\left(t\right)\right) dt \tag{20}$$

For example, under negative corona, negative ions formed at the outer boundary of the corona drift away from the anode under the force of the electric field. A short distance from the corona electrode on the order of 1 m, the potential gradient decreases significantly, and for high-voltage power lines the field at peak is on the order of $10^4 - 10^5$ V/m. With this simplifying assumption, the integral can be solved directly. Using the negative ion

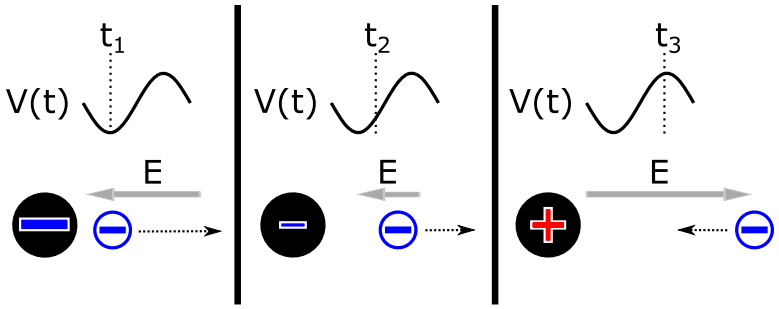

Figure 21: Three time snapshots over the course of an AC cycle. At the negative half of the cycle, negative ions drift away from the corona forming electrode. The low field in the inter-electrode space results in low ion mobility. At the change electrode polarity, the remnant ions drift back toward the now positive electrode. The field at the positive electrode surface is enhanced by the negative ions. For illustrative purposes, it is assumed that there are no positive ions at t_1, although in a steady state cycle there would be positive ion field enhancement as well.

mobility from Table 8, and integrating from the peak of a 60 Hz sinusoidal cycle to the zero crossing, the distance traveled by negative ions comes come out to (21). Right at the electrode surface where corona occurs, ion velocities may be in the thousands of meters per second, but because of the sharp drop in field magnitude, the velocity in the inter-electrode space is only a few meters per second.

Ions that remain in the inter-electrode space at the transmission from negative to positive polarity, or vice versa, create an enhanced electric field. The negative ions that remain a short distance from what is now the positive electrode begin the drift back, and the field at the electrode surface is now the superposition of the neutral field and the field of the remaining ions. Figure 21 illustrates the process of field enhancement.

$$d_{ion} \approx \frac{\mu_{ion} E_{peak}}{2\pi f} \sim 5\text{cm} \tag{21}$$

Figure 22 illustrates corona current measured at the positive and negative half of the AC cycle performed by Trinh [86],[94]. Corona formation was induced on a 7 cm sphere with a 30^o conical boss, and a distance of 25 cm to the ground plane. As this distance is larger than the distance traveled by the ions of about 5 cm, the space charge will accumulate between the sphere and ground to enhance the field. The dominant positive corona modes are the glow corona and positive breakdown streamers, and the dominant negative corona

modes are Trichel pulses and negative glow. Trichel pulse frequency can be observed to increase with voltage and occur at regular intervals. Positive streamers on the other hand are not as predictable and follow a more random distribution. Positive glow and negative Trichel pulses share a similar onset voltage.

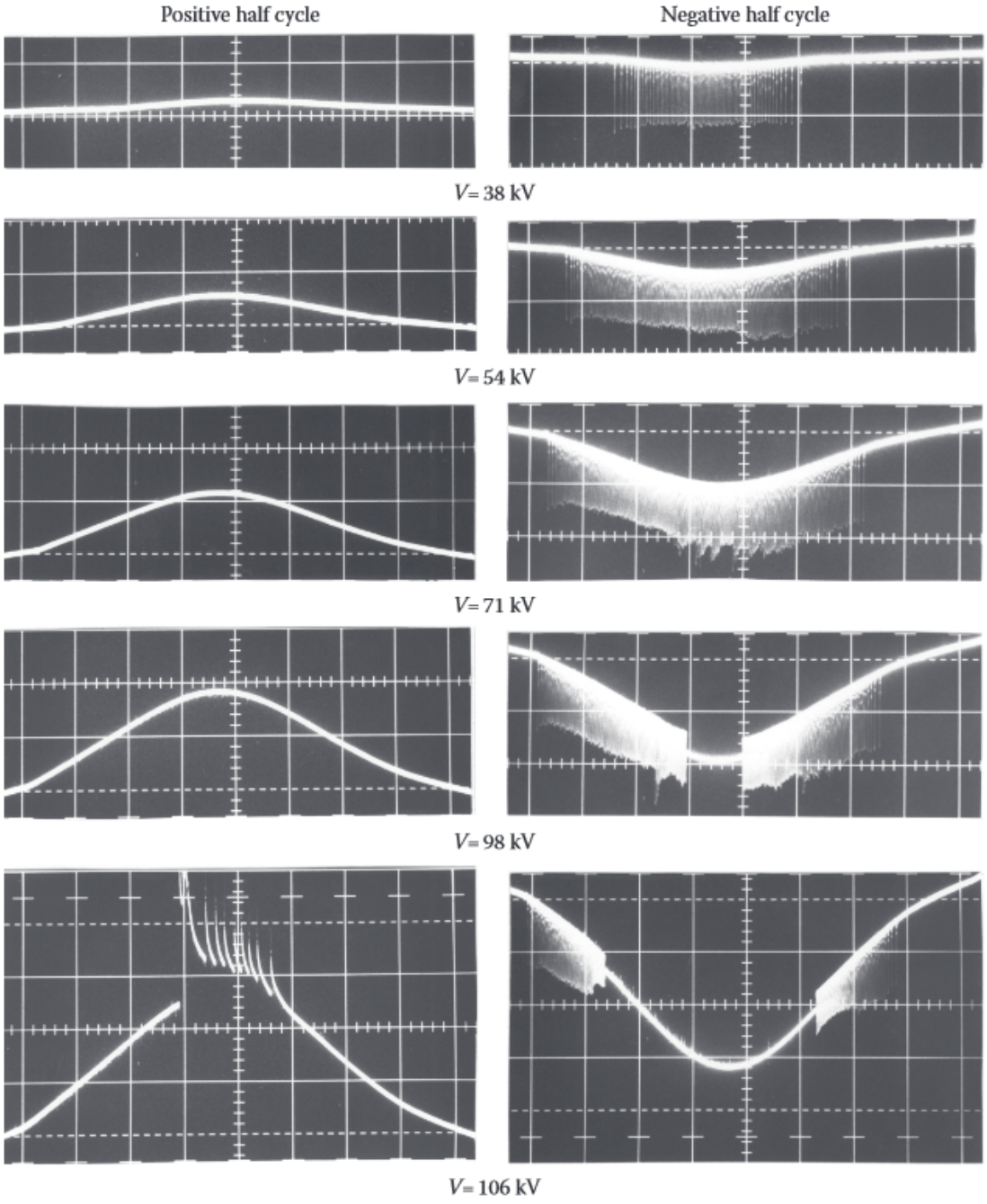

Figure 22: The corona current measured at a high-voltage 7 cm diameter sphere 25 cm from a ground plane. The positive half cycle exhibits positive glow at lower voltages and breakdown streamers at higher voltages. The negative half cycle exhibits Trichel pulses followed by negative glow at higher voltages [86].

Table 6: Table of terms used in Peek's law for parallel wires (22),(23). ρ_{STP} is the air density at Standard Temperature and Pressure.

Variable	Description	Typical value in air	Units
E_v	Visual critical gradient	n/a	kV/cm
E_o	Disruptive critical gradient	30 (DC voltage), 21.2 (AC RMS voltage)	kV/cm
C	Empirical geometrical constant	0.301	$cm^{1/2}$
δ	Relative air density	ρ/ρ_{STP}	1
r	Wire radius	n/a	cm
V_v	Spark-over voltage	n/a	kV
m_v	Irregularity factor of conductor surface	1 (smooth), < 1 (rough)	1
S	Spacing between conductor centers	n/a	cm

2.2.5 Peek's Law

Along with Townsend, another important contributor to the field of corona studies was Frank W. Peek, Jr. Taking a practical approach to corona formation in the world of high-voltage transmission line design, Peek is well known for his empirical formulation of corona onset behavior for the case of two parallel wires. Peek's law for parallel wires can be stated in two equations. The first equation gives the electric field magnitude at the surface of the wire, termed in his writings as the visual critical gradient, at which a visible corona will develop around the wire (22) [80],[75].

$$E_v = E_o\delta\left(1 + \frac{C}{\sqrt{\delta r}}\right) \tag{22}$$

The second equation relates the critical visual gradient, E_v, to a corresponding spark-over voltage, V_v, based on the wire radius and separation (23) [80].

$$V_v = E_v m_v r \ln\left(\frac{S}{r}\right) \tag{23}$$

The terms from (22) and (23) are defined in Table 6. ρ_{STP} is the air density at Standard Temperature and Pressure. The disruptive critical gradient, E_o, is different for the DC and AC ($60Hz$) voltage cases. For wires with a DC voltage, the value of E_o is $30kV/cm$, as given at the end of the previous section. Given an AC RMS voltage, the critical gradient is $30/\sqrt{2} = 21.2kV/cm$ [80].

When dealing with a high-voltage power line above a ground plane, Peek's law can be adjusted using the method of images. If there exists a voltage V_v between two parallel

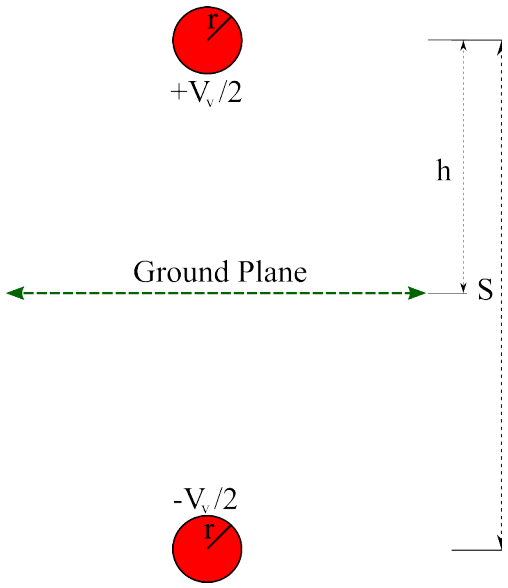

Figure 23: Cross section of a simple power line geometry with its relation to a parallel wire geometry. The red circles are the cross sections of two infinitely long cylindrical conductors at opposite electric potentials, and the green line represents an infinite ground plane.

wires, the geometry can be interpreted as in Fig. 23, where one wire is at a voltage of $+V_v/2$ and the other is at a voltage of $-V_v/2$. Using the method of images, the geometry can be interpreted as a wire above a ground plane, where the height of the wire is $h = S/2$, and the voltage of the wire with respect to the ground plane is $V_v/2$. The second equation of Peek's law (23) can then be restated as (24), where V_{vg} is now the voltage of the wire with respect to the ground plane, and h is the height of the wire above the ground plane.

$$V_{vg} = \frac{1}{2} E_v m_v r \ln\left(\frac{2h}{r}\right) \tag{24}$$

As an example of how Peek's law might be used, let us assume there is a smooth high-voltage AC power line $5m$ above the ground with a radius of $1cm$. The air is at Standard Temperature and Pressure. The RMS voltage at which visible corona formation could appear would be:

$$V_{vg} = \frac{1}{2} E_v m_v r \ln\left(\frac{2h}{r}\right)$$

$$V_{vg} = \frac{1}{2}\left[E_o \delta\left(1 + \frac{C}{\sqrt{\delta r}}\right)\right] m_v r \ln\left(\frac{2h}{r}\right)$$

$$= \frac{1}{2} \times 21.2 \times \frac{\rho_{STP}}{\rho_{STP}} \times \left(1 + \frac{0.301}{\sqrt{1 \times 1}}\right) \times 1 \times 1 \times \ln\left(\frac{2 \times 500}{1}\right)$$
$$= 95.3kV$$

Using Peek's law, simple estimates can be made for the feasibility of corona formation on high-voltage power lines. However, the addition of more complex conductor geometries can alter corona behavior. In addition, corona is not a static process and exhibits temporal changes that vary with geometry as well as electrode polarity. Studies of complex corona formation criteria and scenarios must be handled by means of numerical modeling of the ionization processes in air.

2.2.6 Ionization Processes in Air

Early experimental work focused on simplified scenarios of electrical discharges [61]. Short (on the order of 1 to 10 cm) point-to-plane and cylindrical electrode geometries were tested. Paschen observed that the breakdown voltage of a gas is related to the gap length and pressure [79]. His studies of breakdown between parallel plates in various gases showed that pressure and gap distance were inversely related to the breakdown voltage. In mathematical terms, the product pd can be treated as a single variable, where p is pressure and d is gap distance. If one is increased by a certain factor, and the other decreased by the same factor, the resulting breakdown voltage remains the same. As a result, much of the data on electrical breakdowns in literature is given in units of pd, or similarly related derivable quantities. Townsend ionization coefficients are typically provided with respect to E/p, where E is the applied electric field and p again is the pressure of the gas.

Many experiments on electrical discharges were, and are to this day, performed in vacuum chambers filled with pure gases such as hydrogen, argon, neon, and nitrogen, and oxygen. Performing experiments with pure gases decreases the number of variables (interactions between different gas species) needed in the analysis, and allows for more easily reproducible results. Through simplification of the problem, careful studies can be carried out on the formation characteristics of electrical discharges. Many studies are carried out at low pressures ($\sim$ 1 $Torr$) where uniform column discharges form, not attainable at atmospheric pressure. Also, lower voltages are required to initiate plasma formation at

lower pressures, per Paschen's law. Through the use of symmetrical geometries, such as plane-to-plane, spherical or conical point-to-plane, or coaxial cylinder, field analysis can be performed analytically, and simplifying assumptions made regarding the distribution of ionized particles.

One of the fundamental difficulties in practical atmospheric pressure ($\sim 760\ Torr$) air discharge studies is the large number of parameters in the problem. Firstly, corona forms around areas of small effective radius, which are typically irregular edges and corners where analytical solutions for the electric field are not feasible, and numerical computations must be used. Approximations to the field distribution can be made, and often are, to create a symmetry for electrical discharge simulation. Secondly, the number of reactions between species in air is considerably larger than in pure gases, and the exact concentrations of the various species may vary between experiments. Thirdly, at atmospheric pressure the density of particles is approximately $N_0 = 2.688 \times 10^{25} m^{-3}$ [27], resulting in a separation distance of particles on the order of nanometers. The geometries under consideration for AC power line corona scale from meters (electrode separation distance) to nanometers (particle collisions). Even in the most sophisticated simulations, statistical assumptions and geometric simplifications are utilized in order to make such a problem computationally tractable. Rather than dealing with individual particle interactions, simulations often handle particle densities, utilizing averaged reaction rates.

In air, numerous collisions occur between electrons and molecules resulting in ionization, excitation, photon emission, and recombination. Figure 24 presents a diagram of the primary interactions between species in an air plasma. Becker also provides a more complete table of 60 interactions between oxygen and nitrogen species that take place in air [19]. Interactions between molecular species can result in chemical reactions in addition to ionization. Including other air species such as carbon dioxide, argon, water vapor, helium, etc. greatly increases the number of interactions to account for in an air plasma. Some of these collisional processes can be described more generally in Table 7, reproduced from Meek [64]. A and B are atomic species, A^* and B^* are the atomic species with an electron in an excited state, A^+ and B^+ are positive ions, e is an electron, $h\nu$ is a photon of frequency

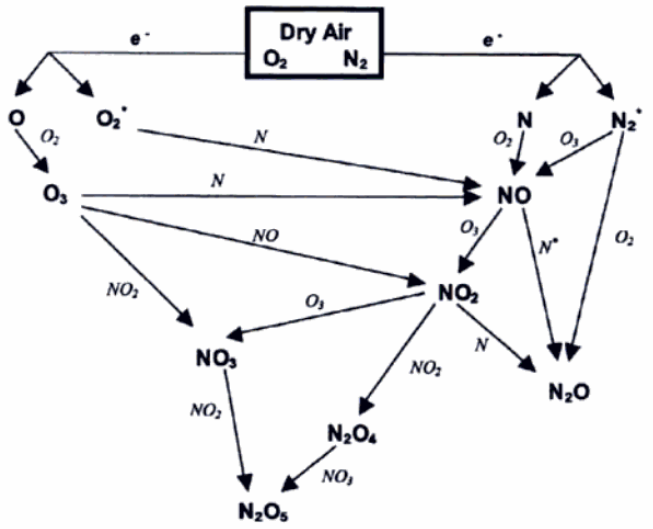

Figure 24: Diagram of the primary reactions in a dry air plasma [19]

ν, and bold species have appreciable kinetic energy. With modern computing capabilities, it is possible to perform complete simulations involving species interactions [96]. There exist commercial packages such as COMSOL Multiphysics Plasma Module that support full species interaction simulations. These methods utilize conservation equations for mass, energy, momentum, and charge along with known reaction rates to generate accurate plasma models. Atmospheric plasma simulation is an active area of interest, particularly for the purposes of biological and chemical processing and insulator design [19]. The details of these processes are beyond the scope of this work. Properly simplified electrical discharge simulations can yield accurate results within certain bounds.

2.2.7 Electrical Discharge Continuity Equations

In a simplified plasma simulation approach, the numerous species and interactions in a gas like air are reduced to three species and four interactions. Electrons, positive ions, and negative ions are considered, with ionization, attachment, detachment, and dissociative recombination reactions [61],[76],[19],. Photo ionization and excitation by atom impact are not treated in the simplest approach, although the same methodology can be extended to account for these interactions with the requisite increase in the number of parameters. For atmospheric pressure plasma streamer formations, the density of excited states is low

Table 7: Types of collisional processes in a plasma

Collision Process	**Reaction Description**
$A + \boldsymbol{e} \rightarrow A^* + \boldsymbol{e}$	Excitation by electron impact
$A + \boldsymbol{e} \leftarrow A^* + \boldsymbol{e}$	A collision of the second kind
$A + \boldsymbol{e} \rightarrow A^+ + \boldsymbol{e} + \boldsymbol{e}$	Ionization by electron impact
$A + h\nu \rightarrow A^*$	Photo excitation
$A + h\nu \leftarrow A^*$	Emission of light
$A + h\nu \rightarrow A^+ + \boldsymbol{e}$	Photo ionization
$A + h\nu \leftarrow A^+ + \boldsymbol{e}$	Radiative recombination
$\boldsymbol{A} + \boldsymbol{B} \rightarrow A^* + \boldsymbol{B}$	Excitation by atom impact
$\boldsymbol{A} + \boldsymbol{B} \rightarrow A^+ + e + \boldsymbol{B}$	Ionization by atom impact
$A^* + B \rightarrow A + B^*$	Excitation by excited atoms
$A^+ + B \rightarrow A + B^+$	Change of charge
$\boldsymbol{A}^+ + B \rightarrow A^+ + \boldsymbol{B}^+ + \boldsymbol{e}$	Ionization by positive ion impact

enough that their omission is a valid approximation to the full solution [48]. The basic continuity equations for simulation of electric discharges are given in (25)-(27), along with Poisson's equation for the electric field (28). The variables are defined in Table 8.

$$\partial n_e/\partial t + \nabla \cdot (n_e \mathbf{w}_e - D_e \nabla n_e) - (\nu_i - \nu_a)\, n_e - \nu_d n_n + \beta_{ep} n_e n_p = 0 \tag{25}$$

$$\partial n_p/\partial t + \nabla \cdot (n_p \mathbf{w}_p) - \nu_i n_e + \beta_{ep} n_e n_p = 0 \tag{26}$$

$$\partial n_n/\partial t + \nabla \cdot (n_n \mathbf{w}_n) - \nu_a n_e + \nu_d n_n = 0 \tag{27}$$

$$\nabla \cdot \mathbf{E} = e\,(n_p - n_e - n_n)\,/\varepsilon_0 \tag{28}$$

The continuity equation for electron density (25) is of second order, necessitating two boundary conditions. The continuity equations for positive (26) and negative 27) ions are of first order and require one boundary condition [89],[93],[19]. The choice of boundary conditions depends on polarity of the electrodes and possible simplifications made in the problem geometry.

The ionization and attachment rates, ν_i and ν_a, respectively, have been measured for dry air at standard atmospheric pressure by Davies [27]. The definition of standard atmospheric

Table 8: Variables in electrical discharge continuity equations (25)-(28)

Variable	Description	Approx. value in air @ STP	Units
n_e	Electron density	Unknown variable	m^{-3}
n_p	Positive ion density	Unknown variable	m^{-3}
n_n	Negative ion density	Unknown variable	m^{-3}
$\mathbf{w}_e$	Electron velocity	$-\mu_e \mathbf{E}$	ms^{-1}
$\mathbf{w}_p$	Electron velocity	$\mu_p \mathbf{E}$	ms^{-1}
$\mathbf{w}_n$	Electron velocity	$-\mu_n \mathbf{E}$	ms^{-1}
μ_e	Electron mobility	$0.14\left(3.7\times10^{-5}\left\|\mathbf{E}\right\|\right)^{-0.25}$ [55] ≈ 0.05 [89]	$m^2V^{-1}s^{-1}$
μ_p	Positive ion mobility	0.000243 [48]	$m^2V^{-1}s^{-1}$
μ_n	Negative ion mobility	0.000270 [48]	$m^2V^{-1}s^{-1}$
D_e	Electron diffusion coefficient	0.18 [55]	m^2s^{-1}
ν_i	Ionization rate	See Appendix A	s^{-1}
ν_n	Attachment rate	See Appendix A	s^{-1}
ν_d	Electron-negative ion detachment rate	0 [89]	s^{-1}
β_{ep}	Electron-positive ion recombination rate	5×10^{-13} [89]	m^3s^{-1}
e	Fundamental charge	1.602×10^{-19}	C
ε_0	Free space permittivity	8.854×10^{-12}	Fm^{-1}

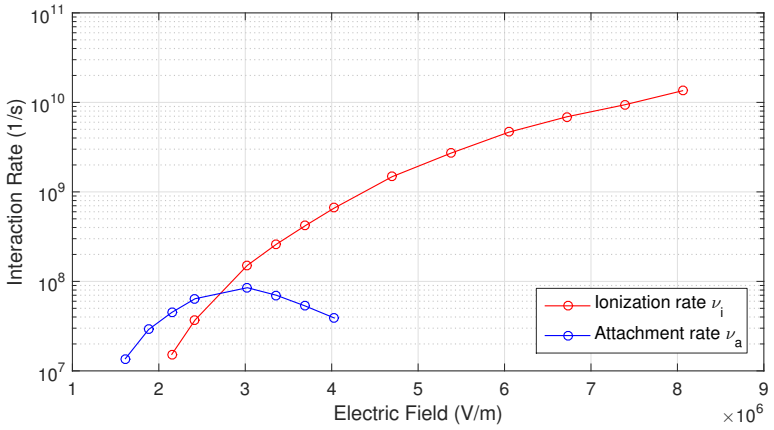

Figure 25: Ionization and attachment rates in air at standard atmospheric pressure measured by Davies [27].

pressure in Davies corresponds to a molecular number density of $N_0 = 2.688\times10^{25}m^{-3}$. The ionization coefficients are tabulated in Appendix A, and plotted here in Figure 25. A curve fit to the ionization coefficient, extrapolated to fields up to 10^8 V/m with data from Zhang [101] produces (A.4).

$$\nu_i = e^{-1.054\times10^4 E^{-0.4527}+31.07} \tag{A.4}$$

The boundary condition for positive ions at the anode boundary r_a is [89]

$$n_p\left(r_a\right) = 0$$

The boundary condition for negative ions at the cathode boundary r_c is [89]

$$n_n(r_c) = 0$$

.

In order to reduce computational complexity, the outer boundary (anode for a negative corona and cathode for positive corona) may be moved closer to the point, creating an artificial boundary where it is assumed ionization no longer occurs because of the low electric field magnitude. This boundary distance r_b can be estimated as the distance where the applied electric field magnitude $|\mathbf{E}|$ is such that

$$\alpha(|\mathbf{E}(r_b)|) - \eta(|\mathbf{E}(r_b)|) = 0.$$

In a positive corona formation, it may be assumed that the negative ion density at this distance is less than the ambient electron density of air, such as $n_n(r_b) = 10^8 m^{-3}$ [25]. For negative corona, this boundary r_b should be set farther to account for the formation of negative ions past the ionization threshold as electrons drift away from the cathode. Chen suggests a distance where the field to particle density ratio is 80 Td, which at atmospheric pressure equates to a field magnitude of $2.15 \times 10^6 V/m$ [26].

The electron density n_e boundary conditions are specified at the anode and cathode, and depend on the polarity of the corona. For negative corona, the normal derivative of the electron density is zero at the anode [89]. At the cathode, electron production can be assumed to occur only by positive ion impact. The number of electrons produced is related to the number of positive ions at the cathode, their velocity, and the secondary electron emission coefficient at the surface γ. The electron density is at the cathode r_c is given by [89]

$$n_e(r_c) = \gamma n_p(r_c) \frac{\mu_p}{\mu_e(r_c)}$$

The secondary emission is estimated to be $\gamma = 0.01$ based on averaged empirical data for various cathode materials [93],[93]. For positive corona, the electron density at the cathode r_c, or outer simulation boundary, can be taken as the average density of free electrons in the atmosphere if the boundary is sufficiently far from the anode

$$n_e(r_c) = 10^9 m^{-3}$$

Otherwise, the electron density at the outer boundary, or cathode, will be given by the electron density produced by photo ionization, which can be computed from the photon emission in the bulk of the plasma [24]. At the anode of the positive corona, electron density is a function of the ionization rate at the anode, the drift of electrons toward the anode, and the electron emission from the anode surface. This boundary condition may be simplified by taking the corona current at the anode as a constant, and specifying the electron density as a function of corona current. Corona current may be measured experimentally for a particular geometry and voltage, and this data used in simulation of electron density. The electron density at the anode r_a for a positive corona as a function of corona current density J, negative ion density n_n and mobility μ_n, and electron mobility μ_e, is given by (29).

$$n_e\left(r_a\right) = \frac{\hat{\boldsymbol{n}} \cdot \mathbf{J}\left(r_a\right) - e n_n\left(r_a\right) \mu_n \hat{\boldsymbol{n}} \cdot \mathbf{E}\left(r_a\right)}{e \mu_e\left(r_a\right) \hat{\boldsymbol{n}} \cdot \mathbf{E}\left(r_a\right)} \tag{29}$$

Simulation of electrical discharges can be carried out numerically using a time stepping algorithm coupled with a non-linear solver capable of solving the coupled system of equations (25)-(28). In order to achieve convergence of the simulation, it is important to maintain a small mesh cell size and time step. During the initial buildup of the electron avalanche, large gradients can exist in electron density, and using a mesh cell size that is too small may result in numerical instabilities when computing gradients. In order to resolve the ionization processes, a mesh cell size is approximately [11]

$$\Delta x \approx 1 - 10 \mu m$$

.

The time step is determined from the smallest mesh cell size. The limitation here is the speed of particle propagation. The fastest speed in the discharge will be for electrons at the electrode surface. The speed of an electron is a function of the electric field (Table 8). The time step is then determined based on the mesh cell size and electric field at the surface of the discharge electrode

$$\Delta t \leq \frac{\Delta x}{\mu_e E_{max}}$$

.

The initial seed electron density for initiation of the electron avalanche is $10^9 m^{-3}$ [48],[25]. This is an approximation for the density of free electrons present in ambient air. Given the density of molecules in air, this evaluates to just 10^{-17} of the particles ionized. The authors in [48] place the initial electron density in a small Gaussian packet in front of the cathode with a peak electron density of $10^9 m^{-3}$. A uniform electron density could also be applied to the entire solution domain.

2.2.8 Streamer Formation

Streamers are thin filamentary self-sustained discharges that are able to propagate beyond the ionization boundary, where the net ionization coefficient due to the applied voltage falls below 0. Positive breakdown streamers develop their own local ionizing electric field through the dense accumulation of positive ions. Positive streamer formation occurs when the electron avalanche is able to achieve its critical amplification. This criterion for atmospheric pressure air can be stated numerically by (30), a result that was derived empirically [76],[14].

$$\int_0^{x_c} \alpha' dx \approx 18 \tag{30}$$

The streamer current can rise to its full magnitude in the range of hundreds of milliamps in a time frame of nanoseconds. The decay of the streamer current then occurs on the order of hundreds of nanoseconds [14]. Streamers propagate by the mechanism of intense ionization resulting in a high positive ion density. The electric field of the positive ion region is sufficient to generate secondary electron avalanches farther from the anode. These avalanches result in positive ions farther from the anode, propagating away in this manner as a self-sustaining discharge. Streamers are capable of propagating beyond the ionization boundary in air of 30 kV/cm. The electric field required to sustain streamer propagation is approximately 4.7 kV/cm[85].

As discussed in Section 2.2.2, the electric fields at the surface of a cylindrical electrode fall off as $1/r$, and $1/r^2$ for a spherical electrode. For a given anode geometry (cylindrical or spherical) with a known radius r_0, the critical electric field at the surface of the electrode can be calculated. An iterative computation was performed to ascertain the critical field

required to incite streamer formation. The integral (30) was computed, where the net ionization coefficient $\alpha' = \alpha - \eta$ is a function of the electric field E (31), as discussed in Section A [76].

$$\int_{r_0}^{r_c} \alpha' \left(\frac{E_0 r_0^m}{r^m} \right) dr = 18 \tag{31}$$

In (31), m is an exponent whose value depends on the electrode geometry. The electric field for a cylinder ($m = 1$) or sphere ($m = 2$) of radius r_0 is used to determine the net ionization coefficient. E_0 is the electric field at the surface of the cylinder or sphere, which is iteratively adjusted until (31) is satisfied. The upper integration boundary r_c is the radius at which the net ionization coefficient is equal to 0.

The results of the computation are shown in Figure 26. A curve fit is found to match the computed results. For a cylindrical anode, the critical surface electric field needed to incite streamer formation is estimated by (32). For a spherical anode, the critical surface electric field needed to incite streamer formation is estimated by (33). The electric field E_C is in units of V/m, and the radius is in units of meters.

$$E_c = 7.751 \times 10^4 r^{-0.5605} + 4.524 \times 10^6 \tag{32}$$

$$E_c = 5.771 \times 10^4 r^{-0.6531} + 5.458 \times 10^6 \tag{33}$$

The ionization boundary r_c, where the effective ionization coefficient is zero, is then calculated for the surface fields in Figure 26. Once the ionization boundary grows larger than this, the positive glow will likely transition to the positive breakdown streamer mode of corona. The difference between the ionization boundary radius and the anode radius is the maximum glow corona thickness, and is plotted in Figure 27. For a cylindrical anode, the positive glow thickness can be estimated from the curve fit relation (34), for a spherical anode from (35).

$$d_{glow} = e^{\left(9.58 r^{0.1258} - 9.413 r^{-0.01163}\right)} \tag{34}$$

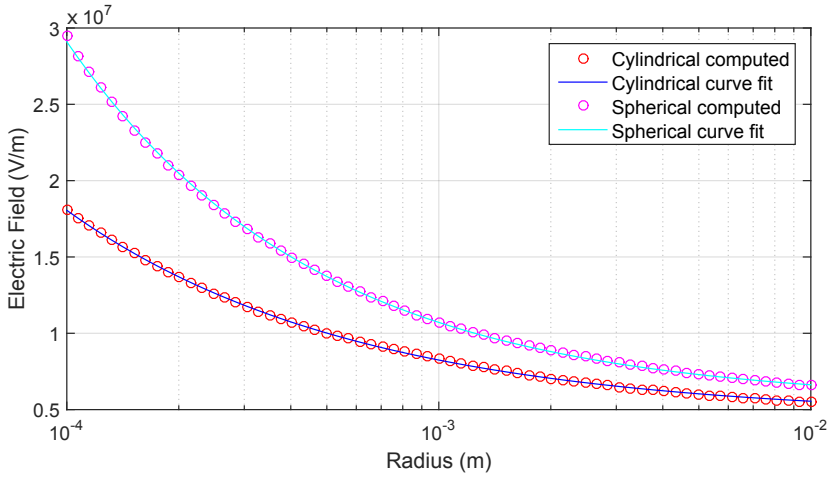

Figure 26: Critical electric field at the surface of a cylindrical or spherical anode above which streamer formation can occur.

$$d_{glow} = e^{\left(8.311r^{0.128} - 8.76r^{-0.02406}\right)} \tag{35}$$

2.2.9 Corona Electron Density

2.2.9.1 Positive Glow, Negative Trichel Pulse, and Negative Glow

The interaction of corona with RF electromagnetic waves largely depends on the electron density, which is discussed in detail in Chapter 4. Using (13)-(18), the electron density distribution is computed for a range of cylindrical and spherical electrodes. The calculation of the electron density is carried out by the algorithm illustrated in Figure 28. The calculation applies to the positive glow, Trichel pulse, and negative glow corona formations. The Trichel pulse varies temporally, but the density profile corresponds with a snapshot of at the initial electron avalanche density before ion drift begins to quench further ionization through shielding the cathode.

First, the initial electric field distribution around the electrode is computed. In these calculations, cylindrical and spherical symmetry are exploited, using (8) for cylindrical and (9) for spherical symmetry. The field magnitude is chosen for each case such that the surface electric field is given by (32) for cylindrical and (33) for spherical symmetry. As discussed in section 2.2.8, these fields correspond to the streamer formation threshold, and present an

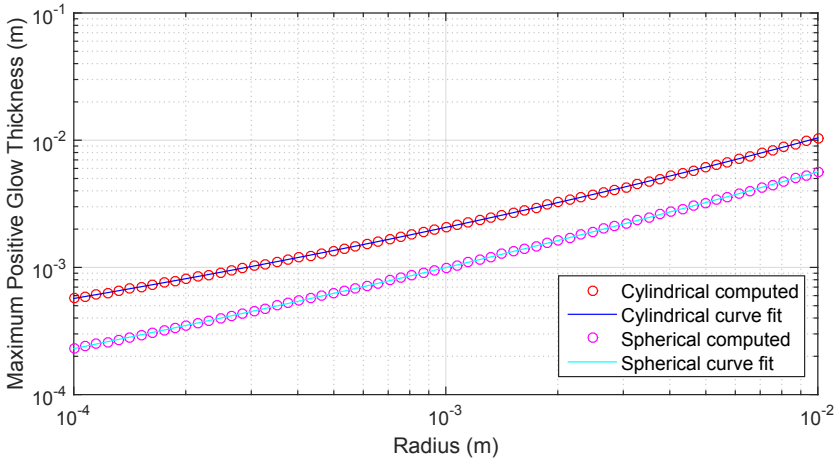

Figure 27: Estimate of the maximum thickness of positive glow corona, based of the criterion for positive streamer formation.

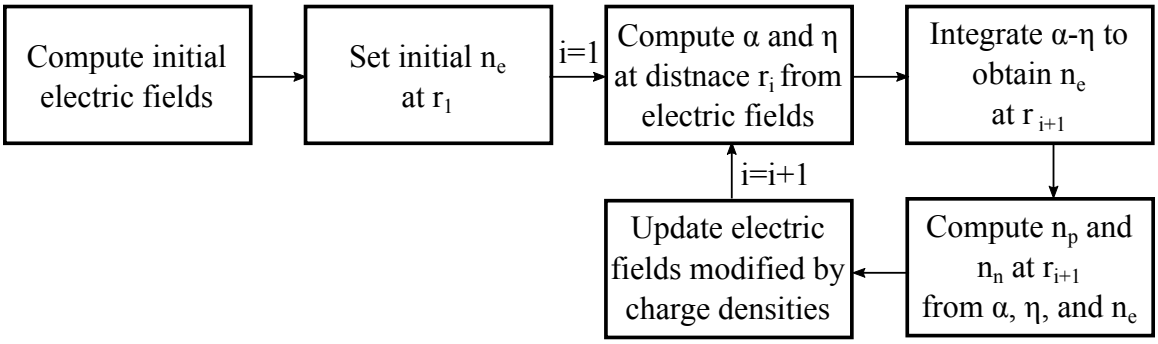

Figure 28: Algorithm used to compute the electron density in a corona discharge.

approximate limit to the positive glow discharge. These fields are also used for computing the negative Trichel pulse electron density. The initial electron density is taken to be the ambient electron density in air resulting from cosmic ray ionization, $n_e = 10^9$ m^{-3} [76]. The negative ion density is fraction of the electron density, estimated at $n_n = 10^8$ m^{-3} [25]. The positive ion density is set to $n_p = 1.1 \times 10^9$ m^{-3} for a neutral medium.

For negative corona, the charge densities are iteratively computed from the cathode surface outwards, following the direction of electron drift. Computation can be terminated at a distance where attachment processes dominate ionization. For positive corona, the charge carrier densities are computed inward to the anode. The starting distance for positive corona computation is chosen to be the distance where the net ionization rate (11) is equal to

zero. This is the ionization boundary. Computation is terminated at the anode surface. The electron densities are presented in Figure 29. Density profiles are presented as a function of distance from the anode (positive corona) or cathode (negative corona) surface, over a number of radii.

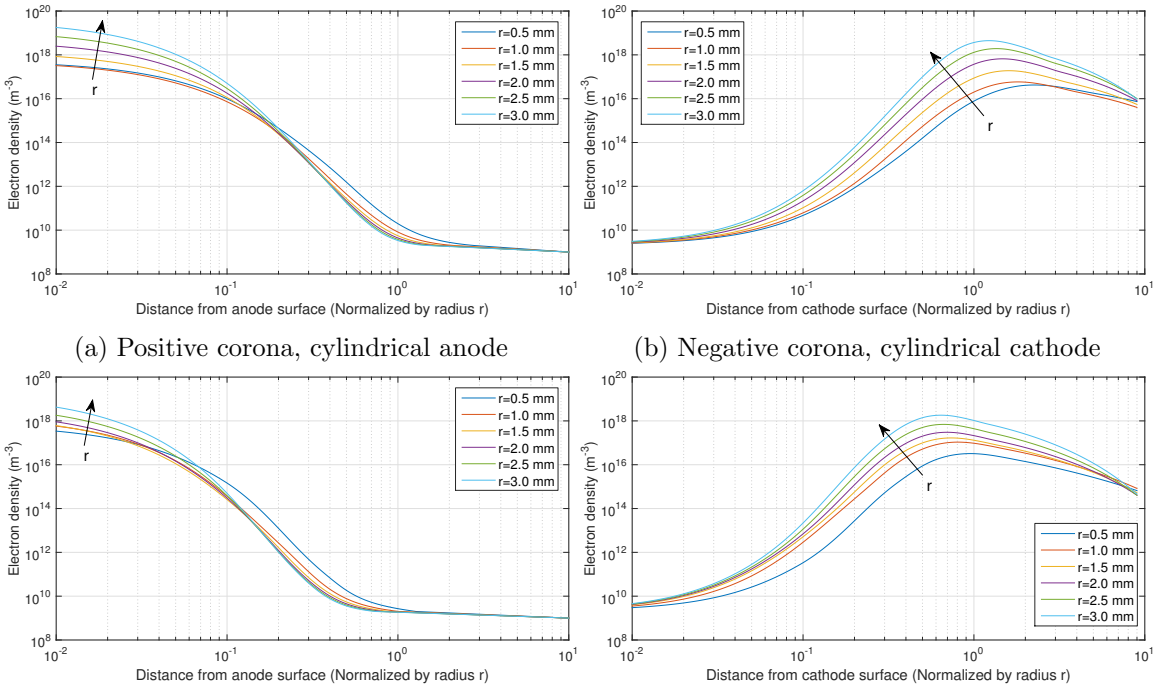

(a) Positive corona, cylindrical anode

(b) Negative corona, cylindrical cathode

(c) Positive corona, spherical anode

(d) Negative corona, spherical cathode

Figure 29: Electron density distribution for positive and negative corona in cylindrical and spherical geometries. The electric field at the electrode surface is computed from the positive streamer initiation criterion ($\int_0^{x_c} \alpha' dx \approx 18$).

Positive corona has an electron density profile that increases rapidly at the anode surface as electron acceleration increases with the increasing electric field. Negative corona on the other hand begins at the electrode surface and electrons are accelerated away from the cathode with decreasing acceleration. The peak electron density occurs at a distance approximately equal to the cathode radius, approximately 2x closer for the spherical than cylindrical geometry. This is the result of higher potential gradients closer to the cathode, since field magnitude falls off as $1/r^2$ for spherical symmetry. The surface electric field and required voltage over a reference 3 m distance to obtain this field are given in Table 9.

The same electron density calculations are also performed for a constant voltage. The voltage is set to 47 kV for the cylindrical symmetry and 6.9 kV for the spherical symmetry,

Table 9: Surface electric field at electrode and voltage over 3 m distance to a ground plane obtain the specified field. These fields are obtained from (32) and (33) to compute the electron densities in Figure 29.

	Cylindrical		Spherical	
Electrode radius (mm)	Surface electric field (kV/cm)	Point-plane 3m voltage (kV)	Surface electric field (kV/cm)	Point-plane 3m voltage (kV)
0.5	100	47.0	137	6.9
1.0	82	71.2	107	10.7
1.5	75	93.2	95	14.2
2.0	70	112.8	88	17.6
2.5	68	131.3	83	20.9
3.0	65	148.9	80	24.0

referenced to a ground plane 3 m from the electrode center. The values are chosen from Table 9, being the lowest voltages marking the streamer formation threshold. The electron density distributions are shown in Figure 30. The peak electron density decreases rapidly with radius because of the decreasing surface potential gradient.

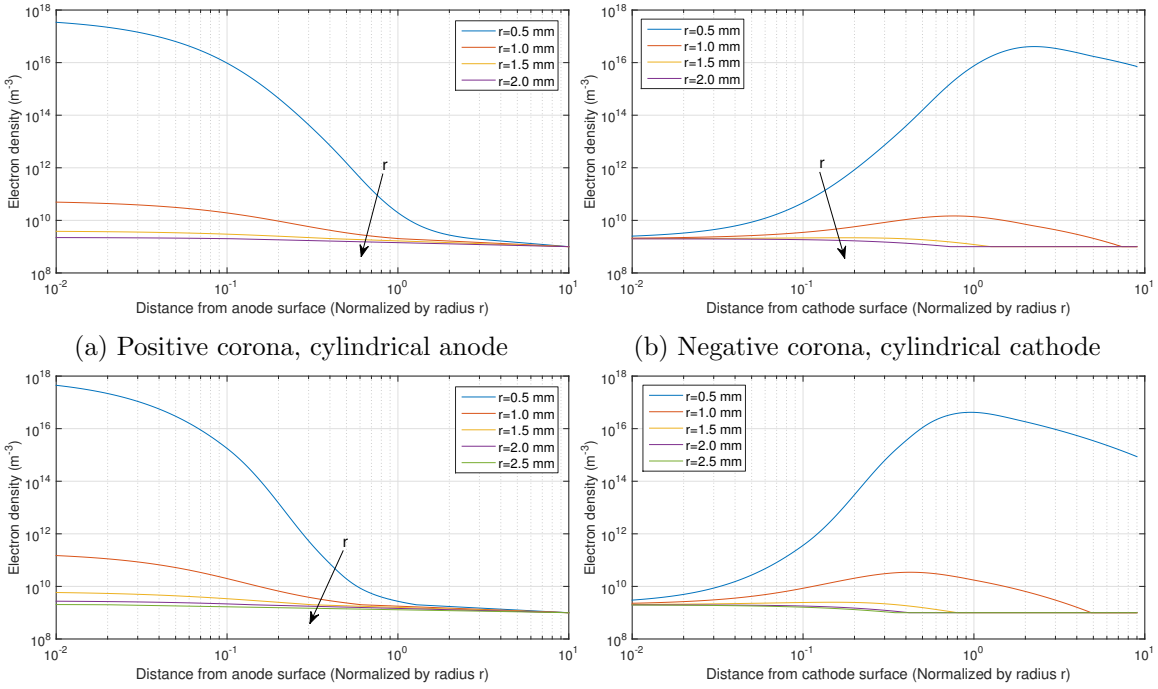

(a) Positive corona, cylindrical anode

(b) Negative corona, cylindrical cathode

(c) Positive corona, spherical anode

(d) Negative corona, spherical cathode

Figure 30: Electron density distribution for positive and negative corona in cylindrical and spherical geometries. The voltage for the cylindrical electrode is 47 kV and for the spherical electrode is 6.9 kV referenced to a plane at a distance of 3 m.

The primary conclusions that can be drawn from these computations are that peak corona electron densities fall in the region of $10^{18} - 10^{19}$ m^{-3}. Higher densities can occur with larger electrode radii. However, for a constant voltage, electrodes with a large radius

also exhibit lower potential gradients at their surface, resulting in significantly lower electron densities.

2.2.9.2 Corona Streamer

The electron densities in streamers, specifically positive streamers which are likely to form in an AC voltage (see Section 2.2.4), are more difficult to compute. Streamers form through intense ionization processes that result in a self-sustaining discharge propagating in the form of a positive ion globule. To capture the transient development of streamers, time-stepped methods must be utilized, discussed in Section 2.2.7. The study of these more advanced computational methods for electrical discharges is beyond the scope of this work. Instead, previously published results are used to augment the data for the electron densities occurring in streamers.

Raizer provides an account of streamer formation and propagation mechanisms relevant to this work [85]. The streamer formation criterion is given by (30), as previously discussed. The peak electric field associated with streamer formation depends on the geometry, but is typically on the order of 60 kV/cm and greater. Table 9 provides the peak fields for different geometries associated with positive streamer formation. The threshold for corona formation in air is 30 kV/cm. Unlike glow corona, streamers are self-sustaining below 30 kV/cm. In dry atmospheric pressure air, streamers require an electric field magnitude over 4.7 kV/cm to propagate [85].

The radius of the ion head of a streamer is $0.03 - 0.1$ mm. The head of the streamer propagates with a velocity of 10^6 m/s, and has an average current of $0.1 - 1$ mA. The growth of the channel radius through diffusion over the lifetime of the streamer only amounts to ≤ 0.04 mm, so the channel can be approximated as a constant radius. The density of electrons in the streamer channel is $4 \times 10^{19} - 4 \times 10^{20}$ m^{-3} [85].

CHAPTER III

WIRELESS CHANNEL FUNDAMENTALS

3.1 High-Voltage Wireless Channel Research

A number of studies have characterized the wireless channel for smart grid applications. These studies focus on the interference generated in a high-voltage environment, such as a power substation, where a large source of interference is corona radiation. In 2006, Li et al. performed a laboratory experiment showing the radiated spectrum of corona to fall below 600 MHz [59]. However, they did observe discharges in SF_6 gas, a common insulator used in high voltage switches and transformers, to generate higher spectral interference up to 2.5 GHz. This is due to the faster quenching of breakdowns in SF_6, resulting in shorter impulses. In 2010, Gungor et al. deployed 802.15.4 sensor nodes at 2.45 GHz in a substation to observe communication performance [37]. Noise floor measurements showed an increase from -105 dBm (ambient) to -90 dBm in the power facility.

Bo et al. performed a comprehensive study in 2012 of substation interference [21],[99]. Their results agree with Li et al., showing that the interference from discharges in SF_6 can overlap with the 2.4 GHz band, resulting in packet loss. In 2009, researchers from the Georgia Institute of Technology (Georgia Tech) Propagation Group studied the effect of corona near an RFID tag antenna ($\sim$ 10 cm) on backscatter communication links at 5.8 GHz. Their results show a decrease in received backscattered signal power with increasing voltage [95]. Jia and Meng published a statistical model of impulsive interference (ionizations) near high voltage equipment. Their results show little effect on 2.45 GHz sensors. However, their work illustrates a different use of wireless sensors, where increased interference from discharges can be used to detect failures in equipment [46].

In order to accurately simulate packetized data communication in a substation, it is important to model the impulsive interference in both time and frequency domains. Most recently, Sacuto et al. used measured impulsive noise in a substation to create a Markov

chain model that can accurately replicate the interference for wireless link simulations [87]. They showed an upper limit on the spectral content around 1.4 GHz.

Recent studies have led to useful statistical models of communication performance under impulsive discharge interference. All these studies have characterized the performance of sensors in a substation environment, assuming that all discharges are isolated from the sensor node itself. If the sensors are physically attached to a high-voltage line, there is an increased chance of discharges on the sensor itself. Currently, significant research is being performed by the Intelligent Power Infrastructure Consortium in developing wireless sensors which can be used directly on high voltage lines and equipment [54],[71],[69]. The research focuses on the energy harvester and sensor design of the "smart sensor." The sensor designs share common themes such as shielding the electronics in a metal shell and using 2.45 GHz communications [70],[69]. Similar to previously cited 2.45 GHz sensor studies, a simple off-the-shelf dielectric shielded wire antenna is used protruding out from a metal shell. While the dielectric offers a level of protection, the potential exists for dielectric failure or wear over time leading to corona on the sharp wire tip beneath. To the best of the author's knowledge, there have been no thorough studies on the effects of high-voltage corona discharges occurring directly on wireless sensor antennas.

3.2 Communication System Overview

Starting in the late nineteenth century, investigations into transmission and detection of electromagnetic radiation were taking place. Not long after, the practical utility of this phenomenon was identified. Pioneers in the field of "wireless telegraphy" like Guglielmo Marconi pushed the science into the forefront of the communication industry. Over the years, wireless communication technologies have evolved from their primitive origins as spark-gap transmitters, to analog radios, to digital transceivers. Today, digital communication is widespread largely due to its robustness and versatility. With a properly designed signal link and coding techniques, data transfer with zero loss can be achieved, even in the presence of interference and a complex channel.

A wireless communication system can be decomposed into a few main blocks, illustrated

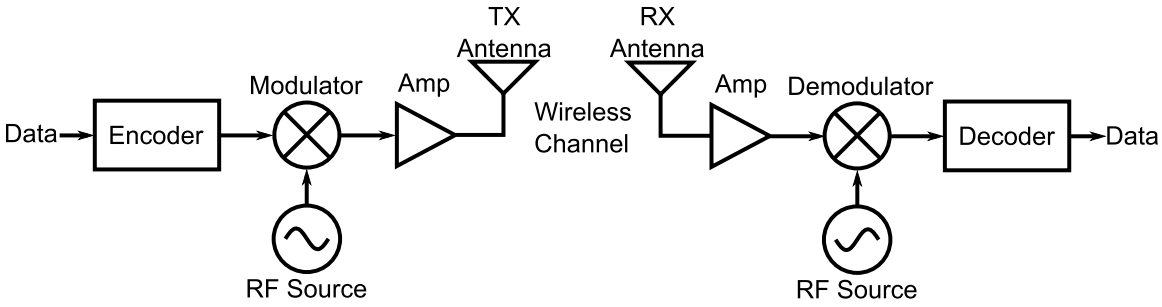

Figure 31: Simplified diagram of the primary blocks associated with a wireless communication link

in Figure 31. Not explicitly shown here are filters and cascaded amplifier stages. Additional complexity could also be introduced through the use of a superheterodyne receiver, where the RX signal is first mixed down to an intermediate frequency (IF) before demodulation. This allows for greater system flexibility and lower cost, especially in frequency agile systems. However, the functional behavior of the system remains the same. The system components are as follows:

1. *Data*: The raw information to be transmitted.

2. *Encoder*: Translates the raw data to a series of bits. This may optionally incorporate an error correction coding technique.

3. *Modulator*: Shifts the baseband encoded data up to a higher radio frequency (RF) for wireless transmission through the channel.

4. *Amp*: Amplifies the signal power for transmission or detection by the receiver.

5. *Antenna*: Transducer that coverts the signal current to propagating electromagnetic fields and vice versa.

6. *Wireless Channel*: The medium in which the electromagnetic fields propagate.

7. *Demodulator*: Shifts the RF signal down to the baseband frequency.

8. *Decoder*: Translates the bits into the original information based on the encoding scheme. Error correction can be used to compensate for errors in the received signal.

3.3 Antenna Characteristics

3.3.1 Impedance

An antenna is a device that converts electrical power into self-sustained electromagnetic radiation. The power input into an antenna often comes in the form of a confined electromagnetic wave on a transmission line. The antenna is connected to the transmission line at the antenna port, the interface between the transmission line and antenna. The currents on the conductors of the transmission line couple onto the antenna conductors, which, with a properly designed antenna, generate propagating electromagnetic fields.

Antenna impedance is a characteristic of an antenna related to its geometry and surrounding medium. As with any linear circuit, the impedance is the relationship between the voltage and current at a node. The antenna impedance is function of frequency and is expressed as a complex ratio of the voltage to the current between the two port conductors. A basic understanding of circuit theory can be extended to understand the antenna impedance. The real part of the antenna impedance represents the dissipative behavior of the antenna, and the imaginary part of the impedance reflects energy storage in the antenna near field (36). Antenna impedance changes with frequency as a function of its geometry, materials, and the surrounding medium. The design of an antenna involves careful consideration of the bandwidth of operation. Variations in antenna impedance over the desired bandwidth are minimized in a well designed antenna. For a narrowband communication link, it is often useful to make a single-frequency approximation for the antenna's impedance, using the measured impedance at the center frequency of the band in calculations.

$$Z(f) = R(f) + jX(f) \tag{36}$$

The energy dissipated in the antenna resistance is dissipated as radiation from the antenna and thermal losses, while the energy stored in the reactance is stored in the near-field of the antenna. These losses affect what is called the *radiation efficiency* of the antenna. The radiation efficiency η_{rad} is the ratio of the radiated power to the incident power on the antenna input port (37). It can vary anywhere from 0 and 1, where 0 implies that all energy

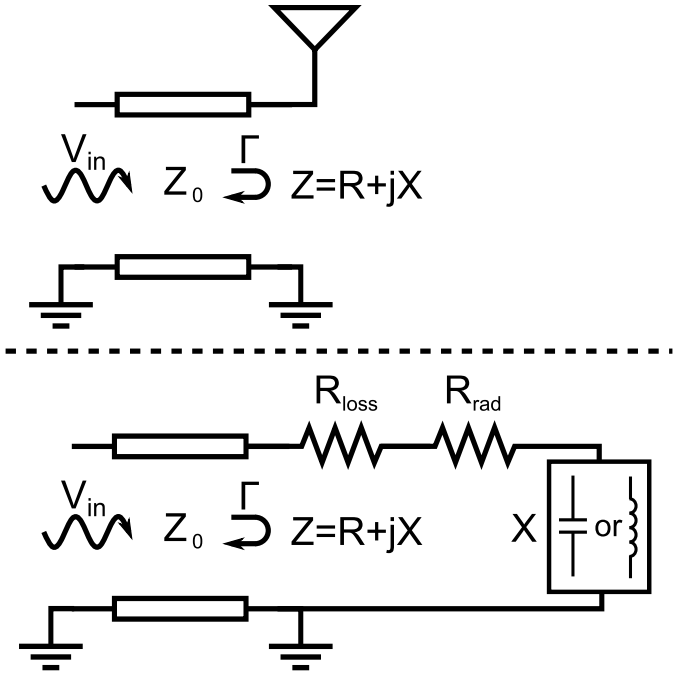

Figure 32: Equivalence between single-frequency antenna impedance and simplified circuit model. The measured input resistance is the sum of the radiation and loss resistance.

dissipated in the antenna is being lost and not radiated.

$$\eta_{rad} = \frac{P_{rad}}{P_{inc}} \tag{37}$$

Figure 32 provides a circuit model for an antenna at a single frequency. It is important to realize that such a simple model is only valid at the single frequency f_0 and will not necessarily provide the correct antenna impedance with small variations in frequency around f_0. While the antenna itself may be an elaborate metal structure with various currents flowing on it in different spots, when simply looking into the two-terminal input port it is indistinguishable from a resistor and capacitor/inductor in series. The choice of capacitor or inductor is determined by the sign of the reactance, positive reactance requiring an inductance and negative reactance requiring a capacitance. As this model does not extend to DC, there is no special significance to having a capacitor or inductor in series with the resistance. R_{rad} is the radiation resistance of the antenna and R_{loss} is the thermal loss resistance of the antenna.

Figure 32 illustrates the antenna connected to a transmission line of characteristic

impedance Z_0. For an ideal lossless transmission line Z_0 is purely real, which is a close approximation for a short transmission line section. With the antenna used for transmission, a voltage generator with series resistance Z_0 is connected to the input (left end) of the transmission line. A voltage wave V_{in} propagates through the transmission line toward the antenna. The current on the transmission line is in phase with and proportional to the voltage waveform by Z_0. At the antenna port (right end), the incident wave excites currents on the antenna. Electromagnetic fields are generated around the antenna structure according to Maxwell's Equations, which in turn interact with the currents on the structure. The currents induced on the antenna by these fields may create a wave at the antenna port, termed the reflected wave, which propagates away from the antenna toward the generator. The magnitude of the reflected wave, and phase with respect to the incident wave, determine the reflection coefficient from the antenna. For a single frequency, the incident and reflected waves can be simplified to complex time-independent phasors of some magnitude and phase. The reflection coefficient Γ is defined as the ratio of the reflected voltage V^- to the incident voltage V^+ (38).

$$\Gamma = \frac{V^-}{V^+} = \frac{Z - Z_0}{Z + Z_0} \tag{38}$$

From the reflection coefficient, the impedance of the antenna at the frequency f_0 can be calculated (39). The impedance Z of the antenna is a complex quantity. R is the real part of the impedance (resistance), and X is the imaginary part of the impedance (reactance) as given earlier in (36).

$$Z = Z_0 \frac{1 + \Gamma}{1 - \Gamma} \tag{39}$$

In order to achieve maximum power transfer from the generator to the antenna, thus maximizing the radiated power, the reflection coefficient is minimized. This corresponds to an antenna impedance complex conjugately matched to the source impedance (40).

$$Z_{in} = Z^* = R - jX \tag{40}$$

In RF engineering applications, transmission lines and signal generators are commonly designed to be 50Ω. Therefore, antennas are designed to have a 50Ω impedance to match. Matching an antenna perfectly to the generator over the entire frequency band of operation would be a practical impossibility. An engineering rule of thumb is employed: the return loss from the antenna should be less than $-10dB$ within the band of operation. The *return loss* (RL) is the decibel value relating the reflected and incident power on the antenna (41). Given the antenna's impedance, the return loss can be computed using (38) and (41).

$$RL = 10\log\left(\frac{P_{refl}}{P_{inc}}\right) = 10\log\left(\frac{|V^-|^2/Z_0}{|V^+|^2/Z_0}\right) = 10\log\left(|\Gamma|^2\right) \tag{41}$$

3.3.2 Gain

With the antenna return loss and radiation efficiency, the power radiated by the antenna can be determined from the incident power. The direction and polarization of the radiated power is given by the *antenna pattern*. The antenna pattern illustrates the proportion of power radiated in any given direction relative to that radiated by an isotropic (equal in all directions) radiator, as in Figure 33. The units are commonly provided in dBi, the decibel representation of this ratio. Despite the designation of the i, the units of dBi are in fact unitless when expressed in linear form and equivalent to dB. The i is used to indicate that the gain of the antenna is measured relative to an isotropic radiator. The *directivity* (D) of the antenna is the value of the antenna pattern in the main beam, or primary direction of radiation, typically the largest value. The *gain* (G) of the antenna, also in units of dBi, is the directivity scaled by the radiation efficiency (42). Scaling the directivity by the radiation efficiency accounts for the energy lost in the antenna in a power link budget calculation.

$$G = D + 10\log\left(\eta_{rad}\right) \tag{42}$$

Equation (43) combines the quantities discussed above to relate the power radiated P_{rad} by the antenna in a given direction θ to the power incident from the generator. The units are included in square brackets following each term.

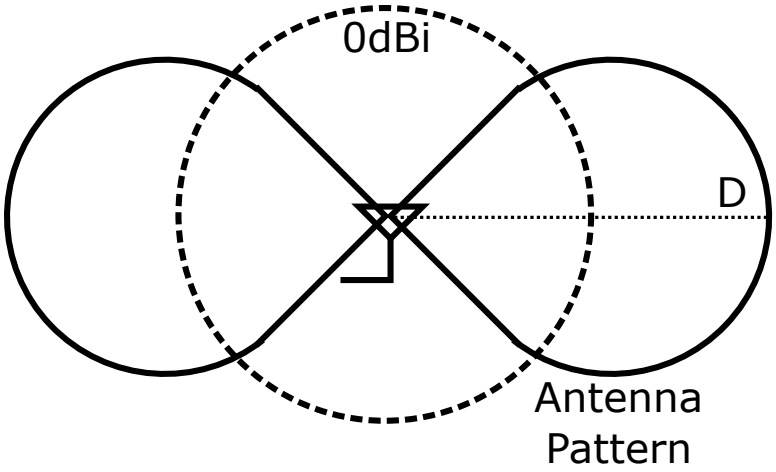

Figure 33: An example of an antenna pattern cross section. The directivity D is typically the largest value of the antenna pattern. The antenna pattern, specified in dBi, is referenced to the spherical pattern of an isotropic radiator, whose pattern in all directions is by definition $0dBi$.

$$P_{rad,\theta}[dBm] = P_{inc}[dBm] + 10\log\left(1 - |\Gamma|^2\right)[dB] + G_\theta[dBi] \tag{43}$$

3.3.3 Antenna Types

Antennas can be designed in numerous topologies (Figure 34 [16],[97],[68],[67]. The geometry of the antenna determines the resonant frequency of the antenna, the bandwidth, and the gain. Classically the simplest antenna design is that of a half-wave dipole. A half-wave dipole is a section of conductor such as wire that is a half wavelength long with the port in the center. Utilizing the method of images, a half-wave dipole can be adapted into a monopole topology, with a quarter wavelength wire protruding from a ground plane. When physical dimensions are a constraint, a dipole can be meandered to reduce the largest dimension with the trade-off of decreased efficiency, radiation resistance, and bandwidth [6].

Certain applications may require radiation only in a specific direction or mounting on a conducting surface. Antennas that incorporate a ground plane are useful in these applications as they restrict radiation to one half plane. The monopole's antenna pattern is maximum at small grazing angles to the ground plane, and null at the perpendicular. A

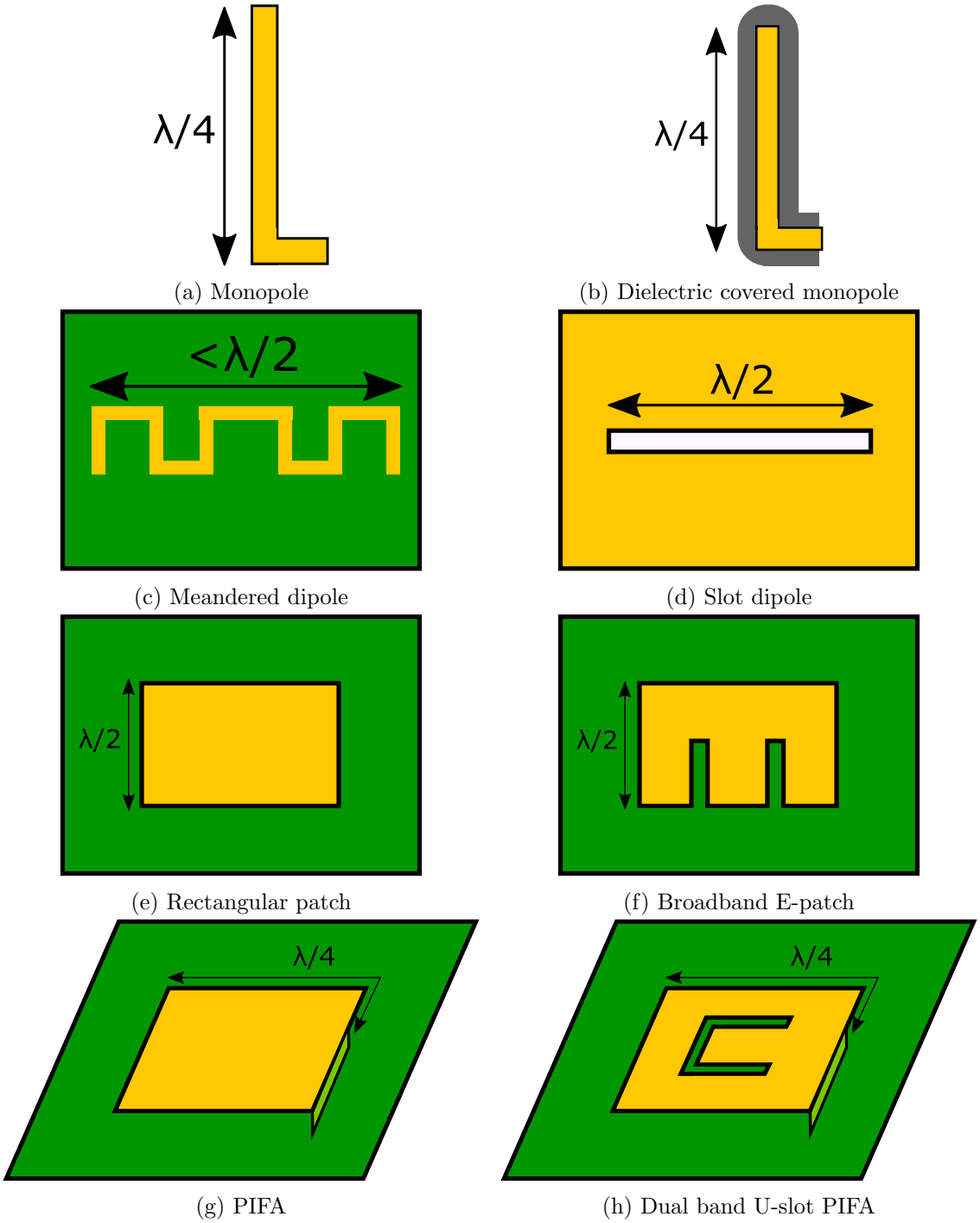

(a) Monopole

(b) Dielectric covered monopole

(c) Meandered dipole

(d) Slot dipole

(e) Rectangular patch

(f) Broadband E-patch

(g) PIFA

(h) Dual band U-slot PIFA

Figure 34: Illustrations for a selection of antenna topologies used in compact wireless devices.

microstrip patch antenna exhibits an antenna pattern with a radiation peak directly perpendicular to the plane. A patch acts as a resonant cavity between the antenna conductor and the ground plane, allowing for low profile design. The dimensions of the patch are on the order of a half wavelength, and can be made in a variety of shapes (rectangular, circular, triangular, etc) depending on the radiation requirements.

Slot antennas are another class of antennas that operate as complementary structures to other traditional antennas. One of the simpler slot antenna topologies is a slot dipole. As the name implies, the slot antenna is the dual to the traditional dipole discussed above, operating according to Babinet's Principle. The slot dipole consists of a large (in theory infinite, in practice much larger than a half wavelength) thin conducting sheet, with a half wavelength slot long slot cut out of it. The slot antenna is fed at the center of the slot, with one conductor on either side of the slot. Slot antennas are commonly used for large high-frequency arrays. Utilizing a single metal sheet with slots cut into it provides an economical and structurally sound method for array construction. Like the patch, the slot antenna offers a low-profile form factor. In addition, consisting of a single metal sheet, the entire antenna structure rests at a single DC potential, which may be advantageous for situations, for example exposure to electrostatic discharge (ESD).

Folded antennas provide another useful subcategory for design. Common designs include the inverted-F antenna (IFA) and planar inverted-F antenna (PIFA). The IFA takes the concept of a monopole antenna over a ground plane, folding the top half parallel to the ground, giving it an "L" shape. Folding the monopole parallel to the ground plane reduces its resistance and increases the capacitance. To compensate, a shorting post is added at a specific distance from the feed. giving it an "F" shape, hence the name. The PIFA is related to the IFA adapted to a patch antenna. A patch antenna can be shortened to $\lambda/4$ or less by shorting a portion of a side to ground. The width of the edge short affects the resonant frequency of the antenna. Patch antennas, including the PIFA, can be modified with slots and cutouts, resulting in wider bandwidths or circular polarizations. The PIFA, popular in handheld devices, is an attractive option for high-voltage applications due to its compactness, incorporation of a ground plane, and electrical short to ground.

3.4 Communication Channel

3.4.1 Path Loss

In designing a wireless communication link, the TX power required to successfully receive and decode a received signal must be calculated. In a free space environment, where multipath is not significant, Maxwell's equations can be simplified and combined to obtain the *electromagnetic wave equations* for the electric and magnetic fields (C.1). The TX and RX antennas are assumed to be in the far field, with a separation distance much greater than a wavelength. For RF frequencies, a wavelength is much less than $1m$, making this a valid assumption for a practical link. With this assumption, one can neglect the reactive fields (near field) surrounding the antenna and only consider the transverse propagating waves.

The power radiated by the antenna propagates in all directions at the speed of light. By the conservation of energy, the total power flux through a spherical surface centered at the antenna must be constant regardless of the distance from the antenna. Therefore, the power density at any distance r must be proportional to the radiated power divided over the area of a sphere (44). The SI units of power density are W/m^2 when power is given in W and distance is given in m.

$$S(r) \propto \frac{P_{rad}}{4\pi r^2} \tag{44}$$

The constant of proportionality here is the antenna pattern of the antenna. The power density varies with angle, and as discussed in the previous section, this relative difference is given by the antenna pattern. The power density can be calculated from (45). The antenna pattern is given by the unitless quantity $D(\theta, \phi)$. At the angle of peak magnitude for the antenna pattern, the value equates to the directivity of the antenna.

$$S(r, \theta, \phi) \frac{P_{rad} D\left(\theta, \phi\right)}{4\pi r^2} \tag{45}$$

For a well matched antenna (i.e. $Z = Z_0$), the power fed into the antenna is known to be equal to the power of the generator. The total power radiated is not necessarily known because of thermal losses in the antenna. Therefore, it is common to see the power

density specified as a function of the power accepted by the antenna, called the *transmitted power*, P_T (46). Here the gain is substituted for the directivity to account for the radiation efficiency.

$$S(r, \theta, \phi) = \frac{P_T G(\theta, \phi)}{4\pi r^2} \tag{46}$$

Based on the power density, a receiving antenna at a distance r will receive an amount of power proportional to its effective area, A_e. If the distance between the TX and RX antennas is much larger than the dimension of the antenna, the power density over the area of the RX antenna can be assumed constant. The power received by an antenna is then (47). The effective area of the receive antenna, depends on the orientation of the antenna with respect to the incident wave from the transmitter. The angles here have subscripts indicating the transmitter T and receiver R. The receive antenna angles are relative to the wave vector of the transmitted wave at r.

$$P_R = \frac{P_T G_T(\theta_T, \phi_T) A_{e,R}(\theta_R, \phi_R)}{4\pi r^2} \tag{47}$$

The physical area of the antenna is not equal to its effective area. The effective area is related to the gain of the antenna. The relationship is a well known analytical solution, stated in (48). The effective area is proportional to the gain the antenna as well as the square of the wavelength being used.

$$A_e = \frac{G\lambda^2}{4\pi} \tag{48}$$

All together, the power received P_R by an antenna with gain G_R from an antenna with gain G_T transmitting power P_T is evaluated from (49).

$$P_R = \frac{P_T G_T(\theta_T, \phi_T) G_R(\theta_R, \phi_R) \lambda^2}{(4\pi r)^2} \tag{49}$$

For the same transmit power and antenna gains, the received power decreases as the frequency increases. This behavior is due to the fact that antenna size scales with the wavelength. An antenna design that is scaled to half its size will operate at a frequency

twice as high with the same antenna pattern. With the gains of the two antennas held constant, the physical (and effective) area of the antennas decreases, resulting in less power density harvested by the RX antenna, and thus less power received. The *path loss*, in dB, for free space is a term accounting for the decrease in received power with distance and frequency (50).

$$PL_{FS} = 10 \log \left(\frac{(4\pi r)^2}{\lambda^2} \right) \tag{50}$$

By analytical or empirical analysis, it may be observed that is realistic scenarios, scattering from objects and attenuation in the environment is not negligible. In certain environments it may be possible to estimate this difference in loss statistically. The path loss can be adjusted by a factor to account for differences in real environmental interactions, such as multipath reflections of the surroundings (51). For free space, the path loss exponent n is equal to 2.

$$PL = 10n \log (r) + 10 \log \left(\frac{(4\pi)^2}{\lambda^2} \right) \tag{51}$$

3.4.2 Frequency Bands

In the United States and around the world, certain frequency bands in the electromagnetic spectrum are allocated for use by unlicensed transmitters. In these bands, the transmit powers are limited and simple frequency hopping must be utilized, but otherwise transmissions are not restricted to a particular party or application. Table 10 provides a list of the commonly used Industrial, Scientific, and Medical (ISM) bands for far-field RF communications. There exist lower frequencies commonly employed in near-field communications. Technologies are also expanding into higher frequencies for use in short-distance high-bandwidth communication. Currently, the most active bands for far-field communication are 915 MHz, 2.45 GHz, and 5.8 GHz. These will be the focus of the current work.

Table 10: Commonly used ISM bands for far field wireless applications

Center Freuqency	**Bandwidth**	**Frequency Range**	
433.92 MHz	1.74 MHz	433.05 MHz	434.79 MHz
915 MHz	26 MHz	902 MHz	928 MHz
2.45 GHz	100 MHz	2.4 GHz	2.5 GHz
5.8 GHz	150 MHz	5.725 GHz	5.875 GHz
24.125 GHz	250 MHz	24 GHz	24.25 GHz

3.4.3 Channel Capacity

The *channel capacity* of a communication link is fundamentally limited by the noise. In a perfect noiseless communication link, an infinite amount of information could be transmitted with an infinitesimal amount of power and bandwidth. In reality, various forms of real world noise degrade the received signal. Analog signals become distorted, as one might notice when listening to AM radio, hearing the hiss in the background. Digital signals are affected statistically. As noise power increases, the probability of correctly decoding a bit decreases.

The simplest form of noise, due to random thermal motion, is *thermal noise*. The thermal noise power is related to the temperature by the relation (52). P_N is the noise power, k_B is Boltzmann's constant, and T is the temperature, in SI units.

$$P_N = k_B B T \tag{52}$$

Thermal noise is modeled by an *additive white Gaussian noise* (AWGN) process. The noise is additive because it can be simply added to the signal or other noise, resulting in the degraded signal. The noise is white because it is frequency-flat, meaning it contains equal power at all frequencies. This is evident from the fact that (52) does not contain have a frequency dependence. Whether the bandwidth is taken from 0 to $1MHz$ or 100 to $101MHz$, the noise power is the same. This has the implication that consecutive noise samples are decorrelated; the noise voltage at any given time has no bearing on the noise voltage at any other time. AWGN is Gaussian, meaning that the voltage amplitudes follow a normal distribution with zero mean. A normal distribution probability density function (PDF) is provided in (53). Figure 35 shows an example of AWGN with a variance of 1. The sampling rate does not affect the noise distribution as all samples are decorrelated.

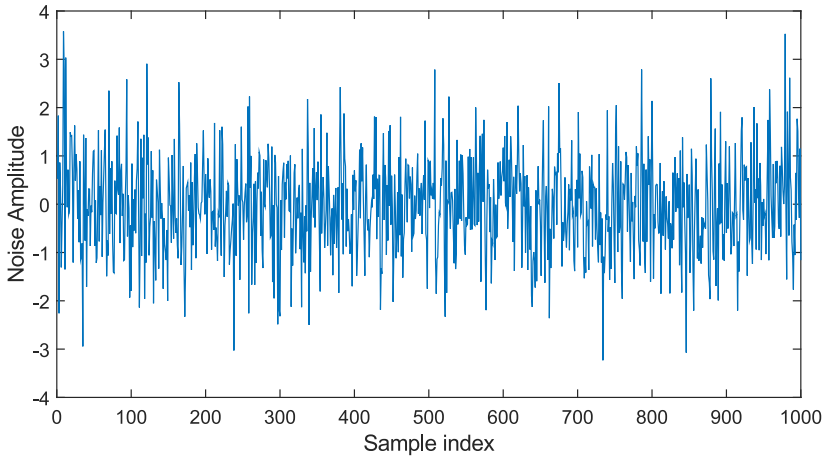

Figure 35: Example of AWGN with a variance of 1 over 1000 samples

$$f(x) = \frac{1}{\sigma\sqrt{2\pi}} e^{-\frac{(x-\mu)^2}{2\sigma^2}} \tag{53}$$

In digital communications, AWGN provides a simple yet powerful noise model for estimating the probability of successfully decoding a received signal. Claude Shannon, an Americal mathematician and engineer dubbed "the father of information theory" derived a fundamental limit for the channel capacity based on the AWGN model. Given a system bandwidth B, signal power P, and noise power P_N, Shannon determined that the maximum channel capacity is related by (54). The channel capacity is the maximum rate at which information can be successfully received and decoded by a receiver, in bits per second. This simple relationship is crucial to designing a working digital communication link.

$$C = B \log_2 \left(1 + \frac{P}{P_N}\right) \tag{54}$$

As it turns out, the ratio of signal power to noise power seen in (54) is ubiquitous in communication theory. The ratio is commonly referred to as the *signal-to-noise ratio*, or SNR. The practical knowledge that arises from the SNR is that if the noise power is increased by a factor, the signal power must also be increased by the same factor to maintain the current bit rate. A common metric for assessing the performance of a communication link is the *bit error rate* (BER). The bit error rate is a statistical metric specifying the ratio of

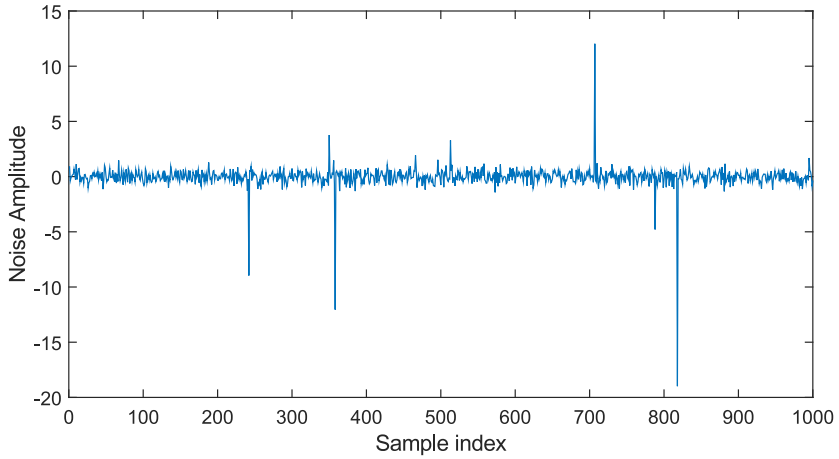

Figure 36: Example of impulsive noise. Large peaks in the amplitude occur that are not the result of random thermal processes. The impulses are added on top of the AWGN.

incorrectly decoded bits to total received bits for a communication link, and is commonly specified as a function of the SNR.

3.4.4 Time varying interference

AWGN is useful for estimating the BER for a particular modulation scheme, and analytical solutions can be obtained in many cases. In the presence of high-voltage corona, impulsive noise must also be considered. Impulsive noise is illustrated in Figure 36. The treatment of impulsive noise is not as straightforward as AWGN. A model for impulsive noise was derived by David Middleton, now named after him: Middleton's noise model [65],[66]. This model accounts for the statistical distribution of pulse occurrence as well as amplitude.

Middleton's noise model Class A is described here. Class A describes noise whose bandwidth is less than or equal to the system bandwidth and does not incur significant ringing in the front end filtering. The PDF of Middleton's noise model Class A is written in (55) [12].

$$f(x) = \sum_{m=0}^{\infty} \frac{a_m}{2\pi\sigma_m^2} e^{\left(-\frac{x^2}{2\sigma_m^2}\right)} \tag{55}$$

$$a_m = e^{-A}\frac{A^m}{m!} \ , \ \sigma_m^2 = \sigma_g^2 \frac{\frac{m}{A} + \Gamma}{\Gamma}$$

In the PDF definition, m is summed over the number of impulsive sources defined by a Poisson distribution with mean parameter A. A is the "impulsive index" of the random process, defined as the average pulse rate multiplied by the average pulse duration, or the average duty cycle of the pulses. A larger value of A corresponds with more pulses. Γ is the "Gauss impulsive power ratio" and is defined as the ratio of variances of the Gaussian to impulsive noise. In other words, it is the ratio of the average background AWGN power to the average power in an impulse. A smaller value of Γ corresponds with more intense pulses. σ_g and σ_m are the AWGN and impulsive noise variances, respectively.

Impulsive noise is generated by corona in several processes. Electron avalanche development leads to a sharp rise of current on as electron density builds through ionization processes. Trichel pulse formation is the cathode corona mechanism by which buildup of residual positive ions inhibits further ionization leading to the neutralization of the corona plasma. The electric current in a Trichel pulse appears as a sharp rising current, reaching a peak in $1 - 10$ ns and decaying approximately exponentially in approximately 100 ns. Streamer formation in an anode corona also takes the form of a pulse. A streamer propagates with a more intense current than a glow corona or Trichel pulse, but with longer rise and fall times that a Trichel pulse. Corona processes are impulsive by their very nature, and a treatment of the RF interference generated requires the use of an appropriate noise model.

The applicability of Middleton's model to these corona formations can be illustrated through an example of how the corona current propagates through a receiver chain of a Wi-Fi system. If corona pulses occur on an antenna, inducing a current at the antenna port, the corona current pulse is added to the signal current on the antenna and they propagate through the RF front end. Figure 37(a) shows a current pulse with a 10 ns rise time and 1 A peak. The time evolution of the current pulse is typical for a negative Trichel pulse, although the current is scaled to 1 for readability [63]. The pulse then passes though a high pass filter (HPF) with a 2 GHz cutoff, shown in Figure 37(b). The actual choice of filter type and cutoff on the front end will vary depending on the application requirements. For this example, a 2.45 GHz operating frequency is chosen.

Following the RF filtering, the pulse is mixed down to baseband with 2.45 GHz continuous wave (CW) and low pass filtered, shown in Figure 37(c). The filtering is shown here in two stages. For computational reasons, the signal is first filtered down to 500 MHz, resampled at a lower rate, then filtered to the final bandwidth of 20 MHz and resampled at 50 Msps, shown in Figure 37(d). A 20 MHz bandwidth is standard for a Wi-Fi link. The filters used in the example were all of the IIR Butterworth form.

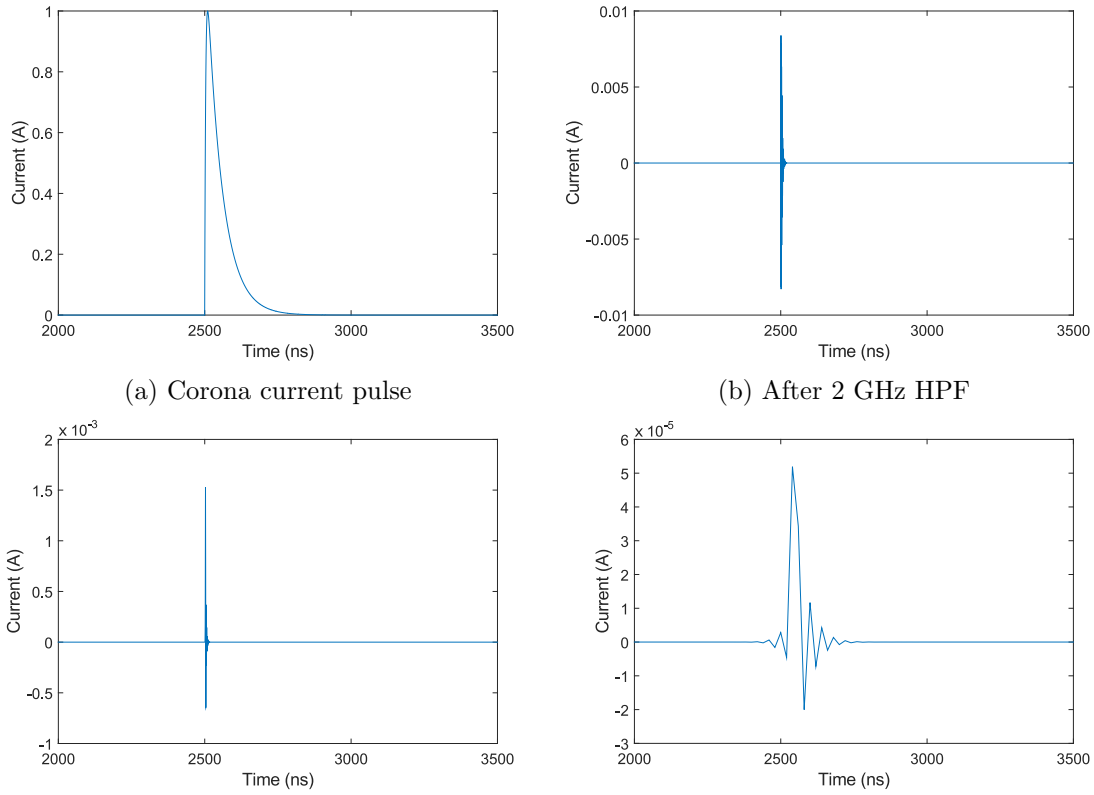

(a) Corona current pulse

(b) After 2 GHz HPF

(c) After 2.45 GHz mixing and 500 MHz LPF

(d) After 20 MHz LPF and 50 Msps resampling

Figure 37: Time domain visualization of current pulse with 10 ns rise time as defined in (80). The current pulse is shown mixed down from 2.45 GHz to baseband and sampled with a 20 MHz bandwidth as in a typical Wi-Fi link. Most of the RF power is contained in the sharp rising edge of the pulse.

Several observations can be made from the pulse analysis in 37. Most of the RF power is contained in the sharp rising edge of the pulse. The initial electron avalanche formation produces a rapid rise in current, generating higher frequency content. The short duration of the rising edge results in a short pulse duration that can be estimated well by Middleton's model. The other observation here is the relative power in the final pulse to the initial pulse.

Simply estimating the power from the peak current values in Figures 37(a) and (d), the power in the final pulse is approximately 90 dB below the power in the initial pulse. This is in agreement with other sources in literature which have measured corona emissions to occur predominantly below 100 MHz [47],[86],[63],[13]. Further discussion of corona current spectrum is treated in the following chapter, section 4.3.

CHAPTER IV

CORONA INTERACTION WITH RF SYSTEMS

The physical processes underlying corona formation were discussed in Chapter 3. This chapter aims to lay out the fundamentals behind the interaction of corona with RF systems. First, a treatment of corona as a non-thermal plasma is employed to derive a dielectric model applicable to electromagnetic analyses. With corona formation on an antenna, it is important to understand how the presence of an additional dielectric affects the gain and impedance. Following, the time domain corona current waveform is investigated to understand the power and spectrum associated with typical corona formation.

4.1 Plasma Dielectric Model

Electrical discharges at atmospheric pressure, such as corona, are a form of nonthermal plasma. The species of the plasma are not at thermal equilibrium. In the case of corona, the electrons are at a much higher temperature that the molecules and ions, which remain around the ambient temperature. When considering the interaction of electromagnetic waves with nonthermal discharges, it is computationally difficult to treat the plasma as a collection of charged particles, namely electrons and ions. Instead, it is useful to reframe the properties of the plasma in terms of the basic electromagnetic material properties of permittivity, permeability, and conductivity. To deduce the electromagnetic properties of the plasma as a function of the physical parameters, one can consider the simplest case of electromagnetic wave interaction, a plane wave, with a uniform plasma.

Assuming a uniform plasma of neutral molecules, positive ions, negative ions, and electrons, the forces of each from an electric field E are given by (56)-(59). The neutral molecules do not interact with the field and thus do not directly affect the plasma electromagnetic properties. In air at atmospheric pressure and density, neglecting the resonances of the molecules, there is a negligible effect on the permittivity from the molecular dipole moments and neutral air is commonly assumed to have a relative permittivity of 1. Due to

the large mass of the positive and negative ions relative the the small mass of the equally charged electrons, the ions do not contribute significantly to the currents induced by the electric field. Electron motion dominates the electromagnetic properties of the plasma and contributions from ions can be neglected [39].

$$F_m = 0 \tag{56}$$

$$\mathbf{F}_p = m_p \ddot{x}_p = e\mathbf{E} \tag{57}$$

$$\mathbf{F}_n = m_n \ddot{x}_n = -e\mathbf{E} \tag{58}$$

$$\mathbf{F}_e = m_e \ddot{x}_e = -e\mathbf{E} \tag{59}$$

The simplified plasma model is then assumed to be composed of free electrons in air, whose bulk relative permittivity is taken to be that of free space, ε. With an incident electromagnetic wave, a current is induced in the plasma from the electric field's force on the electrons. The electrons move freely in the gas, with the exception of collisional interactions with molecules. The collisional interactions with molecules are accounted for statistically by a force term that is proportional to the velocity of the electrons and the average collision frequency of an electron with molecules in the gas. The revised force on a free electron in a nonthermal plasma is given by (60).

$$\mathbf{F}_e = m_e \ddot{x}_e = -e\mathbf{E} - \nu m_e \dot{x} \tag{60}$$

From (60), the relative permittivity of the plasma can be derived. The complete derivation of the relative permittivity of a nonthermal plasma can be found in Appendix D, but the result is given here. Equation (61) shows that the relative permittivity of the plasma is a function of the *plasma frequency* ω_p, the collision frequnecy of electrons with molecules ν, and the frequency of the electric field ω. ε_∞ is the relative permittivity of the plasma as the frequency ω approaches infinity and the second term goes to zero. In other words, this

is the permittivity of the molecules of the medium (air) without free electrons. In the case of air, this is simply taken to be $\varepsilon_\infty = 1$.

$$\varepsilon_r = \varepsilon_\infty - \frac{\omega_p^2}{\omega\left(\omega - j\nu\right)} \tag{61}$$

The plasma frequency ω_p is a property of the free electron density. It describes the response of the electron density to an applied force displacing the electrons by a small amount. The plasma frequency is the natural frequency at which the electron density oscillates. The expression for plasma frequency is given in (62).

$$\omega_p = \sqrt{\frac{n_e e^2}{\varepsilon_0 m_e}} \tag{62}$$

4.1.1 Collision Frequency in Air at STP

The collision frequency used in (61) significantly affects the dielectric properties of the plasma. The collision frequency can be computed from the density of the gas and mean free path of the electrons. At standard temperature and pressure (STP), the density of air can be approximated from the ideal gas law (63). The variables are all in SI units, P is pressure, k_B is the Boltzmann constant, and T is temperature.

$$n_{air} = \frac{N}{V} = \frac{P}{k_B T} = \frac{100000}{1.38 \times 10^{-23} \times 273.15} = 2.65 \times 10^{25} m^{-3} \tag{63}$$

The mean free path of an electron in air is a function of the collision cross section with a molecule. The cross section for electron collisions with molecular nitrogen, the most abundant molecule in air, is on the order of $A_{air} \approx 1 \times 10^{-19} m^2$ [45]. The mean free path of an electron, λ_e, in air at STP can be derived from the density and collision cross section with (64).

$$\lambda_e = \frac{1}{\sqrt{2} n_{air} A_{air}} \approx 0.3 \mu m \tag{64}$$

With the mean free path of an electron in air and the the average velocity of an electron, the time between collisions, and thus the collision frequency, can be computed. The average

velocity of free electrons is a function of their temperature. In an electrical discharge, the temperature of the electrons is on the order of $10^3 K$. The average velocity v_e of the electrons is given by (65), where k_B is the Boltzmann constant, T_e is the electron temperature, and m_e is the electron mass in SI units.

$$\bar{v}_e = \sqrt{\frac{8k_B T_e}{\pi m_e}} = \sqrt{\frac{8 \times 1.38 \times 10^{-23} \times 10^3}{\pi \times 9.1 \times 10^{-31}}} = 1.965 \times 10^5 m/s \tag{65}$$

With the mean electron velocity and mean free path, the mean collision frequency is calculated (66). This is in agreement with the value used in the atmospheric plasma analysis by Laroussi [57].

$$\nu = \frac{\bar{v}_e}{\lambda_e} \approx 10^{12} Hz \tag{66}$$

4.1.2 Electromagnetic Propagation Through Plasma

The propagation of an electromagnetic wave through a plasma governed by (61) can be expressed as a propagation constant. The propagation constant is related to the complex permittivity by (67), where the real and imaginary components can be split up into the attenuation constant α and phase constant β, respectively.

$$\gamma = \alpha + j\beta = j\sqrt{\varepsilon_r}\frac{w}{c} \tag{67}$$

An interesting behavior of the Drude model can be observed here if one assumes the collision frequency to be vanishingly small (i.e. $\nu \ll \omega$). Also it is assumed that the background material of the plasma is a gas such as air. If the wave frequency is less than the plasma frequency, then the relative permittivity is negative. Taking the square root of a negative permittivity, one obtains a completely real propagation constant. With a zero phase constant and a nonzero attenuation constant, the mode of propagation for the wave is evanescent. The wave does not actually propagate in the plasma when its frequency is less than the plasma frequency but decays in a fully evanescent mode according to the attenuation constant. On the other hand, if the wave frequency is greater than the plasma frequency, the attenuation constant is zero and the phase constant is nonzero. The wave

propagates through the plasma unimpeded. This phenomenon was first observed in the ionosphere where the low density (low collision frequency) yields propagation characteristics similar to this. The plasma frequency of the ionosphere is on the order of several megahertz.

In air at surface atmospheric pressures, the collision frequency of electrons is not negligible. The RF frequencies of interest for wireless sensor communication are on the order of 10^{10} Hz, much lower than the collision frequency of electrons. A simplification of the Drude model (61) can be made by first splitting the equation into its real and imaginary components (68).

$$\varepsilon_r = \varepsilon_\infty - \frac{\omega_p^2}{\omega^2 + \nu^2} - j\frac{\omega_p^2 \nu}{\omega\left(\omega^2 + \nu^2\right)} \tag{68}$$

At low wave frequencies ($\omega \ll \nu$), the denominators in (68) are dominated by the collision frequency. The Drude model for an atmospheric pressure nonthermal plasma can be approximated by (69). Here, the permittivity of the medium for high frequencies is assumed to be 1, as it is for air.

$$\varepsilon_r \approx 1 - \frac{\omega_p^2}{\nu^2} - j\frac{\omega_p^2}{\omega\nu} \tag{69}$$

The complex term in (69) has the same form as seen in the effective conductivity for a complex dielectric (D.9). The conductivity of the plasma reduces to (70). Since the plasma frequency is proportional to the square root of the electron density, the conductivity of the plasma is proportional to the electron density of the plasma.

$$\sigma \approx \frac{\omega_p^2 \varepsilon_0}{\nu} = \frac{n_e e^2}{m_e \nu}\ ,\ \omega \ll \nu \tag{70}$$

The real part of the permittivity is also affected by the plasma. If the plasma frequency is much lower than the collision frequency, real part of the permittivity remains constant. For higher plasma frequencies (i.e. electron densities), the real permittivity reduces below 1, resulting in a phase velocity faster than the speed of light, but the group velocity remain below the speed of light [100]. The electron density corresponding with a collision frequency of $\nu = 10^{12}$ Hz, such that $\omega_p = \nu$ is $3 \times 10^{20} m^{-3}$.

At low frequencies, the plasma behavior is that of a conductor of free electrons that lose energy to collisions. As the wave frequency approaches the collision frequency, the imaginary permittivity falls off as $1/\omega^3$, or equivalently the conductivity of the plasma decreases as $1/\omega^2$ (see equation (68)).

Atmospheric pressure electrical discharges have an electron density in the range of 10^{14} to $10^{20} m^{-3}$. For these electron densities, Table 11 provides a listing of the associated plasma frequency, complex permittivity at 2.45 GHz, approximate conductivity σ based on (70), and the attenuation per unit distance. Even on the high end of electron density, the plasma does not attenuate the electromagnetic wave significantly. The conductivities are many orders of magnitude lower than those of common metals ($\sim 10^7 S/m$). The equivalent plasma conductivity is on the order of water, where distilled water has a conductivity around 2×10^{-4} S/m [84].

Table 11: Plasma dielectric properties for electron densities associated with atmospheric pressure electrical discharges.

n_e $[m^-3]$	ω_p [rad/s]	ε_r @ 2.45 GHz	Approximate σ [S/m]	Attenuation [dB/cm]
10^{14}	5.64×10^8	$1.000 - j2.067 \times 10^{-5}$	2.818×10^{-6}	0.000046
10^{15}	1.78×10^9	$1.000 - j2.067 \times 10^{-4}$	2.818×10^{-5}	0.00046
10^{16}	5.64×10^9	$1.000 - j2.067 \times 10^{-3}$	2.818×10^{-4}	0.0046
10^{17}	1.78×10^{10}	$1.000 - j2.067 \times 10^{-2}$	2.818×10^{-3}	0.046
10^{18}	5.64×10^{10}	$0.997 - j0.2067$	0.02818	0.46
10^{19}	1.78×10^{11}	$0.968 - j2.067$	0.2818	4.6
10^{20}	5.64×10^{11}	$0.682 - j20.67$	2.818	46

The phase constant and attenuation constant (67) are plotted in Figures 38 and 39. There are two frequencies in the Drude model at which the propagation behavior changes, which is clearly evident from the attenuation constant plot. At frequencies below $\omega_p^2/(2\pi\nu)$, the attenuation increases with frequency. It then remains approximately constant until the plasma frequency $\omega_p/(2\pi)$, around which the attenuation begins to decrease with increasing frequency. In the limit where the frequency is much greater than the plasma frequency, the attenuation constant goes to zero and waves propagate without dispersion. Figure 40 shows the variation wave attenuation with frequency. Figure 41 shows the real part of the index of refraction at various RF frequencies. The index of refraction is related to the complex permittivity by (71).

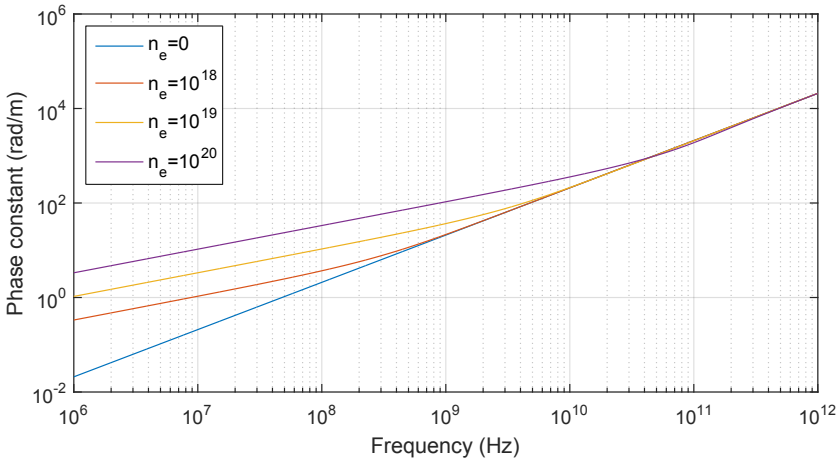

Figure 38: Phase constant β of a plane wave propagating in a Drude plasma dielectric with electron density n_e and plasma collision frequency $\nu = 10^{12}$

$$n = \sqrt{\varepsilon_r} \tag{71}$$

The theory presented here is limited to plane waves in a uniform medium. Corona formation on an antenna is nonuniform and interacts with the near fields of the antenna. The treatment of this situation cannot be handled with simple analytical expressions, but requires computational or experimental methods. Nevertheless, understanding the degree to which a cold plasma interacts with an electromagnetic wave theoretically allows one to understand the degree to which corona formation can impact an antenna. Figure 40 indicates that wave attenuation is higher at higher frequencies. At the upper end of the electron density range of $n_e = 10^{20} m^{-3}$, the attenuation constant at 5.8 GHz is 12.49 dB/cm higher than at 915 MHz. There is little difference below $n_e = 10^{18} m^{-3}$ between the selected frequencies. Figure 41 shows that the index of refraction deviates from 1 more at lower frequencies. With corona formation on an antenna surface, a higher index of refraction may lead to detuning of the antenna resonance. Figure (40) and Figure (41) present tradeoffs in the selection of an RF frequency for the antenna to minimize the impact of plasma formation. One solution may be to design an antenna that is wideband, accounting for the possibility of an additional dielectric that could detune the antenna. The antenna can be designed to be robust against detuning by plasma formation on the surface. However, loss

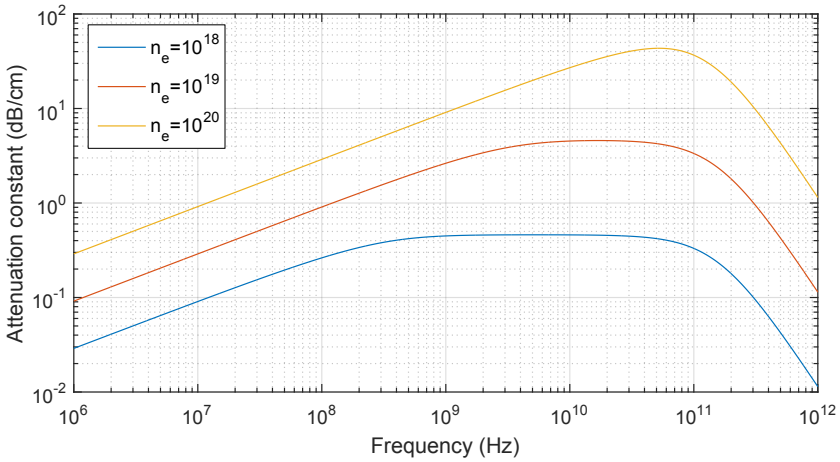

Figure 39: Attenuation constant α of a plane wave propagating in a Drude plasma dielectric with electron density n_e and plasma collision frequency $\nu = 10^{12}$

of electromagnetic energy to the plasma cannot be avoided as easily if the plasma is present on the antenna.

4.2 Magnetized Plasma

The Drude model is valid in a regime where there is no applied magnetic field. When a magnetic field is applied to the plasma, a harmonic electric field not only induces linear motion alone the electric field axis, but also induces gyroscopic motion perpendicular to the direction of the applied magnetic field. The magnetic field here is assumed to be static, with a high harmonic electromagnetic field. The magnetic field of the electromagnetic wave is negligible with respect to its electric field and a large applied magnetic field. Here we will discuss the extent to which magnetic effects must be considered in high-voltage sensing applications.

In the presence of a static magnetic field, a careful tensor derivation of the motion of free electrons results in the Appleton-Hartree equation [40]. The equation is most easily recorded by grouping terms. The equation defines the square of the index of refraction (72). The angle θ is the angle between the magnetic field vector and the wave vector. The $\theta = 0$ case corresponds to propagation along the magnetic field lines, i.e. $\mathbf{B} \parallel \mathbf{k}$. The ω_p is the plasma frequency defined above in (62), and ω is the electromagnetic wave frequency. A

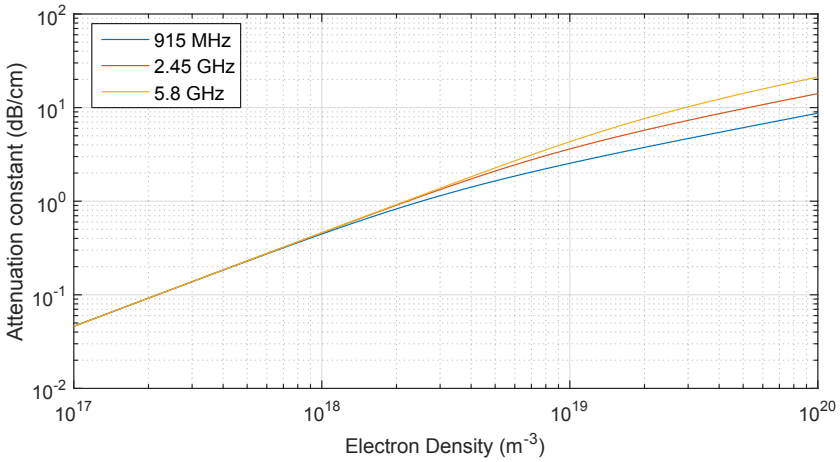

Figure 40: Attenuation constant α of a plane wave propagating in a Drude plasma dielectric with the specified frequency and plasma collision frequency $\nu = 10^{12}$

new variable is defined here, namely the electron gyro frequency, ω_h. The electron gyro frequency, also known as the cyclotron frequency, is the angular rate of the circular motion of an electron with a velocity vector perpendicular to the magnetic field vector. All terms are in SI units, and frequencies expressed in radians per second. The collision frequency is given by ν.

$$n^2 = \varepsilon_r = 1 - \frac{X}{1 - jZ - \frac{\frac{1}{2}Y^2 \sin^2\theta}{1-X-jZ} \pm \frac{1}{1-X-jZ}\left(\frac{1}{4}Y^4 \sin^4\theta + Y^2\cos^2\theta\,(1-X-jZ)^2\right)^{\frac{1}{2}}} \tag{72}$$

$$X = \frac{\omega_p^2}{\omega^2}\ ,\ Y = \frac{\omega_h}{\omega}\ ,\ Z = \frac{\nu}{\omega}\ ,\ \omega_h = \frac{|\mathbf{B}|\,e}{m_e}$$

The $\pm$ sign in the Appleton-Hartree equation differentiates between the polarization modes of propagation. For the $\mathbf{k} \parallel \mathbf{B}$ case, the $+$ sign represents the left-hand circularly polarized mode, and the $-$ sign represents the right-hand circularly polarized mode. For the $\mathbf{k} \perp \mathbf{B}$ case, the $+$ sign represents the ordinary mode where the wave electric field is parallel to the static magnetic field, and the $-$ sign represents the extraordinary mode where the wave electric field is perpendicular the the magnetic field. In the ordinary mode, the magnetic field has no effect on the wave propagation and the index of refraction reduces to the simpler Drude model discussed above.

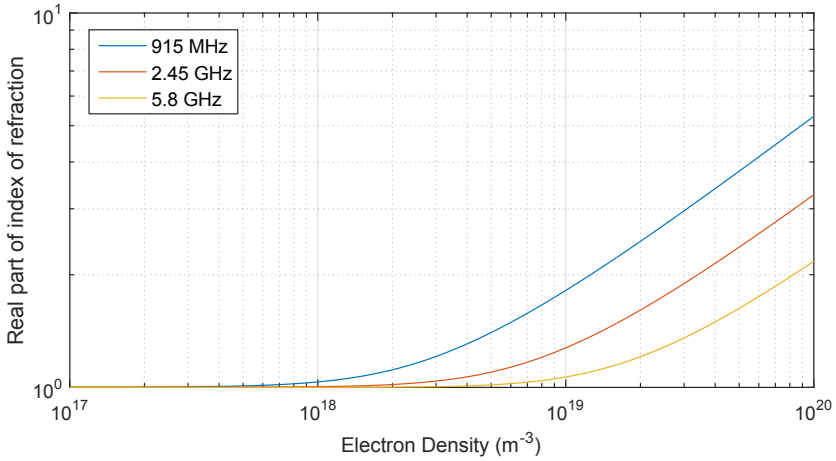

Figure 41: Real part of the index of refraction for a Drude plasma dielectric at the specified wave frequency and plasma collision frequency $\nu = 10^{12}$

This model was first derived to understand the propagation of waves in the ionosphere. The study of Whistler modes is commonly associated with the use of the Appleton-Hartree equation. These propagation modes arise from lightning strikes, and involve the propagation of waves along the magnetic field lines. At atmospheric pressure, the collision frequency ν is much greater than the wave frequency. In addition, the plasma of interest in corona formation is much smaller than a wavelength. The whistler phenomenon does not develop as it does in the ionosphere, and is beyond the scope of this work, but more information can be found in [40].

4.2.1 Current around high-voltage power lines

The primary question to address in determining the need for the Appleton-Hartree equation in this work is the source and magnitude of the magnetic field. There are two primary sources of magnetic field around a high-voltage power line sensor that can be accounted for: the Earth's magnetic field and the magnetic field due to current flowing through the power line. The Earth's magnetic field at the surface varies depending on location from 2.6 to 6.5×10^{-5} T, so an average can be taken of

$$B_{Earth} \approx 5 \times 10^{-5} T$$

.

Assuming the sensor on the power line is much closer to the line than the separation distance to the other phases, the magnetic field at the sensor will be dominated by the current of its mounted line. Current running through the high-voltage transmission lines is on the order of 100 A. Ampere's law for cylindrical symmetry is given in (73), where μ_0 is the free space permeability, I is the current through the line, and r is the distance from the center of the line to the point of corona formation.

$$B = \frac{\mu_0 I}{2\pi r} \tag{73}$$

At a short distance of $5cm$ from the center of the line, the magnetic field of a 100 A current is only 4×10^{-4} T, slightly higher than the magnetic field of the Earth. For the following calculations, it will be assumed that the current is large and the antenna is close to the line conductor, resulting in a magnetic field

$$B_{line} = 10^{-3}\text{T}$$

.

The electron gyro frequency resulting from the line's magnetic field is

$$f_h = \frac{\omega_h}{2\pi} = \frac{|\boldsymbol{B}_{line}|\, e}{2\pi m_e} = 28\text{MHz}$$

.

To determine the impact of the electron gyro frequency in the case of atmospheric pressure electrical discharges near a power line, (72) can be analyzed in four unique cases. The orders of magnitude of each term in the Appleton-Hartree equation can be estimated first for atmospheric pressure plasma, $\nu = 10^{12}$ Hz, with a wave frequency on the order of $\omega \sim 10^{10}$ rad/s, and a plasma electron density on the order of $n_e = 10^{18}$, for a plasma frequency on the order of $\omega_p \sim 10^{11}$ rad/s. The Appleton-Hartree equation parameters in a high-voltage transmission line scenario are estimated to be:

$$Z = \frac{\nu}{\omega} \sim 100$$
$$X = \frac{\omega_p^2}{\omega^2} \sim 100$$

$$Y = \frac{\omega_h}{\omega} \sim 0.01$$

The four cases of the Appleton-Hartree equation, depending on the angle of the applied magnetic field and wave polarization, are:

1. $\theta = \pi/2$, sign in (72) denominator is $+$:

   The Appleton-Hartree equation reduces to

   $$\varepsilon_r = 1 - \frac{X}{1 - jZ}$$

   This is the ordinary mode where the magnetic field has no impact on wave propagation, and the equation reduces to the Drude model.

2. $\theta = \pi/2$, sign in (72) denominator is $-$:

   The Appleton-Hartree equation reduces to

   $$\varepsilon_r = 1 - \frac{X}{1 - jZ - \frac{Y^2}{1 - X - jZ}}$$

   Utilizing the orders of magnitude for the terms given above, the fractional term $\frac{Y^2}{1-X-jZ}$ is on the order of 10^{-6}. This is many orders of magnitude smaller than the Drude model terms preceding it, and therefore negligible. This case simplifies to the Drude model.

3. $\theta = 0$, sign in (72) denominator is $+$:

   The Appleton-Hartree equation reduces to

   $$\varepsilon_r = 1 - \frac{X}{1 - jZ + Y}$$

   The imaginary part of the denominator remains equal to jZ, while the real part is equal to $1 + Y$. The term Y is two orders of magnitude smaller than 1, and can be neglected so long as the actual frequency of consideration is on this order. The wave frequency must be much larger than the gyro frequency of $28MHz$ for this simplification to hold.

4. $\theta = 0$, sign in (72) denominator is $-$:

   The Appleton-Hartree equation reduces to

$$\varepsilon_r = 1 - \frac{X}{1 - jZ - Y}$$

   This case follows the same logic as the previous case, with a change in the sign of Y. The model simplifies to the Drude model so long as the wave frequency is much larger than the gyro frequency of $28MHz$.

According to the analysis above, in a nonthermal plasma at atmospheric pressure forming near a power line, the electron gyro frequency has a negligible impact on the dielectric model for the plasma. The simplification of the Appleton-Hartree plasma model to the Drude model does not hold if the wave frequency is reduced or the line current (and the resultant magnetic field) is increased by a factor of ~ 100.

4.3 Corona Current and Electromagnetic Interference

Electromagnetic radiation is the result of result of a time-varying current. Far from the current density, the radiated electric fields in free space are given by (74) [100]. Location 1 is the point of measurement of the field, and location 2 is the location of the current density $\boldsymbol{j}$. The field measured at location 1 is the time retarded field, as specified in the current density. r_{12} is the separation distance between the source current density at 2 and the measurement point at 1.

$$\mathbf{E}(1) = -\frac{\partial}{\partial t} \int dV_2 \frac{\boldsymbol{j}\,(2, t - r_{12}/c)}{4\pi\varepsilon_0 c^2 r_{12}} \tag{74}$$

Corona and other electrical discharges have long been known to create electromagnetic radiation, resulting in interference in AM radio most notably. The physical mechanism behind this radiation is the acceleration of charges in the electron avalanche (see Section 2.2). The ionizing electric field accelerates electrons in an electron avalanche, resulting in radiation [63].

Consider an electric discharge forming on a high-voltage power line sensor. First, one can make the assumption that the physical size of the discharge is much smaller than the

wavelength of the highest frequency of its radiation. The corona is treated as an electrically small radiator. This assumption allows one to treat the position r_{12} as a constant over the volume current integral, assuming the measurement point 1 is far away. The radiated electric field is then rewritten (75). The time retardation can also be ignored as this would only result in an absolute time shift of the measured field, if r_{12} is considered approximately constant over the volume V_2.

$$\mathbf{E} = -\frac{1}{4\pi\varepsilon_0 c^2 r_{12}} \int dV_2 \frac{\partial \boldsymbol{j}}{\partial t} \tag{75}$$

The volume current density of an electrical discharge is the flow of charged particles. With a volume density of charged particles, the current density is equal to the density of charge multiplied with the velocity of the charge density (76). Here, the current density contribution of each charged species is summed to obtain the net current density. The variable q_i is the charge of the i^{th} species, n_i is the number density, and μ_i is the mobility.

$$\boldsymbol{j} = \sum_i q_i \left(n_i \mu_i \boldsymbol{E}\right) \tag{76}$$

As discussed in Section 2.2, the ions being much more massive than electrons have a much lower mobility. They do not contribute to the current as significantly as the electrons, and to a first approximation can be ignored. The radiated electric field is then given by (77).

$$\mathbf{E} = -\frac{1}{4\pi\varepsilon_0 c^2 r_{12}} \int dV_2 \frac{\partial}{\partial t} \left(n_e(t) \mu_e(t) \boldsymbol{E}(t)\right) \tag{77}$$

Under an applied static electric field beyond the ionization threshold for the medium, an electron avalanche develops. As the avalanche develops, the electron density increases with time, thus increasing the current. In certain corona formations like the negative Trichel pulse, the buildup of positive ions at the cathode causes a decrease in the electric field around the cathode and inhibits further electron avalanche ionization. The current density falls off and reaches zero, at which point the process begins again. Other types of corona formations such as streamers also undergo a time varying current density. In positive

streamer formation, electron avalanches at the anode create a globule of positive space charge. If the positive ion density of the globule is sufficiently high, it can induce further avalanches at its surface, farther from the surface of the cathode. These avalanches in turn leave positive space charge farther yet from the cathode. This process is self-sustaining and can continue beyond the electric field threshold for ionization due to the cathode fields. The streamer process, like Trichel pulses, is eventually arrested by insufficient generation of space charge to be self-sustaining. By taking the Fourier transform of the radiated field, or the Fourier transform of the derivative of the current, the radiated spectrum can be determined.

The accuracy of the radiation characteristics obtained from (77) is limited by the accuracy of the model for electron ionization, drift, and diffusion. Simulations can be carried out in reduced problems and have shown to replicate physical phenomena such as Trichel pulse formation [88],[11],[26]. The results of the simulations are in close agreement with measurements of corona current. Negative Trichel pulse current has been shown in simulations and measurements to have a rise time on the order of $1 - 10$ ns, and duration on the order of 100 ns. Analysis of positive corona and streamer formation shows that the current rise time is one the order of 50 ns with a duration on the order of 250 ns. The corona current can be obtained through simulation of the electron flow (77), but is more readily obtained through measurements.

$$I(t) = K i_p \left(e^{-\alpha t} - e^{-\beta t} \right) \tag{78}$$

The periodic rise and fall of corona current with the development and inhibition of electron avalanches can be modeled more simply by a periodic current waveform of the form (78) [63]. In (78), K is a constant scaling the pulse amplitude, α and β are constants specifying the rise and fall time of the current pulse, and i_p is the current amplitude of the pulse. The constants can be selected to match the measured and simulated corona current waveform of a single pulse. Maruvada presents estimates for the current waveform of a single positive and negative corona pulse given in (79) and (80), respectively [63]. These currents are plotted in Figure 42.

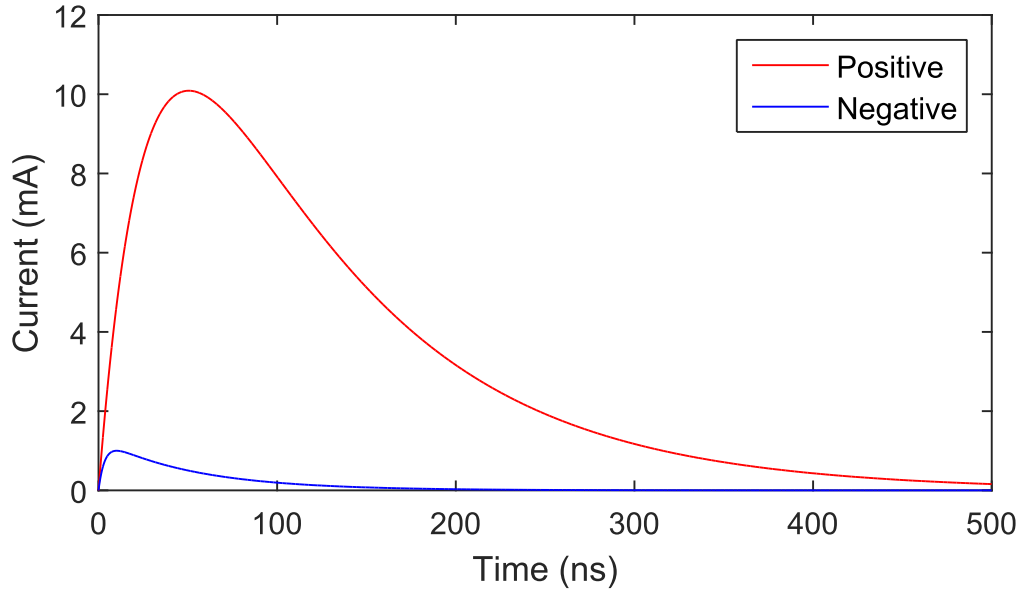

Figure 42: Typical corona current waveform for positive corona streamer pulse and negative corona Trichel pulse.

$$I(t) = 2.335 i_p \left(e^{-0.01t} - e^{-0.0345t}\right) \text{ , Positive corona current pulse} \tag{79}$$

$$I(t) = 1.3 i_p \left(e^{-0.019t} - e^{-0.285t}\right) \text{ , Negative corona current pulse} \tag{80}$$

The Fourier transform of (78) can be worked out analytically, assuming the current $I = 0$ for times less than $t = 0$. The Fourier integration results in (81).

$$I(\omega) = \frac{K i_p (\beta - \alpha)}{(\alpha + j\omega)(\beta + j\omega)} \tag{81}$$

The power in the waveforms shown in Figure 42 is computed and shown in Figure 43, normalized to the DC power of the positive corona.

Figure 43 shows that much of the power in the corona current is at relatively low frequencies, much lower than the RF frequencies of interest in wireless sensing (915 MHz, 2.45 GHz, and 5.8 GHz). The frequency spectrum of typical corona lies below 50 MHz according to the analytical solution. This is in agreement with measurements that have been carried out on interference generated from high-voltage lines. The interference in the

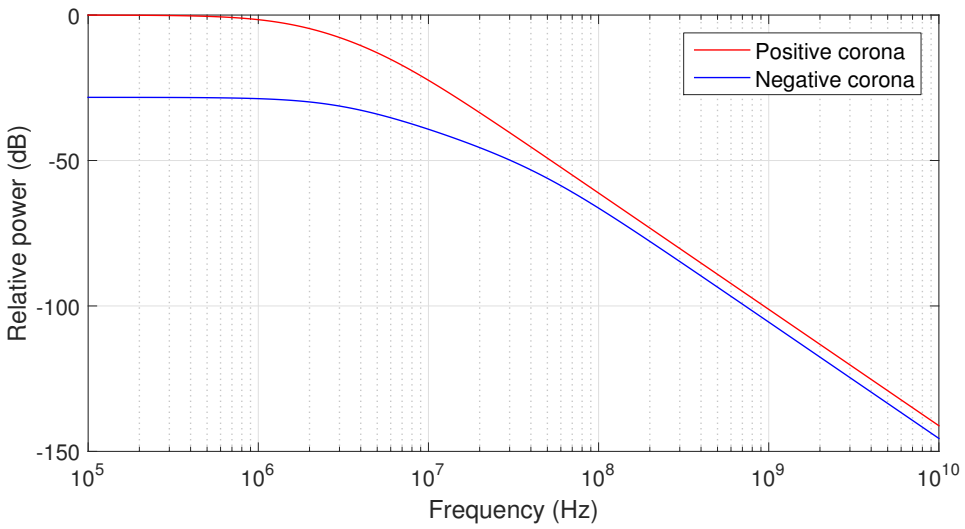

Figure 43: Power spectrum (normalized to streamer) for a positive corona streamer pulse and negative corona Trichel pulse.

MegaHertz range has posed problems for AM radio transmission and some analog television broadcasts.

Morris and Rakoshdas measured the spectra of corona on high-voltage DC lines up to 600 kV [74]. Measurements performed for positive and negative corona up to 10 MHz show that the spectral power falls at approximately 20 dB per decade, although with some significant dips and peaks on the order of 15 dB. A comparison of positive and negative lines indicated higher power radiated from positive than negative lines. The measured interference from positive corona was approximately 20 dB higher than negative corona, although the negative measured power fell within the noise floor in the measurements. Around 1 MHz, the power of positive corona interference fell around $1000\mu V/m$, or -76 dBm. In addition, interference power increased by approximately 6 dB in snowy conditions with frost formation on conductors, as compared with clear conditions.

Juette performed measurements of radiated noise from various types of corona of high-voltage lines [47],[86]. The measurements are reported in Figure 44. The measured interference powers are normalized to 0 dB at 0.15 MHz, with the absolute values of the 0 dB level written in parentheses for each curve. The spectra of the different corona modes are all observed to fall off well below 100 MHz, with the exception of gap noise. Gap noise

here refers to a complete arc between the anode and cathode (or high-voltage and ground) conductors. With proper power transmission line design and spacing arcing is an avoidable discharge phenomenon, and regular interference from arcing should not be an issue in wireless sensing. The positive streamer spectrum falls off around 1 MHz, while negative glow and streamer discharges are shown to fall off closer to 10 MHz. Positive streamer power is also shown to be $35 - 40$ dB higher than negative corona near DC, but falls off more sharply, so has a similar power to negative corona around 100 MHz. The positive streamer power decreases at a rate of 35 dB per decade between 10 MHz and 100 MHz.

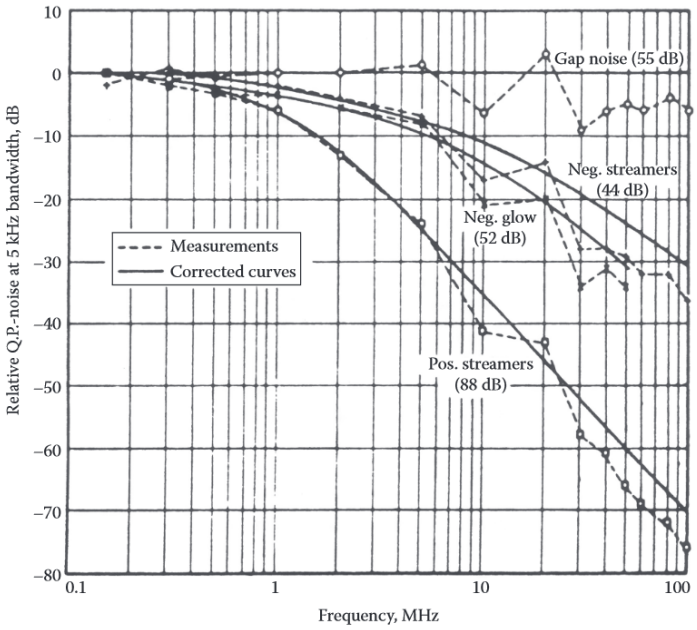

Figure 44: Frequency spectra of different modes of electrical discharge on high-voltage transmission lines [47].

Arora investigated corona electromagnetic interference from various corona discharge types indicating the presence of some higher frequency content [13],[14]. Measurements were performed at a 1 m distance from the corona formation using a broadband antennas. Glow and Trichel corona exhibited a spectral content peak between 30 and 50 MHz, with a measured power as high as -18 dBm at 45 kV applied voltage. The power at 180 MHz was measured at -38 dBm, and lower values of power were measured up to 1 GHz. The power spectrum up to 1 GHz was present in intermittent bands, as opposed to following a

smooth power distribution across frequencies. The spectrum of streamer corona was limited below 160 MHz, with a -28 dBm power peak around 40 MHz with an applied voltage of 45 kV. While the streamer interference bandwidth is lower than that of glow corona, the magnitude is higher. This is in agreement with the model for corona pulse shape in (42), where the streamer has a higher amplitude but longer rise time.

CHAPTER V

EXPERIMENTAL APPROACH

5.1 High-Voltage Measurement Overview

5.1.1 Inverted Voltage Setup

One of the major hurdles in performing measurements on an antenna while undergoing corona formation is the high voltages needed to generate the plasma. In order to produce the electric fields around the antenna capable of ionizing the surrounding air, the antenna must have a voltage of 10s to 100s of kilovolts relative to ground. Placing the antenna at these voltages poses safety risks that must be accompanied with the proper safety precautions. It is important that rigorous safety measures be followed to ensure the safety of all individuals. To minimize risk of contact with high voltage, complete physical isolation should be maintained from all instruments that pose a risk of conduction to high voltage. All control of the measurement equipment mist be performed by remote, non-contact means.

High-voltage measurements of RF behavior also create logistical issues with regard to ensuring all equipment is properly secured and protected, operating within the electrical specifications. When undergoing corona, the antenna is exposed to currents ranging from microAmps to Amps. Difficulties arise when attempting to perform measurements of the antenna impedance using a network analyzer, or spectral measurements using a spectrum analyzer. These instruments are designed to handle low power levels and employ sensitive amplifiers on the front end. The input power levels for these instruments have ratings on the order of $1W$ or less. It is crucial to limit the input power and voltages to the instruments while allowing for precise measurements of high-frequency characteristics. In order to protect the equipment in the event of high-current pulse on antenna, an RF coaxial lightning arrestor, lightning rated high-pass filter, and diode power limiter are employed.

A direct method of measuring antenna characteristics would be to mount the antenna on a high-voltage line or transformer. This poses logistical issues. The measurement equipment

needs to be at the same potential as the antenna. Placing a VNA on a high-voltage electrode poses difficulties in mounting, shielding from corona and arcs, and supplying power. The measurements instead are performed on an alternative setup.

An AC high-voltage test set from Phenix, model BK130, provides the high voltage for corona formation. The unit contains an oil-insulated passively-cooled transformer capable of stepping up $120V$ at $60Hz$ to as high as $130kV$ at $60Hz$. The device also consists of a control unit where the operator can dial the output voltage anywhere between 0 and $130kV$ by way of an analog knob. The control unit presents the user with output voltage and current on a digital display. Access to the test set is provided by Southern States, LLC.

In real power line sensing applications, the AC corona would form around a wireless sensor antenna at high potential relative to the surroundings at earth ground potential, as illustrated in Figure 45. While reproduction of this configuration in laboratory conditions is possible, the high voltage on the antenna poses safety and technical challenges for accurate measurement of the antenna characteristics. Direct connection of the antenna to a network analyzer would require the instrument be at the high voltage as well, necessitating great effort to ensure proper protection and provide a power source.

In order to overcome these obstacles an "inverted" setup is used in which the magnitude of the electric field around the antenna is preserved while the antenna itself remains at a safe ground potential. This "inverted" setup is shown in Figure 46. In this measurement setup, a plane of conductive material is attached to the high-voltage generator. Provided that the plane width is sufficiently large with respect to the antenna-plane separation distance, strong electric fields will exist around the antenna, and corona formation will occur as in the non-inverted case. The primary difference between the two setups is a 180^o inversion of corona and voltage phase. For example, if the high-voltage conducting plane is at $100kV$ with respect to the earth grounded antenna, the problem can instead be interpreted as a conducting plane at $0V$ with the antenna at $-100kV$, since corona formation is only reliant upon the voltage gradients, and subtracting a constant from the voltages does not affect the fields. Variations in the field strength at the antenna between the two setups can be accounted for with electrostatic field simulations.

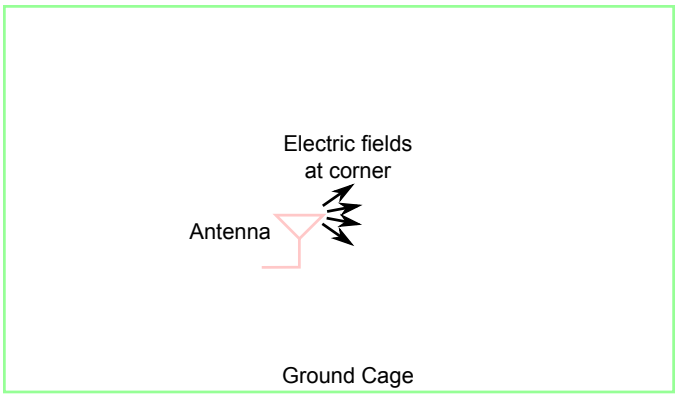

Figure 45: In this non-inverted setup, the antenna at high potential (red) surrounded by earth ground potential (green) at a distance. Strong electric fields form around sharp edges and corners of the antenna.

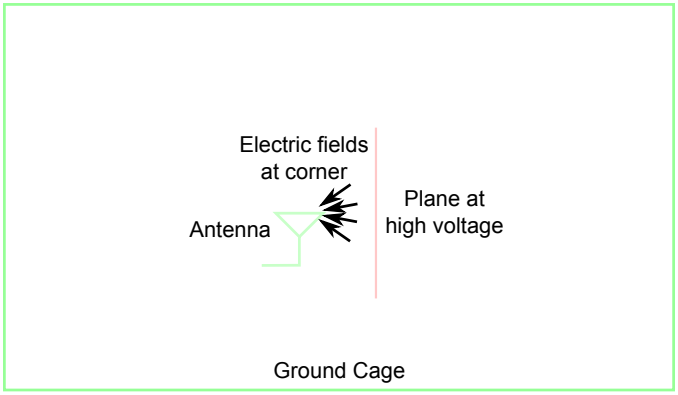

Figure 46: In this inverted setup, the antenna at earth ground potential (green) is surrounded by earth ground potential at a distance. A high potential plane (red) is placed near the antenna, relative to the ground potential surroundings. Strong electric fields form around sharp edges and corners of the antenna, with opposite direction to those in the non-inverted setup.

The equivalence between a power line sensor application and the measurement setup is illustrated in Figure 47.

5.1.2 Measurements and Instrumentation

With corona formation on the antenna in an inverted setup, as in Figure 46, measurements can be performed directly on the antenna more easily. In Figure 5, we define the different variables that could affect wireless communication performance. The purpose of the measurements is to determine to what extent each of these variables actually affects

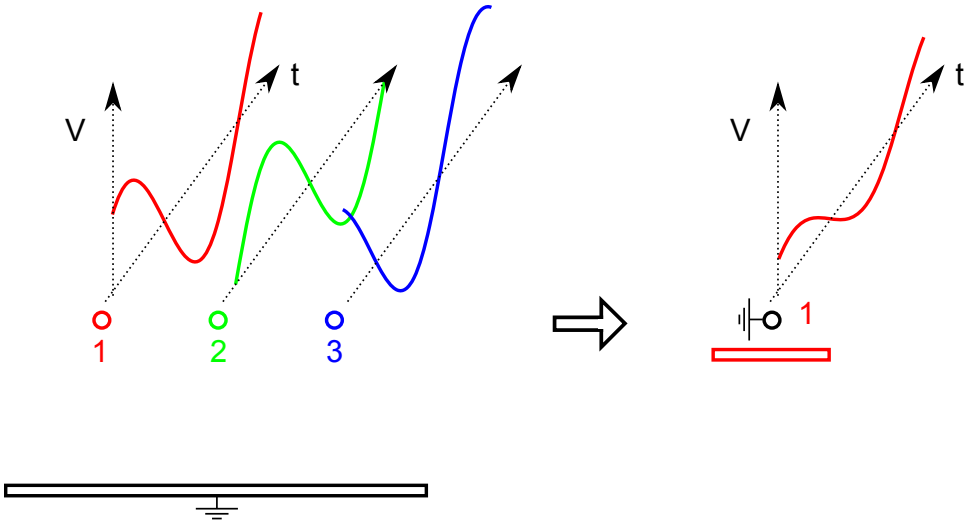

Figure 47: Equivalence between a three-phase high-voltage line topology and the topology utilized in measurements. An HV wireless sensor would be deployed on one of the three HV transmission line phases (left). In the measurement setup, the problem is condensed to a single HV phase (right). The voltage amplitude is smaller, but the distance to ground is decreased, and the potential of the antenna is maintained at earth ground while the single phase voltage is applied to the plane.

communication with corona formation on the antenna. Table 12 provides a listing of the different variables to be measured and the corresponding required instrumentation. Using a vector network analyzer (VNA), the complex antenna impedance and relative gain of the antenna can be computed from the *scattering parameters*. While the impedance of the antenna can be extracted computed exactly from the S_{11} parameter, the gain calculation from the S_{21} parameter (antenna with corona to second antenna) is subject to errors due to multipath scattering from the surroundings.

Table 12: Instrumentation required for assessing antenna under corona

Measured Variable	**Instrumentation**
Antenna Impedance (S_{11})	Vector Network Analyzer
Antenna Gain (S_{21})	Vector Network Analyzer
Radiated Corona Spectrum	Spectrum Analyzer
Directly Coupled Corona Spectrum	Spectrum Analyzer
Corona Current	Oscilloscope

In order to understand the interconnections of the instruments for the various measurement cases, simplified diagrams are presented in Figure 49. In Figure 49(a), the setup for

measuring antenna impedance (S_{11}) and gain (S_{21}) is illustrated. One port of the VNA must be directly connected to the coronating antenna, while a second antenna can be placed a safe distance away. The corona current can be measured by way of a series resistor, across which the voltage is measured using an oscilloscope, shown in Figure 49(b). An alternative method would be to use a current probe. A current probe offers the advantages of being physically decoupled from the antenna, but suffers from difficulties in measuring a large dynamic range of currents, and typically having a lower cutoff frequency in the kHz. For this work, it is important that we be able to capture currents in the $60Hz$ frequency range. The upper cutoff frequency for corona current measured across a resistor is dictated by the capacitance in the setup and the sampling rate of the oscilloscope. The RF power generated by the corona can be measured either as directly coupled power into the coronating antenna (Figure 49(c)) or radiation (Figure 49(d)). To measure the coupled power, a spectrum analyzer must be connected directly to the antenna with corona.

The specific instruments used for measurements are given in Table 13. A picture of the instruments in the high-voltage cage setup is shown in Figure 48.

Table 13: Instrument models used in antenna measurements

Instrument	**Model**	**Frequency Range**	**Input Limits**
VNA	Agilent E5071B	$300kHz - 8.5GHz$	$20dBm$, $10V$ DC
Oscilloscope	Agilent DSO6104A	$DC - 1GHz$	$300V$ RMS
Spectrum Analyzer	Agilent E4407B	$9kHz - 26.5GHz$	$30dBm$ cont ($50dBm$ pulse), $0V$ DC

In the measurement setups of Figure 49(a)(b)(c), the measurement instrumentation may be exposed to high current corona and arc discharges, and high voltage in the event of a short to the transformer output side. When designing the measurement setup in detail, various methods are employed to ensure users and sensitive instruments are protected from the worst case events.

5.1.3 High-Voltage Safety

Safety is *the* priority whenever performing experimental work, especially when it involves equipment capable of grave harm. Basic safety principles are followed to avoid accidents. Procedures are used for turning on and shutting off the high-voltage system. Physical

Figure 48: Instruments used in high-voltage antenna experiments. From top to bottom: Agilent Digital Oscilloscope, Agilent Spectrum Analyzer, Agilent Vector Network Analyzer.

isolation is maintained wherever possible to compartmentalize risk and minimize the number of potential accidents. Two people are present during the high-voltage measurements in case of an emergency.

The high-voltage transformer used in experimentation is located within a grounded cage. All individuals remain outside the cage during live experiments. No physical contact is made with test equipment involved in the experiment, and remote control is used for the instruments. Whenever an individual is working inside the cage, a grounding rod is attached to the transformer. The protection devices used to connect the antenna to the RF instruments are also securely grounded to avoid transient local fluctuations in local ground potential due to high inductance or resistance in the ground path.

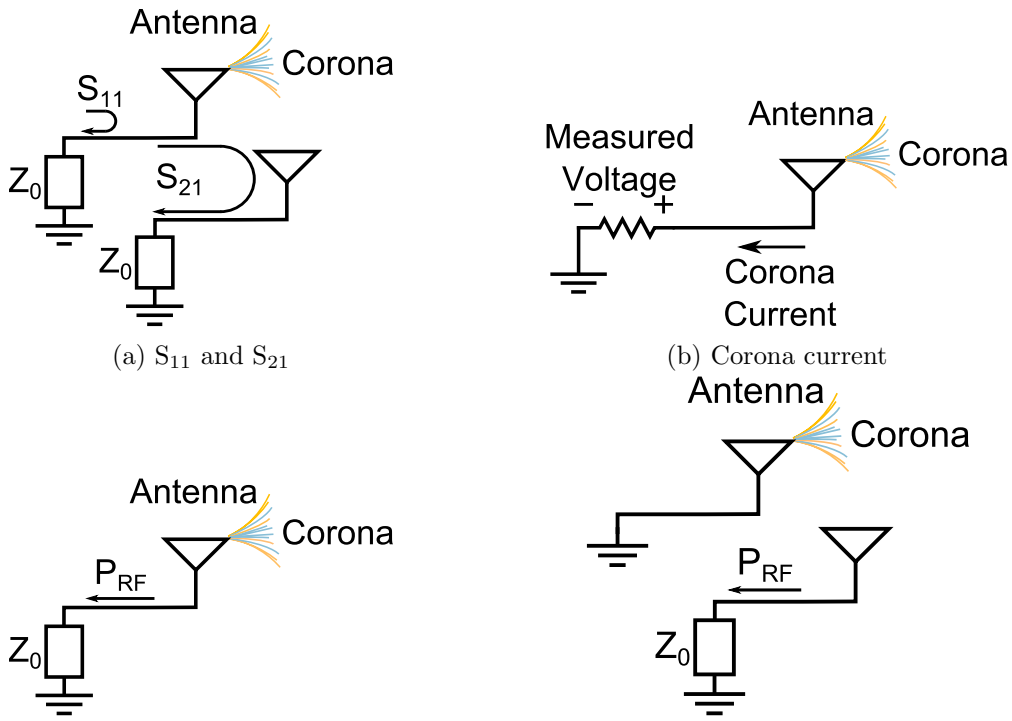

(a) S_{11} and S_{21}

(b) Corona current

(c) Direct spectrum

(d) Radiated spectrum

Figure 49: Simple diagrams of connections required for corona on antenna measurements. The antenna illustrated with corona is under test. All measurements other than radiated spectrum require a physical connection to the antenna under test.

5.2 Measurement Setup

As illustrated simply in Figure 49, four types of measurements are performed on the high-voltage setup. A fifth measurement variation had to be added due to a limitation of the measurement hardware. A variation of Figure 49(a) was made where S_{11} was measured alone, with a trigger correlator (see Section 5.2.5) connected to the second port. This addressed an issue with the VNA where there is a variable delay of up to 15 ms between receiving the trigger and beginning capture. The trigger correlator began modulating a load impedance with a timed code on the second port when the trigger was received. The delay of the capture could be recovered from measurement of the modulated impedance. The five measurements are listed here with their associated setup diagrams.

1. S_{11} and S_{21} - Figure 50

2. S_{11} and trigger correlator - Figure 51

3. Direct spectrum - Figure 52

4. Radiated spectrum - Figure 53

5. Corona current - Figure 54

5.2.1 High-Voltage Test Set

The high-voltage corona measurements are performed at Southern States LLC, located at 30 Georgia Ave, Hampton GA, 30228. The facility in use has an adjustable AC voltage transformer capable of generating up to $130kV$ (Figure 55). The transformer unit resides in a grounded cage for the safety of the user (Figure 56). The large gray box by the transformer is connected to the high-voltages side and insulated from the ground on ceramic stands. It can be used to house instruments and batteries when tests must be performed directly on the high-voltage side. It is not used in these experiments, but is a permanent fixture of the test set at Southern States and cannot be removed.

Figure 58 shows the control unit for the transformer. The "Voltage Control" knob values are in percentage of maximum output voltage and do not correspond to voltage values. As the output voltage is increased by the user, the voltage and current on the high side can be read off on the "Volt Meter (kV AC)" and "Current Meter (AC)" digital displays. The accuracy of the measured voltage is $\pm 1\%$ of the reading, and of the measured current is $\pm 1\%$ of the full scale. The test set runs off a standard US $120V$, $15A$ wall supply. The transformer output current must be kept below $5.6mA$ at $130kV$ to avoid overheating with continuous operation. The maximum permissible current draw is $11.7mA$, but during all testing the current is maintained below the continuous operating limit.

The high-voltage test set has multiple levels of safety mechanisms. Firstly, the transformer is located inside a grounded cage to prevent a low-impedance conducting path to form between the transformer on the inside and an individual on the outside. The cage can be seen in Figure 56. The entrance to the cage is a chain-link metal curtain. To close the curtain there are two latches, shown in Figure 57. The two latches are wired to the control unit, and if either one is open the operator will be unable to engage the high-voltage

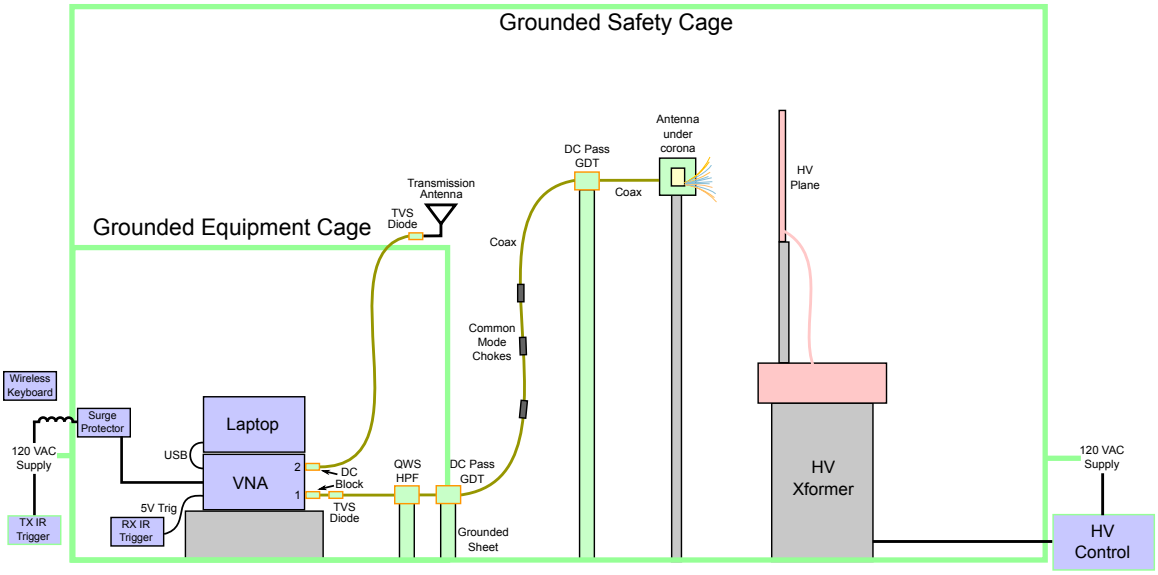

Figure 50: Measurement setup for capturing reflection S_{11} and transmission S_{21} of antenna under corona.

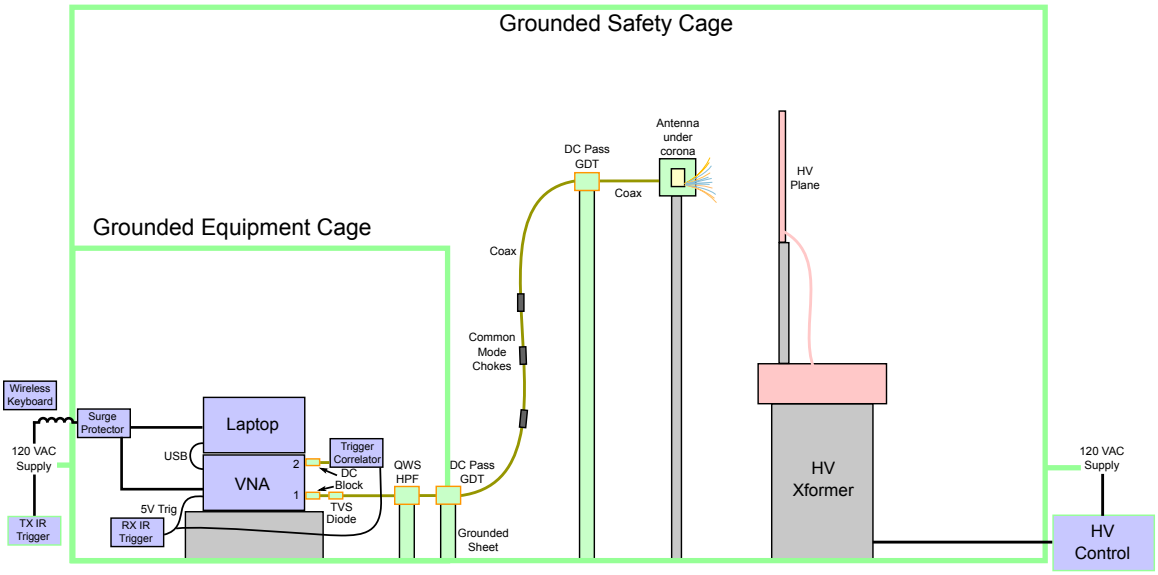

Figure 51: Measurement setup for capturing reflection S_{11} in zero-span mode with a trigger signal correlator on Port 2 of the VNA.

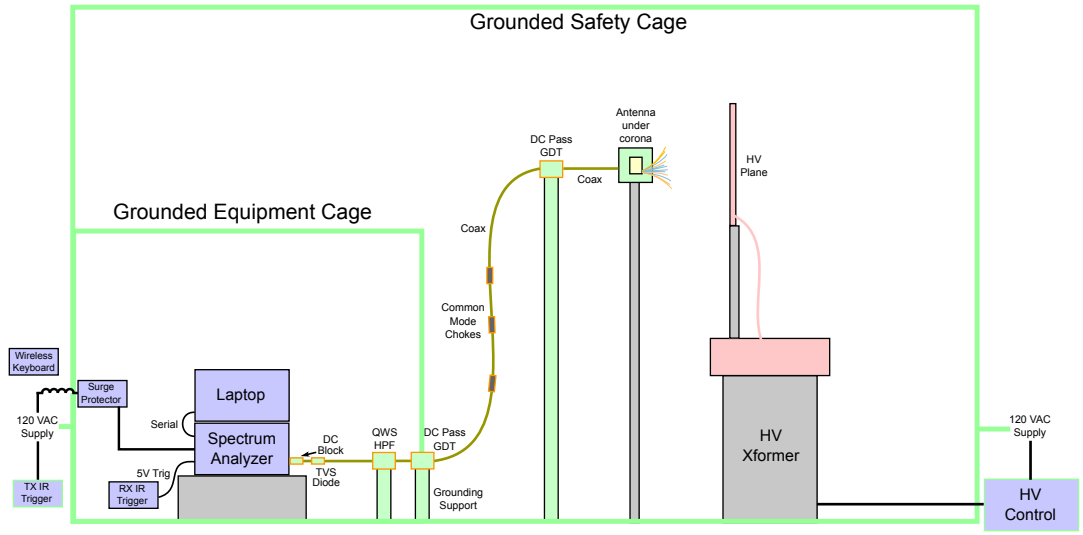

Figure 52: Measurement setup for capturing the corona RF spectrum coupled into the antenna.

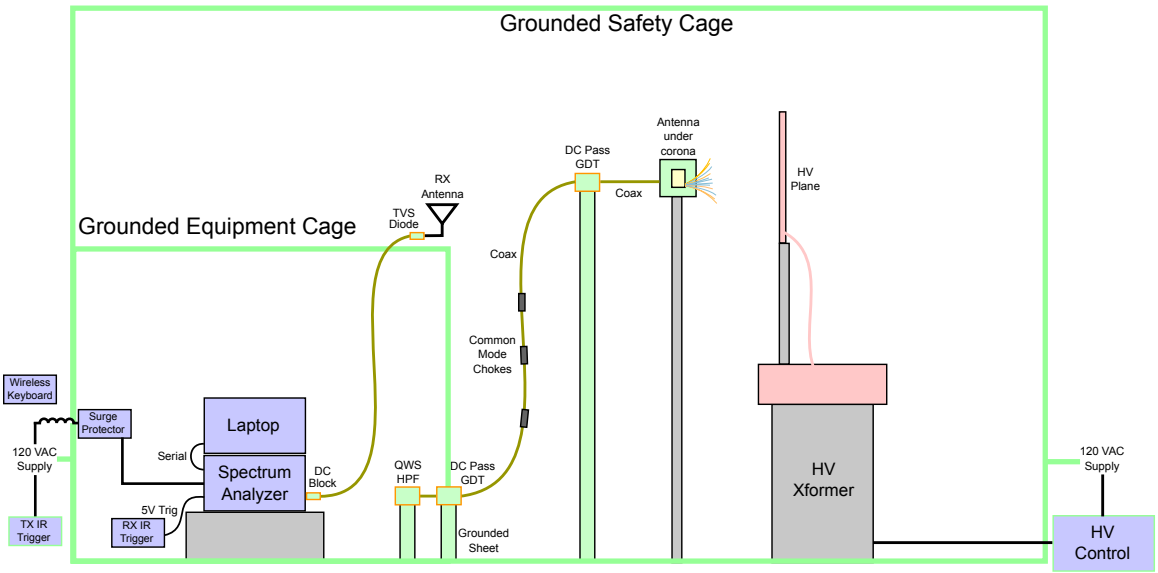

Figure 53: Measurement setup for capturing the radiated spectrum of the corona.

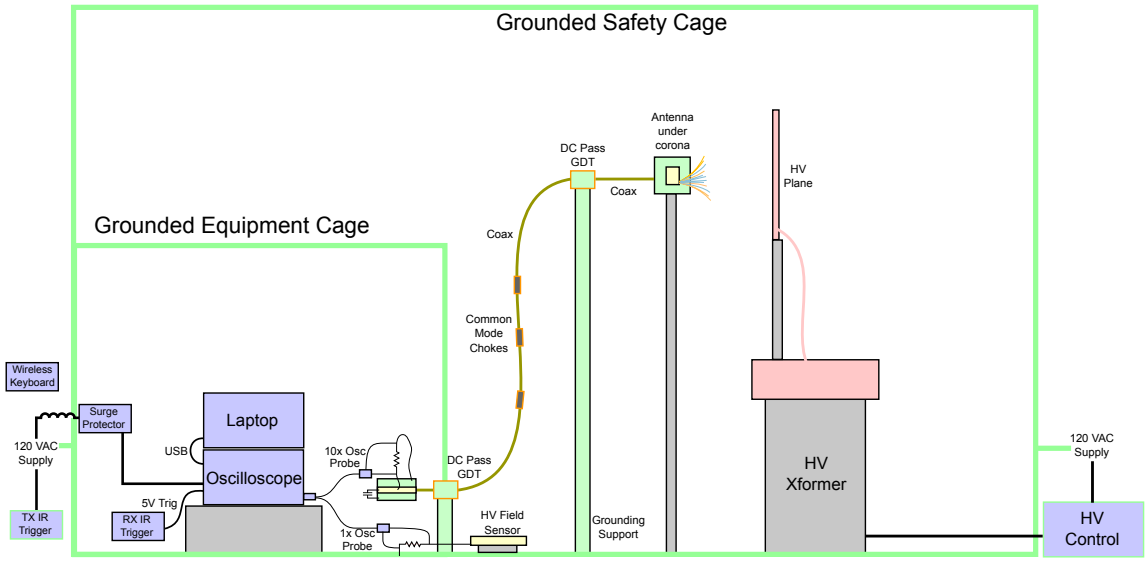

Figure 54: Measurement setup for capturing corona current as a voltage across a resistor using an oscilloscope.

output. A grounding rod is attached to the high-voltage output whenever an individual is working inside the cage. The rod consists of a copper hook at the end of a PVC pole, and connected by wire to the ground, seen in Figure 55. The pole is long enough to allow the user to disconnect from the transformer from outside the cage entrance.

A methodical procedure is followed when turning to test set on and off to maintain safety. The procedures are listed here.

5.2.1.1 High-Voltage Turn On Procedure

1. Visually inspect the high-voltage cage to ensure all parts connected to the high-voltage side of the transformer are clear of ground.

2. Exit the high-voltage cage and make sure no individuals remain inside.

3. Disconnect the grounding rod from the transformer toroid and place on the ground to the side where it will not accidentally short to the high-voltage side.

4. Close the grounding cage, locking the two fail-safe latches (Figure 57).

5. Visually inspect interior of the cage to confirm all previous steps were completed

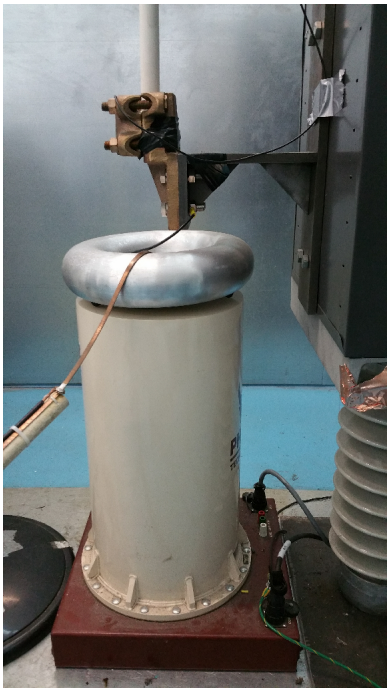

Figure 55: Phenix BK130 high-voltage test set transformer. A grounding rod is connected to the toroidal output whenever someone is working inside the cage.

correctly (Figure 58).

6. Ensure the "Voltage Control" knob on the BK130 control unit is set to 0.

7. Turn on the "Main Power" on the BK 130 control unit by flipping the black switch up (Figure 58).

8. Turn on the "High Voltage" by pressing the red "ON" button on the BK130 control unit (Figure 58).

9. Increase the output voltage using the "Voltage Control" knob, monitoring the "Volt Meter" and "Current Meter" displays to remain within the operating limits (Figure 58).

5.2.1.2 High-Voltage Turn Off Procedure

1. Decrease the output voltage to 0 using the "Voltage Control" knob, monitoring the "Volt Meter" and "Current Meter" displays to remain within the operating limits (Figure 58).

Figure 56: Phenix BK130 high-voltage test set transformer inside the grounding cage.

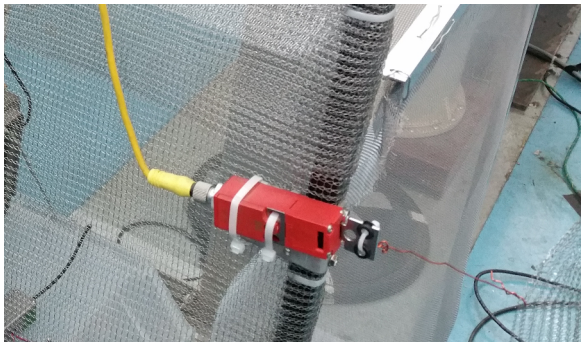

Figure 57: Latches used for securing grounded cage. If either of two latches is diconnected, the supply to the high-voltage transformer is automatically disconnected.

2. Turn off the "High Voltage" by pressing the green "READY" button on the BK130 control unit (Figure 58).

3. Turn off the "Main Power" on the BK 130 control unit by flipping the black switch down (Figure 58).

4. Open the grounding cage, unlocking the two fail-safe latches (Figure 57).

5. Touch the grounding rod to the high-voltage toroid on the transformer, and any other high-voltage connected objects which have the potential to have disconnected from the transformer during experiments and maintain charge.

Figure 58: Phenix BK130 high-voltage test set transformer control box.

6. Connect the grounding rod to the transformer toroid.

5.2.2 High-Voltage Plane

The inverted high-voltage measurements setup relies on a relatively large conducting plane to be placed on the high-voltage side of the test set. The plane is constructed from PVC tubing and wire. A square of $1in$ pvc tubing, $66cm$ on a side, is constructed. The tubing is covered completely with copper tape. Alternatively a metal frame could have been constructed but it was decided that this would be unnecessarily heavy and unwieldy for mounting on the transformer. The copper tape coating on the PVC ensures there are no electric fields inside the PVC tubing when high-voltage is applied. The high-voltage plane is pictured in Figure 59. It is oriented with the plane perpendicular to the ground with the base of the plane $144cm$ above the ground. For the inverted setup to best mimic the fields in a traditional high-voltage antenna arrangement, the plane must be positioned as far from ground as possible.

With the frame constructed, the area of the plane is filled with a conductive material. The most simple solution would be to cover the entire frame with a conducting sheet such as aluminum foil. However, this solution would create issues with the measurement of antenna properties. Recall from Figure 46 that the antenna is to be placed near the plane to induce corona formation. Placing an antenna near a conducting plane can impact the measurement of antenna impedance by coupling with the near field if close enough, or reflecting radiated

Figure 59: High-voltage plane used to induce corona on the proximate antenna in an inverted voltage setup.

power back into the antenna if the antenna, increasing the measured return loss.

In order to mitigate these issues, the surface of the plane is instead filled with parallel wires. Holes are drilled through the top and bottom tubes of the frame at $1.25cm$ intervals and copper wire is spanned between the two. For this purpose, 18 AWG wire with a PVC coating is used (Coleman Cable 18-100-11 Primary Wire). Each strand of wire is soldered to the copper tape of the PVC frame. When an antenna is placed near to the plane such that it is cross-polarized with the direction of the wires (i.e. the radiated electric field is parallel to the wires), the plane has little effect electromagnetically on the antenna as long as the wire diameter is much smaller than a wavelength, which is the case for 18 AWG wire and frequencies less than $6GHz$.

In order to verify the predicted interaction of the wire grid with a nearby antenna, a test is performed where the return loss of a directive horn antenna is measured with different conducting planes 25 cm from the horn aperture. The four tested scenarios are shown in

Table 14: Nominal dielectric strengths of materials used in measurement setup

Material	**Dielectric Strength (kV/cm)**
Air @ STP	30
Acrylic	200 [2]
PVC	215 [3]

Figure 60. Figure 61 shows the measurement results. As predicted, placing a cross polarized wire array in front of the antenna does not affect the return loss, while the co polarized wire array affects the antenna measurement similarly to a metal plate.

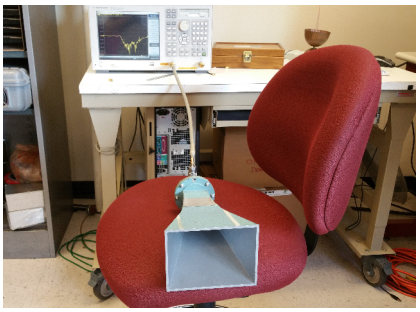

(a) Baseline horn RL measurement

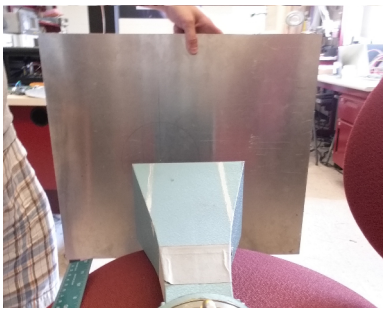

(b) Aluminum plate

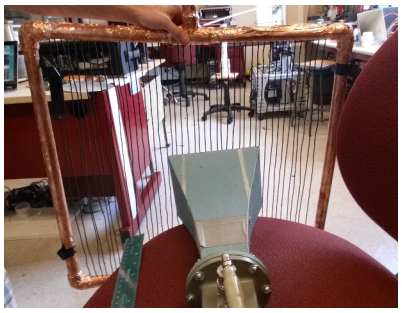

(c) Co polarized wire grid

(d) Cross polarized wire grid

Figure 60: Four test scenarios with various conducting planes 25 cm from the aperture of a horn antenna operating from 3.5 to 7 GHz.

In front of the plane, as seen in Figure 59, is an acrylic sheet. The purpose of the sheet is to prevent direct arcing from the antenna to conductor of the high-voltage plane. The acrylic material has a dielectric strength about 7× larger than that of air. The acrylic sheet between the antenna and the high-voltage plane will halt the advancement of a propagating streamer from the antenna, reducing the current to which the antenna conductor is exposed during experimentation.

During initial testing, it was discovered that the protruding support bars above the

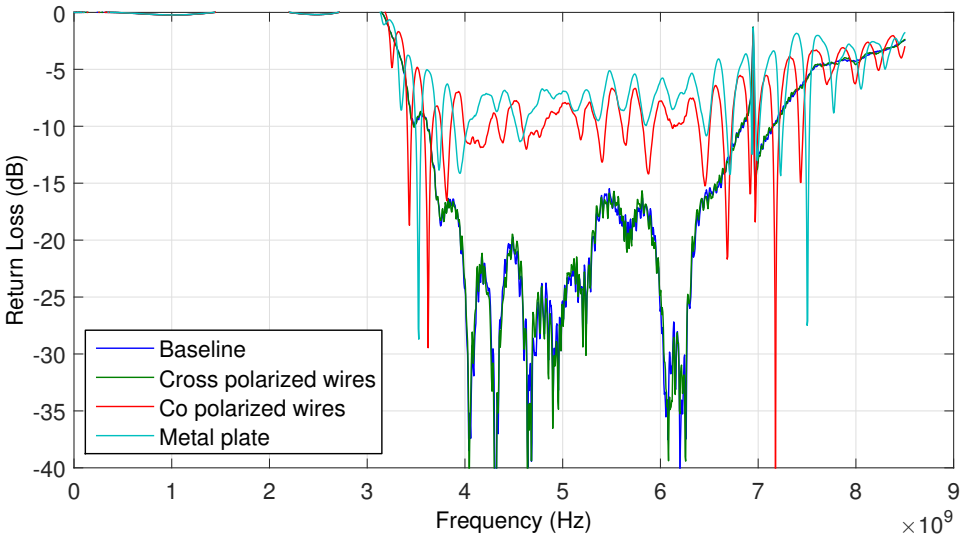

Figure 61: Measured horn return loss with various conducting planes 25 cm from the aperture. The cross polarized wire array does not affect the RL measurements.

transformer (attached to the high-voltage side) induce corona due to their sharp features. A simple aluminum foil shield is constructed underneath the plane, above the transformer, as seen in Figure 59, to minimize corona formation on the HV transformer assembly. In Figure 55 one can see there is a metal bracket protruding above the transformer, used for mounting objects. There is another bar that protrudes at the top of the box as well, just below the base of the square plane. Aluminum foil is wrapped around both these assemblies in a cylindrical fashion to minimize the sharp metal protrusions. This lessened the corona formations at these point when at high-voltage.

5.2.3 Antenna Stand

A PVC stand is assembled to support the antenna and cable assembly, pictured in Figure 62(a). The antenna is supported 177cm above the ground using 3in diameter PVC tubing. PVC is chose for this application because of its insulating properties, and because it is easy to work with; it is easy to cut and drill using hand tools and there is a variety of joints available for joining tubing at different angles. The entire stand can be shifted on the floor to position the antenna closer or farther from the high-voltage plane.

To maintain a modular system capable of accepting a variety of antennas, a standard

(a) Stand in lab

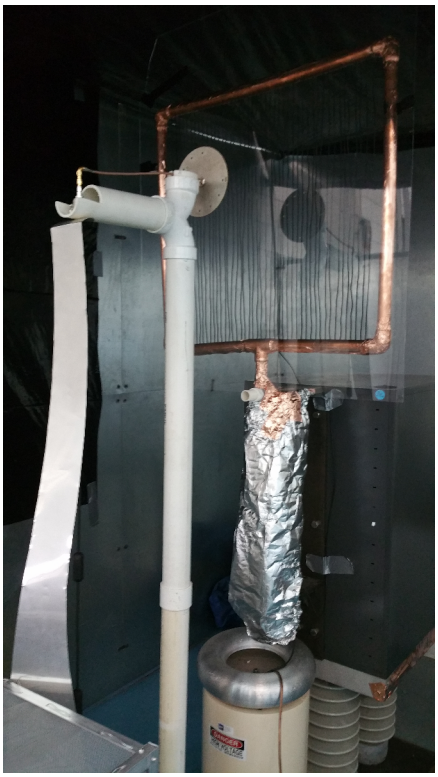

(b) Stand with antenna at HV test set

Figure 62: PVC stand used to support the antenna next to the high-voltage plane

SMA male interconnect is used to connect antennas. At the top of the stand, a $30cm$ coaxial cable distances the vertical hanging coaxial cable from the high voltage transformer (Figure 63). If the coaxial line were run down the length of the PVC stand, the danger of an arc between the cable and the transformer would be greatly increased. The positioning of the stand with reference to the plane is shown in Figure 62(b).

5.2.4 Antenna Connection Cable Assembly

Corona is induced on the grounded antenna near the high-voltage plane, and the effects are measured using a variety of instruments (see Table 12). Since the ultimate goal of this work is to determine how a wireless sensor on a high-voltage power line would work with corona on the antenna, it is important that the interconnection between the antenna and the instruments be representative of the type of connection that would otherwise be present on the sensor. To this end, a standard 50Ω transmission line is used to connect the instruments to the antenna. Instead of a short millimeter-long transmission line between

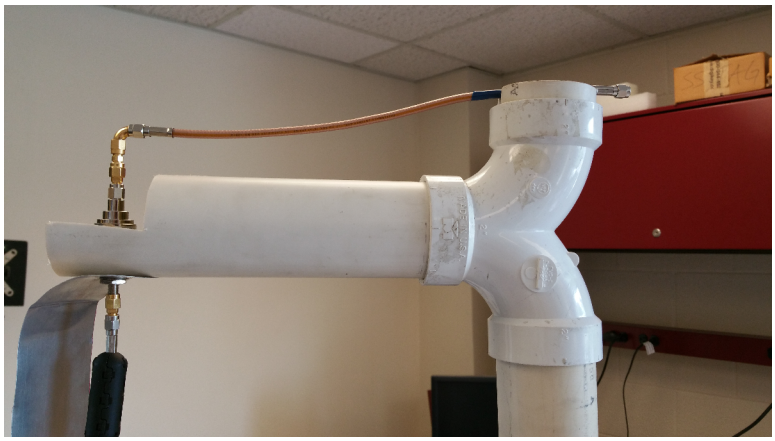

Figure 63: Top of PVC stand used to support the antenna next to the high-voltage plane

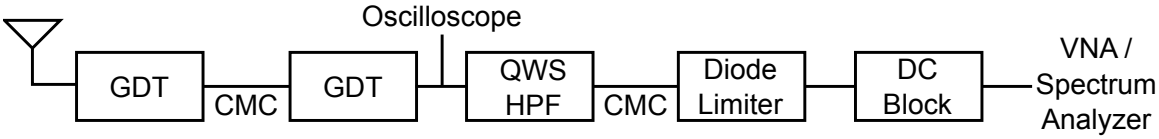

Figure 64: Cascade of protection devices used in high-voltage measurements

the RF hardware and the antenna as would be used on a wireless sensor, here we utilize a longer meter-long transmission line in order to distance the instruments from the high voltage. In performing measurements of antenna impedance, the transmission line effects can be calibrated out with the VNA. When measuring the spectrum, the attenuation of the cable can also be subtracted out from the measurements.

5.2.4.1 Protection Devices

Since the antenna may be exposed to large voltages and currents during measurement using sensitive instruments, a direct connection with a coaxial cable is insufficient. A cascade of protection devices is created to minimize the risks involved in performing these measurements. The cascade is depicted schematically in Figure 64. Details about these various components are given in Table 15. Figure 65 shows the devices used in the experimentation.

The first barrier of protection is two Gas Discharge Tubes (GDT). These coaxial tubes are constructed with a cavity section where the typical PTFE insulation is replaced with a gas (unspecified) that is designed to break down at $90V$. The benefits of GDTs are their

Table 15: Protection devices used in high-voltage antenna measurements

Device	Manufacturer	Model	Comments
GDT	Terrawave Solutions	TW-LP-RPSMA-P-BHJ	50Ω, DC $- 6GHz$, $90V$
CMC	Laird Technologies	28A0593-0A2	407Ω @ $100MHz$, snap-on
QWS	NexTek	QWSNFN0600	50Ω, $2.2 - 7.6GHz$
Diode Limiter	Mini-Circuits	VLM-63-2W+	50Ω, $0.03 - 6GHz$, $11.5dBm$ let-through
DC Block	Mini-Circuits	BLK-89-S+	50Ω, $0.0001 - 8GHz$

(a) GDT Lightning Arrestor

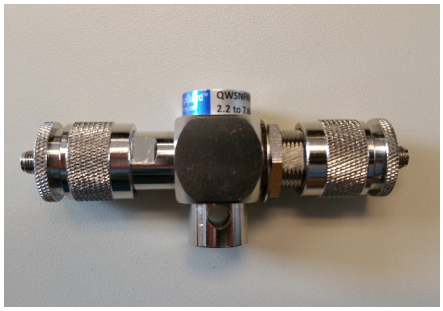

(b) QWS Lightning Arrestor

(c) Diode Power Limiter

(d) DC Block

Figure 65: RF Protection devices used in the course of high-voltage measurements.

ability to pass DC up to very high frequencies while maintaining linearity for voltages below the breakdown. This corresponds with a power of $81W$, or $49dBm$, for the 50Ω device. The tube can also handle large currents, up to $20kA$ for a $20\mu s$ pulse. Despite the excellent pass-through linearity and operational bandwidth, the GDT suffers from two limitations for this application. First, the breakdown power of $81W$ is much higher than the input power limitations of the instruments around $1W$ (see Table 13). Second, the response time of the gas discharge is limited, and may permit very fast transient voltages through. The GDTs being used are specified to break down at $450V$ for a voltage impulse with a rising slope of $1kV/\mu s$. These limitations necessitate further protection.

After the two GDTs, the second barrier of protection is the Quarter Wave Stub (QWS) arresor. The QWS is essentially a high pass filter (HPF) in a coaxial package with a shorting

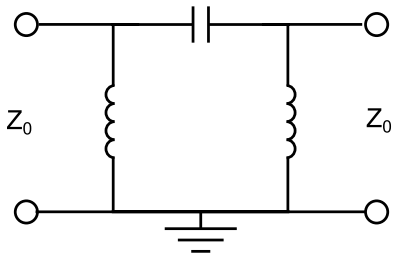

Figure 66: Functional schematic diagram of the Quarter Wave Stub arrestor. The inner coax conductor is DC shorter to ground capable of sinking 60 kA surges.

element from the inner conductor to ground. The shorting element is designed to handle large currents up to $60kA$. The QWS functions by shorting low frequency signals to ground and passing higher RF frequencies. This works as a lightning arrestor on the principle that the frequency content of an electrical arc is much lower than the operating RF frequency (See Section 4.3). A schematic diagram of the QWS is drawn in Figure 66. The advantage of the QWS is the fast response time, but the disadvantage is that it is band-limited. The measured $|S_{21}|$, or insertion loss, of the QWSNFN0600 is plotted in Figure 67. At the lowest frequency of interest for these measurements (915 MHz) the insertion loss is -4.4 dB. This loss value can be handled with post-processing.

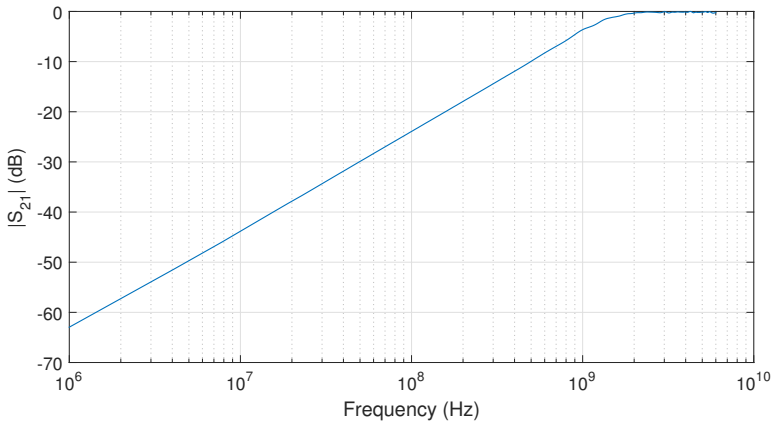

Figure 67: Insertion loss for the quarter wave stub lightning arrestor. The 3 dB cutoff is at 1.1 GHz.

The third level of protection is a diode-based power limiter. The diode limiter is a low-capacitance power limiter (a coaxially packaged transient voltage suppression (TVS) diode). The advantages of the diode limiter are its low clamping power of $11.5dBm$ and

fast response time. The low clamping power, which is below the maximum input values of the VNA and spectrum analyzer (Table 13), makes the diode limiter a suitable candidate for protecting the sensitive instruments. The trade-offs that must be taken in using the diode limiter are a decreased transmission power. While the clamping power of the diode limiter is around $11.5dBm$, the linear region of the diode rests well below this level. According to the specification sheet, the limiter's linear range falls below $4dBm$. In order to ensure linearity in the measurements, the VNA transmit power is limited to $0dBm$ with the power limiter connected at the VNA port.

The fourth level of protection, necessary for the spectrum analyzer, is a DC block. The DC block acts as an open circuit at DC, and a 50Ω transmission line above $100kHz$. By AC coupling the instrument port to the antenna cable assembly, the DC voltage on the port can be maintained at $0V$, within the specifications. While the QWS acts as a DC short, the DC block is added to the cable assembly as an extra measure of protection since it does not otherwise limit the system.

Snap-on Common Mode Chokes (CMC) are fitted around the coaxial cable. They can be seen in Figure 62 as black cylindrical attachments on the hanging coaxial cable. The purpose of the common mode chokes is to attenuate common mode transient currents on the ground shielding of the coaxial cable. In the event of an arc, or a discharging of the GDT, it is undesirable for the pulse to propagate on the ground conductor of the coaxial cable. Common mode currents could lead to local voltage variations in the ground and reduce the effectiveness of the protection devices. The operations of the GDT and diode limiter rely upon a voltage difference between the inner conductor and ground of the device. Once a traveling wave on the coaxial cable shielding reaches the GDT or limiter, it could momentarily raise the local ground potential, further increasing the inner conductor potential necessary to clamp the voltage. CMCs are constructed of a hollowed-out cylindrical ferrite core that is split into two halves so that it can be snapped on around the cable. The ferrite impedance increases with frequency, and is specified up to $500MHz$ on the product sheet. The magnetic field of a high frequency common-mode signal circulating around the ground shield is attenuated reflected and attenuated by the CMC.

The measured insertion loss of the entire cable assembly (without the QWS arrestor attached) is provided in Figure 68. The assembly is as pictured and Figure 62(a) and described in Figure 64. At the highest frequency of 5.8 GHz, 11 dB of loss is incurred for a signal propagating from antenna to the instrument, or the other way around. The attenuation of the signal through the cable assembly impacts the resolution of measurements, especially impedance measurements. It is possible to calibrate out the S-parameters of the cable assembly to measure the complex impedance at the antenna port. However, small perturbations in the cable assembly between calibration and measurement can significantly impact the accuracy of measurements.

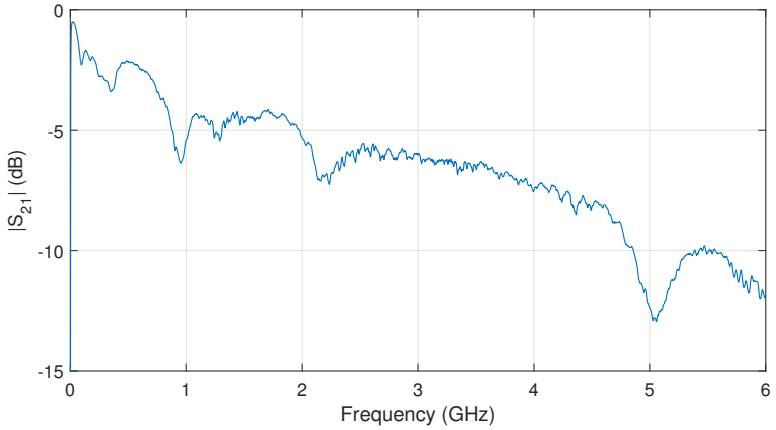

Figure 68: Insertion loss of the entire cable assembly (without the QWS arrestor).

The calibration of the measurement port using an open/short/matched technique is sensitive to resonances in the cable assembly. Because the cable assembly is 2.3 m (many wavelengths) long, small variations in the cable can cause large shifts in a resonance. The cables are secured to minimize movement and not touched after calibration has started. With these limitations, the measurement floor of S_{11} measurements is observed to be -40 dB measured with broadband matched load. This accuracy is sufficient for practical antenna impedance measurements, where matched antennas fall around -10 dB.

Another limitation is the precision of the measurements. Even in still measurements, the measurements will fluctuate within a certain range of values. This is more pronounced at lower return losses near the sensitivity floor. Taking many captures of return loss for a

single still antenna, the precision is observed to be between 0.1 and 0.5 dB. If fluctuations in the S-parameters are measured within half a dB of the control measurement, they cannot be definitively attributed to an external process.

5.2.5 Triggering System

As illustrated in Figure 22, corona formation under an AC voltage is a time dependent process. By extension, the wireless system characteristics are also time dependent. The frequency of the variation is the line frequency of 60 Hz. In order to resolve the time dependence of effects on the wireless system, time domain (zero-span) measurements are taken with the VNA and spectrum analyzer. In order to obtain meaningful results, the capture of the instruments must be correlated with the voltage amplitude.

The high-voltage transformer steps up 115 VAC from a standard 15 A fused outlet up to a maximum of 130 kV at a low current. The phase of the output voltage is therefore locked with the 115 V outlet. The simplest means of triggering the instruments is to monitor the 115 V phase and send a trigger pulse at a specific point, such as the zero crossing ($t = 0$ for a sin wave).

In order to be able to control when and how many times the instruments are triggered, the voltage monitor/trigger transmitter are designed to be outside the high-voltage grounding cage. A separate received is designed to be inside the grounding cage. An infrared (IR) LED/phototransistor link is used to communicate the trigger pulse from outside to inside the cage with minimal latency and complexity.

A picture of the IR TX/RX setup used in measurements is shown in Figure 69.

5.2.5.1 IR Transmitter

The IR transmitter schematic is shown in Figure 70. The circuit in the schematic runs in conjunction with a Texas Instruments MSP430 Launchpad development board. Figure 71 shows pictures of the transmitter housing and internals. Since the device connected to 115 V, a fused (250 mA) power plug and switch are used to connect to the box. The box is completely aluminum, which is securely grounded to the earth ground input. A simple push button is mounted through to the outside of the box. This is used by the user to

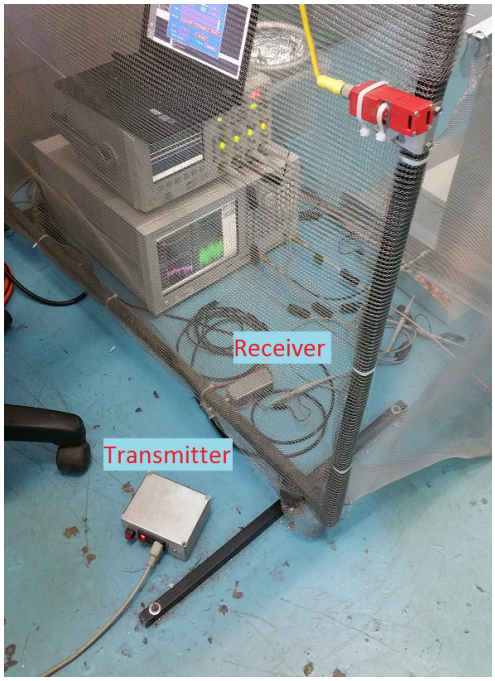

Figure 69: IR trigger system setup. The transmitter is placed just a short distance from the receiver on the other side of the ground cage.

command a trigger on the next zero-phase point of the voltage signal. The electronic in the transmitter are powered directly from the input line power by means of a bridge rectifier and voltage regulator.

5.2.5.2 IR Receiver

The IR receiver schematic is shown in Figure 72. The receiver is a simple NPN phototransistor connected in an emitter follower configuration. The voltage output of the emitter follower is fed into a comparator to generate a pulse with a sharp rising and falling edge. The resistors R4 and R5 are actually a single potentiometer that can be adjusted to raise/lower the comparator threshold voltage. This is used to tune the transition circuit for the output voltage at the phototransistor collector. This circuit runs on 5V taken from a USB port of the laptop in the cage. The output is connected to a BNC splitter (the external trigger connector type used in the VNA and spectrum analyzer) and wires for probing. Figure 73 shows the receiver and internals.

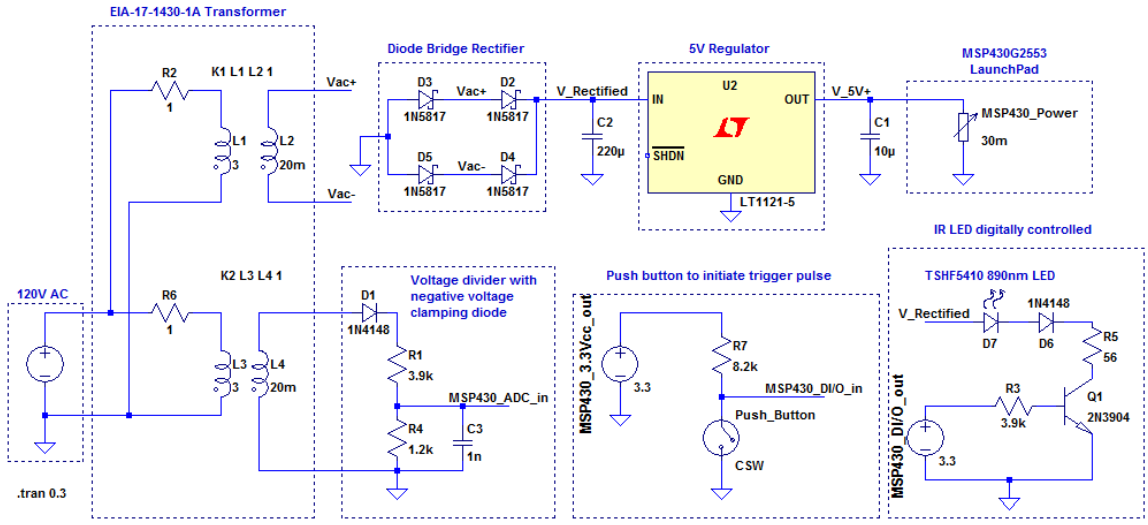

Figure 70: Schematic of the custom IR transmitter used to generate a trigger pulse on a specific phase of 115 VAC. A TI MSP430 LaunchPad dev board runs in conjunction with the circuit, where the interconnect pins are prefixed with MSP430.

(a) Fused power plug and button

(b) IR LED

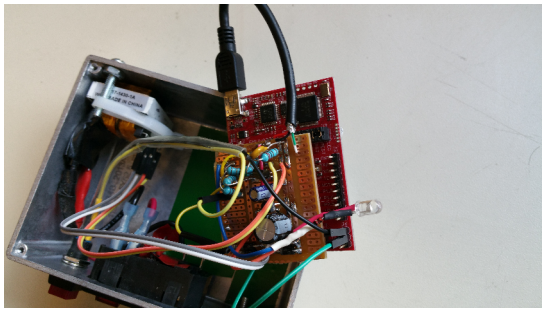

(c) IR transmitter internals

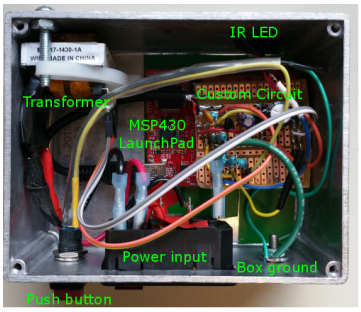

(d) IR transmitter internals

Figure 71: IR trigger pulse transmitter designed for remote triggering of instruments based on power line phase.

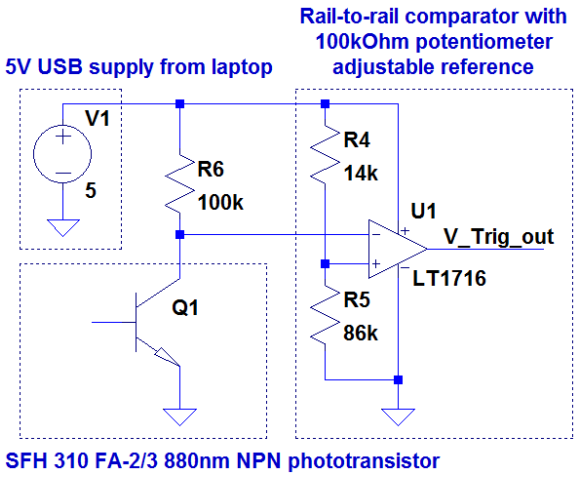

Figure 72: Schematic of the custom IR receiver.

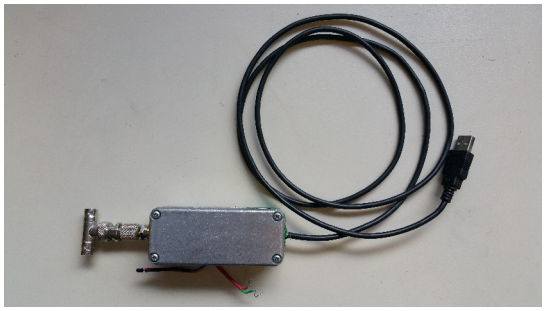

(a) IR receiver with BNC output

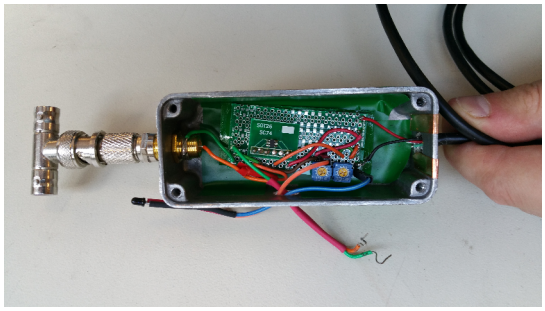

(b) IR receiver internals

Figure 73: IR trigger pulse receiver designed for remote triggering of instruments based on power line phase.

5.2.6 Trigger Correlator

The triggering system described above is capable of generating a 5 V trigger pulse within microseconds of being initiated at the transmitter. It is desired that the latency is no more than 1 ms to distinguish the positive from the negative half of the corona. However, an issue is discovered when the external trigger is used with the Agilent E5071B network analyzer. The VNA architecture is such that upon receiving an external trigger, the VNA requires as much as 20 ms to initiate the hardware before the capture is started. Upon beginning the capture, there is no latency between consecutive frequency (or time in zero-span) measurements. When performing 2 port measurement, the VNA first captures the data on Port 1 immediately followed by Port 2.

To circumvent this issue, a simple load impedance modulation circuit is devised to act as an absolute time reference. Pictured attached to Port 2, the top port, in Figure 74, the trigger correlator circuit is a simple switch used to modulate between two load impedances. An MSP430 microcontroller on the battery-powered board detects detects the trigger signal from the IR receiver via a digital I/O pin. The MSP 430 then utilizes digital I/O outputs to control a Hittite HMC345 RF switch, which switches the SMA connector termination between two different impedances. This results in a change in the measured impedance (return loss and phase) on VNA Port 2.

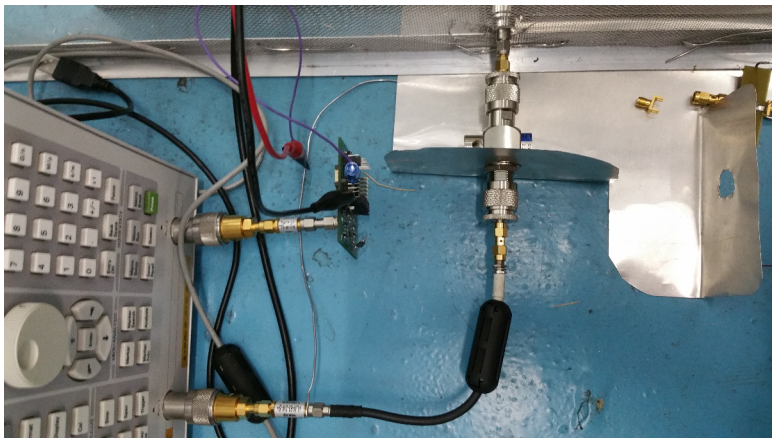

Figure 74: VNA connections for zero-span measurements. Port 1 is connected to the antenna cable assembly, and the trigger correlator is connected to Port 2.

Upon receiving the trigger, the microcontroller initiates the switching, encoding the time elapsed since the trigger in a simple code, illustrated in Figure 75. A 10-bit scheme is used, transmitting a header of "10" followed by the elapsed time since the trigger was received from the IR receiver in an 8-bit word with units of milliseconds. Since the total capture time for Port 1 is known, and it occurs directly before the Port 2 capture, the start time of the Port 1 capture can be recovered. This delay is then used to correlate the measured antenna return loss or phase with an absolute voltage phase. Unfortunately, this method cannot be used for S21 measurements since a third port would be required.

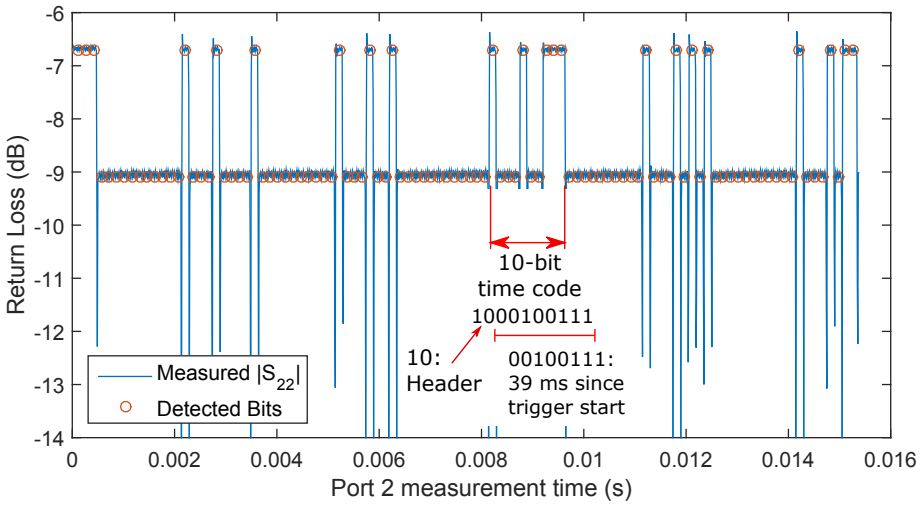

Figure 75: Example of code received by impedance modulation on Port 2 of the VNA. The 10 bit encoding scheme indicates the elapsed time since the external trigger, transmitted in 3 ms increments.

5.2.7 Instrument Control

Instrument control during measurements is accomplished with a laptop running MATLAB. The laptop (powered with its own internal battery) is located inside the instrument cage, shown in Figure 76. The instruments (oscilloscope and VNA) connect to the laptop via USB, and the spectrum analyzer connects via RS-232. MATLAB Instrument Control toolbox is used to program commands for the instruments. Data captured by the instruments is automatically transferred to MATLAB and stored to the laptop. A GUI is developed to make data capture easy for the user during measurements. A Logitech wireless keyboard/mouse is controls the laptop from outside the cage, communicating with a 2.4 GHz USB dongle seen at the top of the figure. This setup allows easy control and capture of data while completely physically isolating the user from the instruments.

The instruments were originally planned to be powered via a deep cycle car battery and power inverter to completely isolate the instruments from the outside of the cage. This was tried but issues quickly arose due to the high power requirements of the instruments. The VNA and spectrum analyzer could only be run for 30 minutes at a time before requiring a change of battery. Restarting the instruments requires recalibration, a time consuming

Figure 76: Instrument control setup during measurements. A laptop running MATLAB communicates with the instruments via USB. The laptop is controlled with a wireless keyboard.

procedure. It was determined that the instruments require power from the 120 V wall outlet. The instruments themselves are at ground potential in the inverted antenna measurement setup (see Section 5.1.1). In the event of a short between the high-voltage and the antenna, there are multiple levels of protection offering direct shorts to ground, minimizing the risk of current flow to the instruments. To further reduce the potential for current flow through the instruments, a 50 ft extension cable is used to connect the instruments to the wall outlet located directly next to the cage. The extension cable is wound in a coil, creating an inductance of approximately 200 μH. The additional inductance of the extension cable creates a high impedance path to ground for the current impulse formed at the antenna in the event of an arc or short. A surge protector is used to split the extension cable power out to the different instruments. The laptop is run off its own internal battery without issue.

5.3 Test Antennas

The focus of this work is on wireless RF communication. The three frequency bands investigated specifically are 915 MHz, 2.45 GHz, and 5.8 GHz due to their ubiquity in wireless sensor networks. As depicted in Figure 34, a variety of antennas could be considered for a wireless sensor design. There are wire antennas such as monopoles and dipoles, monopoles radiating in a half space above a ground plane. Monopoles with a dielectric shielding

(whip antenna) are commonly used in wireless networking hardware such as Wi-Fi routers. Printed antennas such as a meandered dipole and complementary antennas such as a slot offer another option. Patch antennas are commonly used in compact wireless devices. With the addition of loading slots, cutouts, and shorting posts, a wide variety of shapes and characteristics can be obtained from a patch antenna.

In this study, we want to investigate whether certain categories of antenna perform differently under high-voltage. To this end, the antennas that were tested are listed in table 16.

Table 16: Antennas used in high-voltage experiments, categorized by frequency of operation.

915 MHz	**2.45 GHz**	**5.8 GHz**	**Other**
Wire monopole	Wire monopole	Wire monopole	2.6 cm metal sphere monopole
Printed meandered dipole	Slot dipole	Slot dipole	2 mm short monopole
	Broadband E-shaped patch	Rectangular patch	
	Dual-band whip	Whip	
		Dual-band whip	

The metal sphere and short wire are not specially designed to be resonant antennas like the rest. They are tested to observe other special cases of corona formation. The sphere however does behave like a broadband monopole, but its return loss does not offer good performance. With the sphere, the radius of curvature, being larger than a point of a wire monopole and smaller than a flat plane, created a condition where longer streamers were able to develop than seen on other antennas, approximately 1 inch long. The impedance of the sphere was tested to see if large streamers have an effect of radiation the impedance. The short wire was used to measure a change in impedance of an electrically small structure with corona presence. During experiments, it was observed that corona formation occurring at the end of a wire is typically confined to a thin layer near the surface, on the order of the the wire radius. The experiment was to see whether the small corona formation has a bigger impact on electrically small structures.

The antennas are pictured in Figures 77-81.

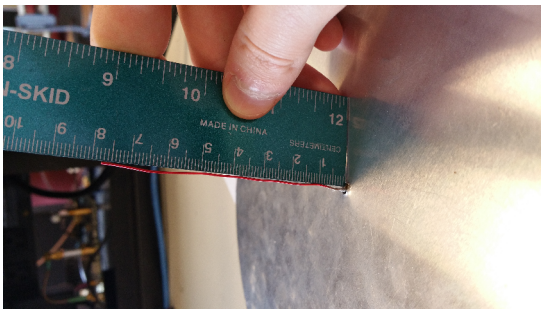

(a) Wire monopole

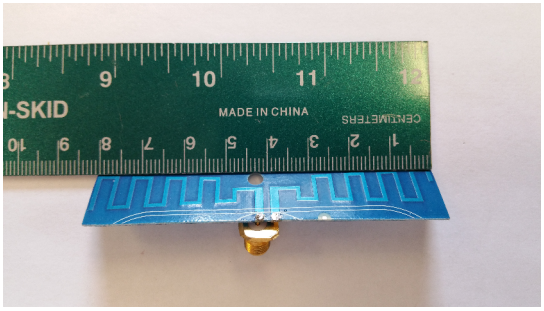

(b) Printed meandered dipole

Figure 77: 915 MHz Antennas

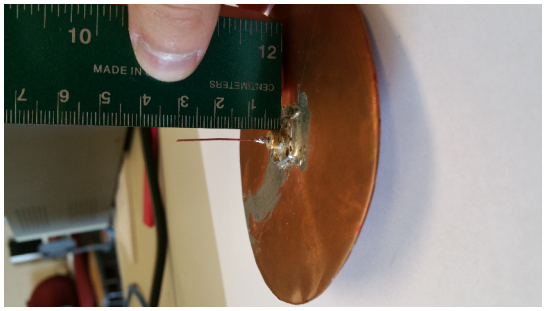

(a) Wire monopole

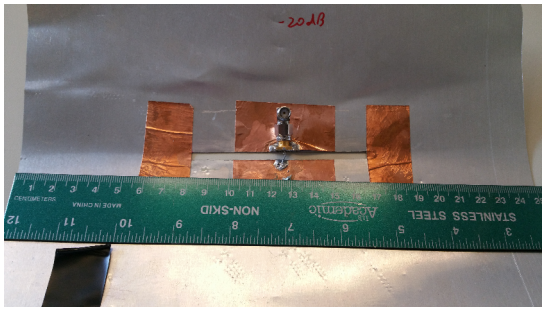

(b) Slot dipole

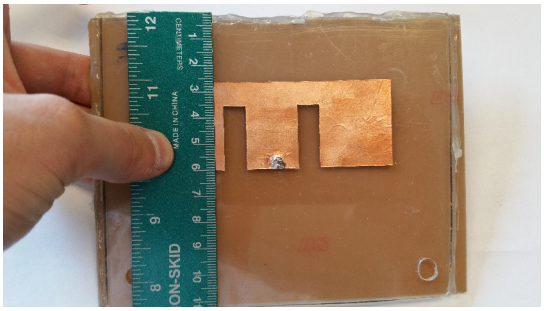

(c) E-Patch

Figure 78: 2.45 GHz Antennas

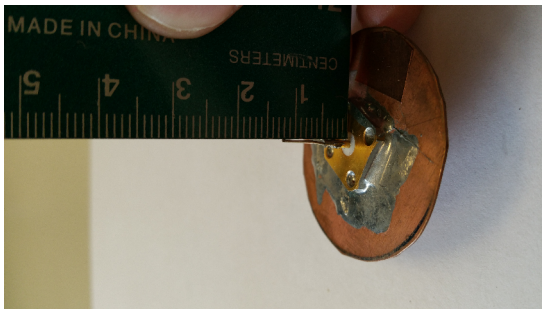

(a) Wire monopole

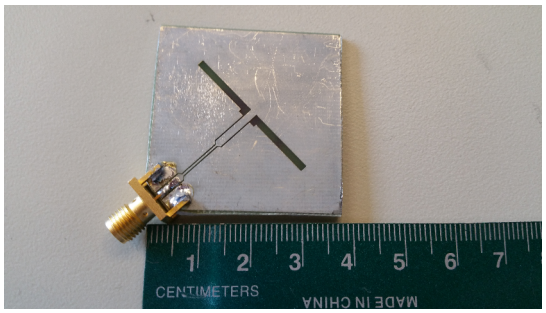

(b) Slot dipole

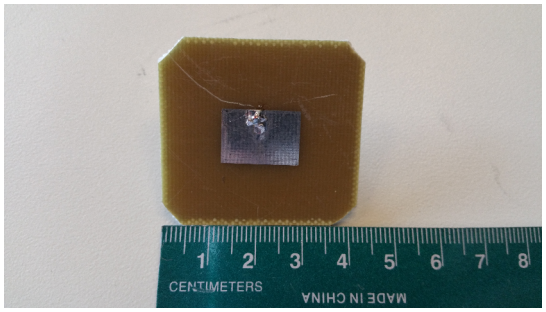

(c) Patch, small ground

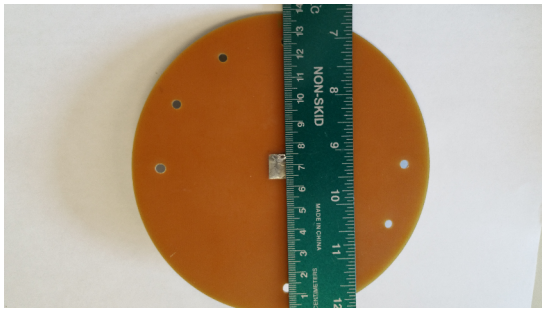

(d) Patch, large ground

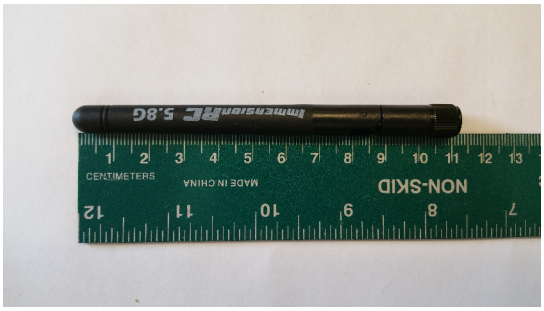

(e) Whip Antenna

Figure 79: 5.8 GHz Antennas

(a) Whip antenna, dielectric shielding

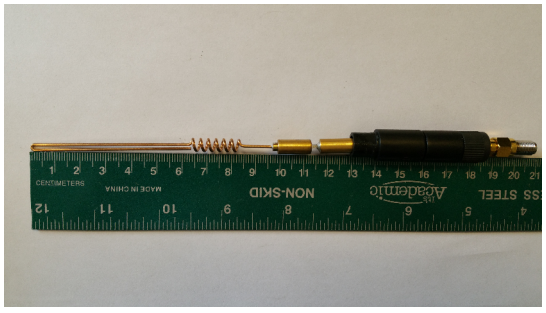

(b) Whip antenna, removed shielding

Figure 80: 2.45/5.8 GHz Dual-Band Antennas

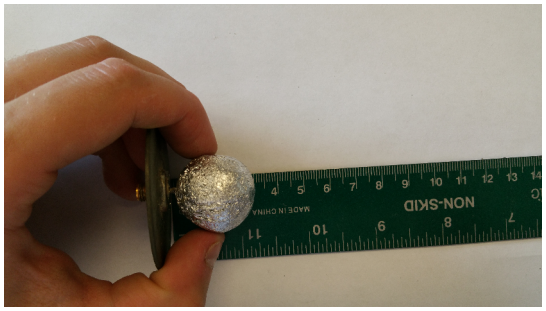

(a) 2.6 cm metal sphere monopole

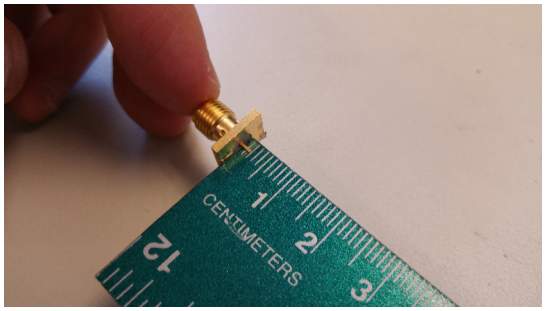

(b) 2 mm short monopole

Figure 81: Other non-resonant structures tested. The short wire monopole is simply the inner conductor of an edge mount SMA connector with the ground legs removed.

The antenna configurations with respect to the HV plane are illustrated in Figure 82 for the various antenna types. One example is shown for each antenna type (i.e. "Monopole antennas" illustrates the mounting orientation for the 915 MHz, 2.45 GHz, 5.8 GHz, and short monopole). All antennas are mounted such that the shortest distance from the antenna to the HV plane is 25 cm. Antennas that radiate in the direction of the HV plane are cross-polarized with the plane wires. The whip antennas are measured in two orientations, parallel and perpendicular to the HV plane.

5.4 Corona Current Measurement

The corona current is measured using a digital oscilloscope (Table 13) as a voltage across a resistor. For antennas that do not have a short to ground on the center conductor of the coax line(like the slot antenna), the current can be measured. For shorted antennas the corona current is shunted to ground and cannot be measured.

Corona current that develops on the antenna flows through the cable assembly (50Ω coaxial line) to the resistor breakout box, pictured in Figure 83. The box houses a 50Ω microstrip board to which a resistor is connected, the other end being connected to the microstrip ground. Originally this breakout box was designed to measure the lower frequency currents using the oscilloscope while simultaneously measuring RF with the VNA or spectrum analyzer. The VNA would be connected to the termination of the breakout box through a high-pass filter (HPF). RF from the antenna propagates through the cable assembly to the 50Ω microstrip board, where there is 50Ω microstrip leading to the VNA in parallel with a large ($\sim$ 1 kΩ) sensing resistor. Most of the RF passes through the board to the VNA. For low frequencies, the HPF appears as a large impedance, and most of the power flows through the sensing resistor. This method was successfully tested, but issues arose with the sensitivity of VNA measurements. Small perturbations in the breakout box significantly affected the calibration of the VNA when making measurements of the antenna impedance. This method of simultaneous testing of RF and low frequency currents was eventually foregone in favor of separate measurements.

The cable assembly connecting the antenna to the sensing resistor is a 50Ω transmission

(a) Monopole antennas

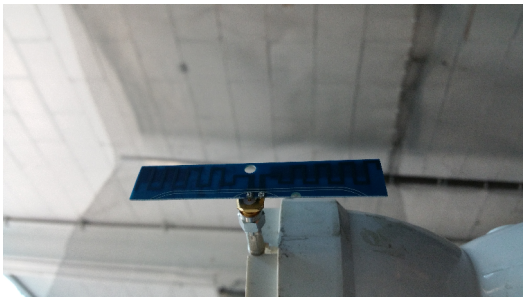

(b) Meandered dipole

(c) Slot antennas

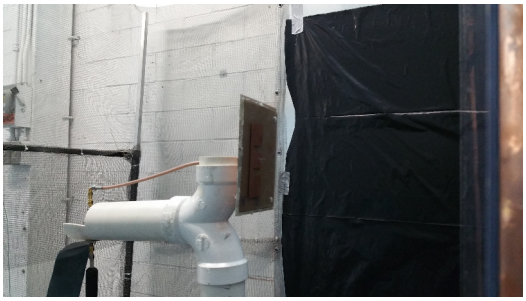

(d) Patch antennas

(e) Whip antennas, perpendicular

(f) Whip antennas, parallel

(g) Metal sphere

Figure 82: Pictures of the various antenna types mounted by the high-voltage plane, showing the orientation. All antennas were mounted 25 cm from the high-voltage plane (to the nearest point of the antenna).

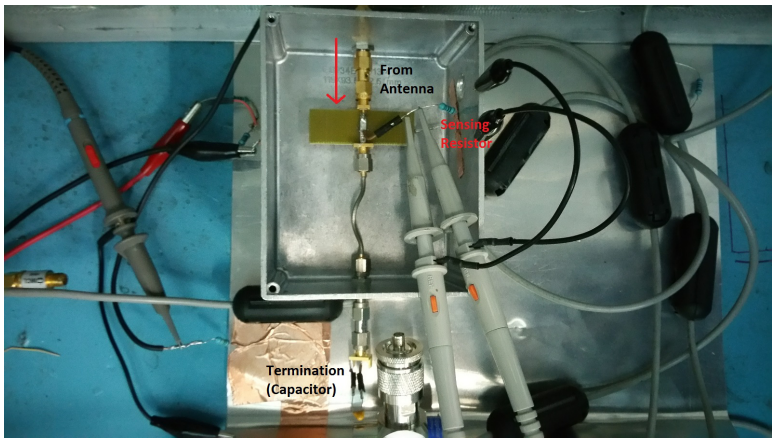

Figure 83: Sensing resistor for measuring the corona current with oscilloscope probes. A capacitor can be attached to the termination for measuring large current pulses.

line. The propagation delay from the antenna port to the resistor is measured to be 10.6 ns using the VNA. A corona current pulse on the antenna can be modeled by a current source at the end of the transmission line with an exponential current profile given by (78). Ideally the current measured across the resistor is exactly proportional to the corona current. However, the cable assembly transmission line introduces a parasitic capacitance, given by (82), where T_D is the propagation delay through the transmission line and Z_0 is the characteristic impedance. For a 50Ω coaxial line with $\varepsilon_e = 2.1$, this is about 33 pF per foot.

$$C = \frac{T_D}{Z_0} \tag{82}$$

This system is modeled in LTSpice (Figure 84) using both the transmission line model and equivalent capacitance model (the series inductance is neglected). The output voltage resulting from the corona current impulse on the resistor is plotted (85). In Figure 85, the red curve is the input current pulse, modeled by (80) with a current peak of $i_p = 1$A. The green curve is the output voltage for the transmission line model and the blue curve is the output voltage for the simple capacitor model.

It is observed that the simple parasitic capacitor model sufficiently captures the low frequency behavior of the output voltage. When measuring corona current as a voltage

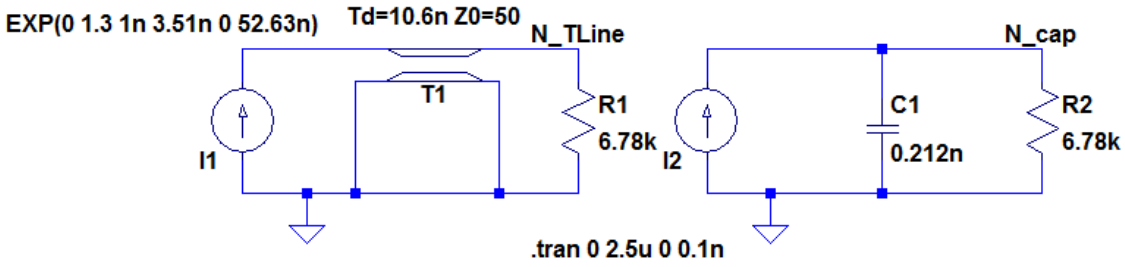

Figure 84: LTSpice schematic of cable assembly transmission line and terminated with current sensing resistor (left) and equivalent capacitance(right)

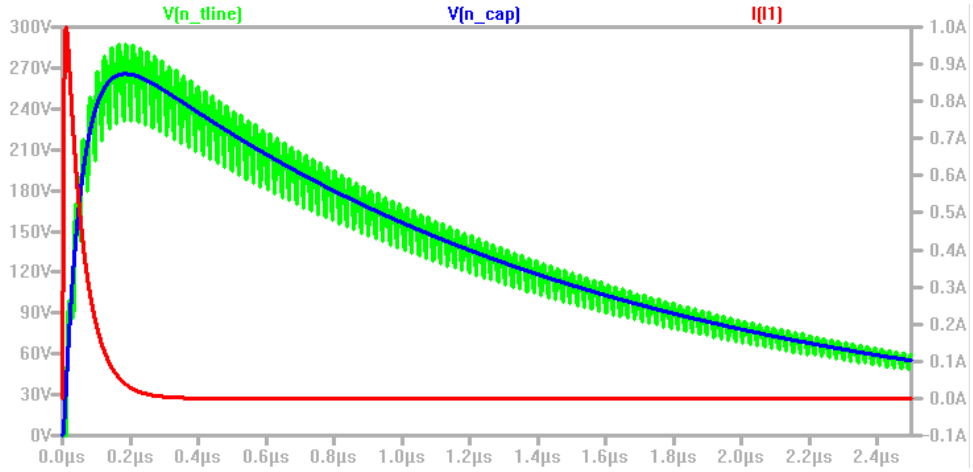

Figure 85: Voltage across sensing resistor from current pulse (red) with a transmission line model (green) and capacitor model (blue).

across a resistor, the system can be modeled as an RC circuit. High frequency features of the corona pulse cannot be resolved. This is a fundamental limitation of this measurement methodology. To improve the measurement bandwidth, the sensing resistor can be chosen to be small, but this comes at a trade-off with the measurement sensitivity.

One solution to this problem is to utilize a transimpedance amplifier. This method was investigated but was not ultimately implemented. Simulations of transimpedance amplifiers using components from Analog Devices were performed in LTSpice. The practical limit for a transimpedance amplifier with off-the-shelf components was found to be approximately 100 MHz. This is far below the RF frequencies being investigated, so this improvement in bandwidth does not add much value to the measurements. A lower bandwidth is sufficient

to observe the timing of the pulses as well as measure the average current. With knowledge of the typical pulse shape from (80) and (79), the current profile could be derived from band limited measurements.

For measuring low corona current amplitudes such as Trichel pulses, a large resistance is used, and the breakout box termination is left open ended. When positive streamers occur, the voltage peaks are much higher, approaching the voltage limits of the oscilloscope. A (parallel) capacitor is added to the breakout box termination and the resistance is reduced. Three RC pairs are utilized during the measurements to capture varying current amplitudes. LTSpice was used to simulate the transmission line system and equivalent capacitor for verification. The RC time constant on the cable assembly is also measured by applying a pulsed voltage to the coax inner conductor and measuring the voltage decay time constant. The results are tabulated in Table 17. For corona current measurement analysis, the measured capacitance is used.

Table 17: RC pairs used in measuring corona current.

R (Ω)	C_{term} (nF)	C_{tot} (nF)	C_{meas} (nF)	τ (μs)
6780	0	0.21	0.25	1.68
678	47	47.21	56.32	38.04
10	200	200.21	193.69	1.95

5.5 Modeling

Numerical modeling is used to augment experimental and analytical results. The extent of corona formation on an antenna is determined by the electric field at the surface of the structure. COMSOL Multiphysics is used to solve the discrete Poisson's equation (10) for the electric field surrounding the antennas. The magnitude of the electric fields is correlated with the ionization rate in air, allowing for prediction of corona onset. Utilizing the Drude dielectric model for corona plasma, RF simulations can be carried out using a finite difference time domain (FDTD) technique to determine the effects of plasma on antenna properties.

The solution to Poisson's equation for a three-dimensional structure can be simulated using COMSOL Multiphysics. In COMSOL, the geometry of the high-voltage setup and antenna is modeled, dielectric properties are applied, and potential boundary conditions

imposed on the structures. The software meshes the geometry using a free tertahedral method that allows for variable mesh density to adequately resolve small geometric features. Around the antenna where large potential gradients exist over short distances, a finer mesh setting is used.

Full wave electromagnetic simulations are carried out in CST Microwave Studio for the antennas with a Drude plasma model. Perfectly matched layer (PML) radiation boundary conditions are used to obtain the antenna radiation properties, namely the input impedance, directivity, and radiation efficiency.

CHAPTER VI

RESULTS AND DISCUSSION

6.1 Corona Formation

Corona formation can be detected by measuring the current into an electrode. The oscilloscope setup illustrated in Figure 54 was used in the measurement of corona current. The raw data for corona current measurements is provided in Appendix E. In this section, the relevant results will be presented and discussed as they relate to the problem of corona formation on antennas for wireless communication.

6.1.1 Electric Field Simulation

The electric field simulations in Section 2.1.3 show that the electric fields around a wire antenna on a 345 kV transmission line sensor setup can reach over 100 kV/cm at the peak. The measurement setup presented in Chapter 5 is employed to generate electric fields of this magnitude on an antenna while allowing for direct antenna measurements. Electrostatic field simulations are performed of the electric fields around the antennas to correlate the field magnitudes with corona formation.

A full 3D model is created of the high-voltage measurement test set. A comparison of the actual and modeled test set is shown in Figure 86. The details in the test set that could affect the calculated fields at the antenna were accounted for. The outer cage is omitted in the model image to allow better viewing of the interior, but it was included in the simulations. Mesh refinement was used to accurately compute the large field gradients in the vicinity of the antennas, depicted with the whip antenna in Figure 87.

The results of simulating the electric fields for the various antenna types are shown in Figure 88. The antennas are simulated in the configurations illustrated in Figure 82, positioned 25 cm from the HV plane. A 100 kV potential difference is applied between the antennas and plane. Since the electric fields scale linearly with the potential, the simulated electric field results can be multiplied by a constant to obtain the fields for any other

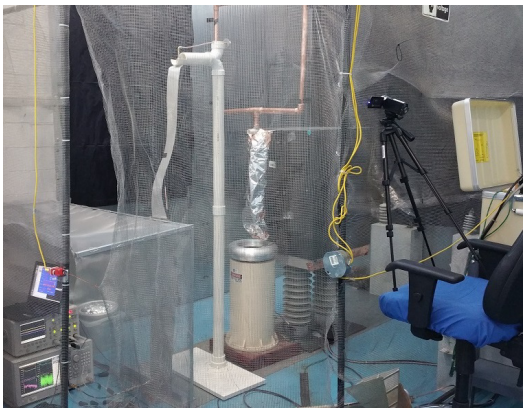

(a) Picture of HV test set

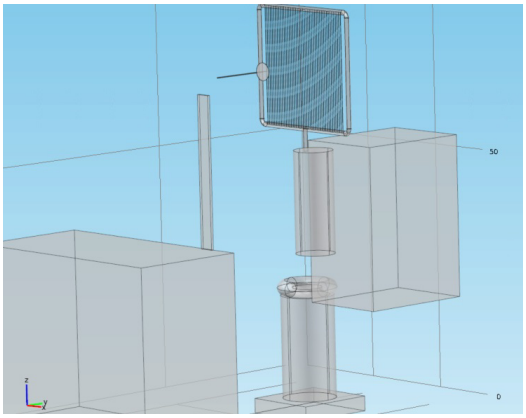

(b) 3D model of HV test set

Figure 86: Comparison of actual (a) and modeled (b) high-voltage test set. The model was created to be as detailed as possible with regard to features that could affect the fields at the antenna.

voltage. The peak voltages applied during experiments were 120 kVAC, or 170 kV peak amplitude. The simulated fields can be multiplied by a constant of 1.7 to obtain the peak fields experienced by the antennas during experimentation.

The electric field is calculated at the closest point of the antenna to the HV plane, along a line perpendicular to the plane. This point corresponds with the location where corona was observed during experimentation. The 915 MHz, 2.45 GHz, and 5.8 GHz monopoles unsurprisingly exhibit the highest electric field magnitudes, between 1200-1700 kV/cm at 170 kV. These fields are greater than the 400 kV/cm computed for a wire monopole on a reference 345 kV line, simulated in Section 2.1.3. This result validates the use of the

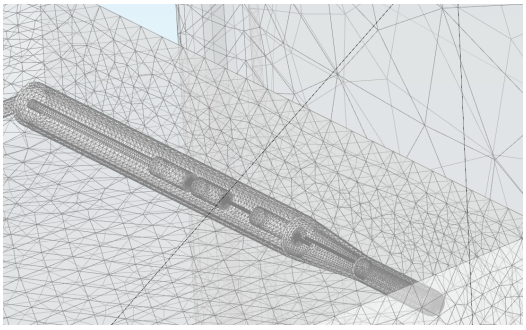

(a) Shielded whip antenna, parallel to HV plane

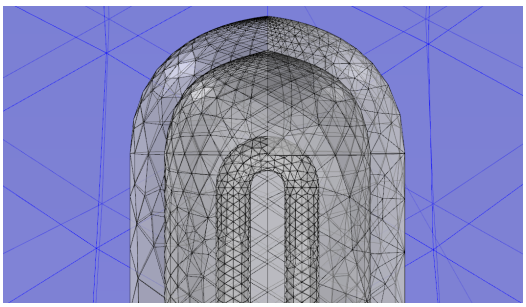

(b) Shielded whip antenna tip

Figure 87: Meshed rendering of the shielded dual-band whip antenna parallel to the HV plane. Mesh refinement is utilized around corners and small curves to accurately capture the potential gradients.

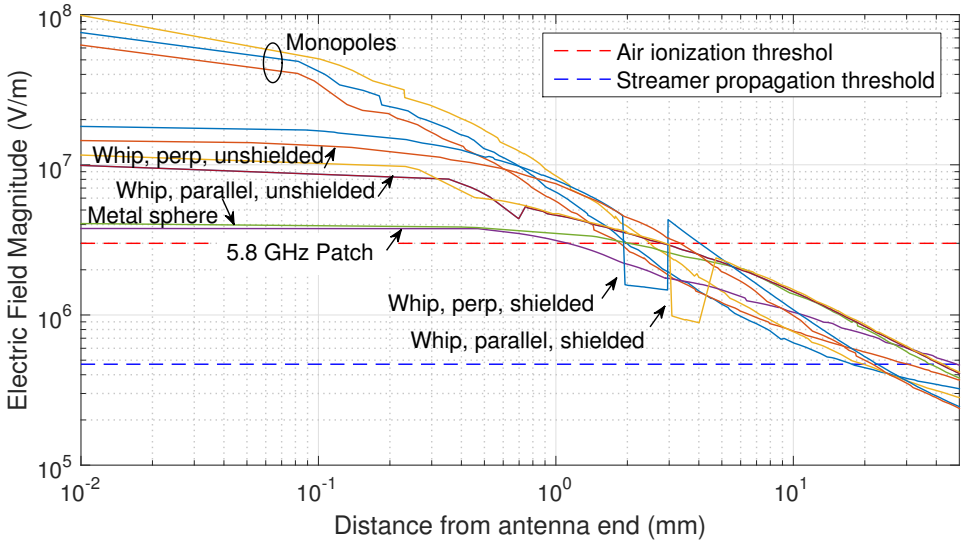

Figure 88: Simulated electric fields at the surface of the antennas with 100 kV applied. The electric field is calculated at the closest point of the antenna to the HV plane, along a line perpendicular to the plane.

measurement setup as a reference for corona formation intensities that may be observed in high-voltage sensing applications.

The shielded whip antenna has a sharp dip in the fields where the dielectric is. As a result, the fields elsewhere for the shielded antenna must also increase to compensate for the drop. An increase of 15-25% in the field at the conductor surface is observed for the shielded antenna compared with the unshielded equivalent. The gap between the conductor surface and dielectric in this antenna is between 2-3 mm. An insulator could be manufactured directly on the surface, decreasing this effect, but partial small gaps within the dielectric material could cause erosion of the dielectric, eventually leading to exposure of the antenna surface [15],[73].

With a larger radius of curvature ($\sim$ 3 mm), the whip antenna has a lower surface electric field than the monopole does at its tip. However, between 1-5 mm from the antenna surface, the field magnitudes are reversed. The potential gradients around the monopole tip are large but fall off steeply, while the fields around the whip antenna fall off more gradually and are greater than the monopole at larger distances. The field magnitudes only greatly diverge within 1 mm of the antenna surface. The metal sphere and 5.8 GHz patch with a

large ground plane (see Figure 79) have the largest effective radii of curvature and therefore the lowest surface electric fields. At a distance of 13 mm, the patch antenna fields are the largest.

The increase in electric fields at a distance for a larger radius of curvature leads to an interesting observed phenomenon. The monopoles with a small (effectively spherical) tip radius incite corona formation at very low voltages. In the experiments, voltages as low as 10 kV were sufficient to incite a measurable corona current, consistent in order of magnitude with the voltage ranges tabulated in Table 9. The metal sphere and unshielded whip antenna develop corona at higher voltages. However, because the fields fall off more gradually and are larger at farther distances from the surface, the more consistent longer streamers were observed. This can be concluded by observing that the fields fall below the streamer propagation threshold at farther distances for larger radii than for smaller radii in Figure 88.

6.1.2 Corona Measurements

Corona formation is observed on the antennas and recorded with video, as well as capturing the corona current with an oscilloscope. Capturing the corona formation visually is difficult because of the faintness of the emitted light. The visible light is the result of excited ions in the plasma falling back to their ground state, emitting a photon in the process. Figure 89 shows images captured of corona formation of a sampling of antennas.

The positive glow and Trichel pulses manifest themselves as a small faint glow just at the surface of the antenna. It is seen in Figure 89 (a) as a glow just at the monopole tip and (d) as a faint glow at the tip of the whip antenna. The streamers vary in length based on the voltage. A large group streamers is seen in (e), approximately 1 cm in length. Streamer formation on the monopole is more irregular, manifesting as individual filaments like that seen in (a). The meandered dipole also exhibited visible streamer formation, seen at the top of (b). One of the difficulties observed in the measurement setup is the development of arcs (f) due to the close spacing between the antennas and HV plane. HV measurements were made up to the breakdown limit.

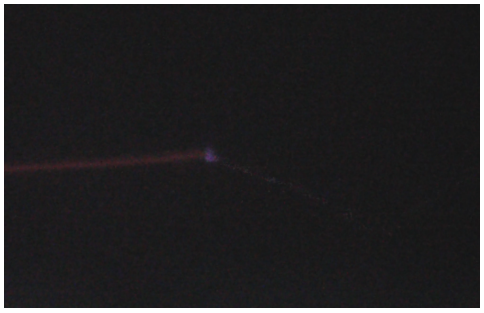

(a) Corona and streamer on 915 MHz monopole

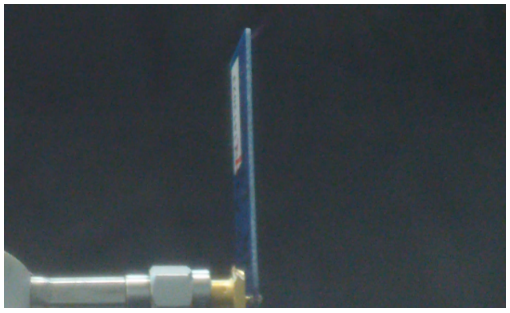

(b) Corona at top corner of meandered dipole

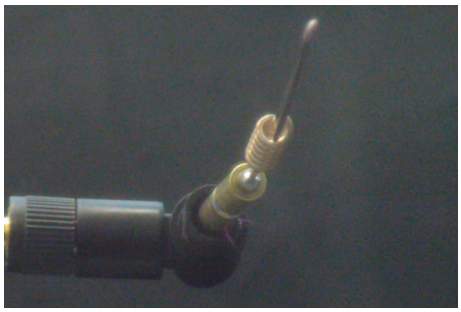

(c) Streamers on unshielded whip side

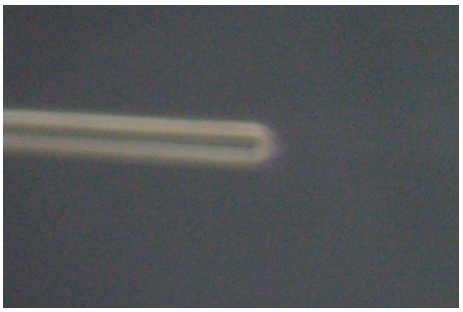

(d) Faint corona on unshielded whip end

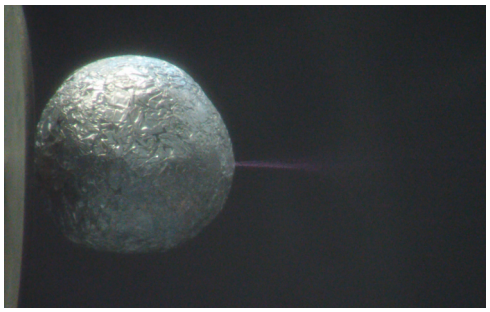

(e) Streamers on metal sphere

(f) Arc formation from monopole to HV plane

Figure 89: Visual captures of corona formation on the antennas during experimentation.

Measurement of the corona current was performed to confirm the degree and type of corona formation on the antenna. The full collection of data for various antennas is provided in Appendix E.6. The relevant results and conclusions are presented here.

The measured corona are primarily of the positive glow, positive streamer, and negative Trichel pulse types. In one case, with the 2.4 GHz monopole at voltages over 100 kVAC, negative glow was observed at the peak of the negative voltage cycle. Trichel pulse current amplitudes ranged from 0.1-10 mA, while positive glow fell around 10 μA. However, if the Trichel pulse current is averaged over the pulses and intermediate time, it falls on the order of 1μA, shown in Figure 90 for a wire monopole at 20 kVAC. While the Trichel pulse amplitude does not vary significantly with voltage, the frequency of pulses increases with voltage, thus increasing the average current. The frequency of Trichel pulses, increases with voltage to a peak on the order of 1 MHz. The pulse frequency is computed for the Trichel pulses on the monopole at 20 kVAC in Figure 91.

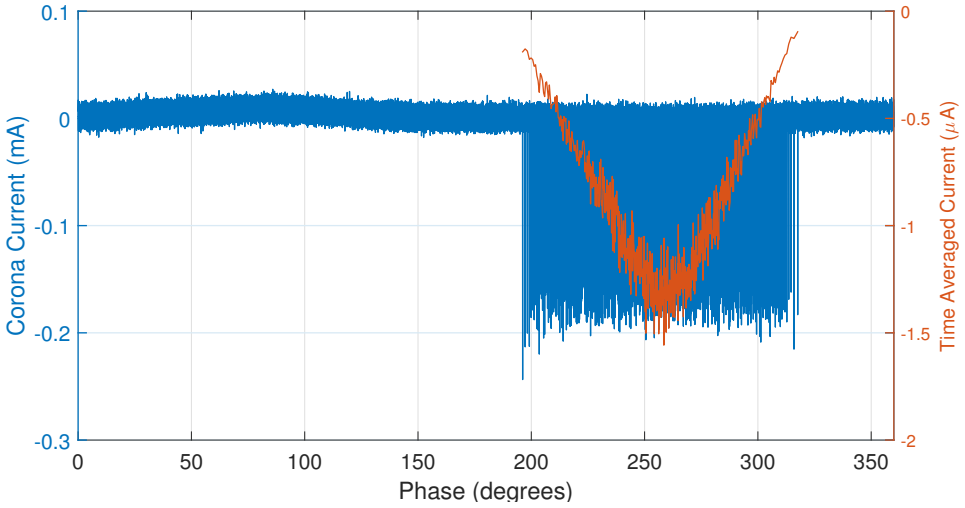

Figure 90: Corona current on 2.45 GHz wire monopole at 20 kVAC. Corona is forming on the wire tip, which is 25 cm from the plane. The positive flow current peak falls around 10μA and the average negative current peaks around 1μA.

Positive streamer inception is characterized by intermittent and irregular pulses with a higher current than observed in the positive glow and negative Trichel pulses. Figure 92 shows a single positive streamer, approximately 50 times higher in current than the Trichel pulses.

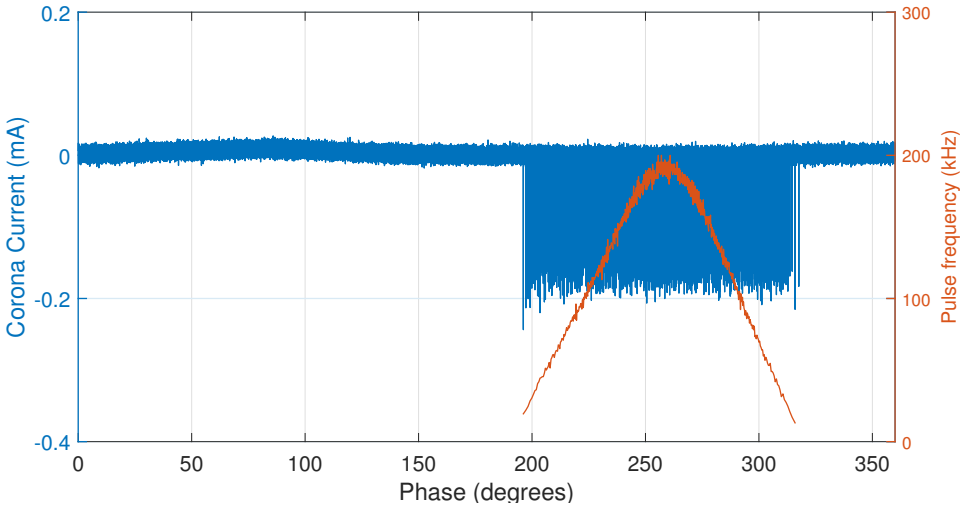

Figure 91: Corona current on 2.45 GHz wire monopole at 20 kVAC. Corona is forming on the wire tip, which is 25 cm from the plane. The frequency of Trichel pulses increases with voltage, while the current amplitude remains constant.

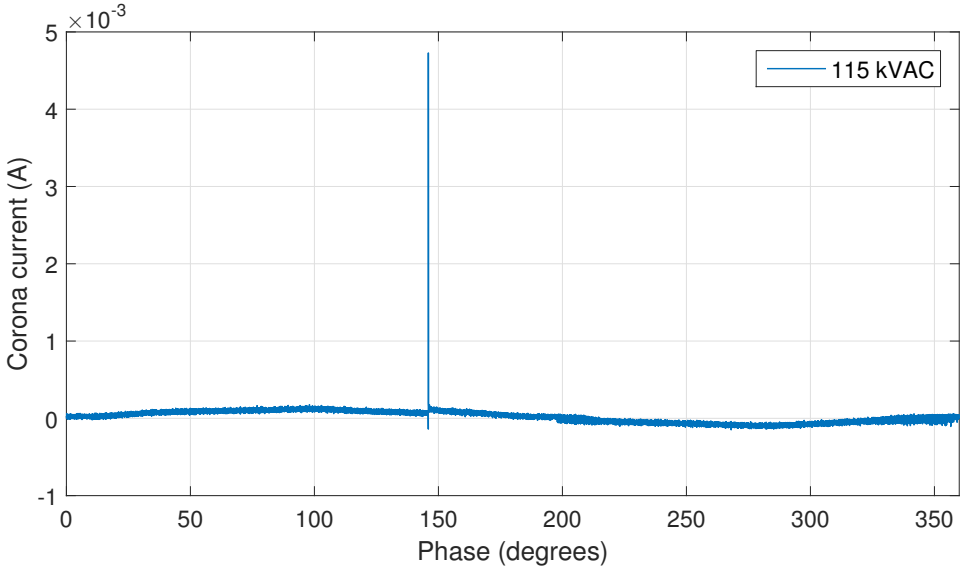

Figure 92: Corona current on 2.45 GHz wire monopole at 115 kVAC. Corona is forming on the wire tip, which is 25 cm from the plane. A streamer pulse is seen on the positive half cycle, 50 times higher than the Trichel pulses.

Streamers vary in current as well as interval. A set of streamers were measured at a higher time capture resolution. Figure 93 shows a measured positive streamer pulse captured by the oscilloscope as a voltage. The corona current is derived from the voltage by extracting it from the measurement cable assembly RC response. The process is performed on a smoothing curve fit to the measured voltage. The peak current is found to be 1 A. Positive streamers can generate large currents. Formation of streamers on the antenna can result in large transients being fed into the RF front end. While the frequency content of corona and streamers is low (<10 MHz (see Section 4.3)), energy at low frequencies and high power can still affect RF front end and electronics performance if not properly filtered.

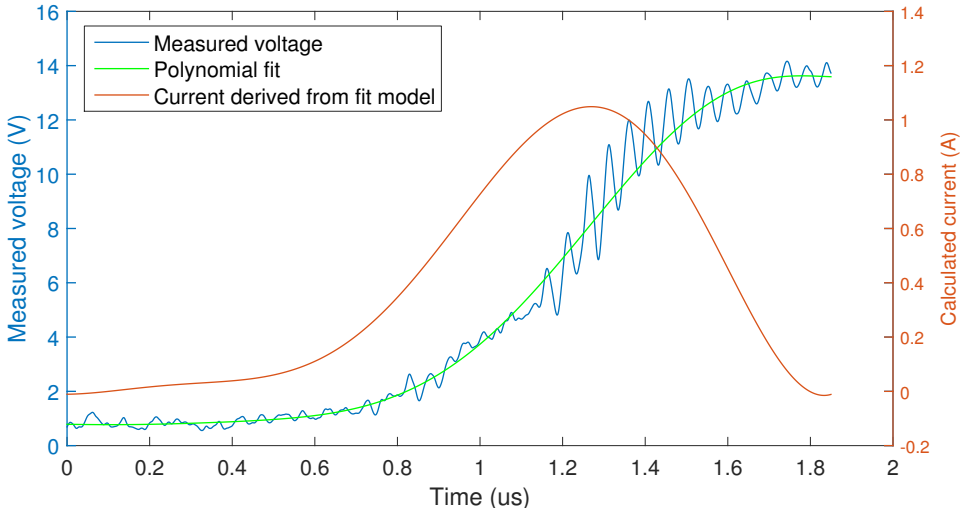

Figure 93: Measured voltage of the rising edge of a streamer (blue), a smoothing curve fit (green), and the current derived from the curve fit voltage obtained by deconvolving the RC response of the system.

A comparison of the corona current on the whip antenna with and without the dielectric shielding provides interesting results regarding the effects of dielectric shielding on the antenna current. Figure 94 shows the measured corona current on the dual-band whip antenna. The voltage is set to 110 kVAC with the antennas either parallel or perpendicular to the HV plane at 25 cm, illustrated in Figure 82. The positive streamer polarity appears reversed in (c), possibly because the streamers were forming on a grounded portion of the antenna.

In Figure 94(a) and (c), negative Trichel pulses, positive glow, and positive streamers

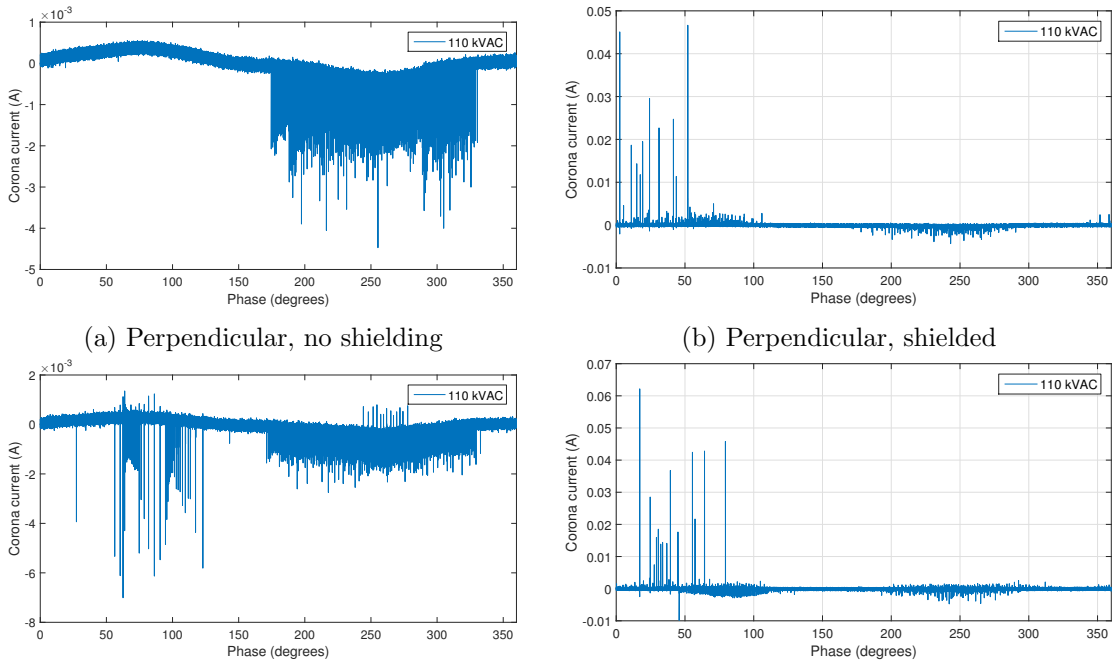

(a) Perpendicular, no shielding

(b) Perpendicular, shielded

(c) Parallel, no shielding

(d) Parallel, shielded

Figure 94: Dual-band whip antenna corona current measured measured with the dielectric shielding in place and removed for a perpendicular and parallel orientation to the HV plane. The results shown are for 110 kVAC at a distance of 25 cm.

are observed at typical current amplitudes of 0.1-10 mA. These cases correspond with no dielectric shielding over the antenna. Subfigures (b) and (d) show corona current with dielectric shielding on the antenna. The dielectric is 2-3 mm from the antenna conductor surface. Corona formation with the dielectric is characterized by :

1. Irregular pulses replace the negative Trichel pulse and positive glow corona regimes.

2. Positive streamer current is higher than for an equivalent antenna with no dielectric shielding.

3. Hysteresis of corona formation relative to the voltage cycle, with an observed 30^o offset.

The results can be explained by charge accumulation on the inner dielectric surface. During negative corona, electrons are accelerated away from the cathode toward the dielectric material. Electron accumulation results in a buildup of static charge on the inner surface of the dielectric [98]. The buildup of negative charge decreases the fields at the

negative cathode, slowing the negative ionization processes. As the voltage on the antenna returns to zero, the field polarity reverses before the antenna voltage crosses 0 because of the large negative charge on the dielectric surface. As a result, positive corona formation is initiated earlier. At the end of the positive cycle, positive ion accumulation at the cathode enhances the field, initiating the negative corona earlier. Although the bandwidth of the system in measuring the pulses was not sufficient to capture the exact temporal evolution of the pulses with dielectric, previous research has shown that partial discharges in dielectrics are much shorter than gaseous streamers, on the order of a few nanoseconds [15]. In the measured case, it is not completely clear whether breakdown is occurring in the dielectric as well as the air, and a study of the processes involved requires future research.

6.1.3 Port Current Simulations

Corona formations on an antenna behave as current sources. If the antenna is DC isolated from ground, like a monopole or patch antenna, corona current on the antenna feeds into the antenna port. Certain antenna designs are made of a single electric conductor. The slot antenna and PIFA are two examples of such antennas. To examine the corona pulse current sinking capability of a grounded antenna, simulation was performed in CST Microwave Studio, shown in Figure 95. Port 1 is a 50Ω discrete port, and Port 2 is a broadband current source set to 1 A.

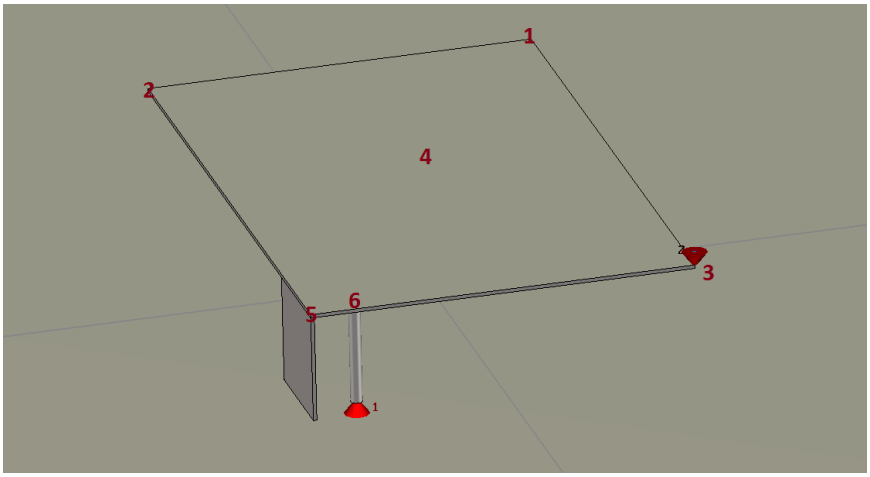

Figure 95: PIFA antenna model in CST Microwave Studio. The points where current is applied are labeled numerically.

A two port simulation is run, monitoring the current on each port. The current in the antenna feed, Port 1, is compared with the the current created by the current source, Port 2. The results in Figure 96 show that at low frequencies the current coupled into the antenna port are much lower than the corona current. The current sinks to ground through the shorting plate. At the antenna resonant frequency there is a peak in the current coupled into the antenna port. The power coupled into the antenna from the feed port when transmitting ($20\log\left(1-|\Gamma|^2\right)$) is plotted first.

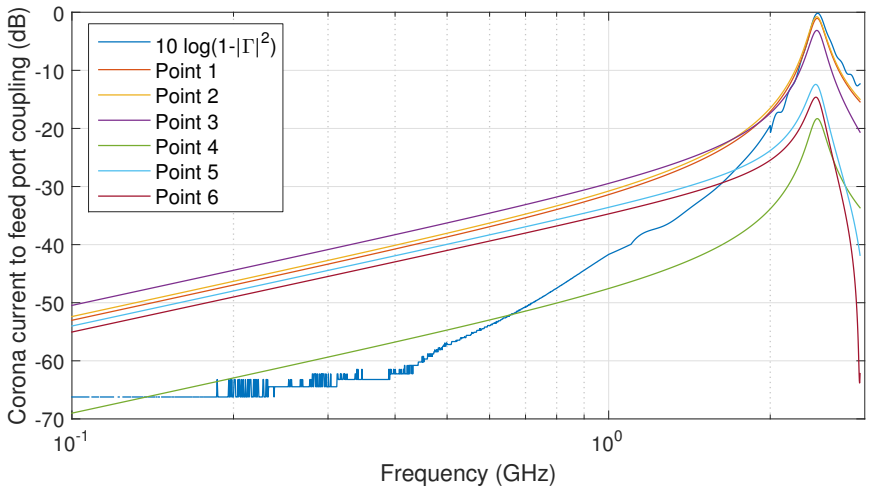

Figure 96: Ratio of current intensity coupled into feed port by corona current source at various points on PIFA element ($20\log(I_{port}/I_{corona})$). The point locations are illustrated in Figure 95.

It can be observed from Figure 96 that the coupled power from the feed port to the antenna is not directly related to the corona current coupled into the antenna port. The impedance of the antenna as seen from the feed port is related to the radiation characteristics of the structure. The current on the antenna is not induced by an incident electromagnetic wave, but is forced onto the structure at a specific point by an external current source, the corona discharge. The point at which the current source is located on the structure affects the power coupled into the port. In the cases simulated, the least current coupled into the antenna when the current source (i.e. corona) is in the center of the PIFA element. Little current coupled into the port with the current source near the port and shorting plate as well. When the current source is on the far corners of the PIFA, resonant modes can build

on the structure and increase coupling of power into the antenna port. In all cases, the power coupled into the port is maximum at the resonant frequency of the structure, and decreases with decreasing frequency.

Placing the current source above the port is not equivalent to feeding the antenna from the antenna port because the source of current is not the same. With the antenna port, current is fed into the antenna with a 50Ω impedance relative to the ground plane. There is an opposing current induced on the ground plane. Electromagnetic energy propagates across the structure as in a microstrip line. With the corona current fed at point 6 in the figure, the current does not flow from the ground plane but from the electric discharge above the antenna. This is not equivalent to the current flow between the PIFA element and ground plane.

Below resonance, the current coupling into the port can be represented by a simple equivalent parallel RL circuit model. The shorting plate acts as an inductance to ground, while the port presents a 50Ω resistance. As the frequency decreases, the proportion of current coupled into the port falls off at 20 dB per decade, the slope observed in Figure 96.

6.2 Antenna Impedance

The results of the measurements show little to no variation on the antenna impedance with the presence of corona. Zero-span measurements performed to resolve temporal variations in antenna impedance showed no change in impedance directly attributable to corona formation. Unable to resolve the time variations in impedance with the zero-span measurements (high IF bandwidth), an averaging approach was also taken. The IF bandwidth was decreased and the impedance measurement was performed as an average over one period of a voltage cycle. Again no significant variations are observed.

The metrics used to characterize the antenna impedance are the return loss, specified in dB, and the reflection phase. The return loss is measured relative to a calibrated 50 Ω source.

$$\text{RL (dB)} = 20 \log |S_{11}|$$

$$\text{Reflection Phase (degrees)} = \angle S_{11}$$

6.2.1 Zero-span Measurements

To resolve possible time variation of the antenna impedance over the course of a measurement cycle, zero-span measurements are performed with 1601 samples over the course of a one 60 Hz period (16.6 ms). In order to achieve a small time step, the IF bandwidth is set to the maximum value of 100 kHz. The trade-off is an increase in measurement noise. With these settings, 1601 data points are taken over one 60 Hz voltage period.

In order to sample at a high rate for the zero-span measurements, a large IF bandwidth had to be used in the VNA, increasing the measurements noise. Variations in the impedance with and without corona fell within the measurement noise. Many runs were performed using zero-span because it would be beneficial to understand how corona affects the antenna at different points in the cycle. Ultimately, it was determined that for practical antenna design considerations, the variations falling in the noise, less than 1 dB, are well within the antenna construction and link design margins.

The zero-span results are shown for two antenna cases: the 2.45 GHz wire monopole, and the 2.45/5.8 GHz dielectric shielded whip antenna. These two results are given as the most severe cases observed during measurements as far as corona formation is concerned. The wire monopole incited corona formation on the tip at voltages starting around 10 kVAC when 25 cm from the HV plane. The whip antenna was the only antenna to exhibit results outside the baseline 0 kVAC case, and generated the highest corona currents.

Considering the use of the inverted voltage setup (see Section 5.1.1), the polarity of the corona formation on the antenna is inversely related to the voltage output of the transformer. To account for this 180^o phase shift of the effective voltage of the antenna relative to the HV plane, the voltage cycle phase in the subsequent plots is adjusted to the polarity of corona formation on the antenna itself. The first half of the cycle represents a positive voltage of the antenna relative to the HV plane (a negative voltage of the HV plane relative to ground). This phase/corona polarity relationship is illustrated in Figure 97.

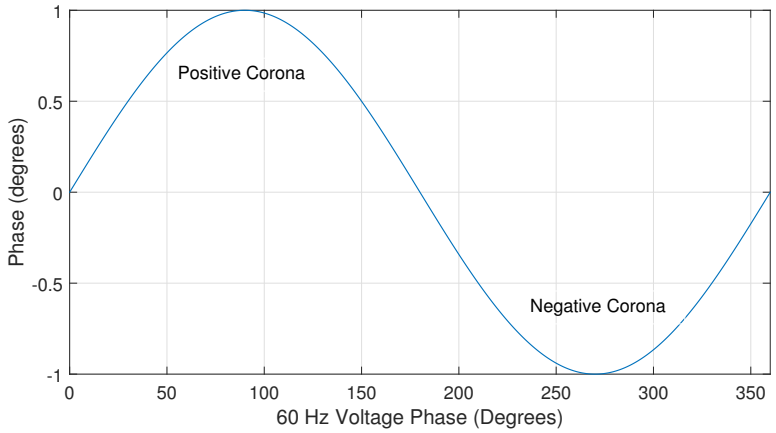

Figure 97: Relationship between voltage phase specified in subsequent figures, and polarity of corona formation on antenna. Voltage is specified as antenna voltage relative to the high-voltage plane.

6.2.1.1 2.45 GHz Monopole

The 2.45 GHz wire monopole antenna was configured as shown in Figure 98. The monopole is positioned 25 cm from the high-voltage plane, and results are shown for a 120 kVAC applied voltage. Figure 99 shows the return loss measured for the 2.45 GHz monopole with an applied 120 kVAC to the high-voltage plane. Positive streamer and negative Trichel pulse formation is observed during the measurement, but no significant variation in the antenna return loss is observed at any voltage phase. The relative difference between the antenna input resistance at 120 kVAC and and the baseline measurement (scaled to the magnitude of the antenna impedance) is plotted in Figure 100. The same is done for the antenna input reactance in Figure 101. No difference is observed in the antenna input resistance or reactance due to positive or negative corona. Changes due to corona would manifest themselves around the 90 and 270 degree phases. The measured differences in impedance under corona formation are within the system noise ($\sim 0.1\Omega$). Results at lower voltages predictably show no variation in the impedance either, so only the highest measured voltage is shown.

Figure 98: Measurement configuration of the 2.45/5.8 GHz whip antenna. The tip of the antenna is 25 cm from the HV plane.

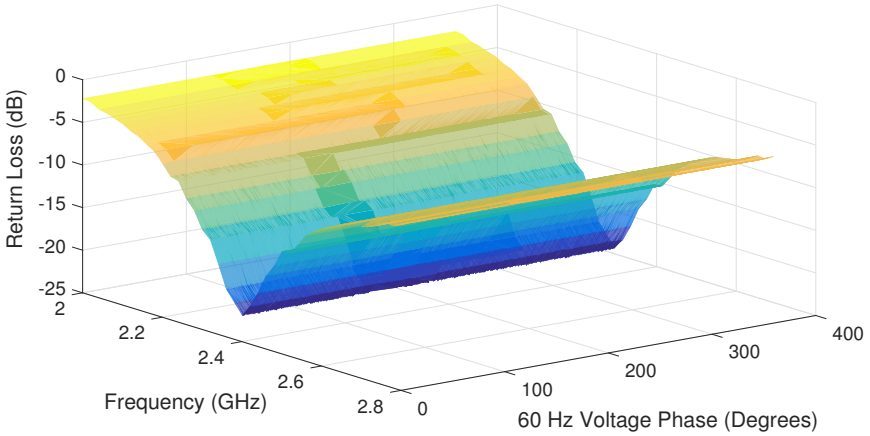

Figure 99: Zero-span return loss measurement taken at multiple frequencies for a 2.45 GHz wire monopole 25 cm from a 120 kVAC plane.

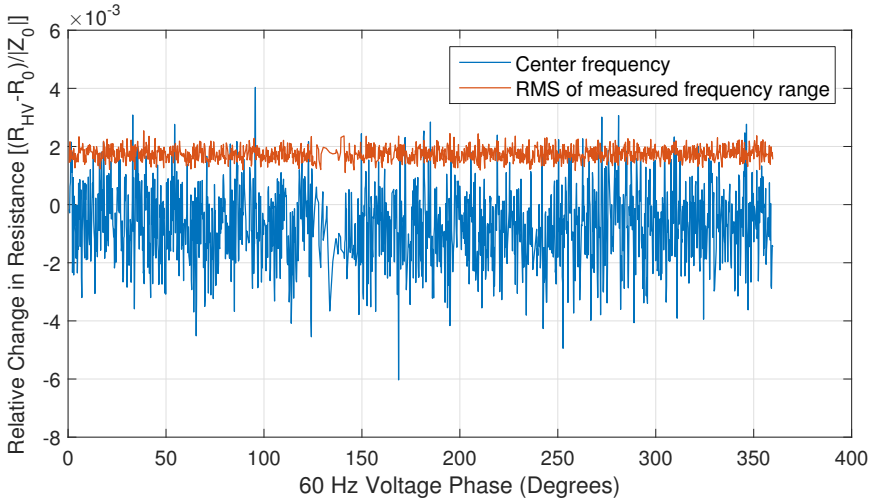

Figure 100: Relative change in antenna (2.45 wire monopole) input resistance over a 60 Hz voltage cycle at 120 kVAC. The change in antenna resistance is relative to the baseline antenna input resistance measured at 0 kV.

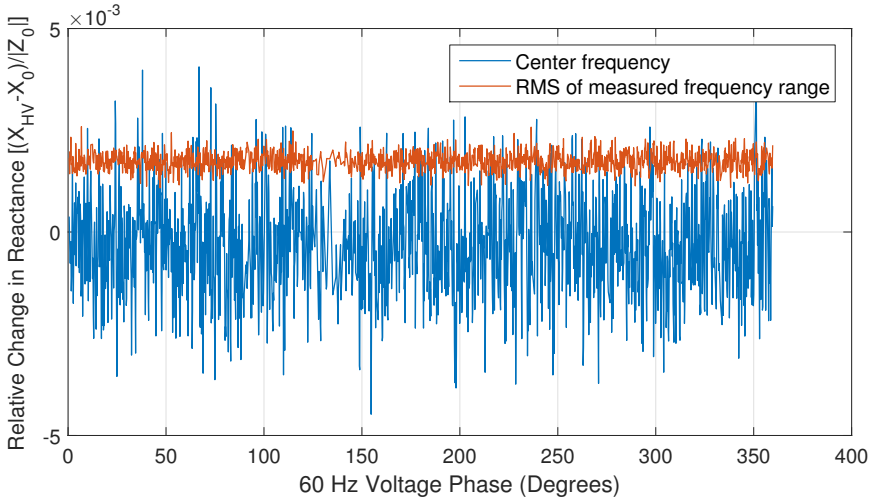

Figure 101: Relative change in antenna (2.45 wire monopole) input reactance over a 60 Hz voltage cycle at 120 kVAC. The change in antenna reactance is relative to the baseline antenna input reactance measured at 0 kV.

6.2.1.2 2.45/5.8 GHz Whip Antenna

The 2.45/5.8 GHz dual band dielectric shielded whip antenna was configured as shown in Figure 102. As with the 2.45 GHz monopole, the results are plotted in Figures 103-105 for the antenna operating at 2.45 GHz, and in Figures 106-108 operating at 5.8 GHz. The results show no significant effects in the antenna input impedance with corona formation at the highest measured voltage of 120 kVAC. However, there is some apparent change in the antenna impedance around the positive half of the voltage cycle (positive corona formation). The change in impedance is less than 1%, correlating to less than 1Ω difference. This in turn correlates with a 0.0004 dB change in the radiated power, insignificant in any practical wireless communication power budget.

Measurements of the positive corona current for the 2.45/5.8 GHz dual-band whip antenna show no significant

Figure 102: Measurement configuration of the 2.45/5.8 GHz whip antenna. The tip of the antenna is 25 cm from the HV plane.

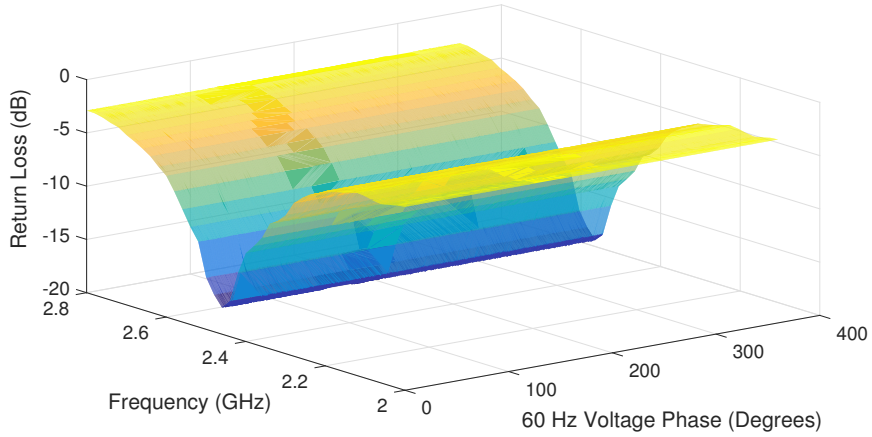

Figure 103: Zero-span return loss measurement taken at multiple frequencies for a 2.45 GHz dielectric shielded whip 25 cm (perpendicular) from a 120 kVAC plane. Measurements are performed for the 2.45 GHz band.

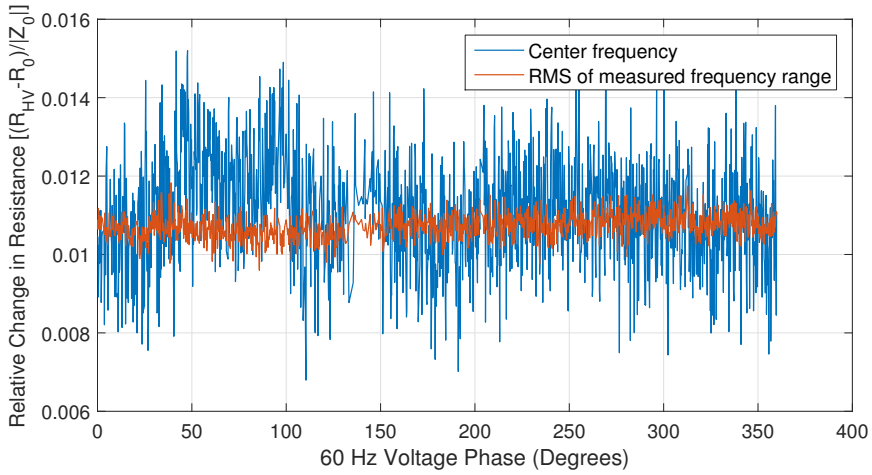

Figure 104: Relative change in antenna (2.45/5.8 GHz dual-band dielectric shielded whip) input resistance over a 60 Hz voltage cycle at 120 kVAC. The change in antenna resistance is relative to the baseline antenna input resistance measured at 0 kV. Measurements are performed for the 2.45 GHz band.

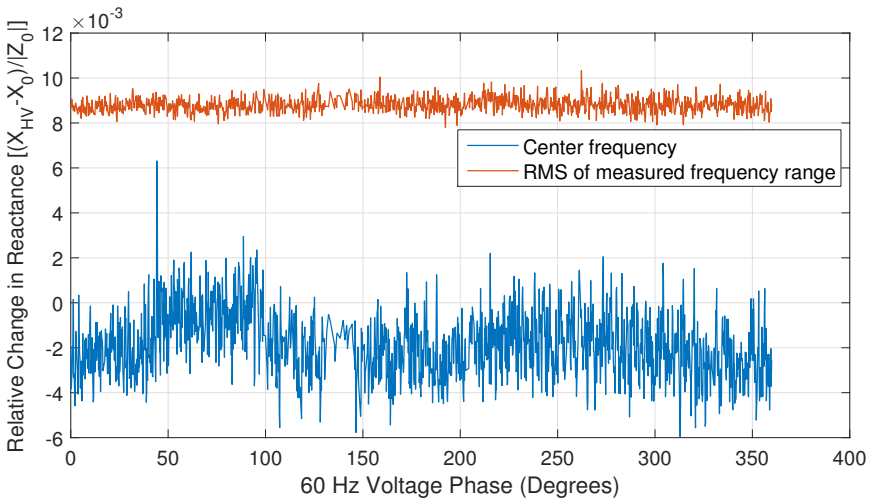

Figure 105: Relative change in antenna (2.45/5.8 GHz dual-band dielectric shielded whip) input reactance over a 60 Hz voltage cycle at 120 kVAC. The change in antenna reactance is relative to the baseline antenna input reactance measured at 0 kV. Measurements are performed for the 2.45 GHz band.

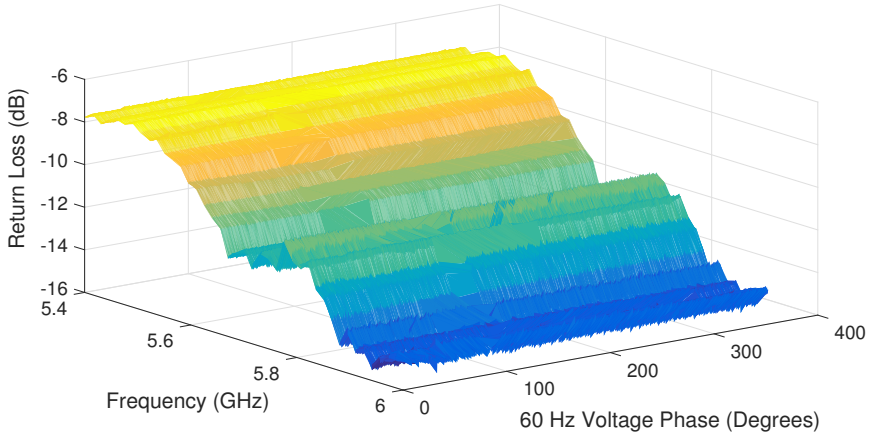

Figure 106: Zero-span return loss measurement taken at multiple frequencies for a 2.45 GHz dielectric shielded whip 25 cm (perpendicular) from a 120 kVAC plane. Measurements are performed for the 5.8 GHz band.

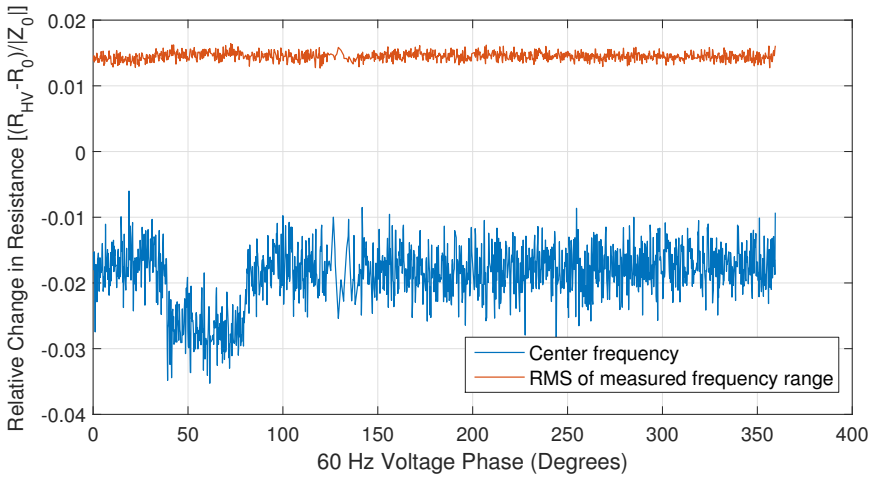

Figure 107: Relative change in antenna (2.45/5.8 GHz dual-band dielectric shielded whip) input resistance over a 60 Hz voltage cycle at 120 kVAC. The change in antenna resistance is relative to the baseline antenna input resistance measured at 0 kV. Measurements are performed for the 5.8 GHz band.

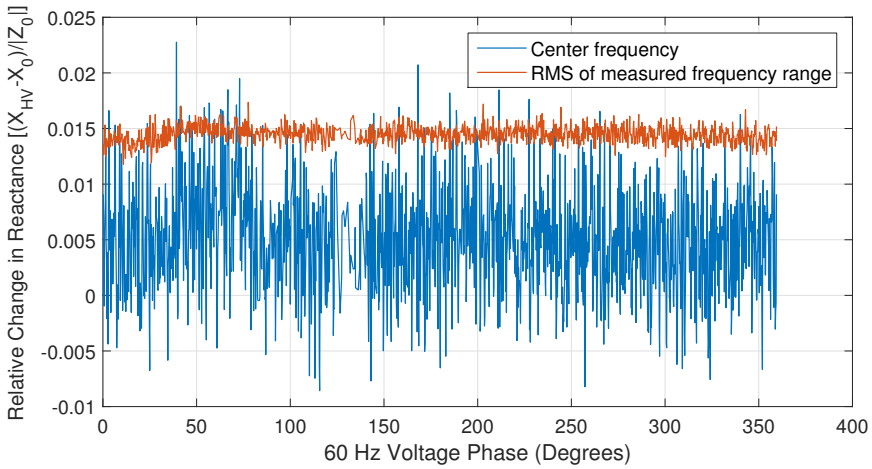

Figure 108: Relative change in antenna (2.45/5.8 GHz dual-band dielectric shielded whip) input reactance over a 60 Hz voltage cycle at 120 kVAC. The change in antenna reactance is relative to the baseline antenna input reactance measured at 0 kV. Measurements are performed for the 5.8 GHz band.

6.2.2 Averaged Measurements

No appreciable changes in the antenna impedance are observed in the course of the zero-span measurements. To improve the resolution of the measurements and possibly detect changes attributable to corona, averaged measurements are taken at a lower IF bandwidth on the VNA. With a lower bandwidth, the noise in the measurements is reduced, at the cost of a longer sample time. A sample time of 16.67 ms is chosen (up from 10 μs for zero-spzn measurements). This time corresponds with one period of the 60 Hz voltage. Since the VNA is sweeping over frequency instead of time now, choosing a sampling period of one voltage cycle ensures consistency between measurements while sweeping over frequency.

All the measured results for different antennas are presented in Appendix E.1. However, even with the improvement in instrument sensitivity, no significant change in antenna impedance was observed. Changes in measured impedance during high-voltage runs were found to be attributable to changes in the test setup, confirmed by performing baseline 0 kV measurements before and after the high-voltage measurement runs. The difference in the baseline measurements before and after runs would result from a change in the cable assembly that is calibrated out before measurements.

Variation in the pre- and post-HV measurements were especially severe in measurements of the dielectric shielded whip antennas and meandered dipole antenna. A measurement of the meandered dipole antenna return loss is shown in Figure 109. Baseline return loss measured after the 120 kV high-voltage run aligns with the return loss captured during the high-voltage run. For the meandered dipole antenna and dielectric shielded antennas, high-current streamers were measured, potentially through partial breakdown mechanisms in the dielectric. A sharp rise in line voltage in the cable assembly RF conductor may have triggered partial breakdown in the cable assembly itself, affecting the measurement results. The oscillatory nature of the 120 kV return loss measurement itself is an indication that the difference is a result of an uncalibrated system. The affects of a plasma of the return loss over such a narrow bandwidth would show a more gradual effect with frequency. Simulation results in [75] indicate that change in return loss with a high density plasma covering the entire antenna appears as a decrease in the Q of the antenna. The plasma adds

as a loss resistance to the antenna impedance. The oscillatory variations in the return loss measurements of the antennas are the result of the high-current corona pulses affecting the measurement calibration.

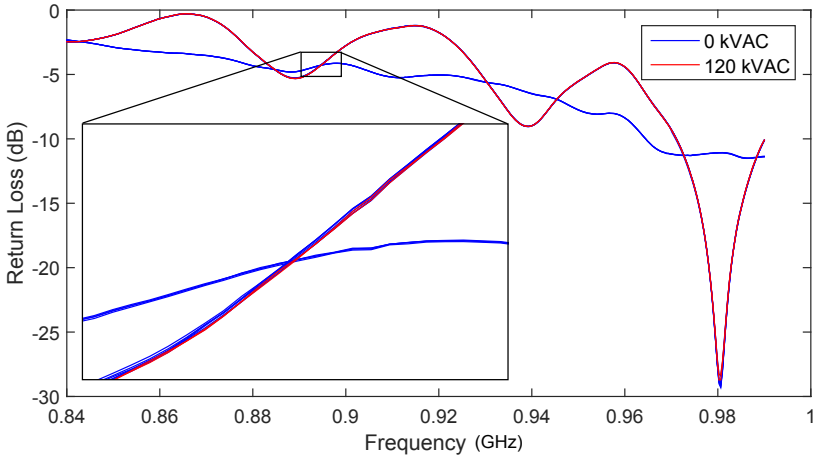

Figure 109: 915 MHz printed meandered dipole, first attempt. The VNA calibration was affected during measurement, obviated by the large change in baseline 0 kV measurements.

6.2.3 Short wire antenna

The reactance of an electrically short monopole is approximated by (83), where a is the monopole radius and h is the monopole length. When no change in antenna impedance was observed due to corona, it was hypothesized that the reason may by the corona formation is too small relative to the antenna length to affect the impedance significantly. The 2mm short monopole (SMA connector) is measured. If corona formation on the tip of the monopole is on the order of the monopole radius (~ 0.5 mm), a change in the short monopole reactance may be measurable. If the corona plasma on the monopole tip acts as a highly conductive medium, an effective extension of the monopole by 0.5 mm would result in an increase in reactance on the order of 50 Ω.

$$X = \frac{-30\lambda}{\pi h}\left(\ln\left(\frac{h}{a}\right) - 1\right) \tag{83}$$

The reactance is measured for the short monopole over a range of frequencies from 1 to 6 GHz. The result of the measurement is shown in Figure 110. The reactance has no

change with increasing voltage. The observed changes in the measurements are on the order of 2Ω and do not follow any trend with regard to applied voltage, indicating they may be due to measurement error. The corona formation on the short monopole is observed to be positive glow and negative Trichel pulses beginning around 40 kV (see Figure E.64). The conclusion to be drawn here is that corona electron density is in corona is too low to have a significant impact on antenna impedance.

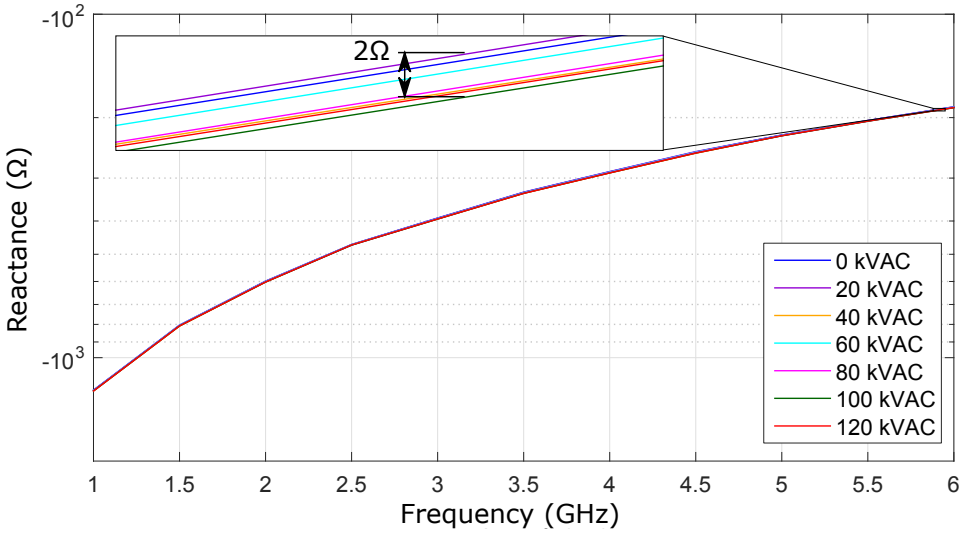

Figure 110: Measured reactance of a 2 mm monopole under corona at varying voltages.

6.3 Transmission

Ultimately the transmission from one antenna to another through the channel is the ultimate measure of a link behavior. Using the VNA, the transmission (S21 or S12) can be measured from the antenna under test to a second antenna. The transmission measurement incorporates all the effects of the channel including the antenna input reflection, corona attenuation, antenna directivity, and channel multipath. For antennas that radiate mainly along the axis of the coaxial feed cable, such as the patch antenna, a second patch antenna is attached to the far wall of the cage for measuring the transmission (Figure 111). The antenna is cross polarized with the wire grid for minimum reflection. For antennas that radiate omnidirectionally, such as the monopole, a ridged horn antenna is placed on the ground beside the test antenna (Figure 112). The horn is convenient due to it being broadband over the range of measurement frequencies. However, it must be placed far enough away from the high-voltage equipment to avoid arcing. There is not sufficient space behind the test set to setup the horn so the patch is chosen as an alternative option.

Theoretical calculations of the received power fail to predict the measurements because of the severe multipath in the cage. The measured transmission for various voltages is compared to a baseline transmission measurement instead. Care is taken to avoid movement of the cage and surroundings during measurements because significant changes in the received signal profile are observed.

The metric used to characterize transmission is the transmission coefficient, specified in dB. When describing power loss through a device, this is also commonly referred to as the insertion loss, given as a positive value.

$$T(dB) = 20\log\left(|S_{21}|\right)$$

6.3.1 Zero-span Measurements

Zero-span measurements are performed at 2.45 GHz for the wire monopole and dielectric shielded whip antenna (Figures 98 and 102, respectively). Twenty captures are taken of the S21 using the VNA. The receive antenna is the ridged horn, positioned as in Figure

Figure 111: Setup of antenna under test (mounted on PVC stand) and second measurement antenna (patch taped to far wall on right edge of picture) for performing transmission measurements with forward directivity. The antennas are cross polarized with the wire grid.

112. The transmission with the wire monopole is -37.7 dB. The transmission with the whip antenna at 2.45 GHz is -41.7 dB. With the application of voltage to the HV plane, corona formation can be measured on the antennas. Measurements of the transmission show no significant change during active corona development. The difference between transmission at the highest voltage (120 kVAC) and the average baseline measurement is shown in Figures 113 and 114, respectively. Table 18 provides the mean and standard deviation of the measured transmission with and without corona (0 and 120 kVAC). No significant difference is observed in the transmission performance despite corona formation for these antennas.

Figure 112: Setup of antenna under test and second measurement antenna (ridged horn on floor) for performing transmission measurements with azimuthal directivity.

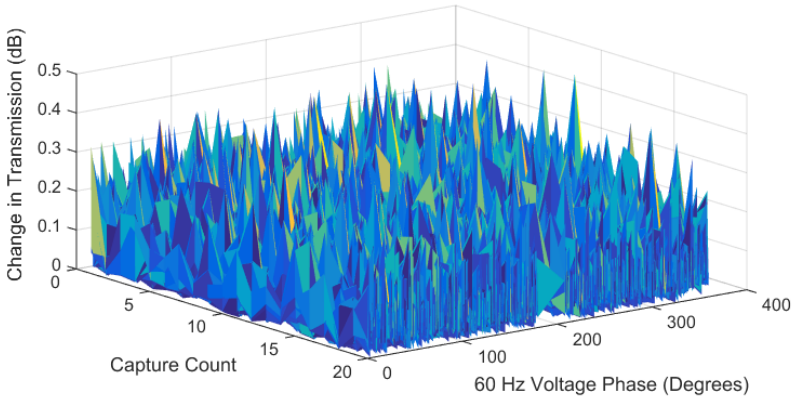

Figure 113: Change in transmission from 2.45 GHz wire monopole with corona formation, compared with baseline transmission. The monopole is 25 cm from a 120 kVAC plane.

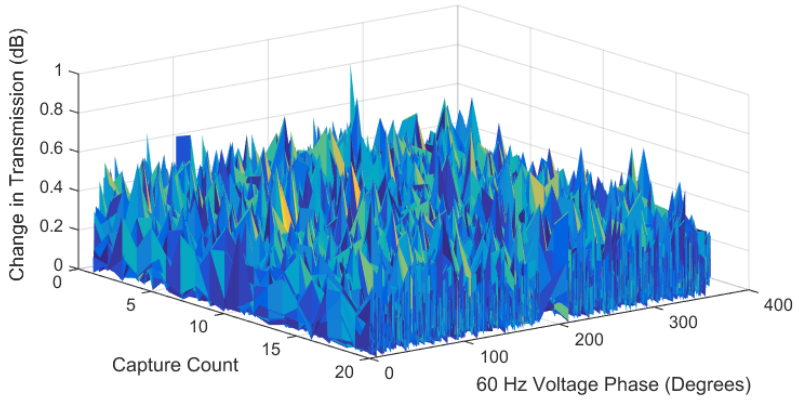

Figure 114: Change in transmission from 2.45 GHz dielectric shielded whip antenna with corona formation, compared with baseline transmission. The monopole is 25 cm from a 120 kVAC plane.

Table 18: Mean and standard deviation of measured transmission from antennas developing corona. The antennas are 25 cm from a plane at the specified voltage.

	Transmission Mean (dB)		**Transmission SD (dB)**	
Antenna	**0 kVAC**	**120 kVAC**	**0 kVAC**	**120 kVAC**
2.45 GHz Monopole	-37.701	-37.713	0.112	0.114
2.45 GHz Whip	-41.785	-41.704	0.1815	0.1810

6.3.2 Averaged Measurements

As with the impedance/return loss measurements, no significant variation is observed in the zero-span measurements. Time-averaged measurements of the antenna transmission are taken with the antennas 25 cm from the high voltage plane using the setup in Figure 50. The VNA IF bandwidth is set to 70 Hz and the measurement time for each frequency sample is 16.67 ms, or one period of the 60 Hz voltage. Several captures are taken for the baseline antenna measurement with no corona formation (0 kV), both before and after high-voltage runs. All measured results are provided in Appendix E.2. The ultimate result is that no variation in the transmission is observed that can be attributed directly to the corona. If corona attenuation is occurring, the impact is lower than the measurement sensitivity of the VNA, less than 0.1 dB. These effects are so small to have no appreciable impact on a

wireless communication link.

6.4 Channel Noise

Channel noise in measurements indicates the presence of RF interference stemming from corona formation. The full measurement results are provided in Appendices E.3-E.5. Measurements taken at 915 MHz, 2.45 GHz, and 5.8 GHz indicate a decrease in interference power with increasing frequency, which agrees with the theory presented in Section 4.3. The highest measured interference spectral power density was -130 dBm/Hz, which is 10 dB above the noise floor of the spectrum analyzer. A Zero-span measurement of the direct RF power coupled into the 915 MHz antenna during corona formation is shown in Figure 115.

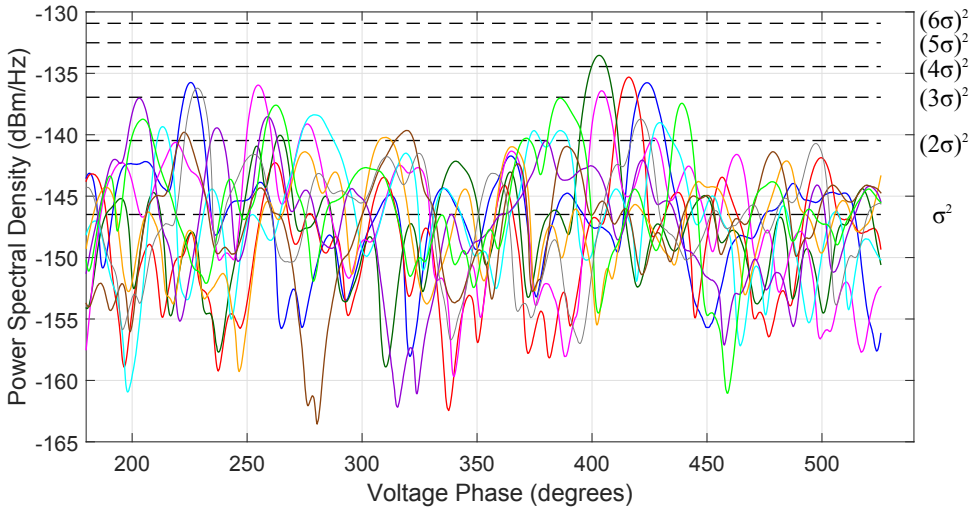

Figure 115: Zero-span measurement of the RF spectrum coupled into a 915 MHz monopole undergoing corona (positive glow and streamers, and negative Trichel pulses). The monopole at ground potential is 25 cm from the high-voltage plane at 110 kVAC. The IF bandwidth is set to 1 kHz and measurement is performed over one cycle of the 60 Hz voltage cycle. Ten separate captures are overlaid, shown with respect to the measurement instrument thermal AWGN floor, σ^2, and multiples of the AWGN standard deviation.

It is clear from the zero span measurement that corona interference is impulsive. Interference is measured at both the positive and negative cycle peak in individual randomly

distributed pulses. The voltage phase in the zero-span figures is specified such that the positive corona peak on the antenna occurs at 90^o (and its multiples of 360^o) and the negative corona peak on the antenna occurs at 270^o (and its multiples of 360^o). The large width of the pulses in the measurement is the result of the narrow IF bandwidth of 1 kHz, set to lower the noise floor in the measurement. Future measurements with a larger IF bandwidth and lower instrument noise figure could provide more detailed temporal interference statistics. The irregular distribution of the interference power peaks indicates the spectral density is the result of random impulses, which fits the behavior of streamer formation. Trichel pulses and positive glow are both regular and exhibit a low current less than a millamp. Streamers can carry significantly higher currents, reaching levels of amps. The irregular impulse formation of positive streamers fits Middleton's Class A noise model well.

One of the difficulties in the measurement process is that corona was found to be forming on the high-voltage measurement test set (transformer and high-voltage plane) itself. This makes it difficult to distinguish whether the measured spectrum is the result of corona formation on the HV plane or the antenna under test. The results in Appendix E.5 are obtained by measuring the radiated spectrum of the HV test set with no antenna present, measured with a broadband ridged-horn antenna. The results indicate the 915 MHz interference measured by the monopole could be radiation from the HV plane. In Figure 115, interference peaks are observed at both the negative and positive halves of the voltage phase. It is most likely that the peaks around 270^o are the result of radiation from positive streamers on the HV plane being received by the monopole, and the peaks around 450^o are the result of positive streamers on the monopole itself. No power is measured in the 2.45 and 5.8 GHz bands from the HV plane radiation.

Interference in the 2.45 and 5.8 GHz bands is measured, capturing each frequency bin over one 60 Hz voltage cycle, with an IF bandwidth of 1 kHz. The results, presented in detail in Appendix E.3, show a measurable power at 2.45 and 5.8 GHz in certain cases. The measurement results do not point to a consistent source for the RF power, and it is difficult to draw conclusions on this. The only case where any increase in RF power was measured in the 5.8 GHz band (-137 dBm/Hz, 3 dB above the noise floor at 110 kV,

Figure E.43) was for the dual-band whip antenna with the dielectric shielding. This points to the presence of dielectric, and potentially dielectric partial discharge, as the source for high frequency RF interference. No measurable power was present at 5.8 GHz with the dielectric removed. The same measurement at 2.45 GHz resulted in a higher measured power spectral density without the dielectric (-137 dBm/Hz with dielectric, -133 dBm/Hz without dielectric, Figures E.40 and E.41). While the dielectric and partial discharge may still play a role in RF interference, there is also a measurable spectral content at 2.45 GHz with streamer corona in air.

Protocols such as IEEE 802.15.4 typically utilize on the order of 1 MHz of channel bandwidth for communication. With measured spectral power densities ranging from -140 dBm/Hz to -130 dBm/Hz, one would be adding an additional -80 to -70 dBm of interference to the system SNR. In a high-voltage wireless sensing link, a transceiver positioned on the high-voltage power line acting as a receiver could be impacted by the additional interference power when receiving data. The remote transceiver with which the sensor communicates would be impacted to a lesser degree by corona interference. With corona originating on and around the high-voltage sensor, the interference power at the remote transceiver would be diminished by the same path loss as the sensor transmitted power, which is much greater than -60 dBm (typically 20 dBm). Therefore, there could be an asymmetry in the link budget for the two transceivers. The high-voltage sensor would be impacted much more heavily in received data.

Communication protocols such as those in 802.15.4 typically require two-way acknowledgement in order to communicate date in either direction. While the remote transceiver may be able to receive the sensor data with low bit error rate, the sensor may not be capable of receiving the acknowledgement data from the remote transceiver due to corona noise. Where it is critical to transmit data from the high-voltage sensor to a remote transceiver, it may be beneficial to implement a one-way communication link from the sensor to the remote transceiver. In this scenario, excess noise power at the sensor would not impair communication.

6.5 Recommendations

Based on the theoretical understanding of corona formation and the measurement results, several recommendations are presented for the design of wireless communication devices for high-voltage applications. The following may affect communication performance on the system, in order of highest to lowest level of impact:

Corona communication system impacts:

1. Low frequency corona current (*High*)
2. RF interference due to corona (*Medium*)
3. Antenna detuning due to plasma (*Low*)
4. Electromagnetic attenuation due to plasma (*Low*)

The low frequency corona current has the highest potential for negative impact on the communication system if not properly designed. RF interference, antenna detuning, and attenuation by the plasma are found to have a negligible impact on a communication system even in the presence of significant corona. In light of the effects of corona on the antenna and wireless communication system, several design recommendations can be put in place.

High-Voltage Wireless Communication System Design Recommendations:

1. Conducting enclosure around electronics to minimize internal fields from high-voltage gradients
2. Planar or receded antenna topology for prevention of corona formation on antenna
3. Avoid use of dielectric materials as a means of shielding from corona
4. Antenna with direct short to ground (PIFA, slot) or shorting stub following antenna
5. Common mode choke for reduction ground currents
6. BPF following antenna to reduce out-of-band interference, especially low frequency corona energy

7. Galvanic isolation of antenna from RF front end electronics

8. Differential RF signaling for interference rejection

9. TVS diode protection for transient suppression

10. For high-voltage sensing applications with bundled conductors, place antenna within bundle where fields are weakened

11. Use higher communication frequencies, because the spectral power of corona decreases with frequency

12. Implement multiple antennas for spatial diversity

Figure 116 provides a reference for a wireless RF high-voltage sensor. The individual sensor sections and recommendations are discussed in the following sections.

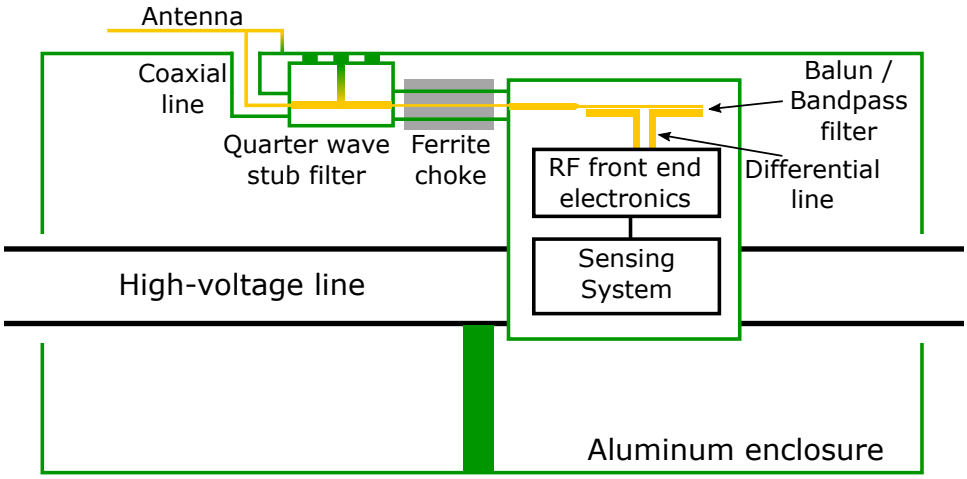

Figure 116: Reference design for a wireless RF high-voltage sensor. The green represents the sensor chassis ground, and the yellow represents the RF transmission line. At the antenna shorting stub and the quarter wave stub, the RF line is shown to be shorted to the chassis ground.

6.5.1 Wireless Sensor Enclosure

In high-voltage design, it is important, and already common practice, to enclose devices and sensors within a conducting case. Within the conducting enclosure, there exists a DC equipotential. With little to no electric fields inside the enclosure, the electronics are

safe from corona formation, and circuit design can be carried out as it would for typical non-high-voltage applications. The thickness of the conductive casing should be chosen to be greater than the skin depth of undesired interference. The skin depth, *delta*, marks the depth into a conductor at which an alternating signal current density has decreased to $1/e$ [100], given as (84).

$$\delta = \sqrt{\frac{2\rho}{\omega\mu}} \tag{84}$$

The quantity ρ is the resistivity of the conductor, ω is the angular frequency of the alternating current, and μ is the permeability of the conductor, all in standard SI units. The frequencies of concern for penetrating the conductive casing are those with short wavelengths, on the order of and smaller than the size of the casing. For wavelengths much longer than the size of the enclosure, the currents are approximately even over the enclosure body, approaching the DC equipotential with no interior fields. The skin depth of aluminum ($\rho = 26.5n\Omega \cdot m$) at 1 MHz ($\lambda = 300$ m) is 0.082 mm. An aluminum casing of just 1 mm thickness attenuates the signal power by over 100 dB. An inexpensive aluminum case with a thickness of 1 mm would suffice for high-voltage sensor applications. In addition, the sensor chassis should be electrically connected to the high-voltage line at a single point to prevent power flow through the sensor chassis instead of the high-voltage transmission line.

6.5.2 Antenna Topology

Following best practices in high-voltage design, hardware structures should minimize potential gradients to prevent corona formation. The probability of corona formation can be decreased by minimizing the peak potential gradient on the antenna. Wire antennas such as monopoles and whip antennas (commonly used in wireless networking applications) are characterized by a small effective radius, especially at the tip of the antenna. For this reason, wire antennas are not recommended for high-voltage applications due to the increased electric fields, and therefore increased likelihood of corona formation.

Low profile antennas provide the benefit of decreased potential gradients at the antenna surface by maintaining a small separation distance from a ground plane (sensor enclosure).

With a ground plane (the antenna ground being the chassis sensor potential) of a substantial radius of curvature, the electric fields at the antenna surface are reduced. Decreasing the electric fields significantly below the breakdown strength of air (3×10^8 m/s) minimized the probability of corona formation on the antenna. If the surface electric fields are near the ionization threshold, changes in environmental conditions, such as humidity and rain could incite corona formation [41].

6.5.3 Dielectric Shielding

Dielectrics such as PTFE have an increased dielectric constant, reducing the interior fields, as well as an increased dielectric strength, increasing the field necessary for dielectric breakdown. These two aspects combine to make dielectric shielding an attractive option for corona prevention. A dielectric covering could be placed over sharp edges and points where corona formation would occur if in an air medium. In theory, this solution will work, and can be implemented. However, in high-voltage applications, it is important that hardware have a high longevity, even when exposed to harsh and varied climate conditions. In real applications, air pockets in the material from production, weathering of the surface, or formation of cracks through thermal expansion could all lead to the formation of partial discharges [14],[73]. Partial discharges in the dielectric can further degrade the shielding, potentially causing a complete failure exposing the conductor to air and corona formation.

The preceding case refers specifically to antennas that may have a dielectric shielding applied directly to the conductor surface. Antennas with a dielectric cover that does not adhere directly to the surface can form corona in the space between the antenna conductor. The experiments show that corona formation in a short gap between the antenna conductor and dielectric exhibit higher currents than corona formation with no dielectric cover. Charge accumulation on the dielectric surface results in breakdowns characterized by short pulses of high current. Measurements of the RF spectrum on antennas with a dielectric coating resulted in a measurable spectral power above the instrumentation noise floor. While the power was low, the measurements showed that breakdowns the the addition of a dielectric barrier may degrade RF interference performance. Antenna designs should avoid dielectric

barriers as a means for insulating the antenna from corona formation.

6.5.4 Antenna Grounding

Corona formation can be characterized as a high-impedance current source. Corona formation on an antenna sinks charge onto the antenna. An increase in charge on the antenna element will increase the potential difference between the antenna and chassis (high-voltage sensor) ground. If the antenna is not electrically connected to the chassis ground, potential buildup between the antenna and chassis ground could damage RF front end components sensitive to large DC potentials. Utilizing an antenna whose feed element is electrically connected to ground provides a low-impedance path for charge accumulated through corona formation. Reciprocal antennas, such as slots, and antennas with shorting pins or stubs, such as a PIFA, provide good options. The PIFA and derivative antenna designs are especially attractive as they radiate in a half space above a ground plane, allowing for easy implementation onto the exterior surface of a conducting enclosure.

The spectral content of the corona current largely falls below 100 MHz, significantly lower than the 915 MHz, 2.45 GHz, and 5.8 GHz bands of interest. Utilizing a ground shorted antenna element also provides filtering for the low frequency currents. If corona formation occurs on a PIFA element for instance, low-frequency power is largely shunted to the chassis ground plane and does not propagate into the sensor chassis interior. This minimizes the risk of low-frequency interference leaking into the interior electronics.

If a grounded antenna topology such as a slot or PIFA is not a feasible solution, the antenna element can be grounded be means of a shorted quarter-wave stub filter. A shorted quarter-wave stub filter can be implemented immediately behind the antenna, shorting the antenna element to ground and filtering out low frequency RF. Both the PIFA shorting plate and basic quarter-wave stub filter provide 20 dB/decade of low-pass filtering. The advantage of utilizing the shorted antenna is that the low-frequency currents are maintained on the outside of the chassis. Otherwise, with an improperly designed transmission line or antenna feed interface, some radiation of the low-frequency power could result, interfering with the internal electronics. If this is observed to be an issue with a PCB stub filter, a

coaxially-packaged quarter wave stub filter can be utilized. Whether using a shorted PIFA or a quarter-wave stub, the shorting element should be able to handle currents much larger than measured corona current. It would be recommended that the shorting element be capable of sinking several Amps of current without potentially damaging thermal stress.

6.5.5 Common-Mode Choke

When designing robust electronics, it is important to prevent interference resulting from common-mode interference [17]. Various solutions exist for common-mode reduction in transmission lines. For coaxial cables, snap-on ferrite chokes provide a simple means for common-mode reduction. While corona currents on a well-grounded enclosure should not leak significantly into the sensor module, it is good engineering practice to implement common mode chokes where current flow on the transmission line shielding may occur.

6.5.6 Band-Pass Filtering

A crucial portion of any wireless design is the band-pass filter to minimize noise and interference entering the RF front end. With a well-implemented grounded antenna element or quarter-wave stub, the band-pass filter should not have to handle significant powers at low frequencies. At RF and microwave frequencies, it may be implemented simple using transmission line filter design techniques [82].

6.5.7 Differential Signaling

Differential signaling is another common practice for robust communication systems [17]. Utilizing a differential transmission line as opposed to a single-ended line decreases interference through electromagnetic coupling. Coupled power into the lines acts a common-mode signal that can be filtered out.

A balun is used to convert a single-ended transmission line to a differential line. The balun and band-pass filter can be implemented in a single passive microstrip circuit. In addition, many balun designs, such as the classic Marchand balun, provide galvanic isolation of the feed to the output. This acts as another level of protection for the RF front end from the low-frequency corona currents.

6.5.8 TVS Diode Protection

In the event of large transients on the front end, TVS diode (power limiter) protection can be implemented as a last-resort level of protection. The capacitance of the TVS diode must be sufficiently small to operate at the RF communication frequency. The TVS diode should be placed between the front end electronics and the band-pass filter to minimize the out-of-band power the TVS diode is exposed to. The TVS diode provides non-linear protection of the electronics by clipping excess power at the expense of signal degradation. The TVS diode should act as a final stage of protection, the linear filtering components being the primary form of corona protection. This diode should only be activated in the case of system failure. The voltages present under normal operating conditions should be well below the diode's forward bias voltage to assure operation free from distortions.

6.5.9 Transmission Timing

Certain applications of wireless sensing, such as for fault detection, require constant updating. For some applications, such as for temperature or tension monitoring, data updates are not time critical. While corona is not measured to have a significant effect on RF communication, a further step may be taken to ensure successful data transmission. Corona formation increases with increasing voltage. Data may be transmitted and received around the 0 V points of the voltage cycle when corona formation is at a minimum. This will reduce any local corona effects on the antenna such as corona current on the antenna. However, in a three-phase system, any corona RF radiation from the remaining two phases can still impact the communication system. Based on the measured results and previous knowledge, the RF radiation power from corona is not a significant contributor to communication interference, especially at 2.45 and 5.8 GHz.

6.5.10 Frequency Selection

Because the most significant issue corona poses to RF front end design is low-frequency corona current (<100 MHz), higher communication frequencies offer increased immunity to corona interference, which decreases with frequency.

6.5.11 Spatial Diversity

The coverage area and reliability of a wireless sensor can be improved by implementing multiple independent antennas (non-arrayed). Implementing two or more antennas provides spatial diversity, improving robustness against small-signal fading due to multipath reflections. Since planar antennas over a ground plane radiate well in a half-space, positioning antennas on opposing sides of the sensor would also improve wireless coverage. In addition, multiple antennas provide redundant backups, improving the longevity of the sensor.

6.5.12 Prototype Antenna Implementation

Presented here is a prototype antenna implementation for a high-voltage sensor. The tubular sensor shape is based on a prototype of a Smart Wires sensor developed by Kreikebaum et. al. [54]. The lack of sharp protruding corners minimizes the likelihood of corona formation. Figure 117 illustrates the prototype antenna implementation. A planar PIFA antenna is implemented on a PTFE substrate with permittivity of 2.1. The choice of substrate for such an antenna must take into account environmental conditions. PTFE provides low moisture absorption, as well as a high dielectric strength.

The PIFA was tuned to 2.45 GHz in the prototype implementation. The radiation pattern (gain) of the antenna mounted on the sensor shows good coverage in the half-space above the antenna ground plane, with gain greater than 1 dBi (Figure 118). To improve the coverage as well as spatial diversity of the communication link, two or more antennas can be mounted on the sensor in opposing positions.

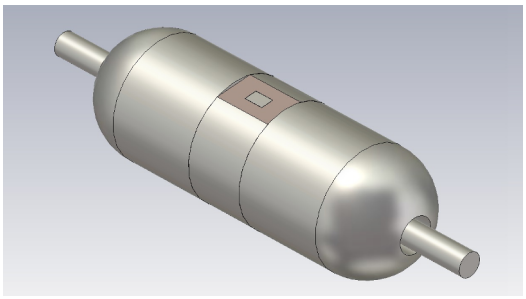

(a) High-voltage sensor module

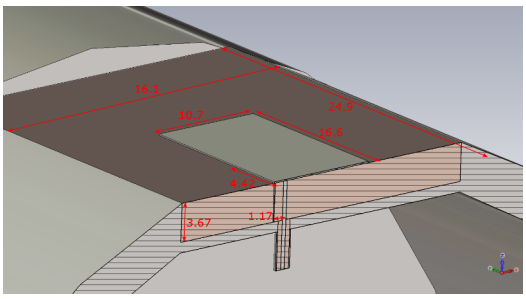

(b) Antenna dimensions (units of mm)

Figure 117: Prototype implementation of an antenna on a high-voltage sensor module. The low form factor of the antenna aids in preventing corona, while the shorting stub of the PIFA shunts low-frequency corona currents to the sensor chassis. The antenna dimensions are provided in mm, and the PTFE substrate permittivity is 2.1.

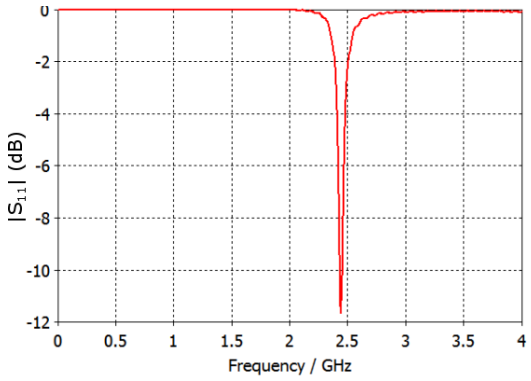

(a) Antenna $|S_{11}|s$

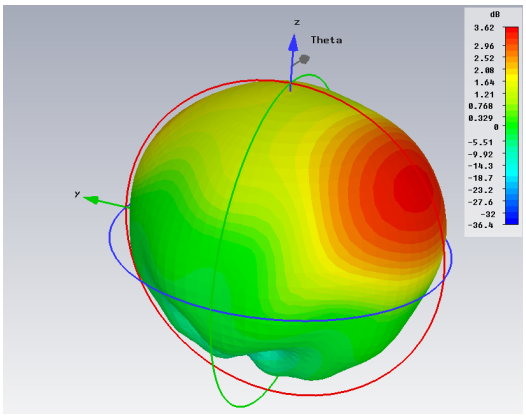

(b) Antenna gain

Figure 118: Return loss and gain of the prototype PIFA implementation on a high-voltage sensor module.

6.6 Conclusions

A study on the wireless communication impact of high-voltage corona formation on an antenna has been carried out. Supported by a theoretical basis, the experimental results show no measurable effect of the corona on antenna impedance or electromagnetic attenuation. While corona formation on the antenna can occur, a number of factors limit the electromagnetic effects on the antenna. First, the electron densities of corona fall below 10^{19} m^{-3} for positive glow and negative Trichel pulses, and 10^{20} m^{-3} for positive streamers. Based on the Drude model for non-thermal plasma, the attenuation of waves by the plasma, and

change in index of refraction do not significantly affect propagation at electron densities below 10^{19} m^{-3}. Second, corona formation is a local process. Corona forms at points or edges where potential gradients may be higher than the ionization threshold of air. With corona formation at a point on an antenna, the electromagnetic interaction of the small plasma volume with the electrically larger antenna is insignificant.

RF interference of corona has been measured. For most cases, RF interference power fell below the noise floor of the measurement instrumentation. This agrees with corona formation theory and previously published work indicating that significant corona interference falls below 100 MHz. At 915 MHz, a peak noise power was measured at -130 dBm/Hz, 10 dB above the instrument noise floor. The noise was correlated in time with the positive and negative voltage peaks of the 60 Hz cycle, and appear as impulse peaks in zero-span measurements. When including interference from corona in channel simulation, rather than treating it as white noise, corona should be treated with an impulsive noise model such as Middleton's Class A noise model.

A set of recommendations were formulated for construction of high frequency antennas and front-ends based on the measurement and theory behind corona formation. Firstly, antenna design should conform to power engineering standards on corona formation, avoiding sharp corners and edges where enhanced potential gradients can lead to corona formation. The foremost source of communication interference in the event of corona formation on the antenna is low-frequency corona current coupling into the RF front end. To avoid distortions due to non-linearities caused by high amplitude of low frequency components, design recommendations are proposed for the filtering and shielding to be implemented in a high-voltage wireless sensor design.

6.7 Future Work

This research lays the foundation for corona research as it affects RF communications. On its own, this work provides high-voltage wireless sensor designers the information they need to create reliable devices, but it also opens the door to further exploration. Future research that can expand upon this work includes:

- Measurements of the antenna impedance and gain, as well as RF interference levels, with an antenna mounted on a high-voltage transmission line. While no significant deviations are predicted between the results in this work and on-line measurements, it is important to test the theories in a practical implementation prior to developing commercial sensors for use in smart grid applications.

- An detailed study of the RF interference levels of corona. In this work, the RF interference was observed and quantified, but difficulties in performing the measurement have left some questions unanswered. Measurable RF interference was produced by corona on the high-voltage plane and transformer without the antenna-under-test present. This resulted in an ambiguity in the source of measured interference during direct spectrum measurements (i.e. whether the measured interference source is from corona on the antenna-under-test or from the HV plane). Also, by performing averaged measurements of a large number of data captures, more accurate statistical models could be developed for RF interference over an AC voltage cycle. This would be particularly useful in distinguishing the interference characteristics of positive and negative corona.

- High temporal resolution measurements of corona current impulses. Using a high sampling rate oscilloscope and high-bandwidth current probe, more accurate measurements of the positive streamer and negative Trichel pulse current could be taken. More precise measurements of corona current would allow for improved specification of filters. In addition, more precise RF interference models could be created using the statistical time distribution and amplitude of current pulses over the course of an AC voltage cycle.

- Bit error rate analysis of various modulation schemes using Middleton's noise model and the statistical distribution of corona current pulses. From such an analysis, the effectiveness of various coding techniques in the presence of corona interference could be determined.

APPENDIX A

IONIZATION AND ATTACHMENT COEFFICIENTS FOR DRY AIR

A.1 Ionization and Attachment Coefficients

The ionization and attachment coefficients, α and η, respectively, relate the number of electrons released and absorbed per unit distance under an applied electric field. These coefficients have been measured empirically for air by a number of authors. Davies provides a comparison of the measured results for the net ionization coefficient $\alpha - \eta$ in Figure A.1.

The ionization and attachment coefficient from Davies is tabulated in Table A.1. According to Davies, for fields greater than 4×10^6 V/m, the attachment coefficient could not be measured independently and the net ionization coefficient can be approximated to be equal to the ionization coefficient. For electric fields less than 1.9×10^6 V/m, no positive ions are detected and the ionization coefficient goes to zero.

Table A.1: Ionization and attachment coefficients for dry air at atmospheric pressure ($N_0 = 2.688 \times 10^{25} m^{-3}$) measured by Davies [27].

Electric Field (10^4 V/m)	**Ionization Coeff. (10^2 1/m)**	**Electric Field (10^4 V/m)**	**Attachment Coeff. (1/m)**
215	1.59	161.3	185.5
241.9	3.39	188.2	344.1
302.4	11.29	215	467.7
336	17.74	241.9	583.3
369.6	26.88	302.4	634.4
403	39.24	336	478.5
470	72.58	369.6	338.7
538	123.65	403	233.9
605	196.22		
672	274.18		
739	344.06		
806	456.96		

For large electric fields ($11.4 < E < 45.6$ V/m), the ionization coefficient can be approximated by (A.1). In air at atmospheric pressure, the coefficients are given by $A = 1.11 \times 10^6$ ionizations/m and $B = 2.77 \times 10^7$ V/m, with the electric field in units of V/m [86].

$$\alpha = Ae^{-B/E} \tag{A.1}$$

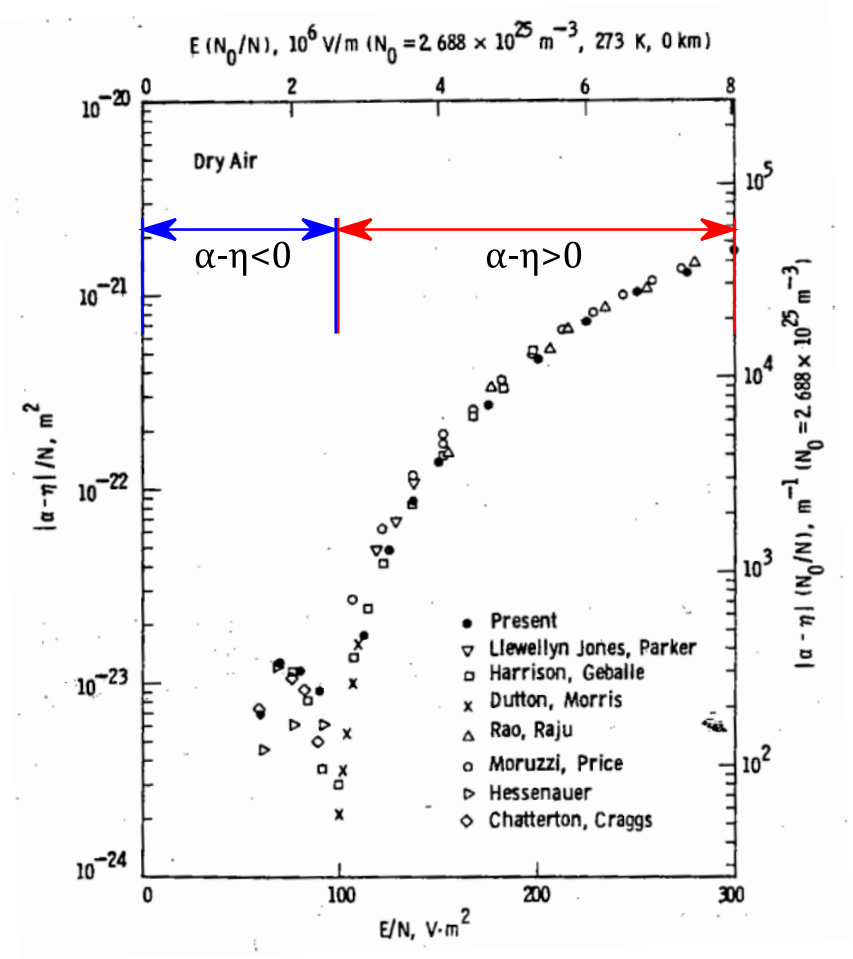

Figure A.1: Net ionization coefficient in air as a function of electric field magnitude. Davies compares the results of several researchers to the currently measured results [27].

Combining the data in Table A.1 and (A.1), the ionization coefficient for air at atmospheric pressure can be expressed by a curve fit (A.2).

$$\alpha = e^{-9.069\times10^5 E^{-0.7867}+14.14} \tag{A.2}$$

A.2 Ionization and Attachment Rates

The ionization and attachment rates, ν_i and ν_a, respectively, relate the number of electrons released and absorbed per second under an applied electric field. The data from Davies in Table A.2 extends up to for the ionization rate 8.06×10^6 V/m. According to Davies, for fields greater than 4×10^6 V/m, the attachment rate could not be measured independently

and the net ionization coefficient can be approximated to be equal to the ionization rate. For electric fields less than 1.9×10^6 V/m, no positive ions are detected and the ionization rate goes to zero.

Table A.2: Ionization and attachment rates for dry air at atmospheric pressure ($N_0 = 2.688 \times 10^{25} m^{-3}$) measured by Davies [27].

Electric Field (10^4 V/m)	**Ionization Rate (10^7 1/s)**	**Electric Field (10^4 V/m)**	**Attachment Rate (10^7 1/s)**
215	1.53	161.3	1.37
241.9	3.7	188.2	2.9
302.4	15.1	215	4.5
336	26	241.9	6.4
369.6	42	302.4	8.5
403	66	336	7.0
470	148	369.6	5.3
538	271	403	3.9
605	465		
672	690		
739	940		
806	1350		

For fields greater than 10^7 V/m, curve fit data is taken from from Zhang and Adamiak [101]. The polynomial curve is given by (A.3). The electric field E is in V/m and the ionization rate is in units of 1/s.

$$\nu_i = -3.4664 \times 10^9 + 5.4197 \times 10^7 EN + 1.81857 \times 10^5 EN^2 \tag{A.3}$$

$$EN = E \times 4.065 \times 10^{-5}$$

Combining the data from Davies and Zhang with a curve fit, an expression for tie ionization rate is given by (

$$\nu_i = e^{-1.054 \times 10^4 E^{-0.4527} + 31.07} \tag{A.4}$$

APPENDIX B

MAXWELL'S EQUATIONS

Table B.1: Maxwell's Equations

Name	Differential Form	Integral Form
Gauss' law for electricity	$\nabla \cdot \mathbf{E} = \frac{\rho}{\varepsilon_0}$	$\oint \mathbf{E} \cdot \mathrm{d}\mathbf{S} = \frac{1}{\varepsilon_0} \int \rho \, \mathrm{d}V$
Gauss' law for magnetism	$\nabla \cdot \mathbf{B} = 0$	$\oint \mathbf{B} \cdot \mathrm{d}\mathbf{S} = 0$
Faraday's law	$\nabla \times \mathbf{E} = -\frac{\partial \mathbf{B}}{\partial t}$	$\oint \mathbf{E} \cdot \mathrm{d}l = -\frac{d}{dt} \int \mathbf{B} \cdot \mathrm{d}\mathbf{S}$
Ampere's law	$\nabla \times \mathbf{B} = \mu_0 \left(\mathbf{J} + \varepsilon_0 \frac{\partial \mathbf{E}}{\partial t} \right)$	$\oint \mathbf{B} \cdot \mathrm{d}l = \mu_0 \int \mathbf{J} \cdot \mathrm{d}\mathbf{S} + \mu_0 \varepsilon_0 \frac{d}{dt} \int \mathbf{E} \cdot \mathrm{d}\mathbf{S}$

APPENDIX C

ANTENNA FAR FIELD PROPAGATION

Maxwell's equations (Table B.1) in the absence of charge can be simplified to (C.1).

$$\begin{aligned}\left(c^2\nabla^2 - \frac{\partial^2}{\partial t^2}\right)\mathbf{E} = 0 \\ \left(c^2\nabla^2 - \frac{\partial^2}{\partial t^2}\right)\mathbf{B} = 0\end{aligned} \tag{C.1}$$

By definition, the far field By making some reasonable assumptions for the character of the radiation from an antenna, the character of the radiation can be determined. It is assumed that the distance from the antenna to the point at which the fields are being measured is much greater than a wavelength and much greater than the largest dimension of the antenna. Geometrically, this implies that if one were to partition the currents on the antenna into electrically small moments (much smaller than a wavelength), the wave vectors of the radiated fields at the distance are approximately parallel. The interference of the radiated fields from all the current moments does not vary with an increase in distance. The radiation is considered to propagate away from the antenna as a spherical wave front centered at the phase center of the antenna. The phase center is assumed to be a single point, commonly chosen as the geometrical center of the antenna, from which the electromagnetic fields propagate spherically. This assumption is valid given the restrictions made on the chosen dimensions.

To evaluate the spreading of the electromagnetic fields away from the antenna at a distance, or in the far field, one can find a solution for the wave equation in spherical coordinates. Since the partial differential equations (PDE) for the electric and magnetic field are equivalent, the solution will be found for one case and applied to the other. The Laplacian (∇^2) operator in spherical coordinates is given by (C.2).

$$\nabla^2 = \frac{1}{r^2}\frac{\partial}{\partial r}\left(r^2\frac{\partial}{\partial r}\right) + \frac{1}{r^2\sin\theta}\frac{\partial}{\partial\theta}\left(\sin\theta\frac{\partial}{\partial\theta}\right) + \frac{1}{r^2\sin\theta}\frac{\partial^2}{\partial\phi^2} \tag{C.2}$$

The assumptions of a wave front propagating spherically away from the antenna (point) imply that the wave vectors are oriented in the $\hat{\boldsymbol{r}}$ direction, and consequently the $\mathbf{E}$ and $\mathbf{B}$ fields must be oriented in the $\hat{\boldsymbol{\theta}}$ and $\hat{\boldsymbol{\phi}}$ directions. The fields themselves my vary with distance from the antenna r, θ, ϕ, and t. Therefore the electric field $\mathbf{E}$ may be given as a function (

$$\mathbf{E} = f\left(r,\theta,\phi,t\right)\hat{\boldsymbol{\theta}} + g\left(r,\theta,\phi,t\right)\hat{\boldsymbol{\phi}} \tag{C.3}$$

Combining (C.1) and (C.2) one obtains the PDE for spherical coordinates (C.4)

$$\frac{c^2}{r^2}\frac{\partial}{\partial r}\left(r^2\frac{\partial \mathbf{E}}{\partial r}\right) + \frac{c^2}{r^2\sin\theta}\frac{\partial}{\partial\theta}\left(\sin\theta\frac{\partial \mathbf{E}}{\partial\theta}\right) + \frac{c^2}{r^2\sin\theta}\frac{\partial^2\mathbf{E}}{\partial\phi^2} - \frac{\partial^2\mathbf{E}}{\partial t^2} = 0 \tag{C.4}$$

(C.3) can be inserted into (C.4) to obtain (C.5). It is evident from (C.5) that the solution for the $\hat{\boldsymbol{\phi}}$ fields are independent of $\hat{\boldsymbol{\theta}}$ fields, but otherwise share a common form. Therefore, only one coordinate direction must be considered, and the other solution for the other coordinate direction can be added back in at the end.

$$\begin{aligned}
&\frac{c^2}{r^2}\frac{\partial}{\partial r}\left(r^2\frac{\partial f\left(r,\theta,\phi,t\right)}{\partial r}\right)\hat{\boldsymbol{\theta}} + \frac{c^2}{r^2\sin\theta}\frac{\partial}{\partial\theta}\left(\sin\theta\frac{\partial f\left(r,\theta,\phi,t\right)}{\partial\theta}\right)\hat{\boldsymbol{\theta}} + \\
&\qquad \frac{c^2}{r^2\sin\theta}\frac{\partial^2 f\left(r,\theta,\phi,t\right)}{\partial\phi^2}\hat{\boldsymbol{\theta}} - \frac{\partial^2 f\left(r,\theta,\phi,t\right)}{\partial t^2}\hat{\boldsymbol{\theta}} + \\
&\frac{c^2}{r^2}\frac{\partial}{\partial r}\left(r^2\frac{\partial g\left(r,\theta,\phi,t\right)}{\partial r}\right)\hat{\boldsymbol{\phi}} + \frac{c^2}{r^2\sin\theta}\frac{\partial}{\partial\theta}\left(\sin\theta\frac{\partial g\left(r,\theta,\phi,t\right)}{\partial\theta}\right)\hat{\boldsymbol{\phi}} + \\
&\qquad \frac{c^2}{r^2\sin\theta}\frac{\partial^2 g\left(r,\theta,\phi,t\right)}{\partial\phi^2}\hat{\boldsymbol{\phi}} - \frac{\partial^2 g\left(r,\theta,\phi,t\right)\hat{\boldsymbol{\theta}}}{\partial t^2}\hat{\boldsymbol{\phi}} = 0
\end{aligned} \tag{C.5}$$

Considering only the $\hat{\boldsymbol{\theta}}$ fields, one can solve the PDEs in (C.5) by guessing the form of the solution through consideration of the physical behavior of propagation. The PDE states that the Laplacian and second time derivative terms be equal. This limits the solutions to ones with a symmetry between the time and space variables. Knowledge of wave propagation suggests the oscillatory form for the solution of (C.6). As explained above the waves propagate in the radial direction so the r spatial direction is used. The solution of inward propagating waves, with the sign of kr flipped to +, is also a valid solution but

can be discarded following the reasoning of causality, that the wave at a distance from the antenna is only measured after it occurs at the antenna.

$$\mathbf{E} \sim E_0 e^{j(\omega t - kr)} \tag{C.6}$$

The second derivative in the r direction involves r terms that break the symmetry between the spatial and time derivatives. The solution is scaled by an r term to account for this effect. In this case, the solution is simply scaled by $1/r$ (C.7). Because the only source is assumed to be a point at the center of the spherical wave front, variations in the field in the angular directions are considered to be constant with radial distance. Therefore, variations in the fields with angle only add a scaling term to the solution. The variation in the fields with azimuth and elevation is specified by the arbitrary functions $f_\theta(\theta)$ and $f_\phi(\phi)$.

$$\mathbf{E} = \frac{E_0}{r} f_\theta(\theta) f_\phi(\phi) e^{j(\omega t - kr)} \tag{C.7}$$

The solution (C.7) is run through the PDE (C.5) to check for validity.

The radial derivative term in (C.5) evaluates to (C.8).

$$\frac{c^2}{r^2}\frac{\partial}{\partial r}\left(r^2 \frac{\partial f\left(r,\theta,\phi,t\right)}{\partial r}\right) = -\frac{c^2 k^2 E_0}{r} f_\theta(\theta) f_\phi(\phi) e^{j(\omega t - kr)} \tag{C.8}$$

The elevation derivative term in (C.5) evaluates to (C.9).

$$\frac{c^2}{r^2 \sin\theta}\frac{\partial}{\partial \theta}\left(\sin\theta \frac{\partial f\left(r,\theta,\phi,t\right)}{\partial \theta}\right) = \frac{E_0}{r^3}\frac{d^2 f_\theta(\theta)}{d\theta^2} f_\phi(\phi) e^{j(\omega t - kr)} + \frac{E_0}{r^3 \tan\theta}\frac{d f_\theta(\theta)}{d\theta} f_\phi(\phi) e^{j(\omega t - kr)} \tag{C.9}$$

The azimuth derivative term in (C.5) evaluates to (C.10).

$$\frac{c^2}{r^2 \sin\theta}\frac{\partial^2 f\left(r,\theta,\phi,t\right)}{\partial \phi^2}\hat{\boldsymbol{\theta}} = \frac{E_0}{r^3 \sin\theta} f_\theta(\theta)\frac{d^2 f_\phi(\phi)}{d\phi^2} e^{j(\omega t - kr)} \tag{C.10}$$

The time derivative term in (C.5) evaluates to

$$\frac{\partial^2 f\left(r,\theta,\phi,t\right)}{\partial t^2}\hat{\boldsymbol{\theta}} = -\frac{\omega^2 E_0}{r} f_\theta(\theta) f_\phi(\phi) e^{j(\omega t - kr)} \tag{C.11}$$

Combining equations (C.8)-(C.11), considering only the azimuth oriented fields currently, one obtains (C.12).

$$-\frac{c^2k^2E_0}{r}f_\theta(\theta)f_\phi(\phi)e^{j(\omega t-kr)}+\frac{\omega^2E_0}{r}f_\theta(\theta)f_\phi(\phi)e^{j(\omega t-kr)}+$$
$$\frac{E_0}{r^3}\frac{d^2f_\theta(\theta)}{d\theta^2}f_\phi(\phi)e^{j(\omega t-kr)}+\frac{E_0}{r^3\tan\theta}\frac{df_\theta(\theta)}{d\theta}f_\phi(\phi)e^{j(\omega t-kr)}+\frac{E_0}{r^3\sin\theta}f_\theta(\theta)\frac{d^2f_\phi(\phi)}{d\phi^2}e^{j(\omega t-kr)}=0 \tag{C.12}$$

The PDE of the guessed solution for $\boldsymbol{E}$ results in two types of terms, ones that fall off as $1/r$ and ones that fall off as $1/r^3$. For large distances $r >> 0$, the PDE expression is dominated by the $1/r$ terms as the $1/r^3$ terms go to 0. Ignoring the higher order terms for large distances, the expression can be written more succinctly as (C.13). From (C.13), one obtains the relationship between wave number and angular frequency (C.14), which is the condition for the validity of the solution (C.7).

$$\frac{c^2k^2E_0}{r}f_\theta(\theta)f_\phi(\phi)e^{j(\omega t-kr)}=\frac{\omega^2E_0}{r}f_\theta(\theta)f_\phi(\phi)e^{j(\omega t-kr)} \tag{C.13}$$

$$c^2k^2=\omega^2 \tag{C.14}$$

Using (C.7), the solution for the electric far fields from a radiating antenna are given by (C.15). The magnetic far fields have the same form as the electric fields, and can be related by (C.16). In these solutions, since the fields are radiating away from the antenna, the wave vector points in the radial direction ($\hat{\boldsymbol{k}}=\hat{\boldsymbol{r}}$).

$$\mathbf{E}=\frac{E_0}{r}f(\theta,\phi)e^{j\left(\omega t-\frac{\omega}{c}r\right)}\hat{\boldsymbol{\theta}}+\frac{E_0}{r}g(\theta,\phi)e^{j\left(\omega t-\frac{\omega}{c}r\right)}\hat{\boldsymbol{\phi}} \tag{C.15}$$

$$\boldsymbol{B}=\frac{1}{c}\hat{\boldsymbol{r}}\times\boldsymbol{E} \tag{C.16}$$

APPENDIX D

DRUDE MODEL DERIVATION

The Drude model is a complex dielectric model for metals or cold plasma, consisting of a free electron density. Since the ions are much more massive than the electrons, they do not contribute significantly to the interaction of the plasma with an incident electromagnetic wave. To determine the effective dielectric constant of the plasma, consider first a plane wave with electric field **E** in a uniform plasma. The force on an electron in the plasma due to the electric field of the plane wave is given by (D.1). Here, F_e is the force on the electron in N, m_e is the electron mass in kg, x_e is the electron position, e is the fundamental charge, and ν is the collision frequency of electrons with gas molecules in Hz. This last term in the equation is a collisional damping term due to collisions. At low gas densities, such as in the ionosphere, the plasma behaves differently than a plasma at the surface of the Earth because of the electron collisions in a denser gas.

$$\mathbf{F}_e = m_e \ddot{x}_e = -e\mathbf{E} - \nu m_e \dot{x} \tag{D.1}$$

The electric field at a cross section of the uniform medium can be defined as a harmonic wave by (D.2). Substituting into (D.1), one obtains (D.3). Without loss of generality here, the plane wave field **E** is assumed to be linearly polarized, and the electric field component E is taken in the direction of polarization.

$$E = E_0 e^{j\omega t} \tag{D.2}$$

$$F_e = m_e \ddot{x}_e = -eE_0 e^{j\omega t} - \nu m_e \dot{x} \tag{D.3}$$

Utilizing the time harmonic definition of the time derivative $d/dt = j\omega$, the equation becomes (D.4). Solving for the displacement x, the result is (D.5). The first time derivative

of the displacement is (D.6), obtained by plugging (D.2) into (D.5) and deriving.

$$m_e (j\omega)^2 x = -eE - \nu m_e (j\omega) x \tag{D.4}$$

$$x = \frac{eE}{m_e \omega (\omega - j\nu)} \tag{D.5}$$

$$\dot{x} = -\frac{eE}{m_e (\nu + j\omega)} \tag{D.6}$$

The volume current density in the plasma resulting form the electric field (in the direction of the electric field) is given by (D.7). J is the current density in A/m^2 and n_e is the electron density in m^{-3}. The current is simply the flow of the electrons defined by their velocity $\dot{x}$. The current density is also equivalent to the conductivity pf the medium σ multiplied by the electric field. Conductivity has units of S/m. Substitution of (D.6) into (D.7) and solving for σ results in (D.8).

$$J = -n_e e \dot{x} = \sigma E \tag{D.7}$$

$$\sigma = \frac{n_e e^2}{m_e (\nu + j\omega)} \tag{D.8}$$

Having derived the conductivity, an electrical property of a material, from the basic kinematic equations for an electron in the plasma, there is just one more step to be taken. The electrical conductivity can be reformulated as a complex permittivity. The complex permittivity is related to the conductivity by (D.9). ε_r' is the real relative permittivity of the dielectric (1 for air). Inserting (D.8) into (D.9) yields an expression for the complex permittivity in terms of fundamental parameters and the collision frequency (D.10).

$$\varepsilon_r = \varepsilon_r' - j\frac{\sigma}{\varepsilon_0 \omega} \tag{D.9}$$

$$\varepsilon_r = \varepsilon_r' - \frac{n_e e^2}{m_e \varepsilon_0} \frac{1}{\omega (\nu + j\omega)} \tag{D.10}$$

It can be seen in (D.10) that several terms including the electron density can be grouped together into a term known as the plasma frequency. The plasma frequency, the natural frequency at which a mass of electrons oscillates, is a fundamental plasma parameter defined as (D.11). With this final simplification, the complex permittivity of the cold plasma of free electrons is (D.12). Sometimes the relative dielectric constant ε_r' is written as ε_∞, simply indicating that this quantity represents the relative permittivity of the plasma as the wave frequency tends to infinity. This complex dielectric model for metals and cold plasma is commonly known as the *Drude model*.

$$\omega_p = \sqrt{\frac{n_e e^2}{\varepsilon_0 m_e}} \tag{D.11}$$

$$\varepsilon_r = \varepsilon_r' - \frac{\omega_p^2}{\omega\left(\omega - j\nu\right)} \tag{D.12}$$

APPENDIX E

MEASUREMENTS RESULTS

E.1 Return Loss

These measurements of the antenna return loss were taken with the antennas 25 cm from the high voltage plane using the setup in Figure 50. The VNA IF bandwidth is set to 70 Hz and the measurement time for each frequency sample is 16.67 ms, or one period of the 60 Hz voltage. Several captures are taken for the baseline antenna measurement with no corona formation (0 kV), both before and after high-voltage runs.

E.1.1 915 MHz Antennas

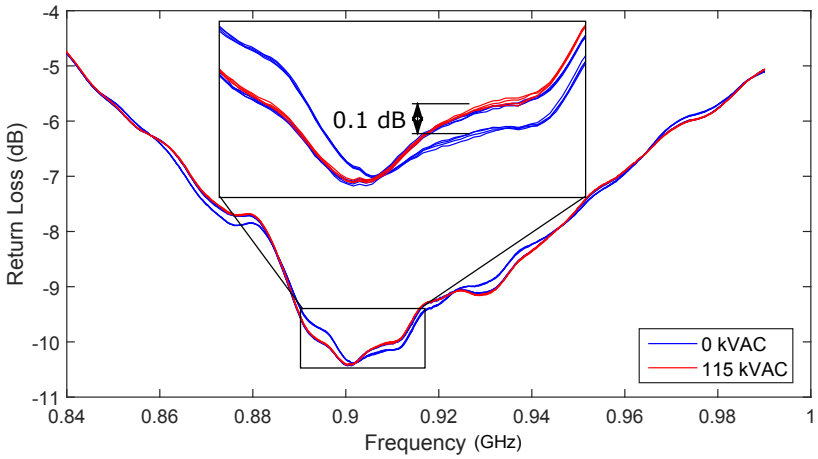

Figure E.1: 915 MHz wire monopole.

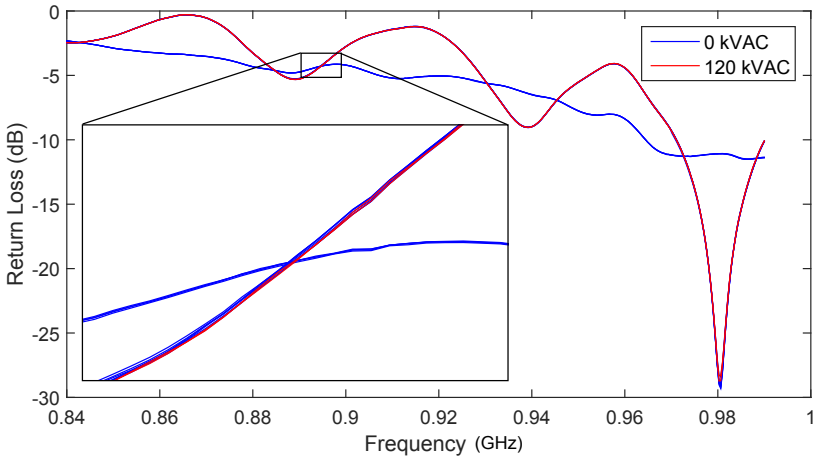

Figure E.2: 915 MHz printed meandered dipole, first attempt. The VNA calibration was affected during measurement, obviated by the large change in baseline 0 kV measurements.

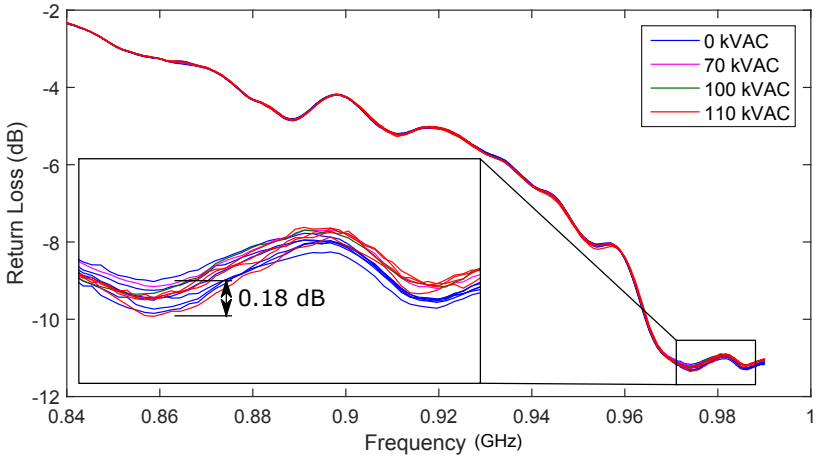

Figure E.3: 915 MHz printed meandered dipole, second attempt.

E.1.2 2.45 GHz Antennas

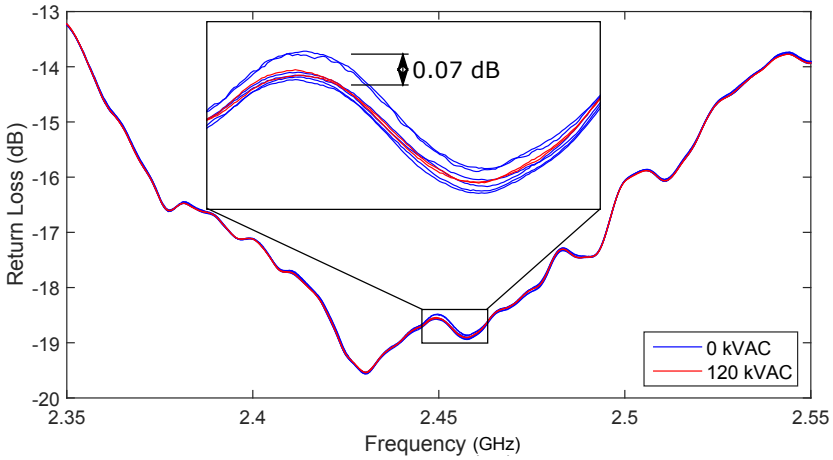

Figure E.4: 2.45 GHz wire monopole.

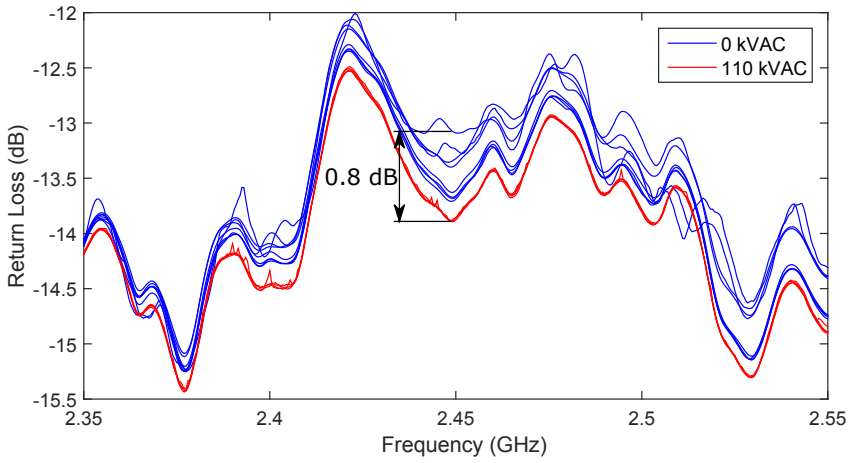

Figure E.5: 2.45 GHz slot dipole.

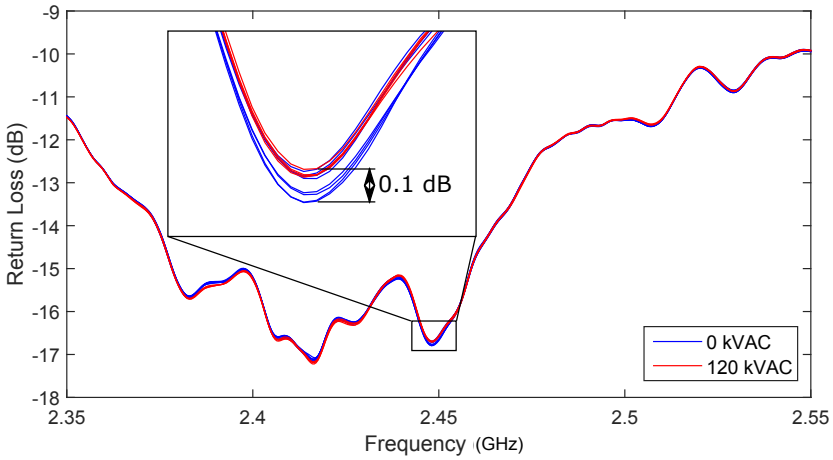

Figure E.6: 2.45 GHz broadband E-shaped patch.

E.1.3 5.8 GHz Antennas

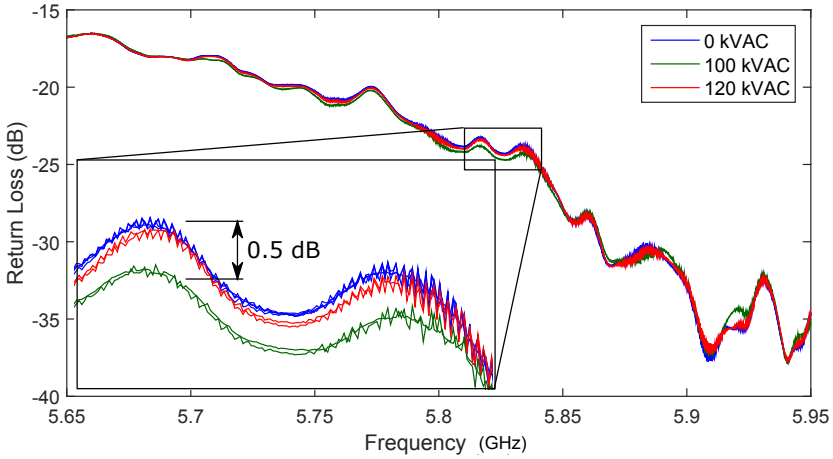

Figure E.7: 5.8 GHz wire monopole.

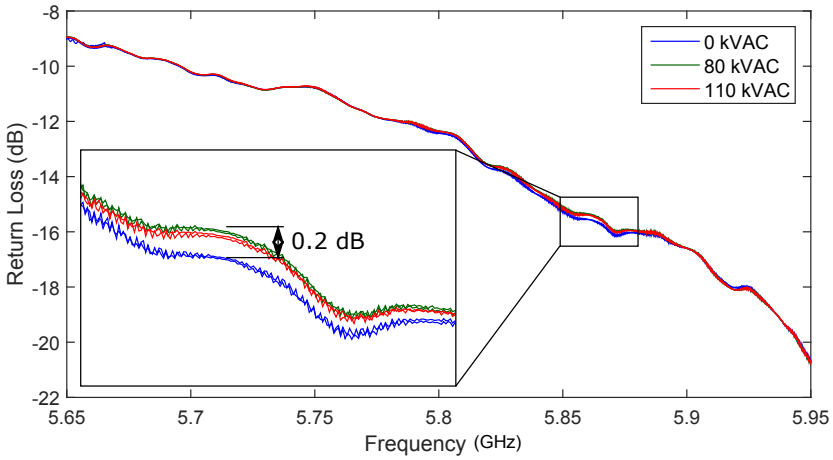

Figure E.8: 5.8 GHz slot dipole.

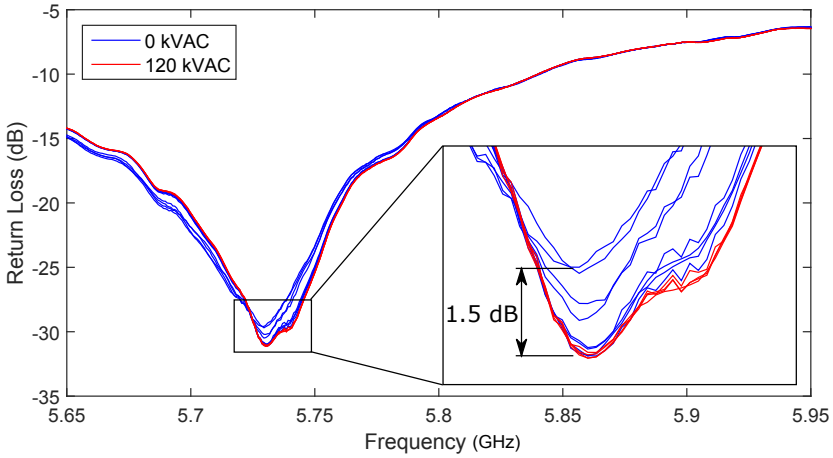

Figure E.9: 5.8 GHz rectangular patch, small ground.

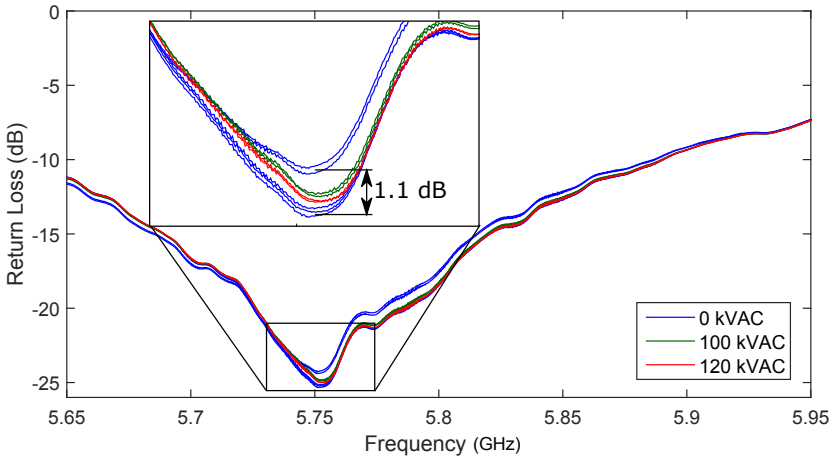

Figure E.10: 5.8 GHz rectangular patch, large ground

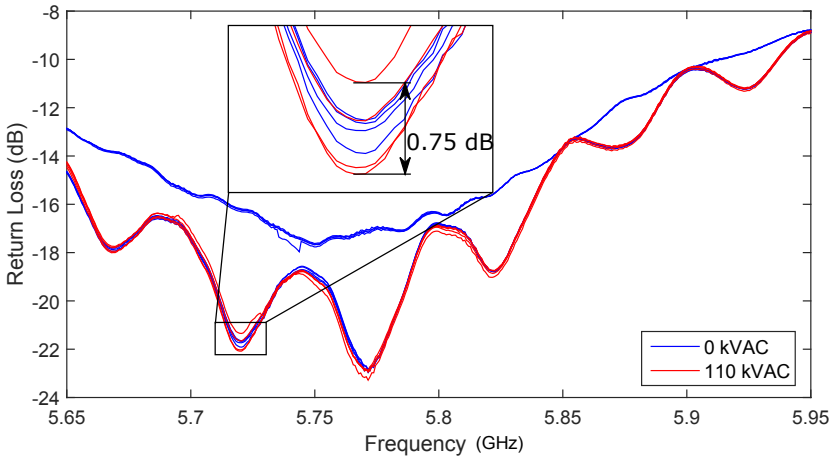

Figure E.11: 5.8 GHz whip antenna with dielectric shielding, first attempt. The corona affected the calibration of the system observed from the change in baseline measurement. The antenna was bent at a 90^o angle to be parallel to the HV plane, radiating through the plane.

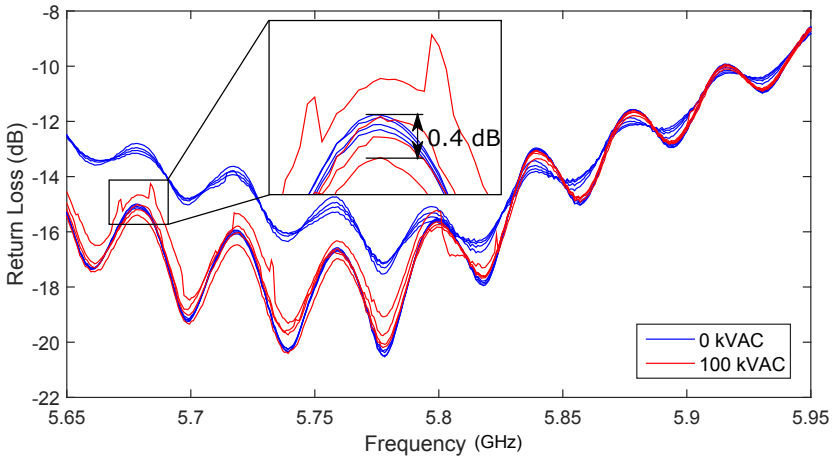

Figure E.12: 5.8 GHz whip antenna with dielectric shielding, second attempt. The corona affected the calibration of the system observed from the change in baseline measurement.

E.1.4 2.45/5.8 GHz dual-band antenna

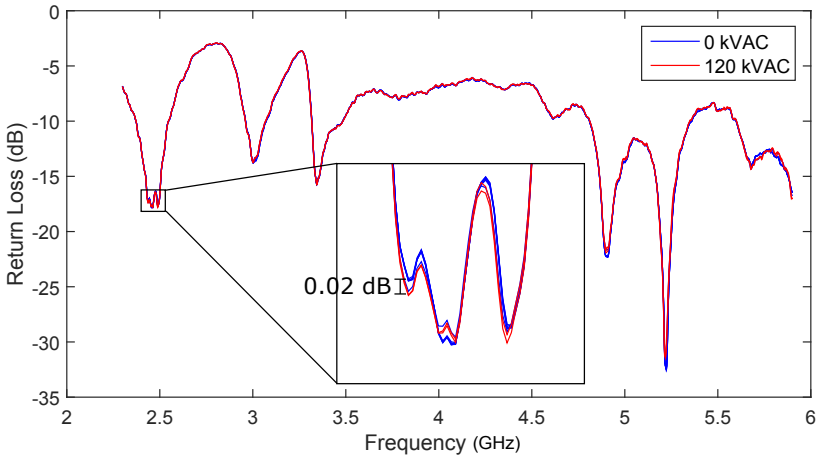

Figure E.13: 2.45/5.8 GHz dual-band whip antenna with dielectric shielding, broadband frequency sweep. The antenna was oriented perpendicular to the HV plane.

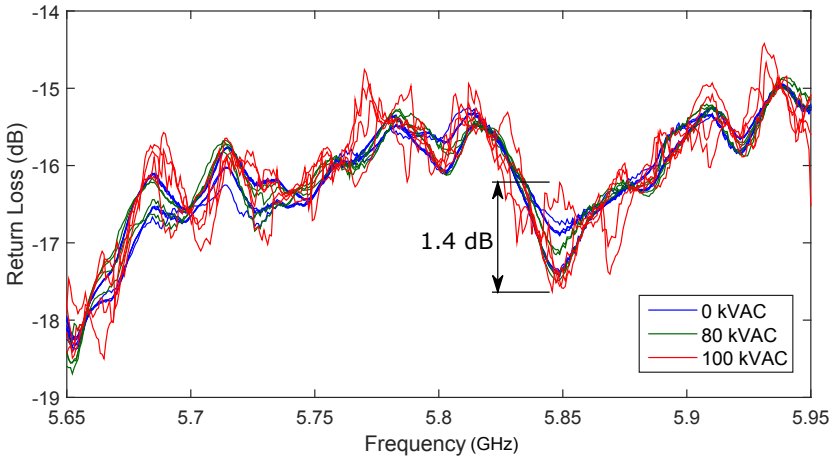

Figure E.14: 2.45/5.8 GHz dual-band whip antenna with dielectric shielding, 5.8 GHz sweep. The antenna was bent at a 90^o angle to be parallel to the HV plane, radiating through the plane.

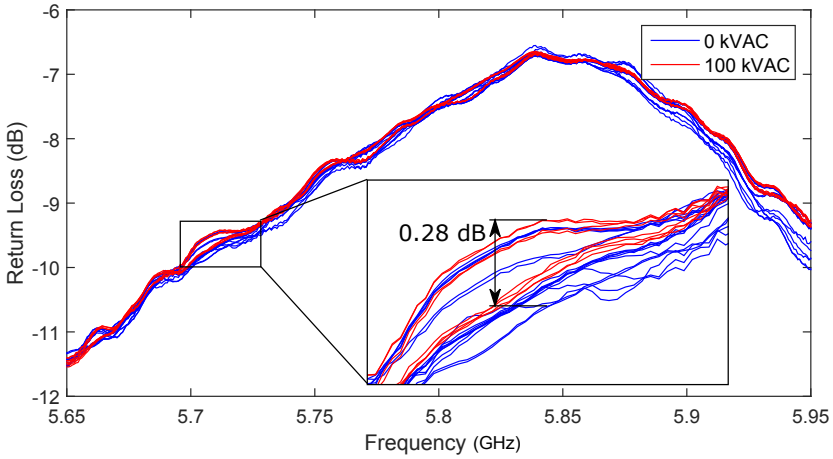

Figure E.15: 2.45/5.8 GHz dual-band whip antenna with dielectric shielding removed, 5.8 GHz sweep. The antenna was bent at a 90^o angle to be parallel to the HV plane, radiating through the plane.

E.1.5 Metal sphere monopole

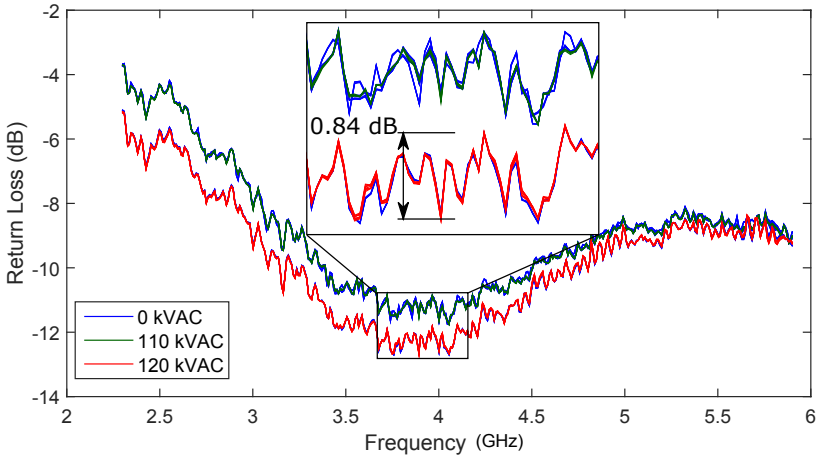

Figure E.16: 2.6 cm diameter aluminum foil sphere over a ground plane, broadband sweep of return loss.

E.2 Transmission

These measurements of the antenna transmission were taken with the antennas 25 cm from the high voltage plane using the setup in Figure 50. The VNA IF bandwidth is set to 70 Hz and the measurement time for each frequency sample is 16.67 ms, or one period of the 60 Hz voltage. Several captures are taken for the baseline antenna measurement with no corona formation (0 kV), both before and after high-voltage runs.

E.2.1 915 MHz Antennas

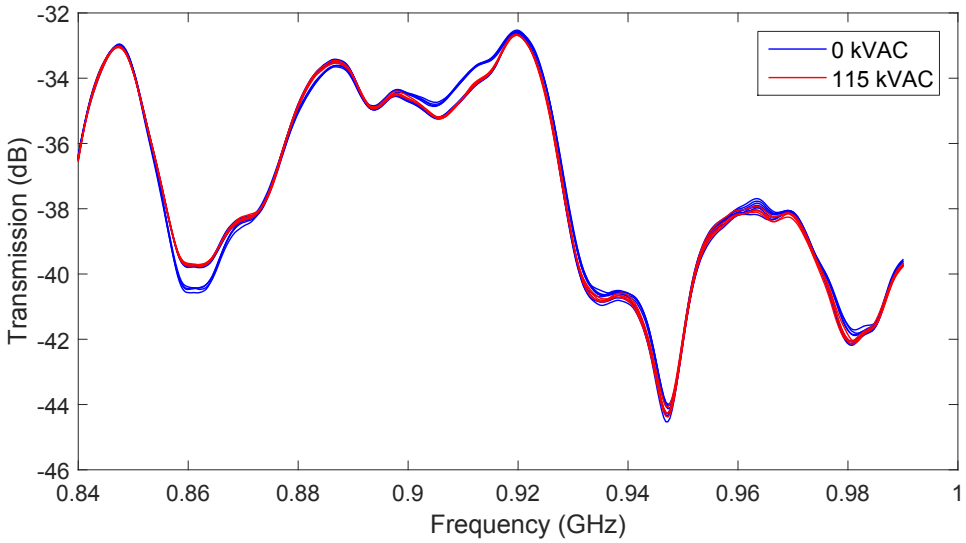

Figure E.17: 915 MHz wire monopole.

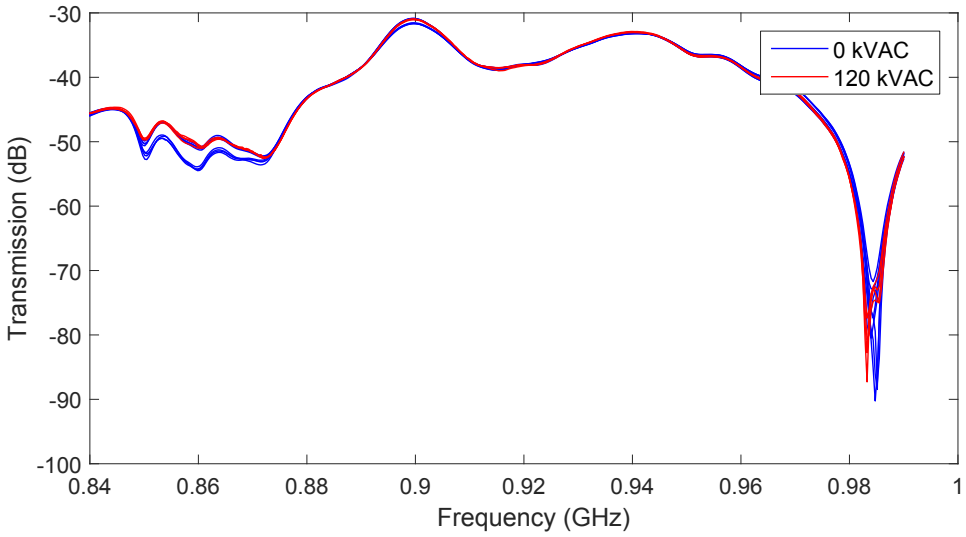

Figure E.18: 915 MHz printed meandered dipole, first attempt. The VNA calibration was affected during measurement, obviated by the large change in baseline 0 kV measurements.

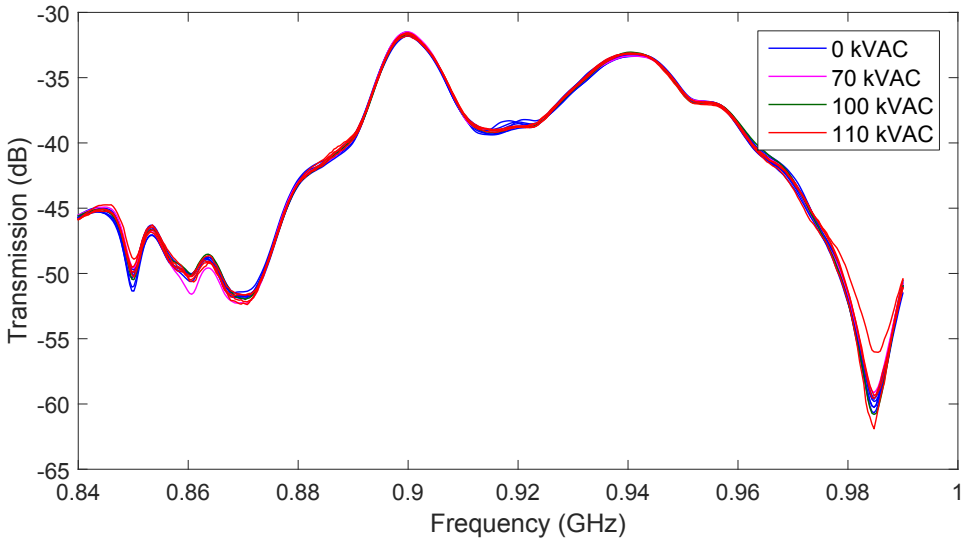

Figure E.19: 915 MHz printed meandered dipole, second attempt.

E.2.2 2.45 GHz Antennas

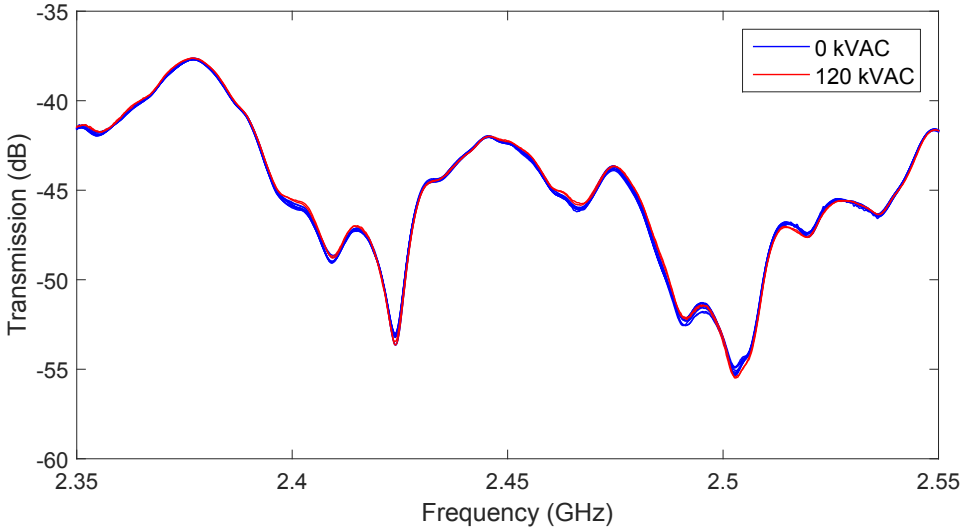

Figure E.20: 2.45 GHz wire monopole

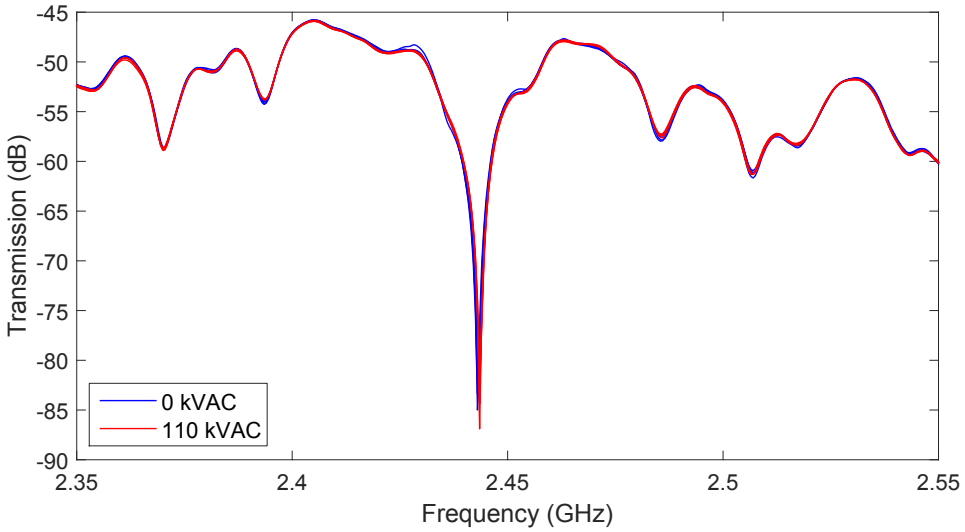

Figure E.21: 2.45 GHz slot dipole.

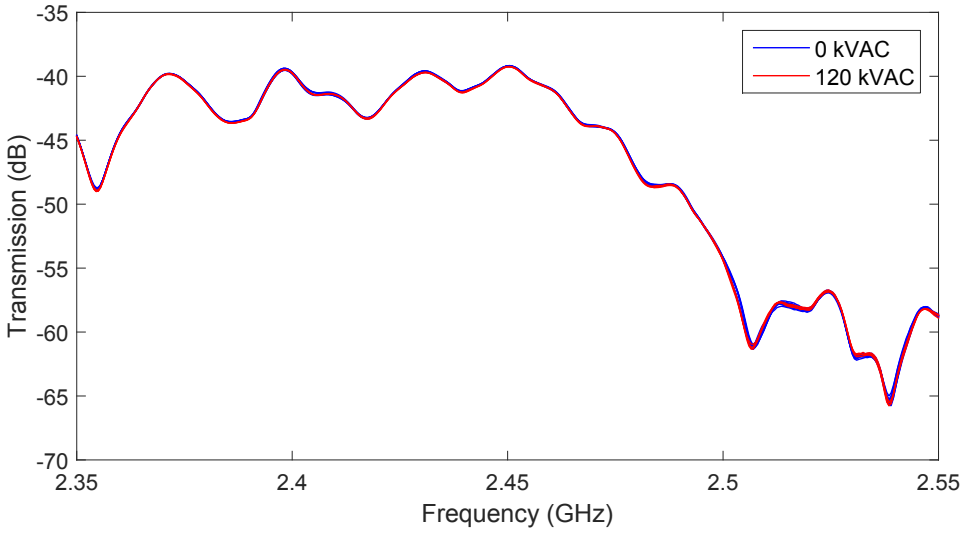

Figure E.22: 2.45 GHz broadband E-shaped patch.

E.2.3 5.8 GHz Antennas

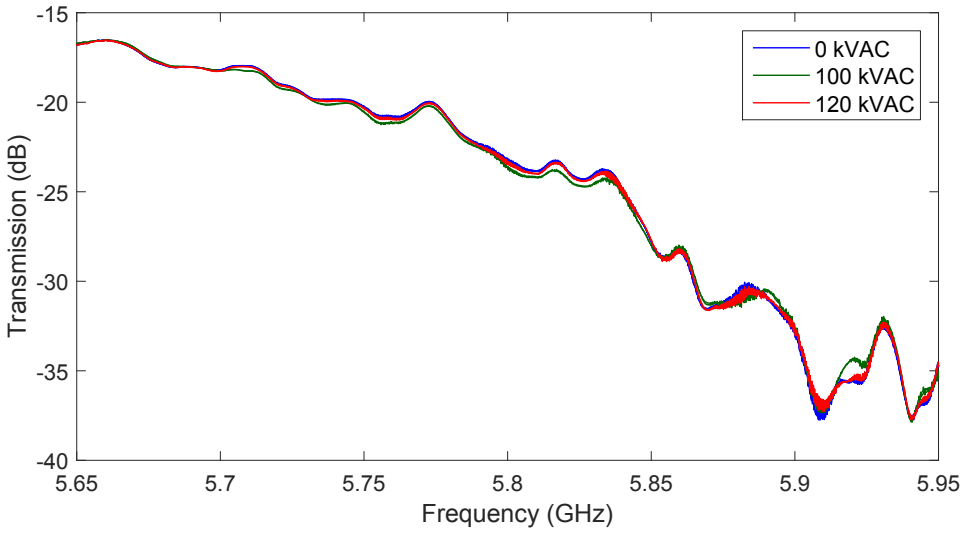

Figure E.23: 5.8 GHz wire monopole.

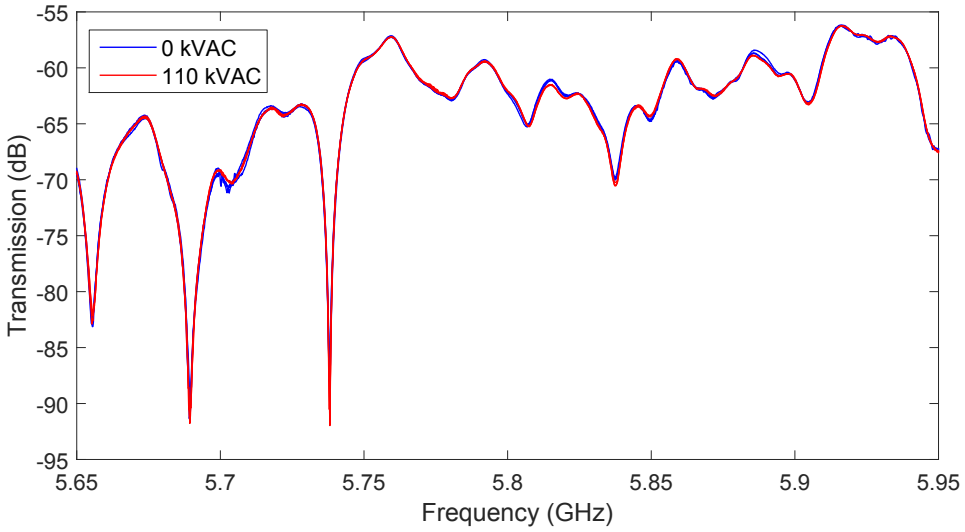

Figure E.24: 5.8 GHz slot dipole.

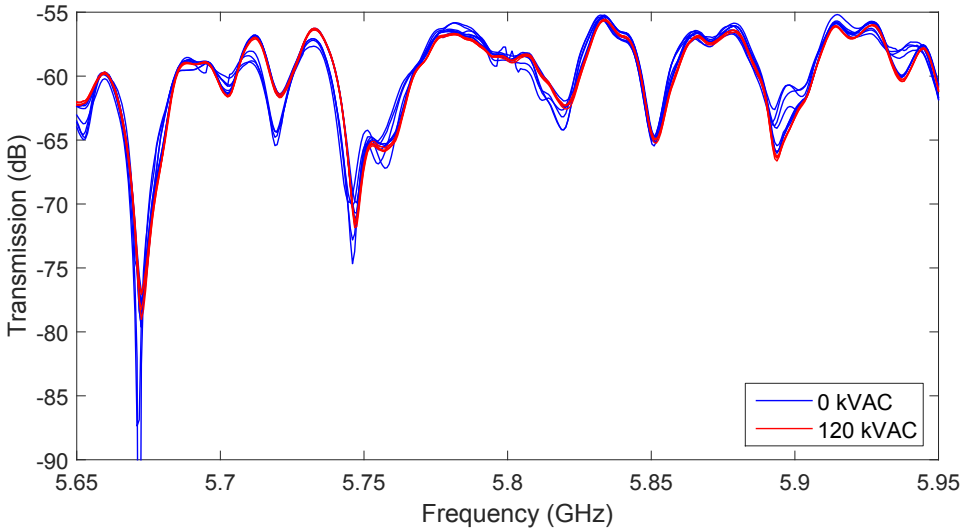

Figure E.25: 5.8 GHz rectangular patch, small ground.

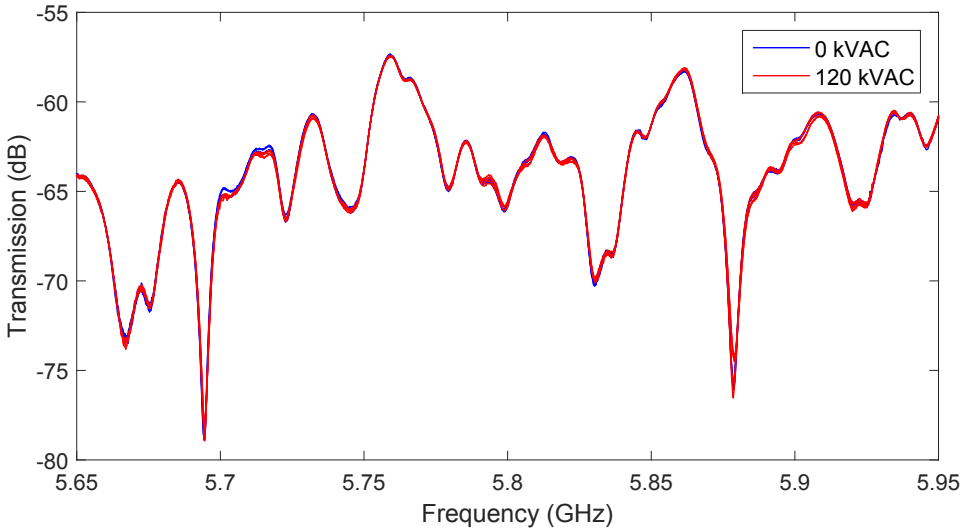

Figure E.26: 5.8 GHz rectangular patch, large ground

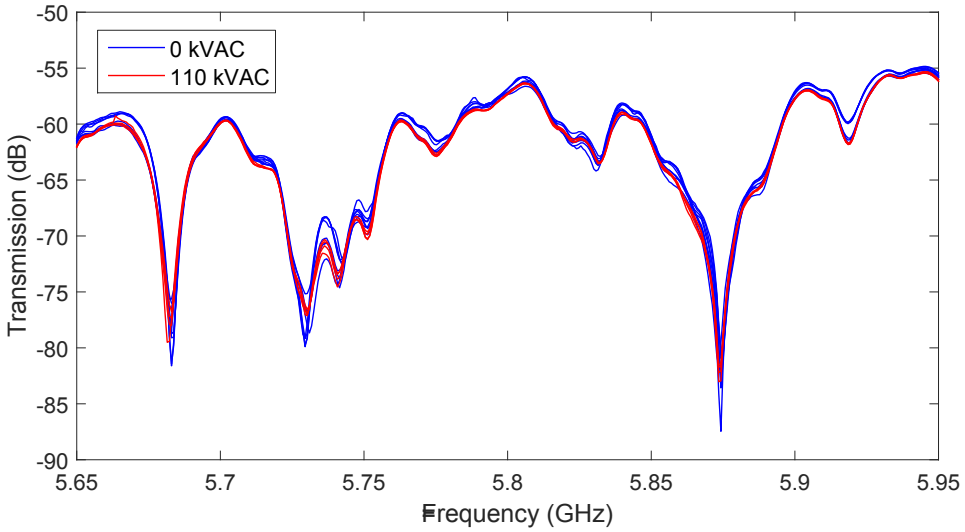

Figure E.27: 5.8 GHz whip antenna with dielectric shielding, first attempt. The corona affected the calibration of the system observed from the change in baseline measurement. The antenna was bent at a 90^o angle to be parallel to the HV plane, radiating through the plane.

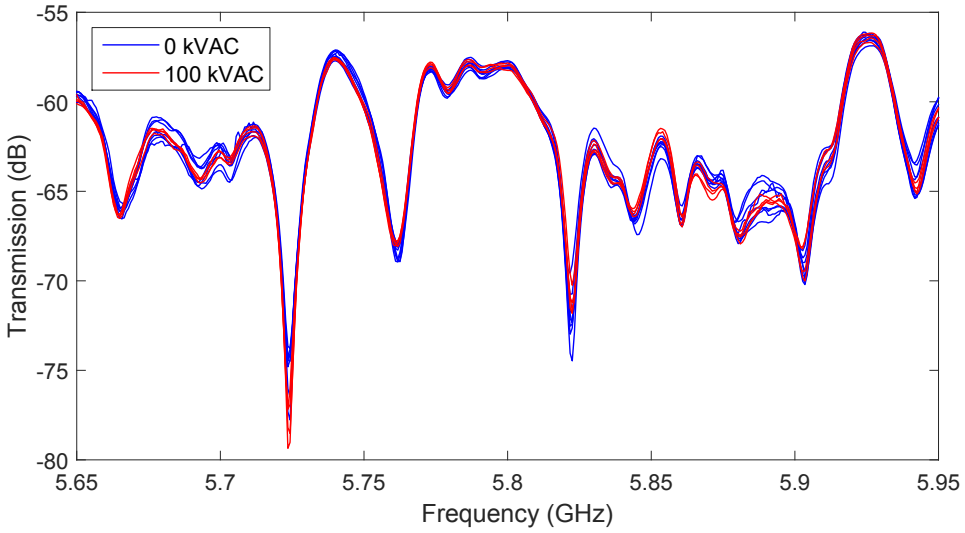

Figure E.28: 5.8 GHz whip antenna with dielectric shielding, second attempt. The corona affected the calibration of the system observed from the change in baseline measurement.

E.2.4 2.45/5.8 GHz dual-band antenna

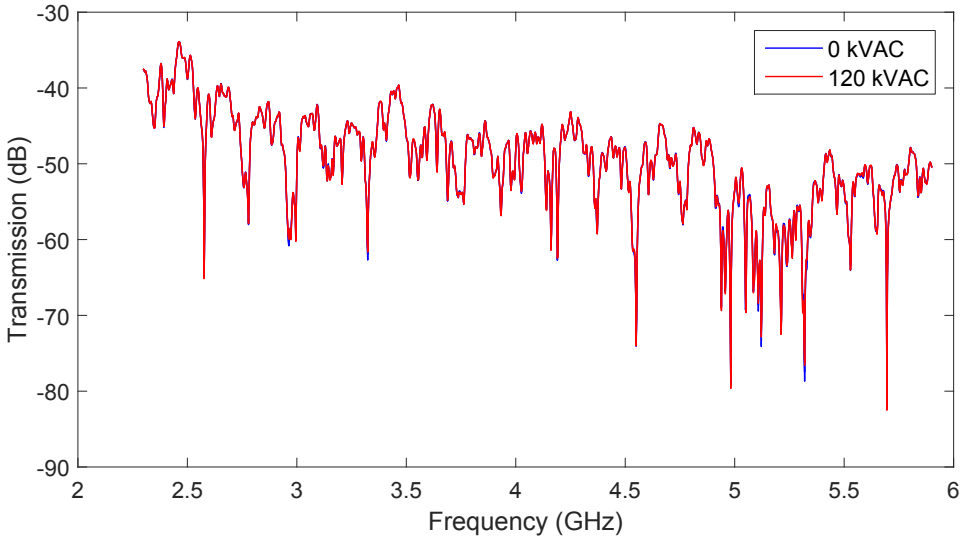

Figure E.29: 2.45/5.8 GHz dual-band whip antenna with dielectric shielding, broadband frequency sweep. The antenna was oriented perpendicular to the HV plane.

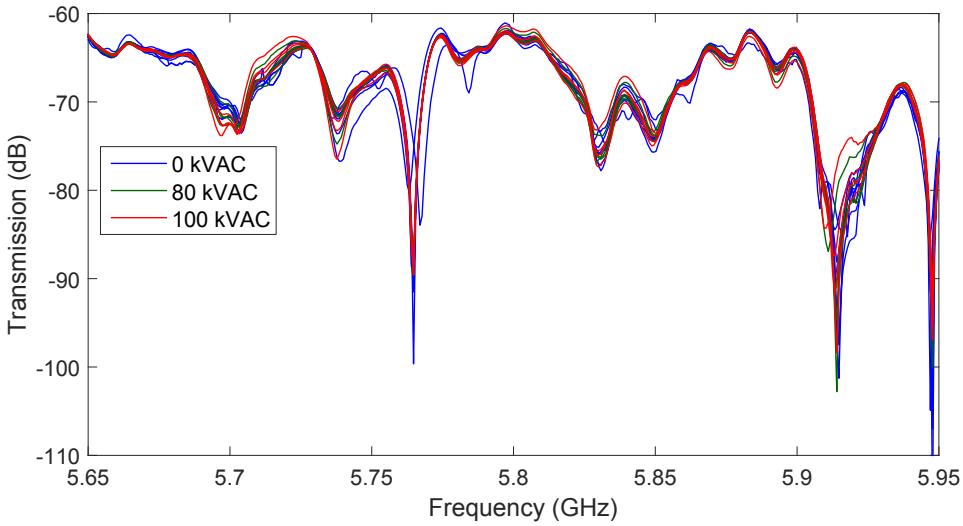

Figure E.30: 2.45/5.8 GHz dual-band whip antenna with dielectric shielding, 5.8 GHz sweep. The antenna was bent at a 90^o angle to be parallel to the HV plane, radiating through the plane.

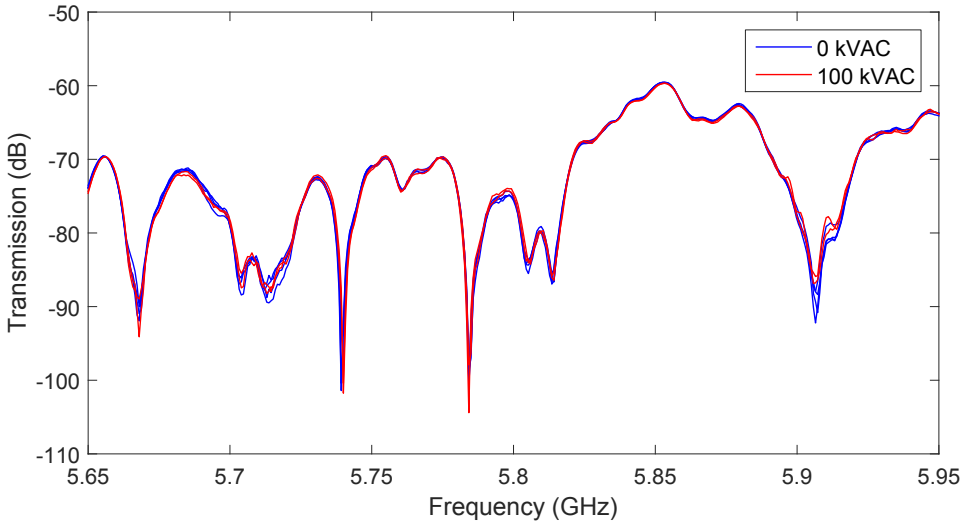

Figure E.31: 2.45/5.8 GHz dual-band whip antenna with dielectric shielding removed, 5.8 GHz sweep. The antenna was bent at a 90^o angle to be parallel to the HV plane, radiating through the plane.

E.2.5 Metal sphere monopole

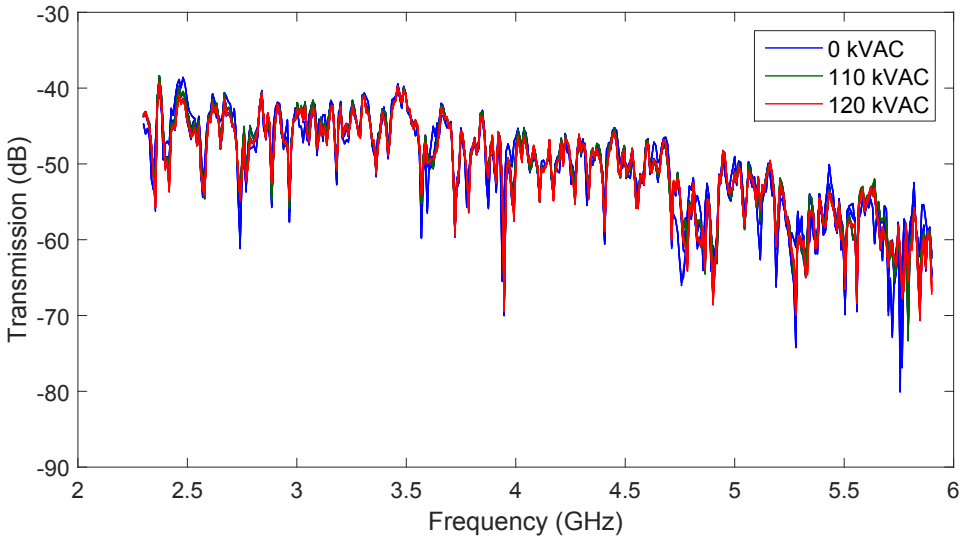

Figure E.32: 2.6 cm diameter aluminum foil sphere over a ground plane, broadband sweep of transmission to ridged horn antenna.

E.3 Direct Spectrum

These measurements of the spectrum coupled directly into the antenna under corona were taken with the antenna 25 cm from the high voltage plane using the setup in Figure 52. The spectrum analyzer IF bandwidth is set to 1 kHz and the measurement time for each frequency sample is 16 ms, or approximately one period of the 60 Hz voltage. Several captures are taken for the baseline antenna measurement with no corona formation (0 kV), both before and after high-voltage runs. The results given here for each voltage are the average of measurements (between 2 and 4) recorded at the specified voltage.

E.3.1 915 MHz Antennas

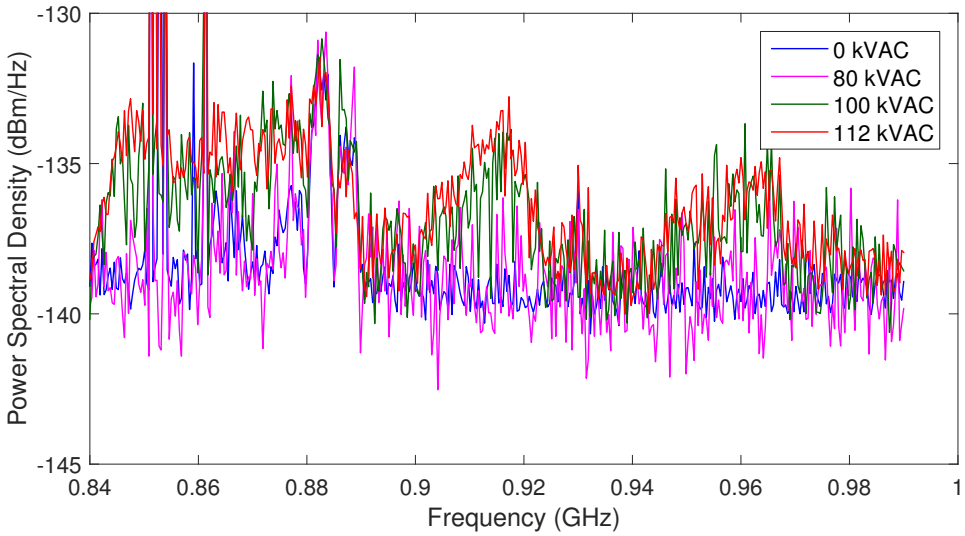

Figure E.33: 915 MHz wire monopole.

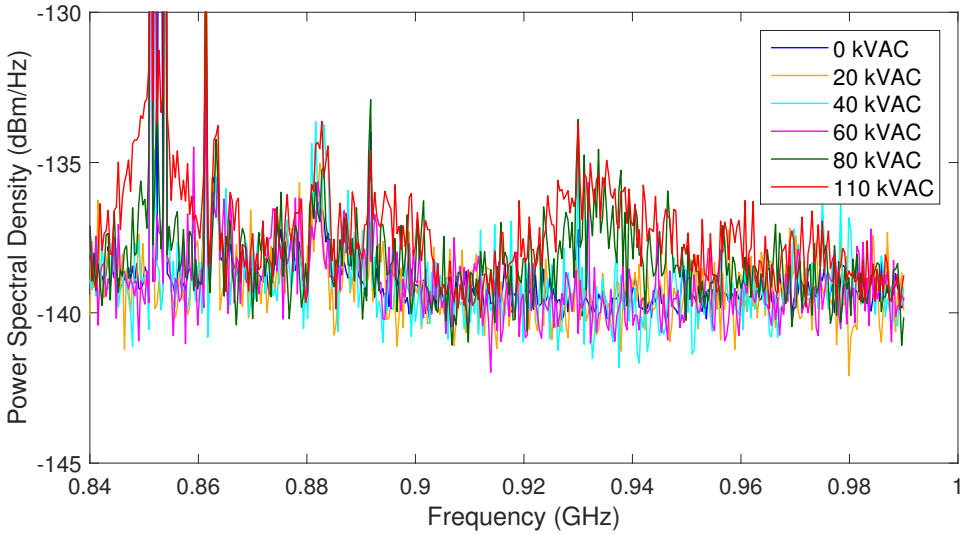

Figure E.34: 915 MHz printed meandered dipole.

E.3.2 2.45 GHz Antennas

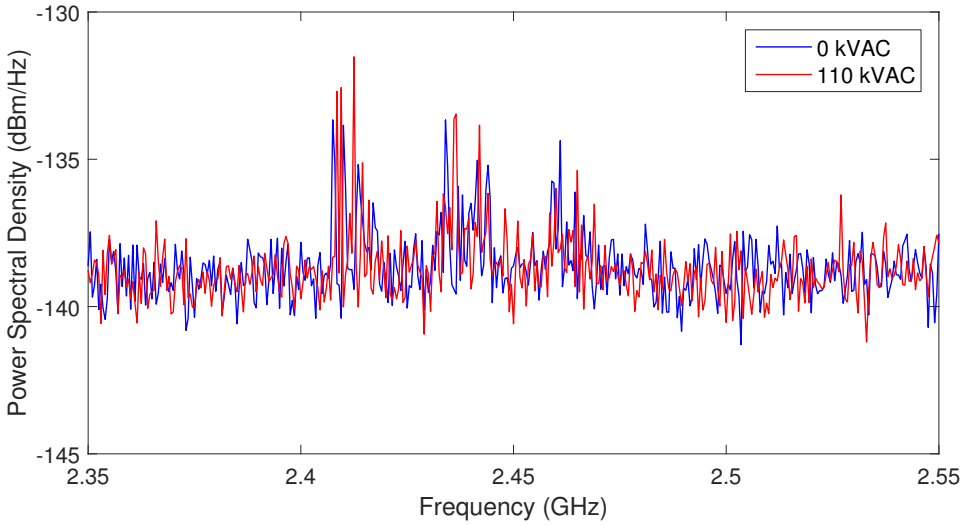

Figure E.35: 2.45 GHz wire monopole.

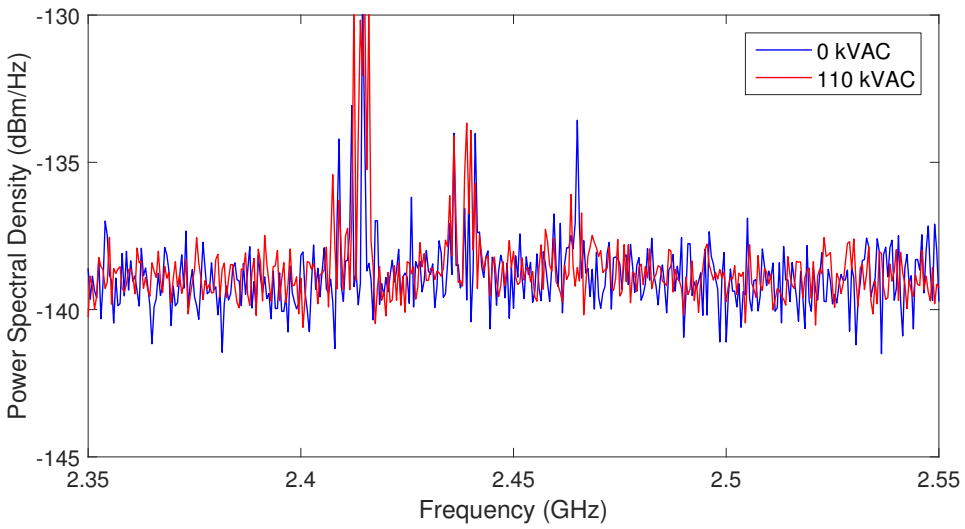

Figure E.36: 2.45 GHz slot dipole.

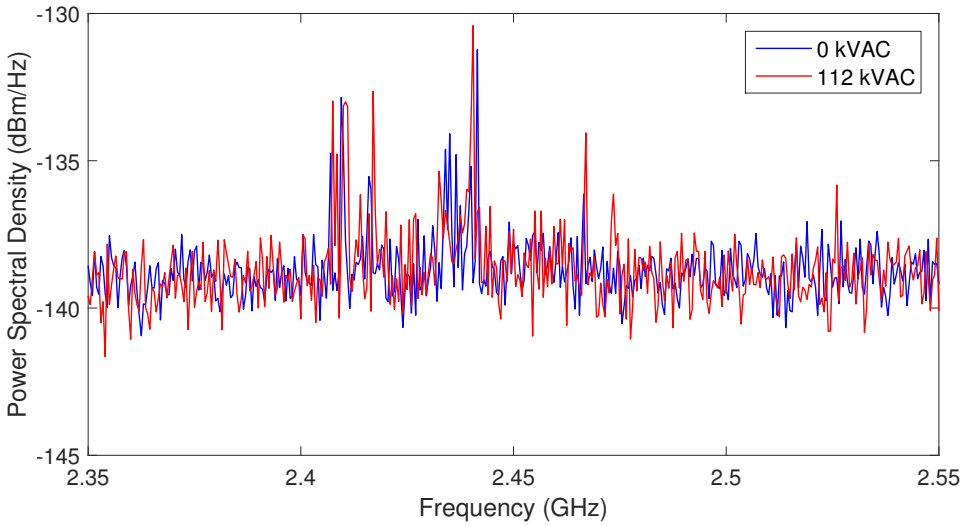

Figure E.37: 2.54 GHz broadband E-shaped patch.

E.3.3 5.8 GHz Antennas

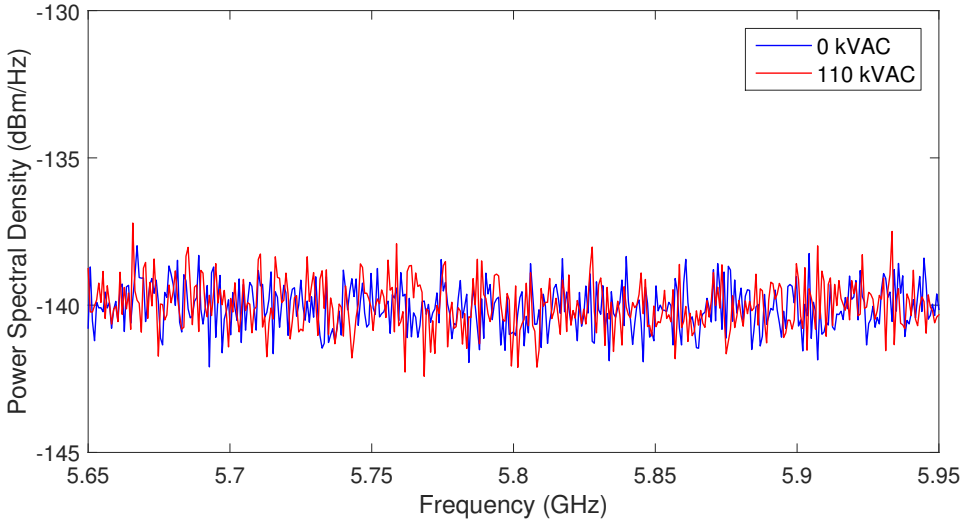

Figure E.38: 5.8 GHz whip antenna with dielectric shielding.

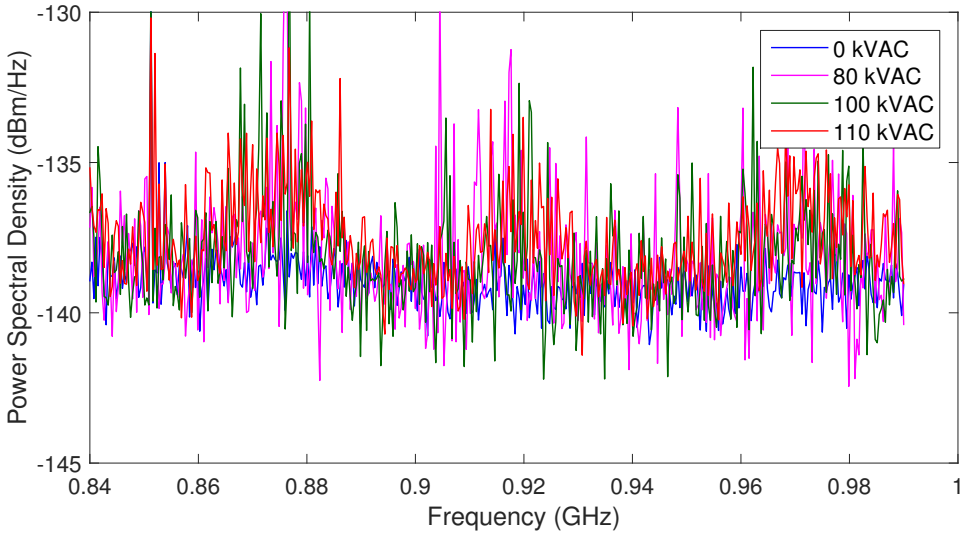

Figure E.39: 5.8 GHz whip antenna with dielectric shielding. Measurement of spectrum taken at 915 MHz.

E.3.4 2.45/5.8 GHz dual-band antennas

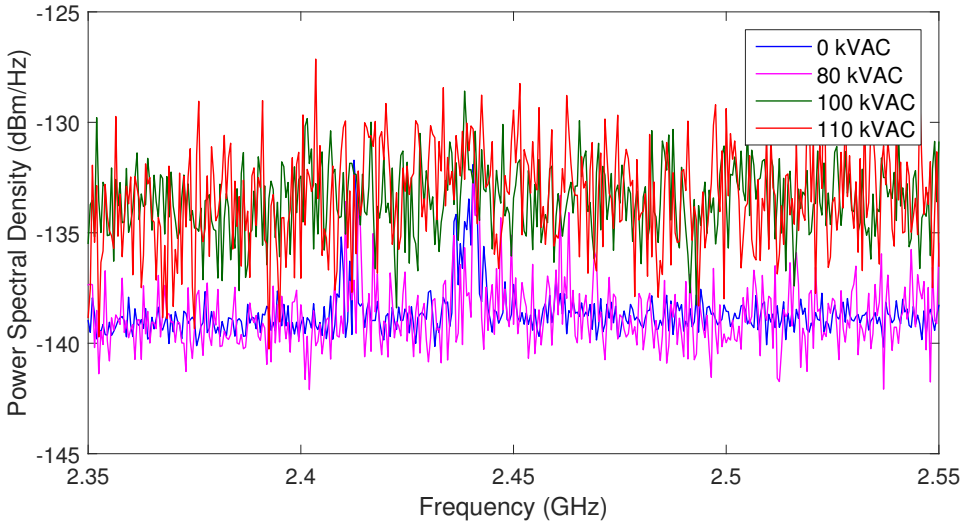

Figure E.40: 2.45/5.8 GHz dual-band whip antenna with dielectric shielding removed, 2.45 GHz sweep. The antenna was oriented parallel to the HV plane.

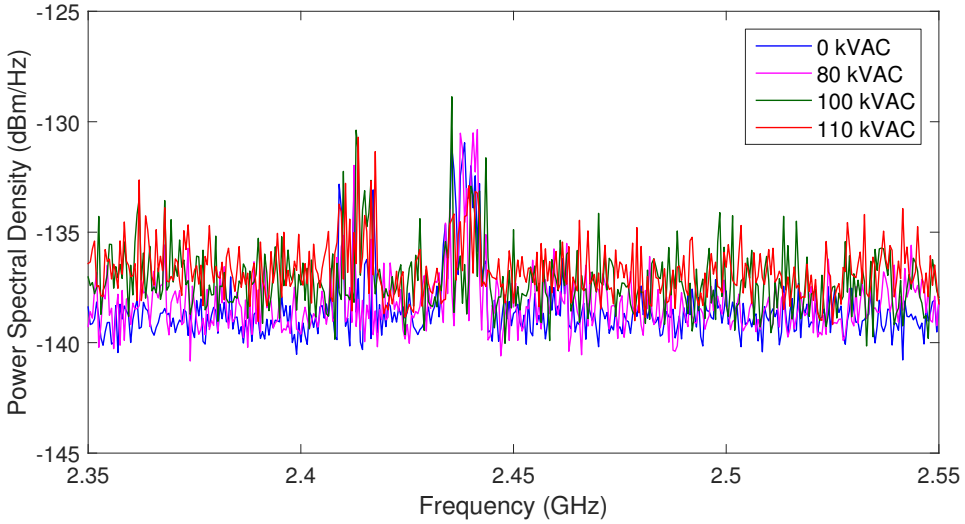

Figure E.41: 2.45/5.8 GHz dual-band whip antenna with dielectric shielding, 2.45 GHz sweep. The antenna was oriented parallel to the HV plane.

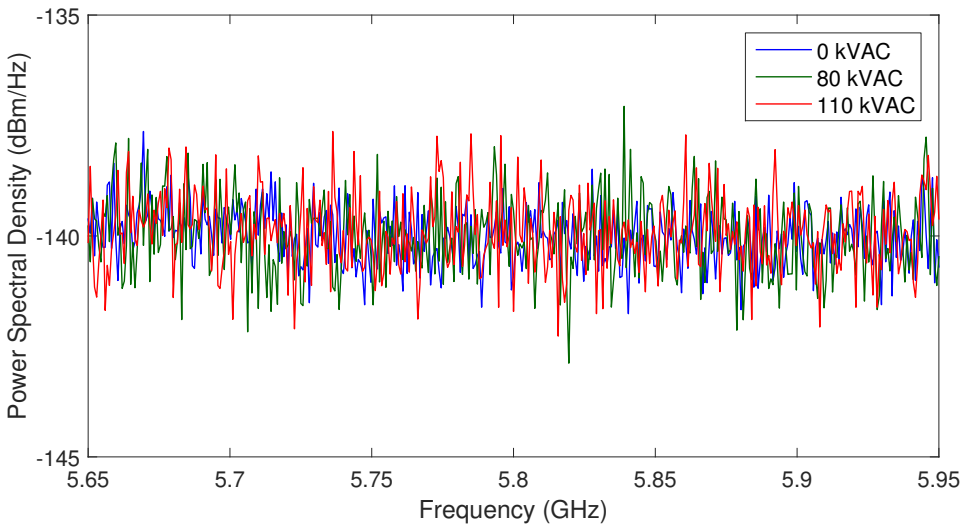

Figure E.42: 2.45/5.8 GHz dual-band whip antenna with dielectric shielding removed, 5.8 GHz sweep. The antenna was oriented parallel to the HV plane.

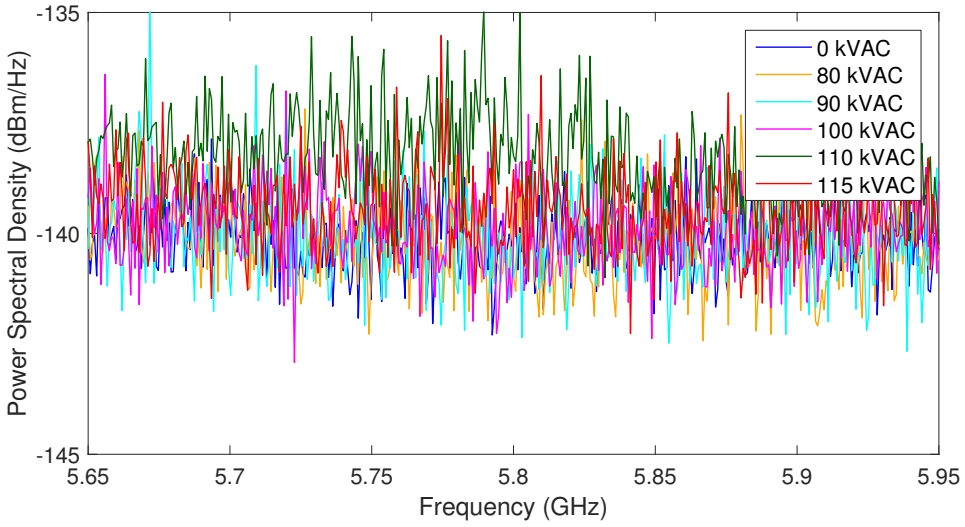

Figure E.43: 2.45/5.8 GHz dual-band whip antenna with dielectric shielding, 5.8 GHz sweep. The antenna was oriented parallel to the HV plane.

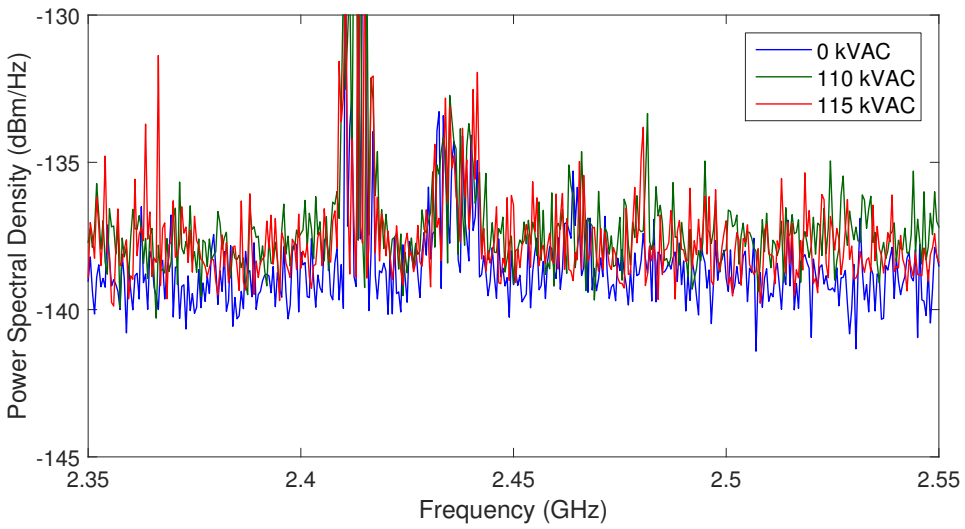

Figure E.44: 2.45/5.8 GHz dual-band whip antenna with dielectric shielding, 2.45 GHz sweep. The antenna was oriented perpendicular to the HV plane.

E.3.5 Metal sphere monopole

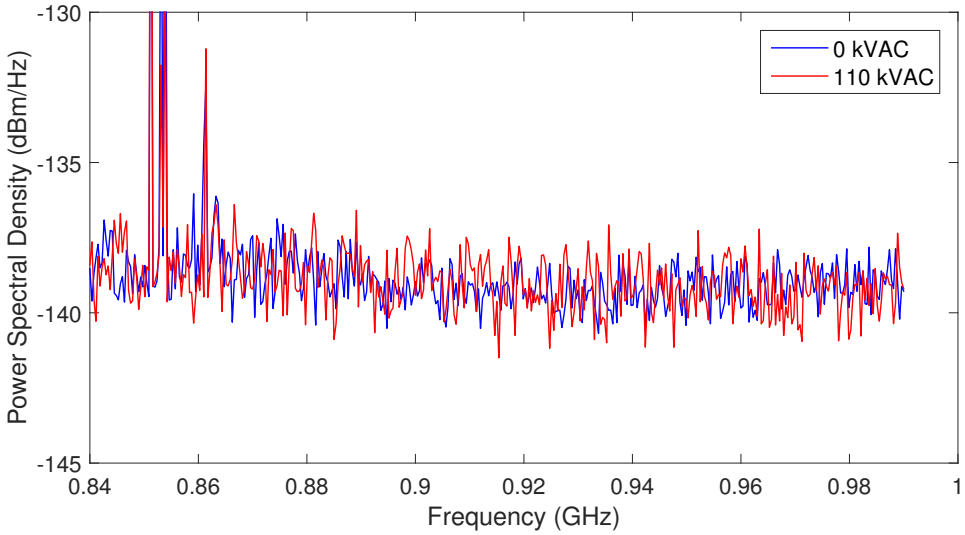

Figure E.45: 2.6 cm diameter aluminum foil sphere over a ground plane, 915 MHz sweep.

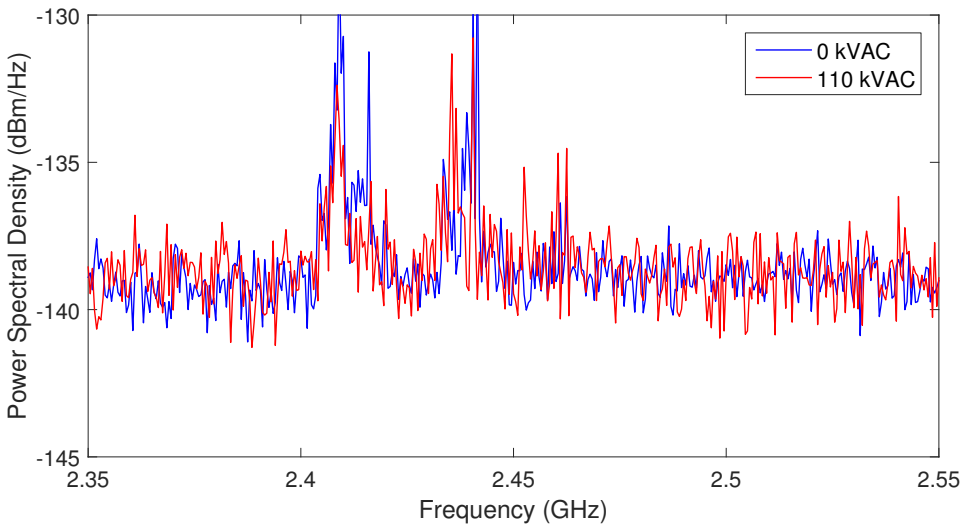

Figure E.46: 2.6 cm diameter aluminum foil sphere over a ground plane, 2.45 GHz sweep.

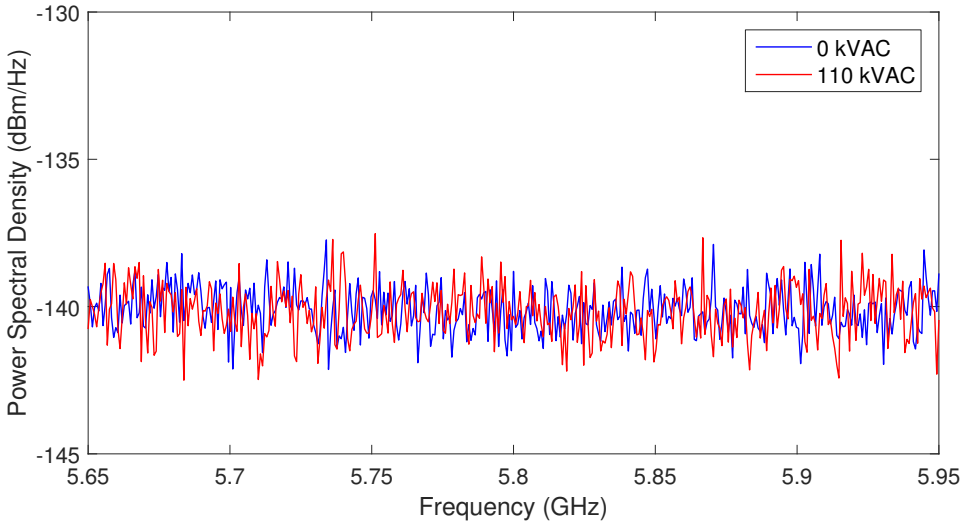

Figure E.47: 2.6 cm diameter aluminum foil sphere over a ground plane, 5.8 GHz sweep.

E.4 Direct Spectrum: Zero-Span

These measurements of the spectrum coupled directly into the antenna under corona were taken with the antenna 25 cm from the high-voltage plane using the setup in Figure 52. The spectrum analyzer IF bandwidth is set to 1 kHz. A zero-span measurement is made, sweeping over 1601 time samples in 16 ms total, or a little less than one period of the 60 Hz voltage waveform. Ten separate captures of the RF power spectral density during

corona formation are overlaid, shown with respect to the measurement instrument thermal AWGN floor, σ^2, and multiples of the AWGN standard deviation. The voltage phase in the zero-span figures is specified such that the positive corona peak on the antenna occurs at 90^o (and its multiples of 360^o) and the negative corona peak on the antenna occurs at 270^o (and its multiples of 360^o).

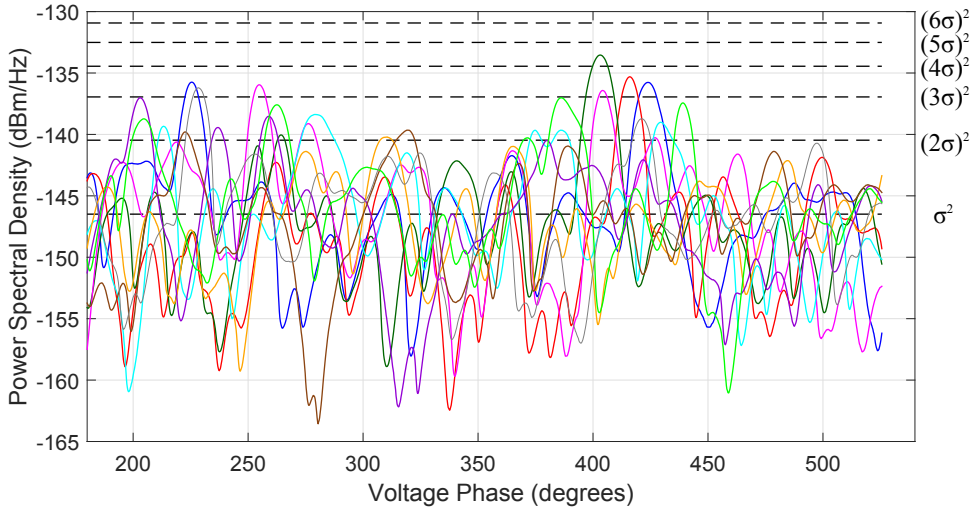

Figure E.48: Zero-span measurement of the RF spectrum coupled into a 915 MHz monopole undergoing corona (positive glow and streamers, and negative Trichel pulses). The monopole at ground potential is 25 cm from the high-voltage plane at 110 kVAC. The IF bandwidth is set to 1 kHz and measurement is performed over one cycle of the 60 Hz voltage cycle. Ten separate captures are overlaid, shown with respect to the measurement instrument thermal AWGN floor, σ^2, and multiples of the AWGN standard deviation. Interference is observed at the negative and positive voltage peaks. The interference during negative corona formation may be the result of radiation from positive corona on the HV plane coupling into the antenna.

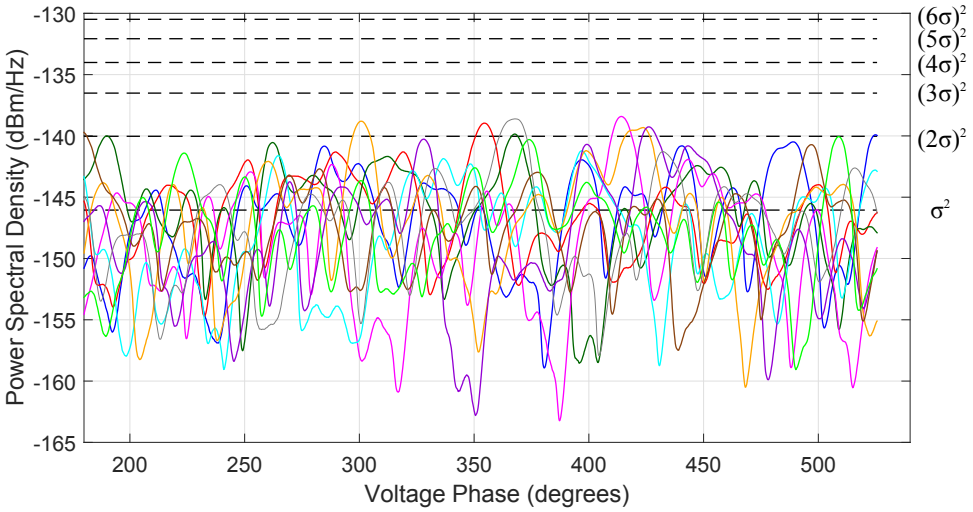

Figure E.49: Zero-span measurement of the RF spectrum coupled into a 2.45 GHz monopole undergoing corona (positive glow and streamers, and negative Trichel pulses). The monopole at ground potential is 25 cm from the high-voltage plane at 115 kVAC. The IF bandwidth is set to 1 kHz and measurement is performed over one cycle of the 60 Hz voltage cycle. Ten separate captures are overlaid, shown with respect to the measurement instrument thermal AWGN floor, σ^2, and multiples of the AWGN standard deviation. There is no observed interference.

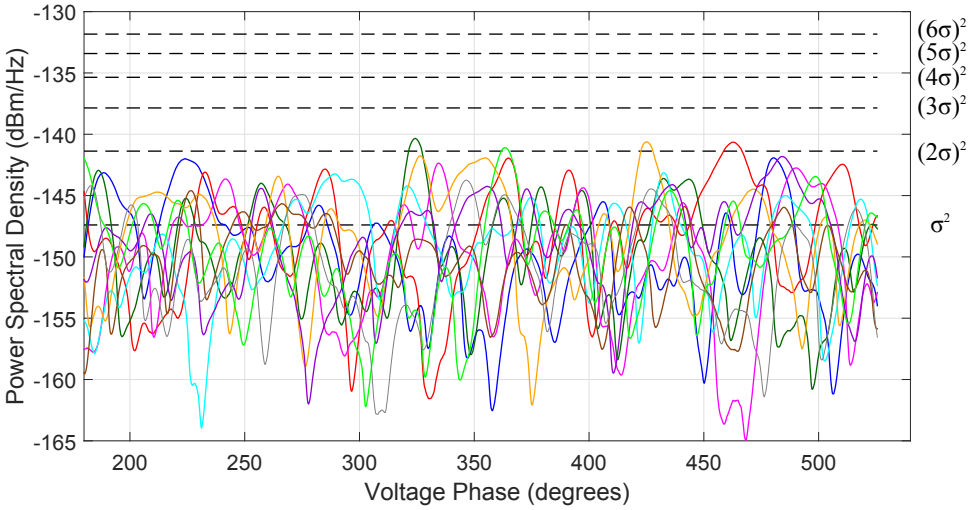

Figure E.50: Zero-span measurement of the RF spectrum coupled into a 5.8 GHz monopole undergoing corona (positive glow and streamers, and negative Trichel pulses). The monopole at ground potential is 25 cm from the high-voltage plane at 110 kVAC. The IF bandwidth is set to 1 kHz and measurement is performed over one cycle of the 60 Hz voltage cycle. Ten separate captures are overlaid, shown with respect to the measurement instrument thermal AWGN floor, σ^2, and multiples of the AWGN standard deviation. There is no observed interference.

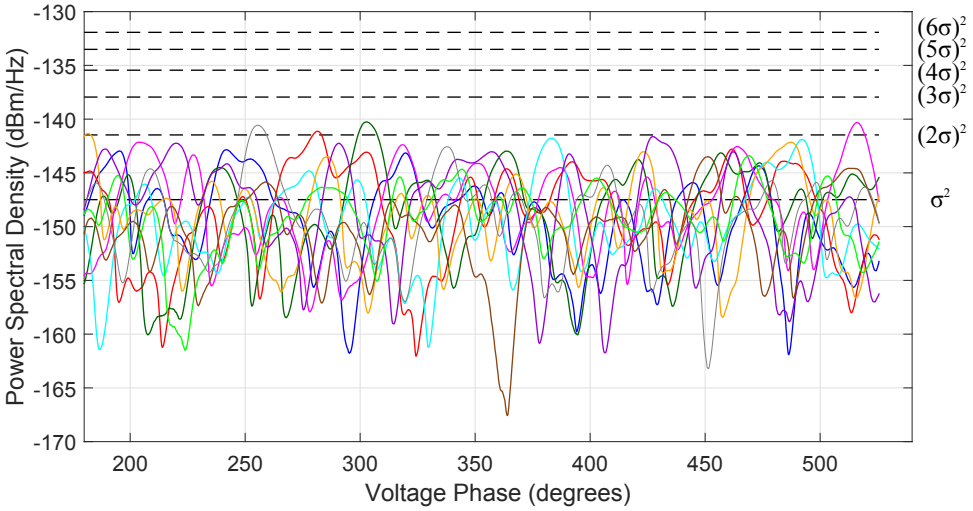

Figure E.51: Zero-span measurement of the RF spectrum coupled into a 5.8 GHz rectangular patch (large ground plane) undergoing corona (positive glow and negative Trichel pulses). The patch at ground potential is 25 cm from the high-voltage plane at 120 kVAC. The IF bandwidth is set to 1 kHz and measurement is performed over one cycle of the 60 Hz voltage cycle. Ten separate captures are overlaid, shown with respect to the measurement instrument thermal AWGN floor, σ^2, and multiples of the AWGN standard deviation. There is no observed interference.

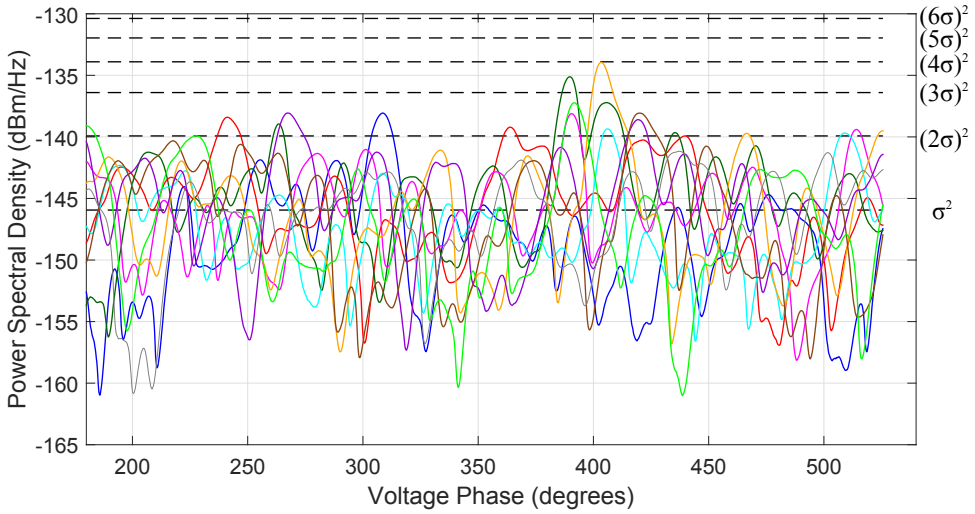

Figure E.52: Zero-span measurement of the RF spectrum coupled into a 2.45/5.8 GHz dual-band whip antenna with dielectric shielding, taken at 2.45 GHz. The antenna was oriented perpendicular to the HV plane, and is undergoing corona (Random discharges shown in Figure E.65). The whip at ground potential is 25 cm from the high-voltage plane at 115 kVAC. The IF bandwidth is set to 1 kHz and measurement is performed over one cycle of the 60 Hz voltage cycle. Ten separate captures are overlaid, shown with respect to the measurement instrument thermal AWGN floor, σ^2, and multiples of the AWGN standard deviation. Interference is observed with positive corona.

Figure E.53: 2.45/5.8 GHz dual-band whip antenna with dielectric shielding, 2.45 GHz sweep. The antenna was oriented perpendicular to the HV plane.

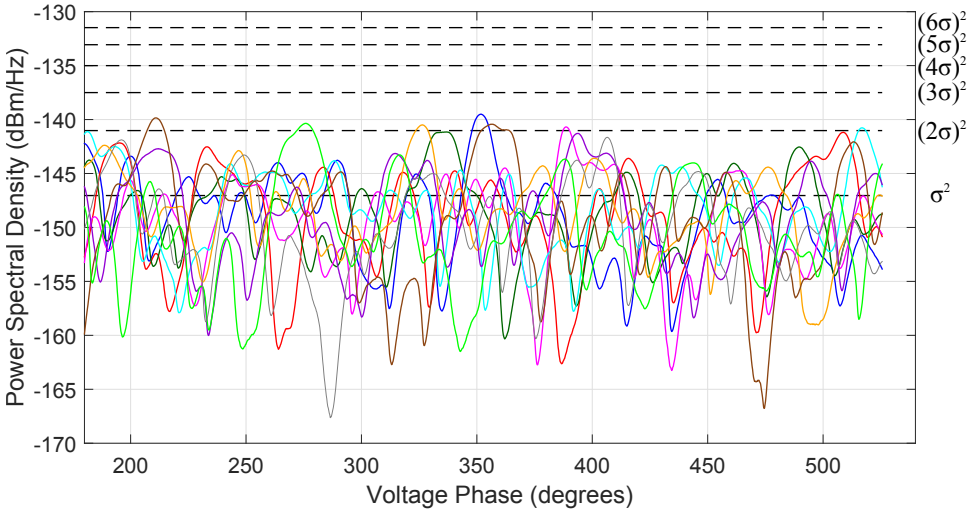

Figure E.54: Zero-span measurement of the RF spectrum coupled into a 2.45/5.8 GHz dual-band whip antenna with dielectric shielding, taken at 5.8 GHz. The antenna was oriented perpendicular to the HV plane, and is undergoing corona (Random discharges shown in Figure E.65). The whip at ground potential is 25 cm from the high-voltage plane at 115 kVAC. The IF bandwidth is set to 1 kHz and measurement is performed over one cycle of the 60 Hz voltage cycle. Ten separate captures are overlaid, shown with respect to the measurement instrument thermal AWGN floor, σ^2, and multiples of the AWGN standard deviation. There is no observed interference.

E.5 Radiated Spectrum

These measurements of the radiated spectrum were taken using the setup in Figure 53. The boradband ridged horn antenna is positioned 1 m from the high-voltage plane, vertically polarized with respect to the ground. The horn has a gain of 5.0 dBi, 9.3 dBi, and 10.9 dBi at 915 MHz, 2.45 GHz, and 5.8 GHz, respectively. The spectrum analyzer IF bandwidth is set to 1 kHz and the measurement time for each frequency sample is 16 ms, or approximately one period of the 60 Hz voltage. Several captures are taken for the baseline antenna measurement with no corona formation (0 kV), both before and after high-voltage runs. The results given here for each voltage are the average of measurements (between 2 and 4) recorded at the specified voltage. Figure E.59 is a zero-span measurement at 930

MHz showing the temporal behavior of the RF interference from corona over an AC voltage cycle.

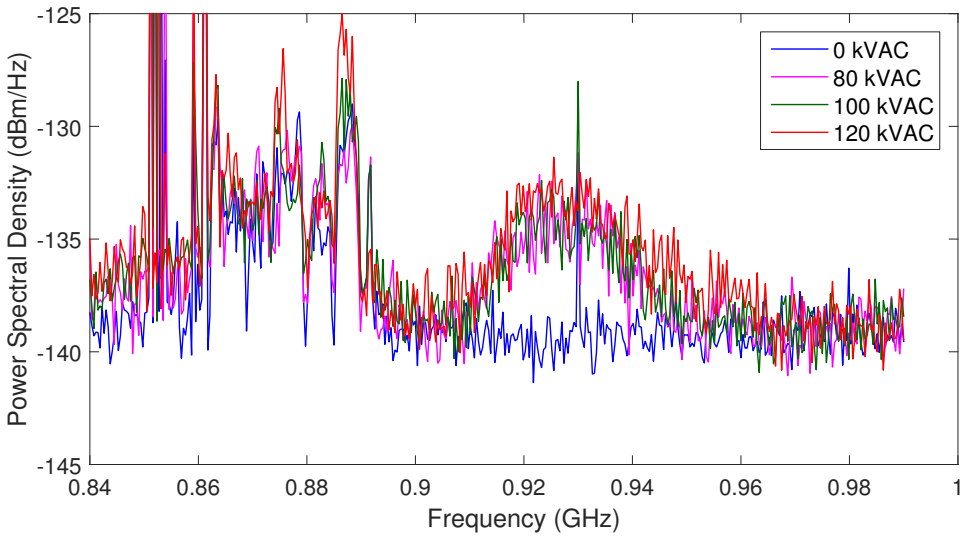

Figure E.55: Radiated spectrum in 915 MHz band. No antenna under corona is present in this measurement. The unwanted corona radiated from the HV plane is measured.

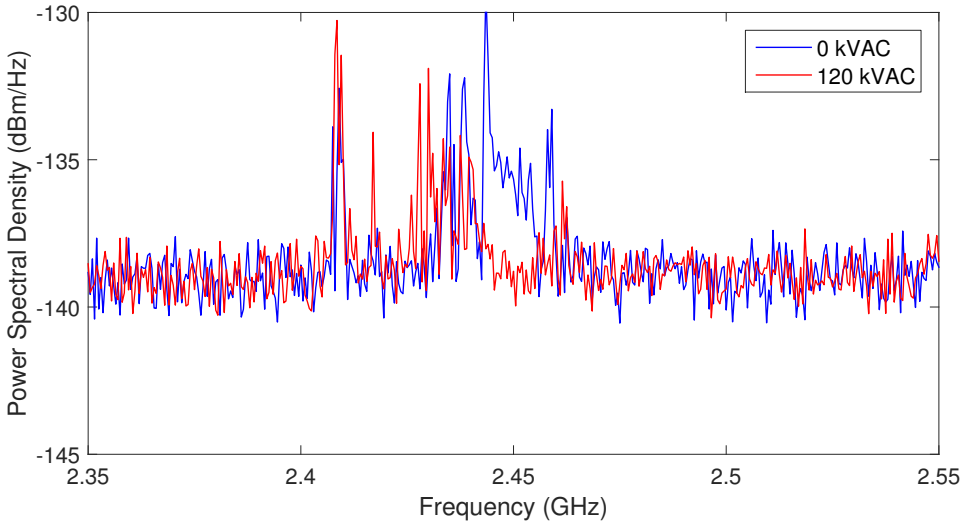

Figure E.56: Radiated spectrum in 2.45 GHz band. No antenna under corona is present in this measurement. The unwanted corona radiated from the HV plane is measured.

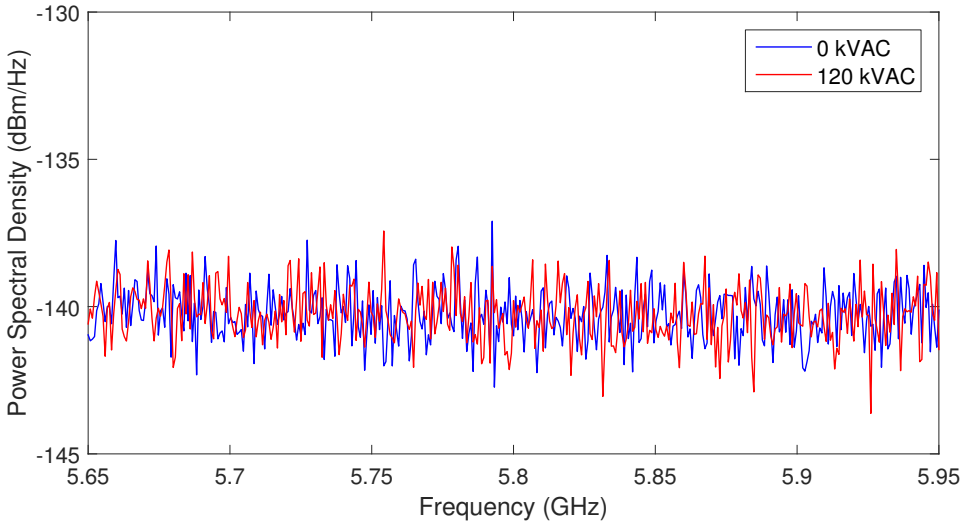

Figure E.57: Radiated spectrum in 5.8 GHz band. No antenna under corona is present in this measurement. The unwanted corona radiated from the HV plane is measured.

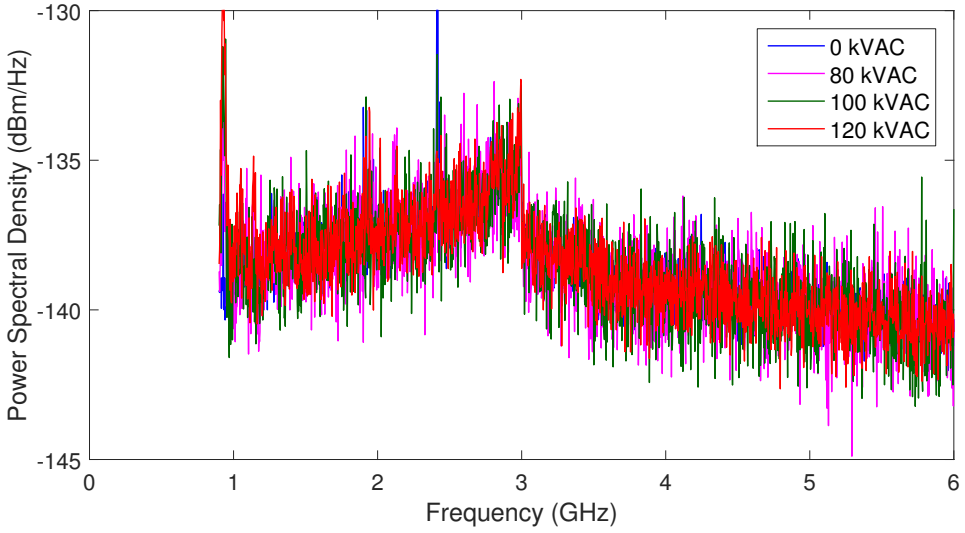

Figure E.58: Radiated spectrum sweep from 915 MHz to 5.8 GHz bands. No antenna under corona is present in this measurement. The unwanted corona radiated from the HV plane is measured.

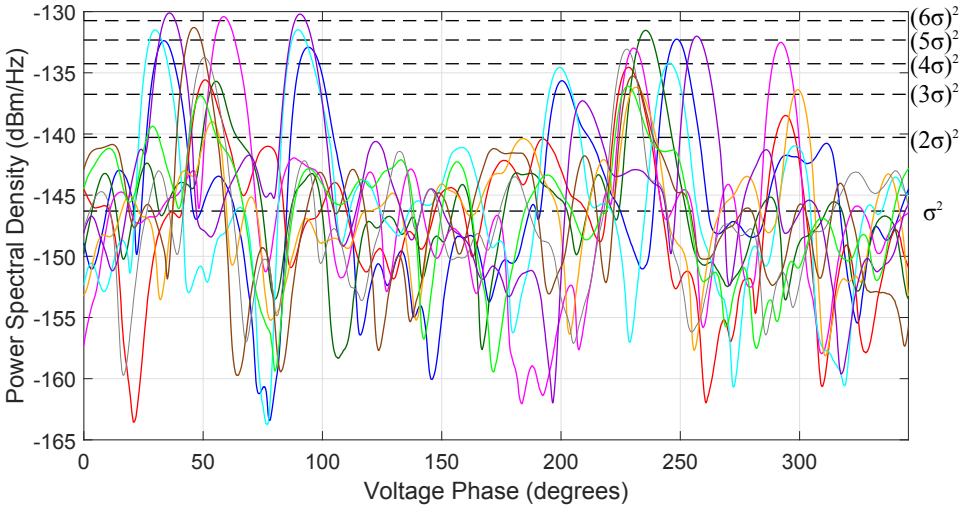

Figure E.59: Zero-span measurement of the RF spectrum radiated from the high-voltage (120 kVAC) test set and plane at 930 MHz, with 1 kHz IF, plotted over one 60 Hz voltage cycle. Ten separate captures are overlaid, shown with respect to the measurement instrument thermal AWGN floor, σ^2, and multiples of the AWGN standard deviation. Interference is observed at the negative and positive voltage peaks.

E.6 Corona Current

These measurements of the radiated spectrum were taken using the setup in Figure 54. A 6.78 kΩ resistor was connected between the antenna feed (coaxial inner conductor) and ground. Voltage is measured on the oscilloscope via a 10:1 probe across the resistor. Current can be derived from the measured voltage. The coaxial transmission line acts as an effective capacitance at lower frequencies, limiting the bandwidth of measurements. The setup is modeled as a simple capacitance in parallel with the sensing resistor to determine the corona current from the measured voltage.

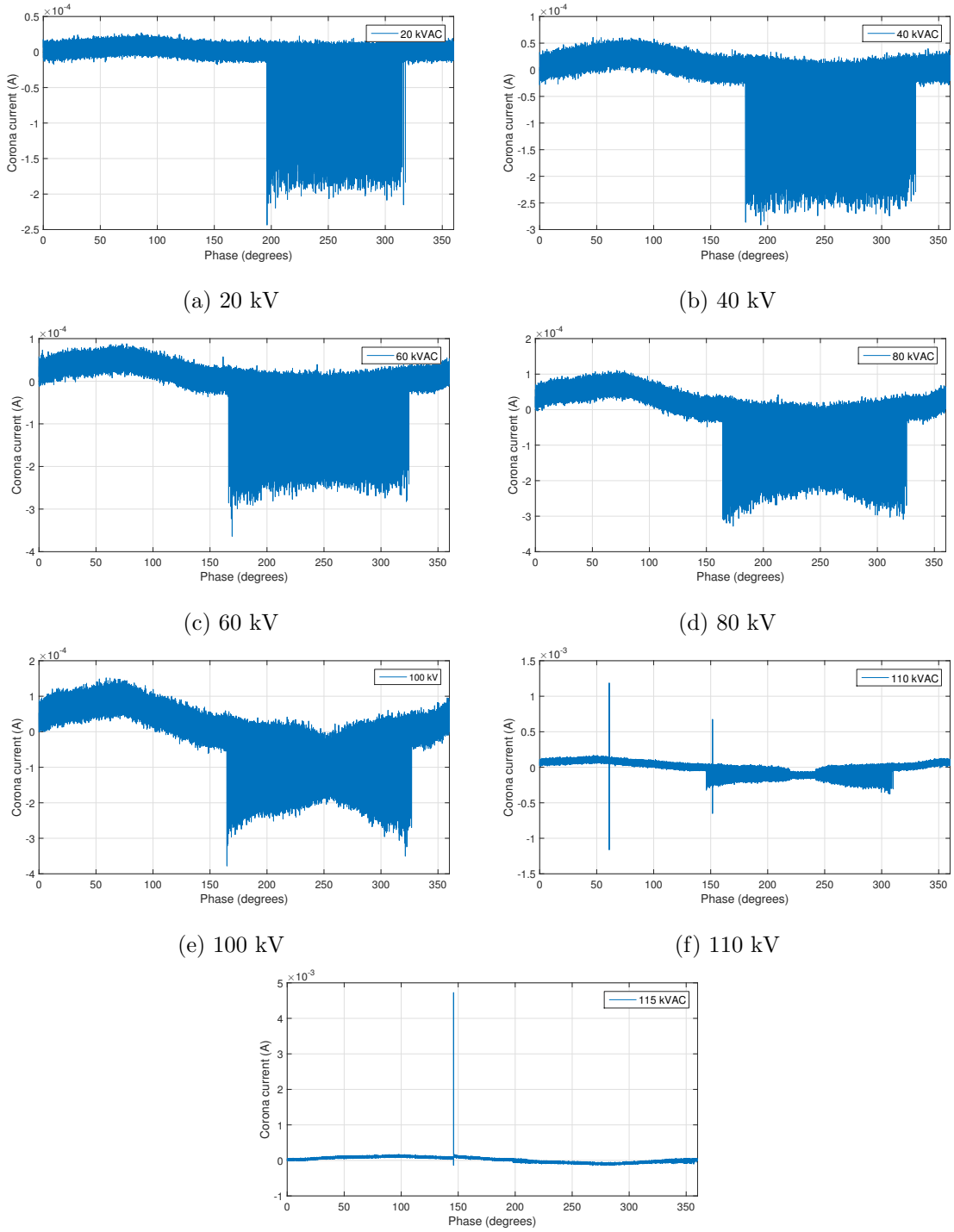

(a) 20 kV

(b) 40 kV

(c) 60 kV

(d) 80 kV

(e) 100 kV

(f) 110 kV

(g) 115 kV

Figure E.60: Corona current on 2.45 GHz wire monopole at different voltages.

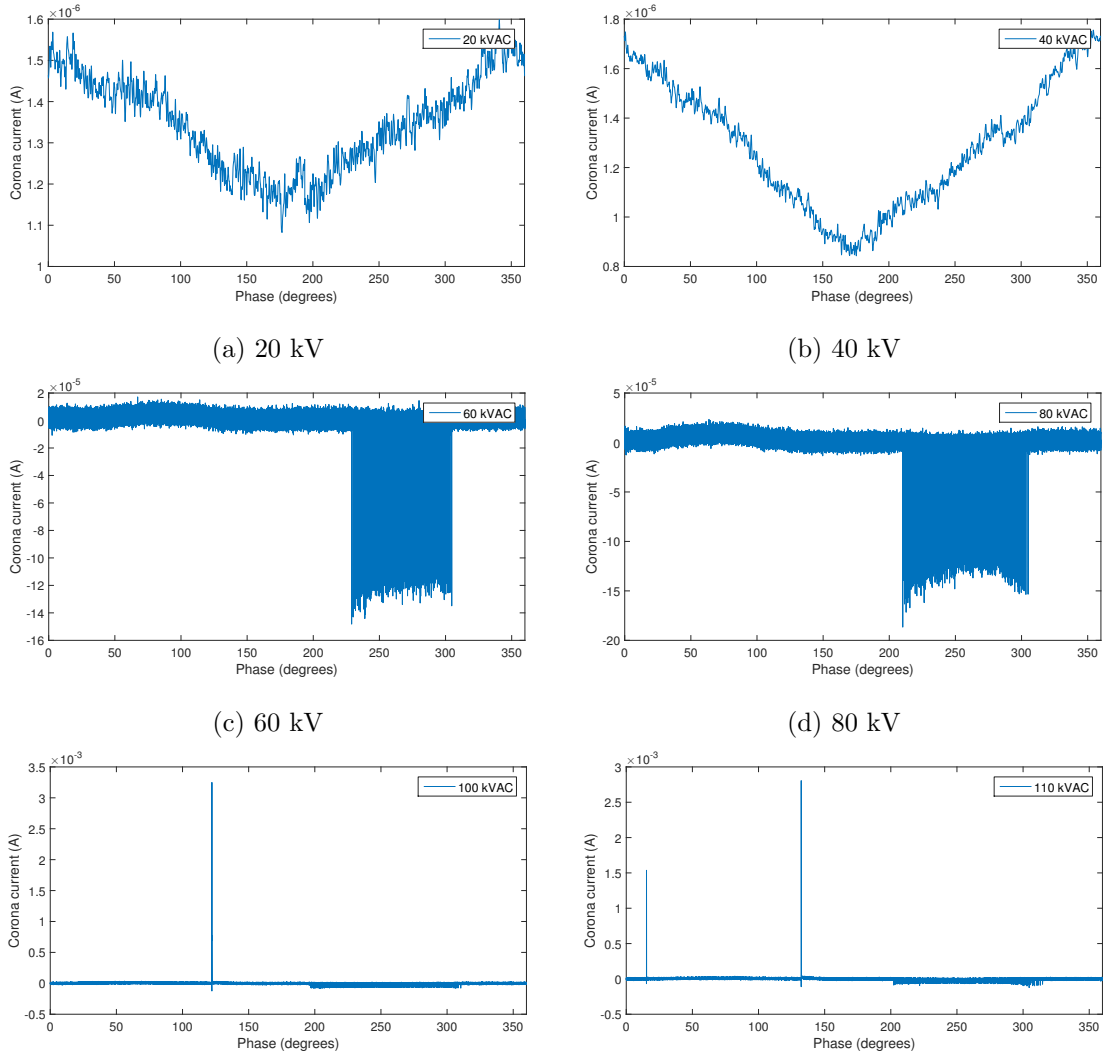

(a) 20 kV

(b) 40 kV

(c) 60 kV

(d) 80 kV

(e) 100 kV

(f) 110 kV

Figure E.61: Corona current on 5.8 GHz rectangular patch with large ground plane at different voltages. A 3mm wire was soldered to the patch, inducing corona formation.

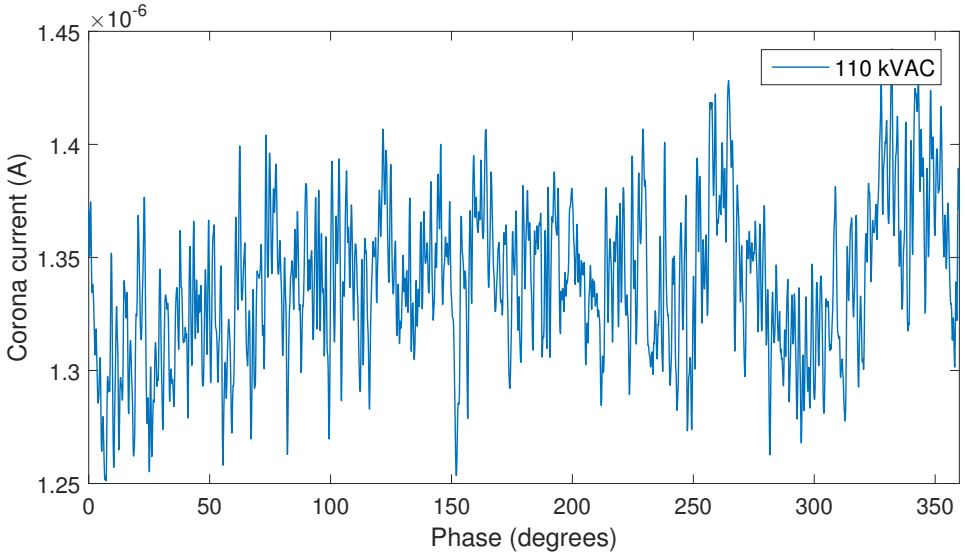

Figure E.62: Corona current on 5.8 GHz slot antenna. No current detectable despite corona formation because of current sinking directly to ground.

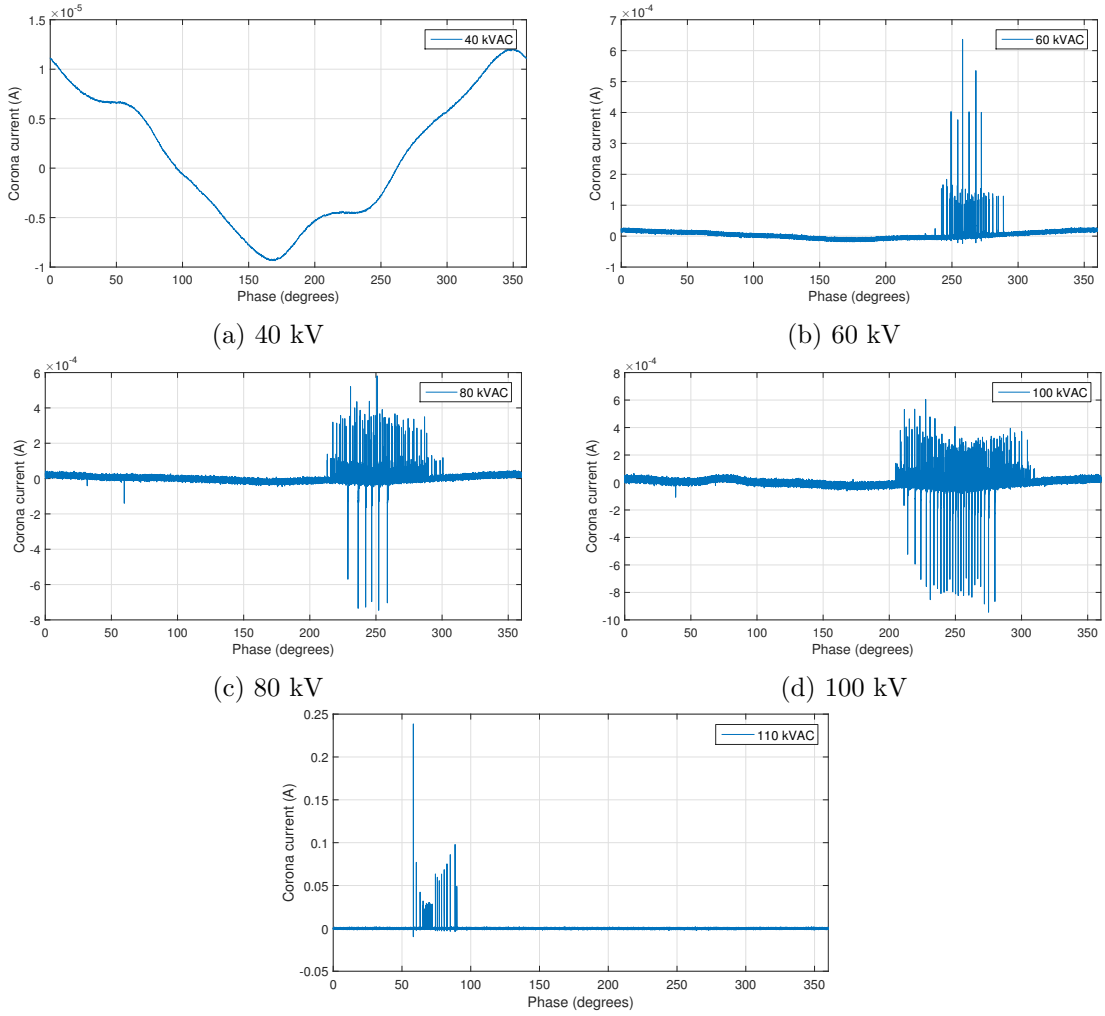

(a) 40 kV

(b) 60 kV

(c) 80 kV

(d) 100 kV

(e) 110 kV

Figure E.63: Corona current on metal sphere of 2.6 cm diameter. Negative corona is observed below 100 kV. At 110 kV, significant positive streamers are observed both visually, and as corona current.

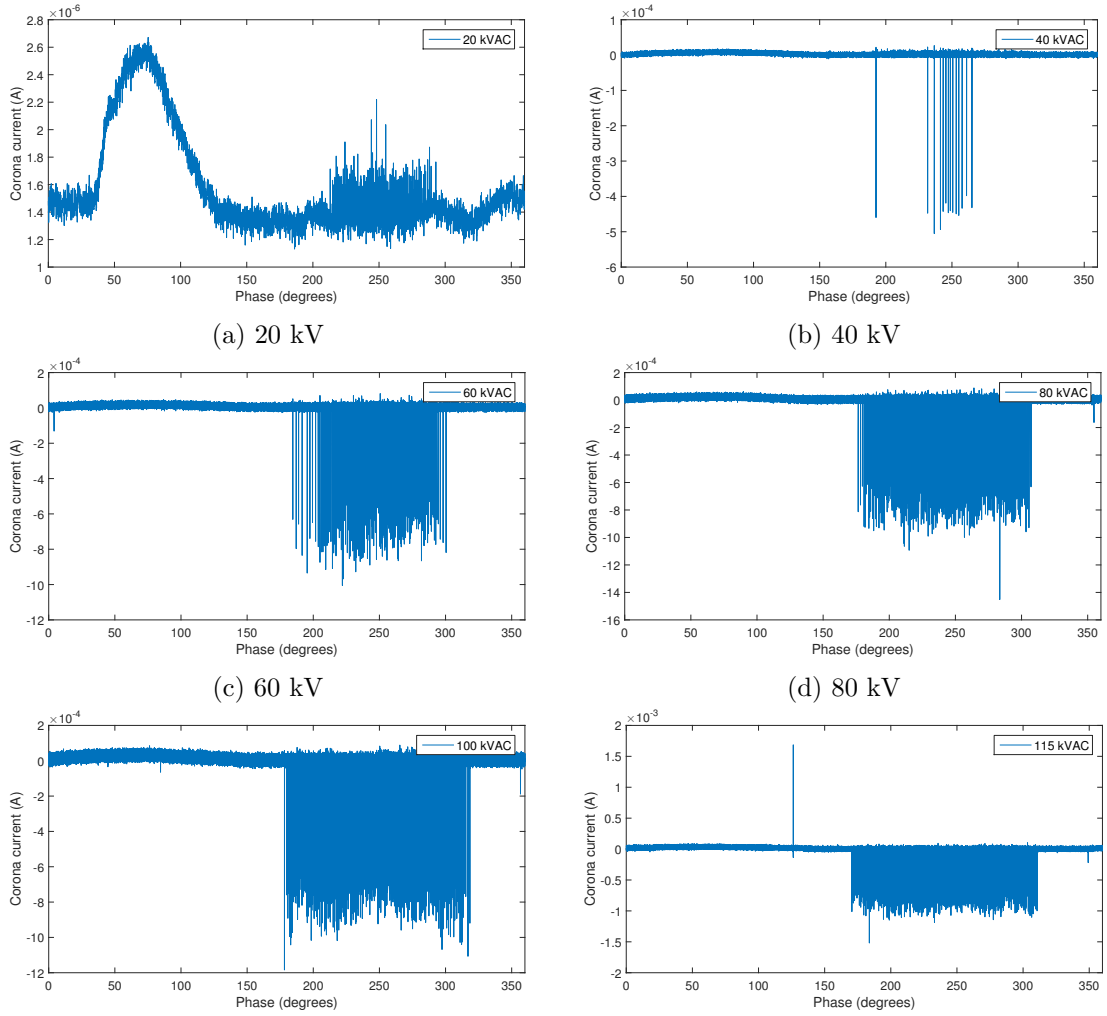

(a) 20 kV

(b) 40 kV

(c) 60 kV

(d) 80 kV

(e) 100 kV

(f) 115 kV

Figure E.64: Corona current on the short 2 mm monopole. Negative corona Trichel pulses are positive glow are the dominant form of corona measured up to 100 kV. At 115 kV intermittent positive streamer formation is observed.

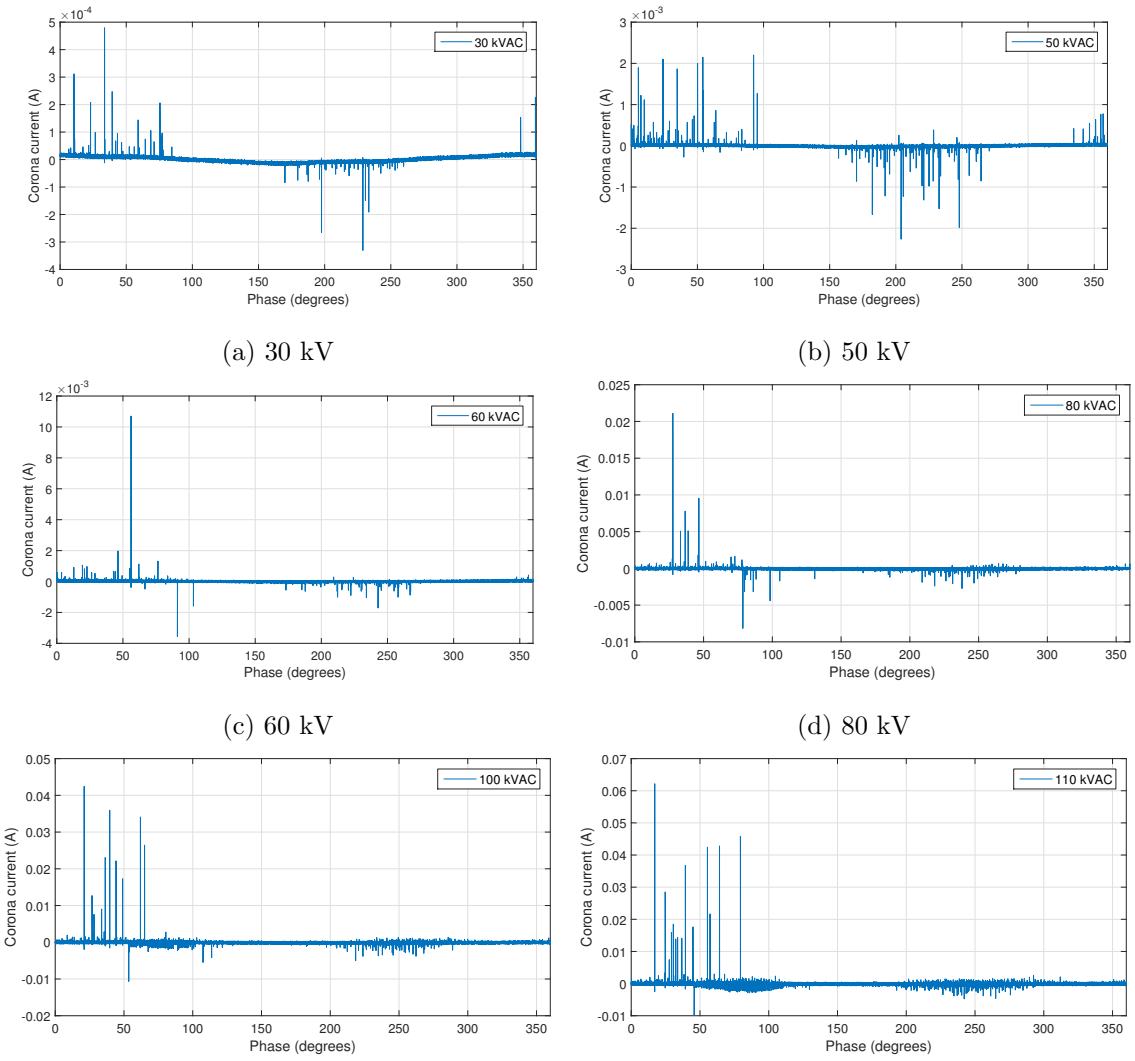

(a) 30 kV

(b) 50 kV

(c) 60 kV

(d) 80 kV

(e) 100 kV

(f) 110 kV

Figure E.65: Corona current on 2.45/5.8 GHz dual-band whip antenna with dielectric shielding. The antenna was oriented parallel to the HV plane.

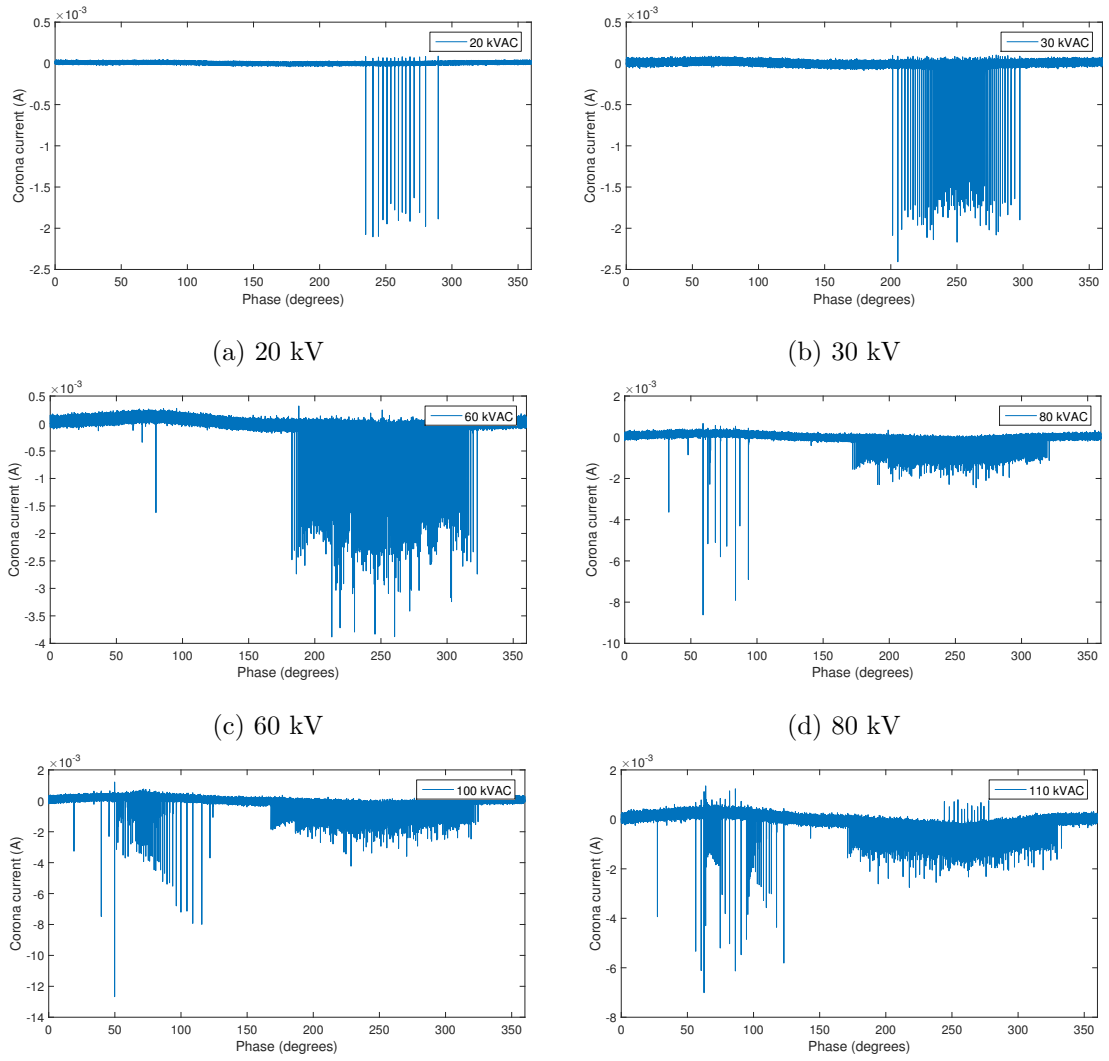

(a) 20 kV

(b) 30 kV

(c) 60 kV

(d) 80 kV

(e) 100 kV

(f) 110 kV

Figure E.66: Corona current on 2.45/5.8 GHz dual-band whip antenna with dielectric shielding removed. The antenna was oriented parallel to the HV plane.

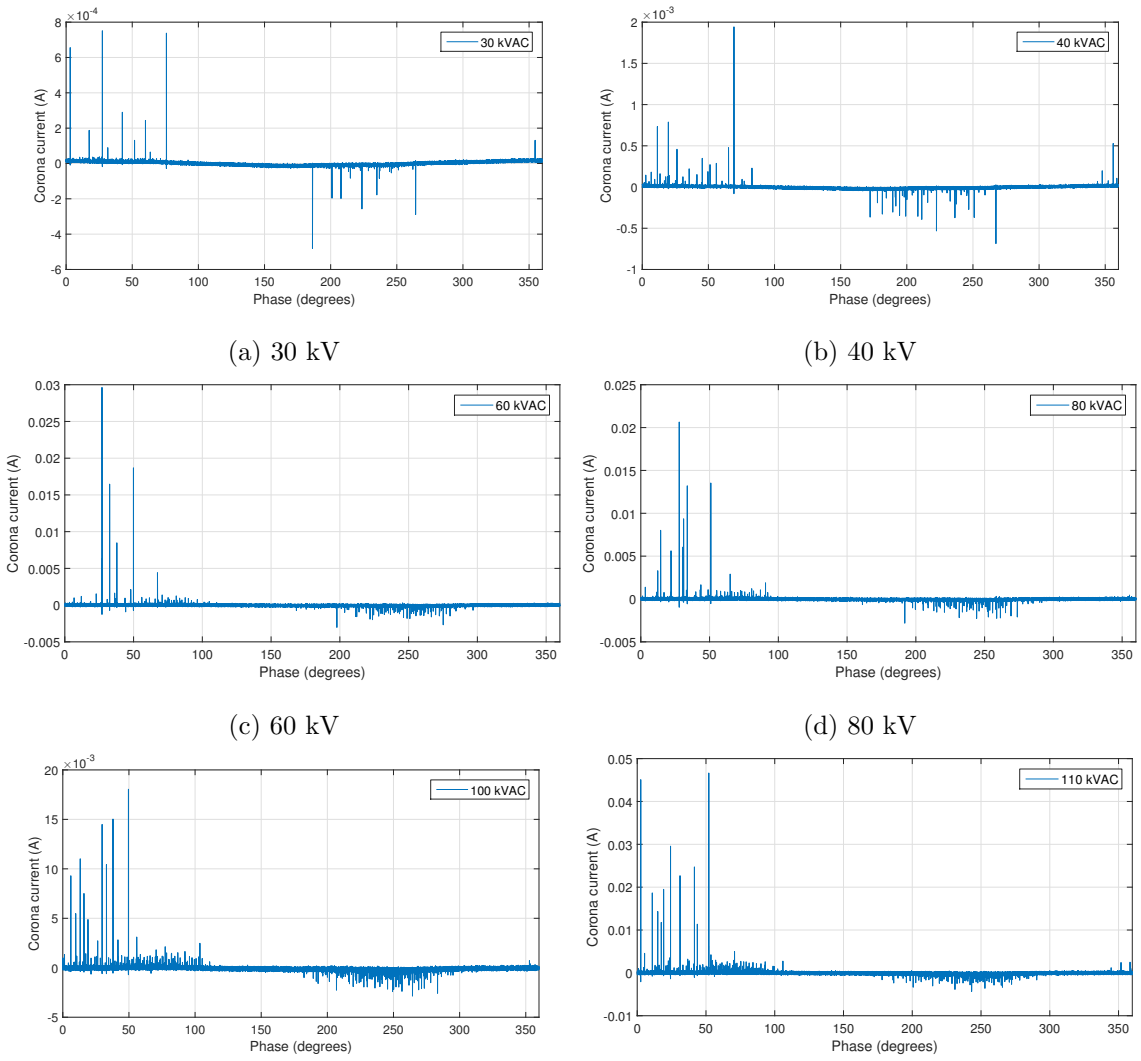

(a) 30 kV

(b) 40 kV

(c) 60 kV

(d) 80 kV

(e) 100 kV

(f) 110 kV

Figure E.67: Corona current on 2.45/5.8 GHz dual-band whip antenna with dielectric shielding. The antenna was oriented perpendicular to the HV plane.

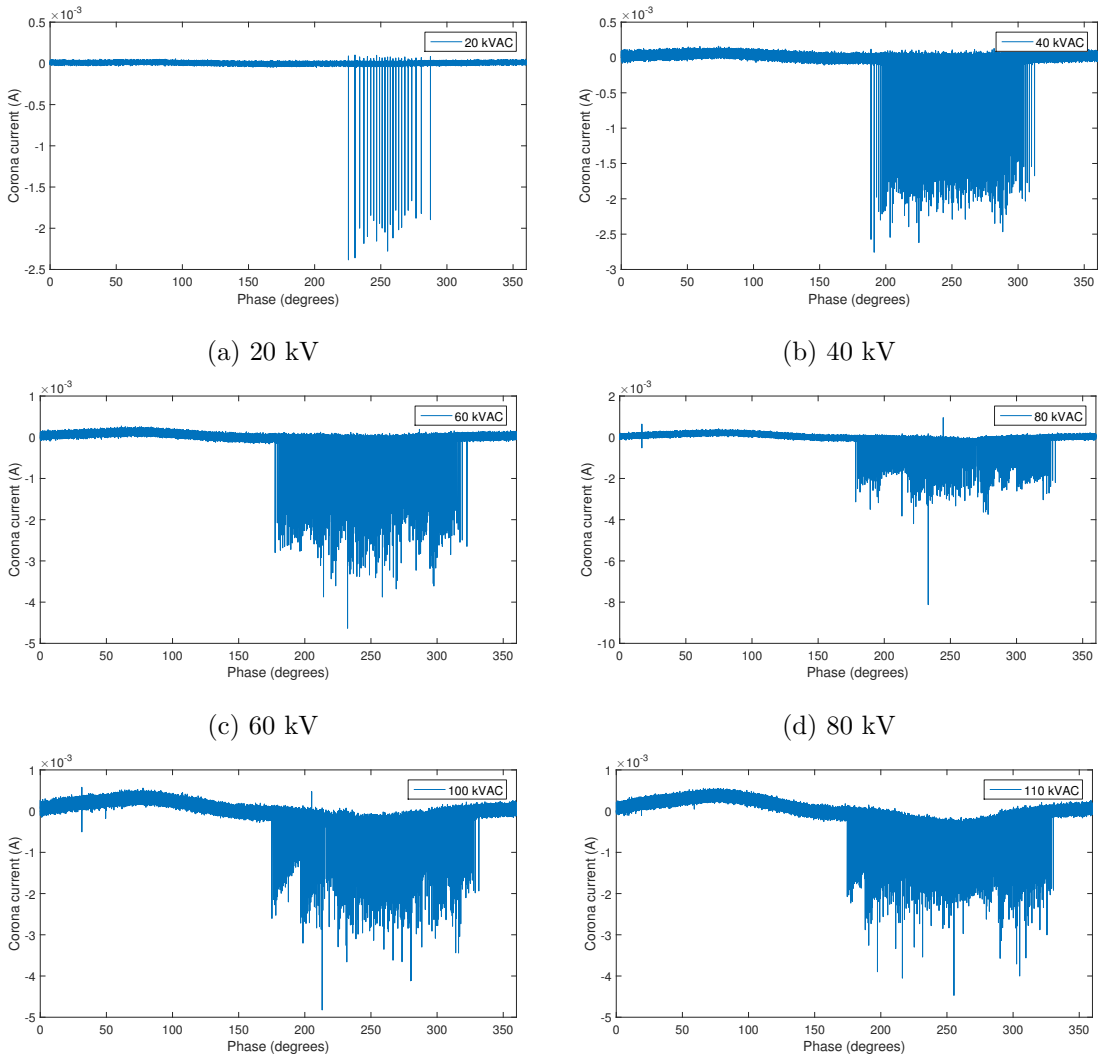

(a) 20 kV

(b) 40 kV

(c) 60 kV

(d) 80 kV

(e) 100 kV

(f) 110 kV

Figure E.68: Corona current on 2.45/5.8 GHz dual-band whip antenna with dielectric shielding removed. The antenna was oriented perpendicular to the HV plane.

Bibliography

[1] "CMD II: Current measurement device."

[2] "Optix CC continuous cast acryic sheet - physcial properties."

[3] "PVC (polyvinyl chloride)."

[4] "Final report on the august 14, 2003 blackout in the united states and canada: Causes and recommensations," tech. rep., U.S.-Canada Power System Outage Task Force, Apr. 2004.

[5] "A policy framework for the 21st century grid: Enabling our secure energy future," tech. rep., Executive Office of the President of the United States, Washington, D.C., June 2011.

[6] "Compact integrated antennas: Designs and applications for the MC1321x, MC1322x, and MC1323x," Application Note AN2731, Freescale Semiconductor, Dec. 2012.

[7] "Smart grid r&d multi-year program plan (2010-2014) - september 2012 update," tech. rep., U.S. Department of Energy, Office of Electricity Delivery & Energy Reliability, Washington, D.C., Sept. 2012.

[8] "Aged national power grid leaves u.s. vulnerable to outages from spring storms," Apr. 2013.

[9] "Economic benefits of increasing electric grid resilience to weather outages," tech. rep., Executive Office of the President of the United States, Washington, D.C., Aug. 2013.

[10] "Large power transformers and the u.s. electric grid," tech. rep., U.S. Department of Energy, Apr. 2014.

[11] Akishev, Y., Kochetov, I., Loboiko, A., and Napartovich, A., "3-dimensional model for trichel pulses: results of numerical studies for air," in *Proc. 8th Int. Symp. on High Pressure Low Temperature Plasma Chemistry (Puhajarve, Estonia)*, pp. 1–5, 2002.

[12] Anatory, J. and Theethayi, N., *Broadband Power-line Communications Systems: Theory & Applications*. WIT Press, Jan. 2010. Ch. 7.

[13] Arora, R., Kalra, P., and Srivastava, R., "An investigation of electromagnetic interference caused by different types of coronas in air," in *Conference Record of the 1992 IEEE International Symposium on Electrical Insulation*, pp. 287–290, June 1992.

[14] Arora, R. and Mosch, W., *High Voltage and Electrical Insulation Engineering*. John Wiley & Sons, Aug. 2011.

[15] Arora, R. and Mosch, W., *High Voltage and Electrical Insulation Engineering*. John Wiley & Sons, Aug. 2011.

[16] Balanis, C. A., *Antenna Theory: Analysis and Design*. John Wiley & Sons, Dec. 2012.

[17] Barnes, J. R., *Robust Electronic Design Reference Book: no special title*. Springer Science & Business Media, Jan. 2004.

[18] Bayliss, C., Bayliss, C. R., and Hardy, B. J., *Transmission and Distribution Electrical Engineering*. Elsevier, 2012.

[19] Becker, K., Kogelschatz, U., Schoenbach, K., and Barker, R., *Non-Equilibrium Air Plasmas at Atmospheric Pressure*. Philadelphia, PA: Institute of Physics Publishing, 2005.

[20] Blandford, R. D. and Thorne, K. S., "Chapter 20. waves in cold plasmas: Two-fluid formalism," in *Applications of Classical Phtsics*, Pasadena, CA: California Istitute of Technology, Apr. 2005.

[21] Bo, A., Weidong, Z., Xiang, C., Jikun, L., Yingbin, S., and Shaoyu, L., "A study on immunity of wireless sensor unit in substation," in *2012 International Symposium on Electromagnetic Compatibility (EMC EUROPE)*, pp. 1–5, Sept. 2012.

[22] Bouhafs, F., Mackay, M., and Merabti, M., "Links to the future: Communication requirements and challenges in the smart grid," *IEEE Power Energy Mag.*, vol. 10, pp. 24–32, Jan. 2012.

[23] Campbell, R. J., "Weather-related power outages and electriv system resiliency," tech. rep., Congressional Research Service, Aug. 2012.

[24] Chen, J. and Davidson, J. H., "Ozone production in the positive DC corona discharge: Model and comparison to experiments," *Plasma Chem. Plasma Process.*, vol. 22, no. 4, pp. 495–522, 2002.

[25] Chen, J. and Davidson, J. H., "Electron density and energy distributions on the positive DC corona: Interpretation for corona-enhanced chemical reactions," *Plasma Chem. Plasma Process.*, vol. 22, June 2002.

[26] Chen, J. and Davidson, J. H., "Model of the negatice DC corona plasma: Comparison to the positive DC corona plasma," *Plasma Chem. Plasma Process.*, vol. 23, Mar. 2003.

[27] Davies, D., "Measurements of swarm parameters in dry air," Theoretical Note 346, Westinghouse Electric Corporation, May 1983.

[28] Dawson, G. and Winn, W., "A model for streamer propagation," *Z. Phys.*, no. 183, pp. 159–171, 1965.

[29] Deschamps, G., "Impedance of an antenna in a conducting medium," *IRE Trans. Antennas Propag.*, vol. 10, pp. 648–650, Sept. 1962.

[30] Elgohary, N. A., "Design manual for high voltage transmission lines," Bulletin 1724E-200, U.S. Department of Agriculture, Rural Utilities Service, May 2009.

[31] Fan, Z., Kulkarni, P., Gormus, S., Efthymiou, C., Kalogridis, G., Sooriyabandara, M., Zhu, Z., Lambotharan, S., and Chin, W. H., "Smart grid communications: Overview of research challenges, solutions, and standardization activities," *IEEE Commun. Surv. Tutor.*, vol. 15, no. 1, pp. 21–38, 2013.

[32] Fang, X., Misra, S., Xue, G., and Yang, D., "Smart grid - the new and improved power grid: A survey," *IEEE Commun. Surv. Tutor.*, vol. 14, no. 4, pp. 944–980, 2012.

[33] Galli, S., Scaglione, A., and Wang, Z., "Power line communications and the smart grid," in *Smart Grid Communications (SmartGridComm), 2010 First IEEE International Conference on*, pp. 303 –308, Oct. 2010. 00067.

[34] Galli, S., Scaglione, A., and Wang, Z., "For the grid and through the grid: The role of power line communications in the smart grid," *Proc. IEEE*, vol. 99, pp. 998 –1027, June 2011.

[35] Gillman, E. D., Foster, J. E., and Blamkson, I. M., "Review of leading approaches for mitigating hypersonic vehicle communications blackout and a method of ceramic particulate injection via cathode spot arcs for blackout mitigation," Tech. Rep. NASA/TM-2010-216220, University of Michigan/Glenn Research Center, Feb. 2010.

[36] Goldman, M. and Sigmond, R., "Corona and insulation," *IEEE Trans. Electr. Insul.*, vol. EI-17, pp. 90–105, Apr. 1982.

[37] Gungor, V., Lu, B., and Hancke, G., "Opportunities and challenges of wireless sensor networks in smart grid," *IEEE Trans. Ind. Electron.*, vol. 57, pp. 3557–3564, Oct. 2010.

[38] Hartunian, R. A., Stewart, G. E., Fergason, S. D., Curtiss, T. J., and Seibold, R. W., "Causes and mitigation of radio frequency (RF) blackout during reentry of reusable launch vehicles," Contractor Final Report ATR-2007(5309)-1, The Aerospace Corporation, El Segundo, CA, Jan. 2007.

[39] Heald, M. A. and Wharton, C. B., *Plasma Diagnositics With Microwaves*. New York: Wiely, 1965. 00000.

[40] Helliwell, R. A., *Whistlers and Related Ionospheric Phenomena*. Courier Corporation, June 2014.

[41] Heroux, P., Maruvada, P., and Trinh, N., "High voltage AC transmission lines: Reduction of corona under foul weather," *IEEE Trans. Power Appar. Syst.*, vol. PAS-101, pp. 3009–3017, Sept. 1982.

[42] Hodara, H., "The use of magnetic fields in the elimination of the re-entry radio blackout," *Proc. IRE*, vol. 49, no. 12, pp. 1825–1830, 1961.

[43] IEEE 802.15, "IEEE 802.15 WPAN - task group 4g," 2014.

[44] Iizuka, K. and King, R., "The dipole antenna immersed in a homogeneoous conducting medium," *IRE Trans. Antennas Propag.*, vol. 10, pp. 384–392, July 1962.

[45] Itikawa, Y., "Cross sections for electron collisions with nitrogen molecules," *J. Phys. Chem. Ref. Data*, vol. 35, no. 1, p. 31, 2006.

[46] Jia, J. and Meng, J., "Partial discharge impulsive noise in electricity substations and the impact on 2.4 GHz and 915 MHz ZigBee communications," in *2013 IEEE Power and Energy Society General Meeting (PES)*, pp. 1–5, July 2013.

[47] Juette, G., "Evaluation of television interference from high-voltage transmission lines," *IEEE Trans. Power Appar. Syst.*, vol. PAS-91, pp. 865–873, May 1972.

[48] Kang, W. S., Park, J. M., Kim, Y., and Hong, S. H., "Numerical study on influences of barrier arrangements on dielectric barrier discharge characteristics," *IEEE Trans. Plasma Sci.*, vol. 31, pp. 504–510, Aug. 2003.

[49] Kezunovic, M., "Smart fault location for smart grids," *IEEE Trans. Smart Grid*, vol. 2, pp. 11–22, Mar. 2011.

[50] Kiessling, F., Nefzger, P., Nolasco, J. F., and Kaintzyk, U., *Overhead Power Lines: Planning, Design, Construction*. Springer, July 2014.

[51] Kinzer, G. and McGee, J., "Army-navy precipitation-static project: Part IV-investigations of methods for reducing precipitation-static radio interference," *Proc. IRE*, vol. 34, pp. 234–240, May 1946.

[52] Kofoid, M., "Permanently magnetized ferrite antenna windows for improving electromagnetic wave transmission through a plasma," *IEEE Trans. Antennas Propag.*, vol. 14, no. 2, pp. 251–252, 1966.

[53] Korotkevich, A. O., Newell, A. C., and Zakharov, V. E., "Communication through plasma sheaths," *J. Appl. Phys.*, vol. 102, no. 8, p. 083305, 2007.

[54] Kreikebaum, F., Das, D., Yang, Y., Lambert, F., and Divan, D., "Smart wires — a distributed, low-cost solution for controlling power flows and monitoring transmission lines," in *Innovative Smart Grid Technologies Conference Europe (ISGT Europe), 2010 IEEE PES*, pp. 1–8, IEEE, Oct. 2010.

[55] Kulikovsky, A. A., "Positive streamer between parallel plate electrodes in atmospheric pressure air," *J. Phys. Appl. Phys.*, vol. 30, no. 3, p. 441, 1997.

[56] Langan, M. and Barr, "CapX hamptop-rochester-la crosse 345kv and 161kv transmission lines project: Final environmental impact statement," tech. rep., Minnesota Department of Commerce, Aug. 2011.

[57] Laroussi, M., "Interaction of microwaves with atmospheric pressure plasmas," *Int. J. Infrared Millim. Waves*, vol. 16, no. 12, pp. 2069–2083, 1995. 00048.

[58] Laroussi, M. and Anderson, W. T., "Attenuation of electromagnetic waves by a plasma layer at atmospheric pressure," *Int. J. Infrared Millim. Waves*, vol. 19, no. 3, pp. 453–464, 1998.

[59] Li, Z., Huang, Y., Wang, X., Zeng, R., Yao, L., and Sasse, C., "Immunity research of wireless communication in switch cabinet monitoring and control," in *2006 IEEE International Symposium on Electromagnetic Compatibility, 2006. EMC 2006*, vol. 2, pp. 351–355, Aug. 2006.

[60] Lo, C.-H. and Ansari, N., "The progressive smart grid system from both power and communications aspects," *IEEE Commun. Surv. Tutor.*, vol. 14, no. 3, pp. 799–821, 2012.

[61] Loeb, L. B., *Fundamental Processes of Electrical Discharge In Gasses*. New York: John Wiley & Sons, Inc., 1939.

[62] Manning, R. M., "Analysis of electromagnetic wave propagation in a magnetized re-entry plasma sheath via the kinetic equation," tech. rep., Glenn Research Center, Cleveland, OH, Dec. 2009.

[63] Maruvada, P. S., *Corona Performance of High-voltage Transmission Lines*. Research Studies Press, Jan. 2000.

[64] Meek, J. M. and Craggs, J. D., *Electrical Breakdown of Gases*. Oxford: Clarendon Press, 1953.

[65] Middleton, D., "Statistical-physical models of electromagnetic interference," *IEEE Trans. Electromagn. Compat.*, vol. EMC-19, pp. 106–127, Aug. 1977.

[66] Middleton, D., "Canonical non-gaussian noise models: Their implications for measurement and for prediction of receiver performance," *IEEE Trans. Electromagn. Compat.*, vol. EMC-21, pp. 209–220, Aug. 1979.

[67] Milligan, T. A., *Modern Antenna Design*. John Wiley & Sons, July 2005.

[68] Miron, D. B., *Small Antenna Design*. Newnes, Mar. 2006.

[69] Moghe, R., Iyer, A., Lambert, F., and Divan, D., "A robust smart sensor for smart substations," in *2012 IEEE Power and Energy Society General Meeting*, pp. 1–8, July 2012.

[70] Moghe, R., Iyer, A., Lambert, F., and Divan, D., "A low-cost wireless voltage sensor for monitoring MV/HV utility assets," *IEEE Trans. Smart Grid*, vol. 5, pp. 2002–2009, July 2014.

[71] Moghe, R., Lambert, F. C., and Divan, D., "Smart "stick-on" sensors for the smart grid," *IEEE Trans. Smart Grid*, vol. 3, pp. 241–252, Mar. 2012.

[72] Mohsenian-Rad, A.-H., Wong, V., Jatskevich, J., Schober, R., and Leon-Garcia, A., "Autonomous demand-side management based on game-theoretic energy consumption scheduling for the future smart grid," *IEEE Trans. Smart Grid*, vol. 1, pp. 320–331, Dec. 2010.

[73] Moreno, V. and Gorur, R., "Impact of corona on the long-term performance of nonceramic insulators," *IEEE Trans. Dielectr. Electr. Insul.*, vol. 10, pp. 80–95, Feb. 2003.

[74] Morris, R. and Rakoshdas, B., "An investigation of corona loss and radio interference from transmission line conductors at high direct voltages," *IEEE Trans. Power Appar. Syst.*, vol. 83, pp. 5–16, Jan. 1964.

[75] Morys, M., *Patch Antenna Characterization in a High-Voltage Corona Plasma*. Master of science in electrical and computer engineering, Georgia Institute of Technology, Atlanta, GA, 2013.

[76] Nasser, E., *Fundamentals of Gaseous Ionization and Plasma Electronics*. New York: Wiley-Interscience, 1971.

[77] Olivares, D., Mehrizi-Sani, A., Etemadi, A., Canizares, C., Iravani, R., Kazerani, M., Hajimiragha, A., Gomis-Bellmunt, O., Saeedifard, M., Palma-Behnke, R., Jimenez-Estevez, G., and Hatziargyriou, N., "Trends in microgrid control," *IEEE Trans. Smart Grid*, vol. 5, pp. 1905–1919, July 2014.

[78] Parfomak, P. W., "Physical security of the u.s. power grid: High-voltage transformer substations," CRS Report R43604, Congressional Resesearch Service, June 2014.

[79] Paschen, F., "Ueber die zum funkenübergang in luft, wasserstoff und kohlensäure bei verschiedenen drucken erforderliche potentialdifferenz," *Ann. Phys.*, vol. 273, no. 5, pp. 69–96, 1889.

[80] Peek, F. W., *Dielectric Phenomena in High Voltage Engineering*. New York: McGraw-Hill, 1929.

[81] Phillips, D., Olsen, R., and Pedrow, P., "Corona onset as a design optimization criterion for high voltage hardware," *Dielectr. Electr. Insul. IEEE Trans. On*, vol. 7, no. 6, pp. 744–751, 2000.

[82] Pozar, D. M., *Microwave Engineering*. Wiley, Aug. 1997.

[83] Qingyun, Y., Xijun, Z., Guozhi, S., and Jie, Y., "Research on frequency characteristics of signal radiated from corona discharge," in *8th International Conference on Electronic Measurement and Instruments, 2007. ICEMI '07*, pp. 3–913–3–916, Aug. 2007.

[84] Queenslan Government Department of Agriculture and Fisheries, "Measuring salinity with conductivity meters."

[85] Raizer, Y. P., *Gas Discharge Physics*. Springer Berlin Heidelberg, Sept. 2011.

[86] Rizk, F. A. and Trinh, G. N., *High Voltage Engineering*. Boca Raton, FL: CRC Press, Taylor & Francis Group, LLC, 2014.

[87] Sacuto, F., Labeau, F., and Agba, B., "Wide band time-correlated model for wireless communications under impulsive noise within power substation," *IEEE Trans. Wirel. Commun.*, vol. 13, pp. 1449–1461, Mar. 2014.

[88] Sattari, P., Castle, G. S. P., and Adamiak, K., "Numerical simulation of trichel pulses in a negative corona discharge in air," *IEEE Trans. Ind. Appl.*, vol. 47, pp. 1935–1943, July 2011.

[89] Sattari, P., Castle, G., and Adamiak, K., "Numerical simulation of trichel pulses in a negative corona discharge in air," *Ind. Appl. IEEE Trans. On*, vol. 47, no. 4, pp. 1935–1943, 2011.

[90] Setient Energy, Inc., "Sentient energy: MM3 intelligent sensor."

[91] Sum, C.-S., Kojima, F., and Harada, H., "Coexistence of homogeneous and heterogeneous systems for IEEE 802.15.4g smart utility networks," in *2011 IEEE Symposium on New Frontiers in Dynamic Spectrum Access Networks (DySPAN)*, pp. 510–520, May 2011.

[92] Townsend, J. S., *The Theory of Ionization of Gases by Collision*. London: Constable & Company Ltd, 1910.

[93] Tran, T., Golosnoy, I., Lewin, P., and Georghiou, G., "Two dimensional studies of trichel pulses in air using the finite element method," in *IEEE Conference on Electrical Insulation and Dielectric Phenomena, 2009. CEIDP '09*, pp. 592–595, Oct. 2009.

[94] Trinh, N., "Partial discharge XIX: discharge in air part i: physical mechanisms," *IEEE Electr. Insul. Mag.*, vol. 11, pp. 23–29, Mar. 1995.

[95] Valenta, C. R., Graf, P. A., Trotter, M. S., Koo, G. A., Durgin, G. D., and Schafer, B. J., "Backscatter channel measurements at 5.8 GHz across high-voltage corona," (Hilo, HI), Nov. 2010.

[96] Van Gaens, W. and Bogaerts, A., "Kinetic modelling for an atmospheric pressure argon plasma jet in humid air," *J. Phys. Appl. Phys.*, vol. 47, p. 079502, Feb. 2014.

[97] Volakis, J., Chen, C.-C., and Fujimoto, K., *Small Antennas:Miniaturization Techniques & Applications*. McGraw Hill Professional, June 2010.

[98] Warne, L. K., Jorgenson, R. E., and Nicolaysen, S. D., "Ionization coefficient approach to modeling breakdown in nonuniform geometries," Tech. Rep. SAND2003-4078, Sandio National Laboratories, Albuquerque, NM, Nov. 2003.

[99] Weidong, Z., Bo, A., Xiang, C., Jikun, L., Yingbin, S., and Shaoyu, L., "A study on electromagnetic disturbance in substation to wireless sensor unit," in *2012 International Symposium on Electromagnetic Compatibility (EMC EUROPE)*, pp. 1–6, Sept. 2012.

[100] Zangwill, A., *Modern Electrodynamics*. Cambridge University Press, 2013.

[101] Zhang, J. and Adamiak, K., "A multi-species DC stationary model for negative corona discharge in oxygen; point-plane configuration," *J. Electrost.*, vol. 65, pp. 459–464, June 2007.

[102] Zimmermann, H., "OSI reference model–the ISO model of architecture for open systems interconnection," *IEEE Trans. Commun.*, vol. 28, pp. 425–432, Apr. 1980.